

# Computational modelling of the Fischer-Tropsch reaction on iron carbides

## ***Citation for published version (APA):***

Broos, R. J. P. (2020). *Computational modelling of the Fischer-Tropsch reaction on iron carbides*. [Phd Thesis 1 (Research TU/e / Graduation TU/e), Chemical Engineering and Chemistry]. Technische Universiteit Eindhoven.

## ***Document status and date:***

Published: 12/02/2020

## ***Document Version:***

Publisher's PDF, also known as Version of Record (includes final page, issue and volume numbers)

## ***Please check the document version of this publication:***

- A submitted manuscript is the version of the article upon submission and before peer-review. There can be important differences between the submitted version and the official published version of record. People interested in the research are advised to contact the author for the final version of the publication, or visit the DOI to the publisher's website.
- The final author version and the galley proof are versions of the publication after peer review.
- The final published version features the final layout of the paper including the volume, issue and page numbers.

[Link to publication](#)

## ***General rights***

Copyright and moral rights for the publications made accessible in the public portal are retained by the authors and/or other copyright owners and it is a condition of accessing publications that users recognise and abide by the legal requirements associated with these rights.

- Users may download and print one copy of any publication from the public portal for the purpose of private study or research.
- You may not further distribute the material or use it for any profit-making activity or commercial gain
- You may freely distribute the URL identifying the publication in the public portal.

If the publication is distributed under the terms of Article 25fa of the Dutch Copyright Act, indicated by the "Taverne" license above, please follow below link for the End User Agreement:

[www.tue.nl/taverne](http://www.tue.nl/taverne)

## ***Take down policy***

If you believe that this document breaches copyright please contact us at:

[openaccess@tue.nl](mailto:openaccess@tue.nl)

providing details and we will investigate your claim.

A 3D molecular model illustrating the Fischer-Tropsch reaction on an iron carbide surface. The surface is composed of large, orange-red spheres representing iron atoms. Various molecules are shown: carbon monoxide (black and white spheres), carbon dioxide (black, white, and red spheres), and water (white and red spheres). Some molecules are adsorbed on the surface, while others are in the gas phase above it. The background is a dark gray gradient.

# Computational Modelling of the Fischer-Tropsch Reaction on Iron Carbides

**Robin J. P. Broos**

---

# Computational Modelling of the Fischer-Tropsch Reaction on Iron Carbides

PROEFSCHRIFT

ter verkrijging van de graad van doctor aan de Technische Universiteit Eindhoven,  
op gezag van de rector magnificus prof.dr.ir. F.P.T. Baaijens, voor een commissie  
aangewezen door het College voor Promoties, in het openbaar te verdedigen op  
woensdag 12 februari 2020 om 16:00 uur

door

Robin Johannes Petrus Broos

geboren te Roosendaal en Nispen

---

Dit proefschrift is goedgekeurd door de promotoren en de samenstelling van de promotiecommissie is als volgt:

voorzitter:	prof.dr. F. Gallucci
1 <sup>e</sup> promotor:	prof.dr.ir. E.J.M. Hensen
copromotor:	dr.ir. I.A.W. Filot
leden:	prof.dr.ir. K.P. de Jong (Universiteit Utrecht)
	prof.dr. G. Rothenberg (Universiteit van Amsterdam)
	dr.ir. B. Ensing (Universiteit van Amsterdam)
	prof.dr.ir. J.A.M. Kuipers
	dr.ir. J. van der Schaaf

*Het onderzoek dat in dit proefschrift wordt beschreven is uitgevoerd in overeenstemming met de TU/e Gedragscode Wetenschapsbeoefening.*



---

*To my parents and my brother*

---

**Robin J. P. Broos**

*Computational modelling of the Fischer-Tropsch reaction on iron carbides*

A catalogue record is available from the Eindhoven University of Technology Library

**ISBN: 978-90-386-4978-8**

Copyright © 2020 by Robin J. P. Broos



*The work described in this thesis has been carried out at the Inorganic Materials & Catalysis group at the Eindhoven University of Technology.*



*The Netherlands Center for Multiscale Catalytic Energy Conversion (MCEC) is acknowledged for financial support.*



*The Netherlands Organization for Scientific Research is acknowledged for providing access to computational resources.*



*This work was carried out on the Dutch national e-infrastructure with the support of SURF Cooperative.*

Printed by: Proefschrift Maken

Cover design: Robin J. P. Broos

## Table of contents

1. Introduction	1
1.1 Introduction	1
1.2 Catalysis	2
1.3 A brief history of the Fischer-Tropsch reaction	3
1.4 Proposed mechanisms in the Fischer-Tropsch reaction	6
1.5 Fischer-Tropsch catalysts	7
1.6 Iron-based Fischer-Tropsch catalysts	7
1.7 Fischer Tropsch to olefins	9
1.8 Scope of the thesis	10
2. Computational Methods	15
2.1 Introduction	15
2.2 Many-body calculations	15
2.3 Microkinetics simulations	22
3. A Quantum-Chemical DFT Study on the CO dissociation on various $\chi$ -Fe <sub>5</sub> C <sub>2</sub> Hägg Carbide surfaces	31
3.1 Introduction	32
3.2 Method	33
3.3 Results and Discussion	35
3.4 Conclusions	51
Appendix A	54
A.1 Derivation of the rate equations	54
A.2 Adsorption Energies for CO adsorption on Hägg carbide surfaces	58
A.3 Kinetic parameters for Direct and H-assisted CO dissociation on the (510) <sub>0.0</sub> surface	58
4. First-principles based microkinetics simulations of the Fischer-Tropsch reaction on $\chi$ -Fe <sub>5</sub> C <sub>2</sub>	61
4.1 Introduction	62
4.2 Method	63
4.3 Results and discussion	67
4.4. Conclusions	86
Appendix B	89
Appendix B.1 Geometries from DFT	89
Appendix B.2 Microkinetics simulations at the zero-conversion limit	98
Appendix B.3 Microkinetics simulations in the CSTR model	99
5. A Quantum-Chemical DFT and Microkinetic Modelling Study of the Fischer-Tropsch Reaction on $\epsilon$ -Fe <sub>2</sub> C	101
5.1 Introduction	102
5.2 Methods	104
5.3 Results and Discussion	107

5.5 Operation regime $\epsilon$ -Fe-carbide	130
5.6 Conclusions	132
Appendix C	136
Appendix C.1 Geometries from DFT	136
Appendix C.2 Microkinetics simulations	141
6. A quantum-chemical study of CO dissociation mechanism on low-index Miller planes of $\theta$ -Fe <sub>3</sub> C	145
6.1 Introduction	146
6.2 Methods	147
6.3 Results and Discussion	150
6.4 Conclusions	161
Appendix D	165
Appendix D.1 Geometries from DFT	165
Appendix D.2 Relative reactivity and relative rates	169
Appendix D.3 Atomic population analysis	171
Summary and Outlook	175
List of Publications	181
Acknowledgements	183
Curriculum Vitae	187

# 1. Introduction

## 1.1 Introduction

Over the last century, humanity witnessed a dramatic increase in the energy demand (Figure 1.1). The energy demand is expected to double by 2050 with respect to the current energy demand. Most of the energy demand is covered by fossil resources such as gas, oil and coal. The rapid growth of the energy demand in the last decades has already led to depletion of the easily accessible gas and oil reserves. At the same time, it is becoming increasingly clear that the emissions of greenhouse gasses such as CO<sub>2</sub> lead to climate change. Based on predictions how burning of fossil resources will adversely affect the climate, there is growing consensus that a 'business as usual' scenario is not realistic. Accordingly, alternative renewable energy sources need to be tapped into to replace gas, oil and coal.

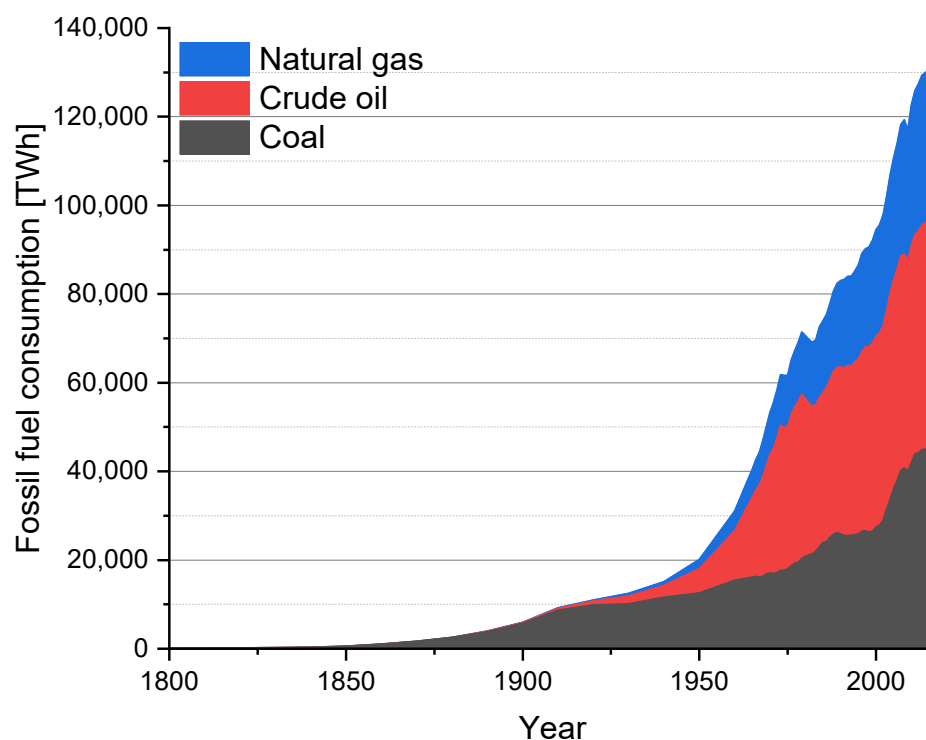


**Figure 1.1:** Annual usage of fossil feedstock between 1800 and 2017.[1]

Sustainable alternatives such as solar, geothermal and wind power are coming up, but they are relatively sparse at the moment and their growth rate is insufficient to bridge the gap to a society that runs solely on sustainable energy. Nuclear power is an interesting and robust technology for electricity generation with low CO<sub>2</sub> emissions, but suffers from a very negative public opinion, high investment cost and long lead times. Finally, biomass as a renewable resource competes with food production, meaning it is not a viable main substitute of fossil resources.

In the past century, a significant amount of research and investment has been made to reduce the dependency on crude oil by the utilization of other carbon-containing resources. There remains significant interest in using coal in view of its abundance and, relatedly, the low prices in different parts of the world. The main problem with coal is that it has the lowest H/C ratio among fossil resources, meaning that the CO<sub>2</sub> emissions per unit of energy generated are higher than for oil and gas. Furthermore, the chemical composition of coal is relatively stable and its direct conversion, other than burning it for its caloric value, is therefore difficult. Hence, catalysts play a pivotal role in coal utilization. Natural gas, which on the contrary has the highest H/C ratio, is therefore increasingly considered as a transition resource, given its relatively low CO<sub>2</sub> emissions. Moreover, technological developments have led to opportunities to use other natural gas resources such as shale gas.

## 1.2 Catalysis

Catalysts modify the rate of a chemical reaction by offering a different reaction pathway. The catalyst converts the reactants to the products, without being consumed in the process.

Catalysis is often categorized by the phases wherein the reactants, products and the catalyst material are situated. When the catalyst is in a different phase as the reactants or products, this is termed heterogeneous catalysis. When the catalyst is in the same phase as the reactants or products, this is termed homogeneous catalysis. The majority of the bulk industrial processes utilize heterogeneous catalysts, whereas homogeneous catalysis is more often employed in the food industry or in pharmaceuticals.[2]

An overall reaction from reactants to products can be decomposed into so-called elementary reaction steps. These elementary reaction steps correspond to the minimum energy pathways over a potential energy surface that connects the two stable states that are located on either side of a dividing

surface.[3] A catalyst acts by offering a new route over the potential energy surface that is lower in energy than the non-catalytic route. This is schematically depicted in Figure 1.2.

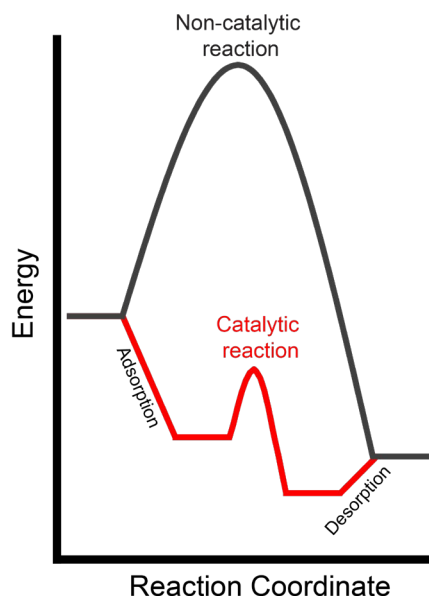


**Figure 1.2:** Reaction progress in an uncatalysed reaction (black) and a catalysed reaction (red). Note that the catalytic pathway typically consists of multiple elementary reaction steps.

For the catalyst to participate in the conversion process, the reactants first need to adsorb onto the catalyst leading to bond formation. Bond formation between catalyst and adsorbate typically leads to destabilization of the chemical bonds within the adsorbate by electron donation into anti-bonding orbitals, thereby activating the complex for chemical conversion. Via one or multiple elementary reaction steps, the reactant adsorbate is converted to the (adsorbed) product state, after which the adsorbate leaves the catalyst in a desorption step. This brings the catalyst back into its original state, closing the catalytic cycle.

### 1.3 A brief history of the Fischer-Tropsch reaction

A prominent heterogeneously catalysed process for the utilization of non-oil-based feedstocks is Fischer-Tropsch synthesis. Synthesis gas derived from carbonaceous feedstock such as natural gas, coal or biomass is selectively converted to liquid fuels and chemical feedstocks. A schematic representation of this process can be found in Figure 1.3.

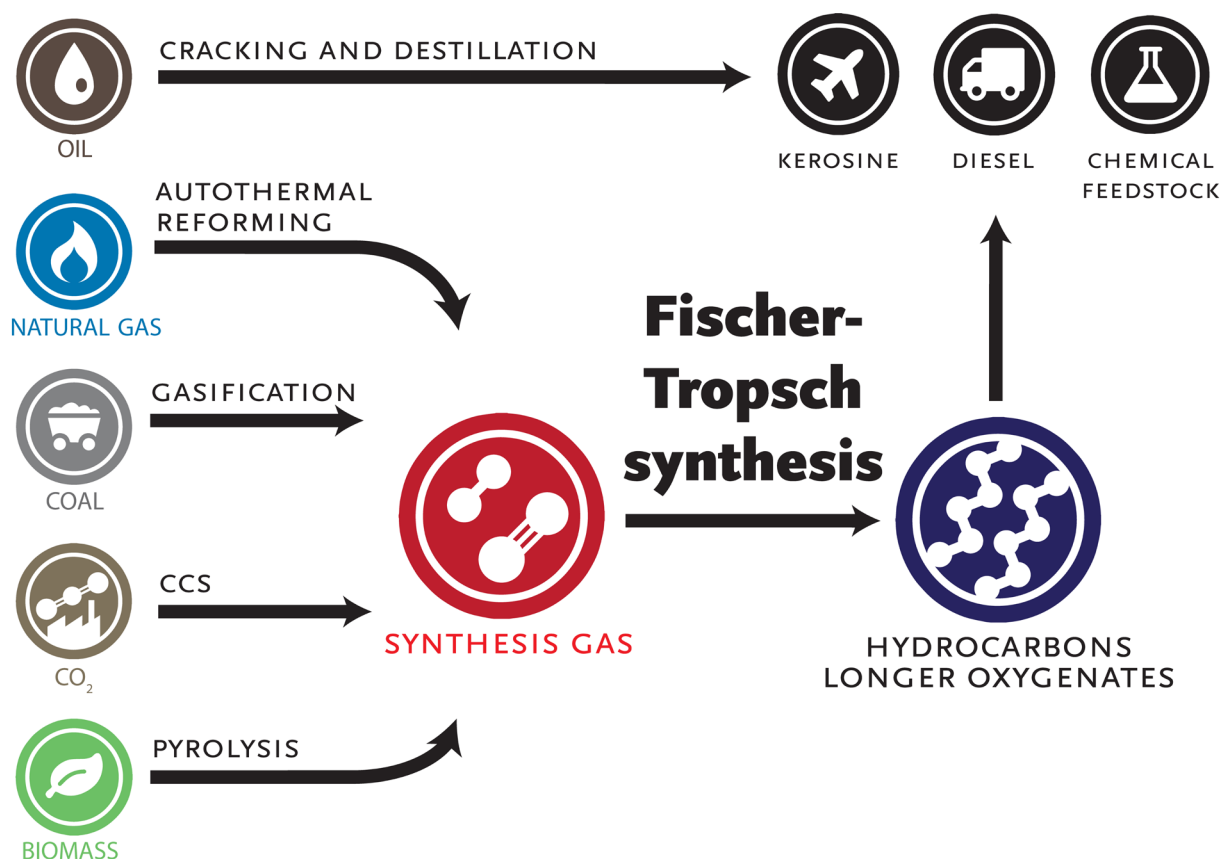


**Figure 1.3:** A schematic representation of the different feedstocks that can be used for the production of liquid fuels and chemicals. Picture taken from reference.[4]

Nowadays, natural gas and coal are respectively being used as the feedstock in gas-to-liquid (GTL) and coal-to-liquid (CTL) processes. It is prospected though that in the near future, biomass and CO<sub>2</sub> can be employed as the feedstock for the Fischer-Tropsch synthesis reaction in either a CO<sub>2</sub>-neutral or even negative CO<sub>2</sub> emission scenario. A brief overview of the history of the Fischer-Tropsch process is provided below.

In the past, boycotts on oil, (e.g. during World War II in Germany in the beginning of the 1940s, and the Apartheid regime in South-Africa during the 1960s), have led to the development and growth of the Fischer-Tropsch Synthesis reaction. The Fischer-Tropsch reaction was discovered in Germany in 1925 at the Kaiser-Wilhelm-Institut für Kohlenforschung, by Hans Tropsch and Franz Fischer. The first commercial Fischer-Tropsch plant was built in 1934 by Ruhrchemie A.G. and went into operation in 1936. By 1940, the plant produced over 1,000,000 tons of liquid products per year.[5] Due to a fear of an impending shortage of petroleum, the interest in the FT process was kept alive. An FTS plant was therefore built by Hydrocarbon Research Inc. in the 1950s in Brownsville,



Texas, producing 5000 barrels per day.[6] This process used syngas produced from methane, but an increase in the methane price caused the plant to be shut down.[7]

Due to this fear and the predictions of increasing oil prices worldwide, the Suid-Afrikaanse Steenkool-, Olie- en Gasmaatskappy (Sasol) was founded in 1950. In the early years, Sasol focused on the conversion of coal into synthetic fuels and chemicals. Later, Sasol also started to focus on using GTL plants. Sasol started building their first plant in 1954, which became operational in 1955 in Sasolburg, South Africa, and produced around 3000 barrels per day.[8] Due to the support of western nations of Israel during the Yom Kippur War, an oil embargo was issued in October 1973 by the members of the OPEC.[9] This led to the so-called first oil shock. By March 1974, the price of oil had risen by 400%[10]. Consequently, Sasol decided to build two more plants, delivered in 1980 and 1982 in Secunda, South Africa, producing 25,000 barrels per day.[8] Together with Qatar Petroleum, Sasol built the Oryx GTL plant in 2007 in Ras Laffan, Qatar, with a production of 34,000 barrels per day. In 2014, Escravos, a plant similar to the Oryx GTL plant, was commissioned in Nigeria by a collaboration between Sasol, Chevron and the Nigerian National Petroleum Corporation.

Further development of catalysts for the Fischer-Tropsch reaction has been performed by companies such as Royal Dutch Shell and Sasol, which focus on converting natural gas, a waste product from the oil fields. In 1992, Mossgas (merged to PetroSA in 2002) built world's first GTL plant in Mossel Bay, South Africa, which used Fe as a catalyst and nowadays produces approximately 45,000 barrels per day.[11] In 1993, Royal Dutch Shell established their first gas-to-liquids (GTL) plant for producing middle distillates, in Bintulu, Malaysia, which used Co as a commercial catalyst and currently produces approximately 12,500 barrels per day.[12] Based on the plant built in Bintulu, Shell and Qatar Petroleum built the Pearl GTL plant in Ras Laffan, Qatar, which became operational in June 2011, and is currently the world's largest GTL plant, producing 140,000 barrels per day.

The use of Fischer-Tropsch synthesis technology in China is also increasing due to the high availability and low cost of coal. The largest coal-to-liquids (CTL) plant was commissioned in 2016 by CHN Energy, under the Shenhua Ning Mei project, which is able to produce 100,000 barrels per day. The project uses a medium temperature (275°C) Fischer-Tropsch technology[13] with an iron based catalyst in a slurry-bed reactor. CHN Energy is going to build a new CTL plant in the near future, which is able to produce 75,000 barrels per day. Sasol is planning on building a GTL plant in the near future, in collaboration with Petronas and Uzbekneftegaz, in Uzbekistan, which is able to produce 38,000 barrels per day.

### 1.4 Proposed mechanisms in the Fischer-Tropsch reaction

Although the Fischer-Tropsch reaction is known for almost 100 years, the exact mechanism is still a topic of considerable debate. In essence, the Fischer-Tropsch reaction is a polymerisation reaction with the in situ generation of  $C_1$  monomers. Various pathways have been proposed for chain initiation and for chain-growth. The initial step involves C-O bond scission of adsorbed CO. This can occur in either a direct or a hydrogen-assisted manner. In hydrogen-assisted pathways, the C-O bond scission occurs via a HCO or COH intermediate. In a C-assisted mechanism, a C-C bond is formed between a surface carbon of the lattice and an adsorbed CO molecule, after which the C-O bond is broken.

The majority of the proposed chain propagation mechanism in Fischer-Tropsch synthesis pertain to one of two major schools of thought. On the one hand, in the so-called carbide mechanism coined by Biloen and Sachtler, C-C bond formation between the growing hydrocarbon chain and a  $C_1$  monomer occurs after C-O bond scission of the CO reactant. [14, 15] On the other hand, the alternative pathway envisioned by Pichler and Schultz, known as the CO-insertion mechanism, envisions that C-C bond formation occurs prior to C-O bond scission. The two different mechanisms are schematically depicted in Figure 1.4.

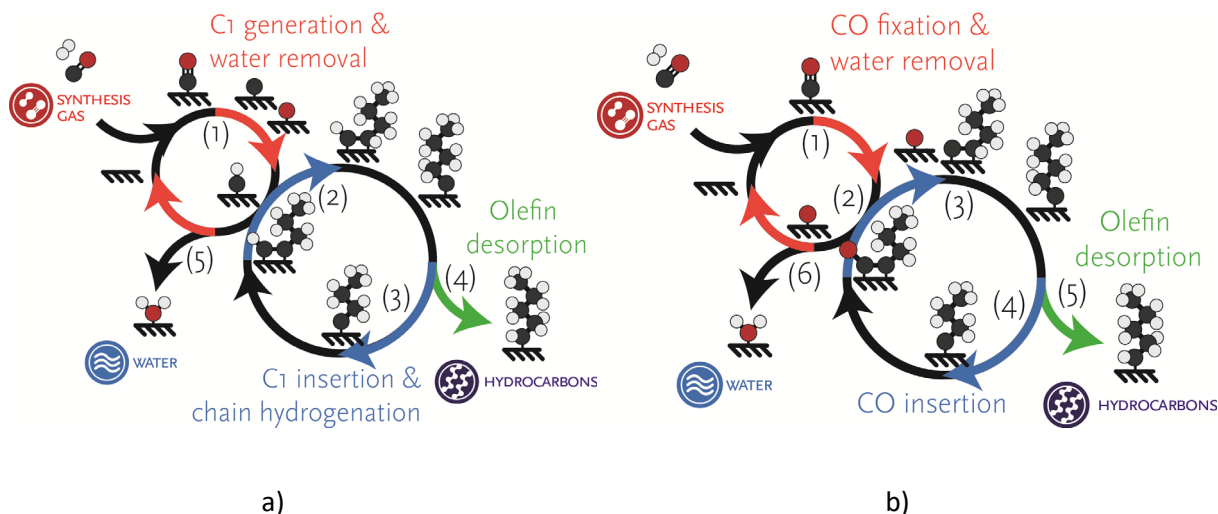


**Figure 1.4:** The Carbide mechanism (a) is the mechanism in Fischer-Tropsch synthesis, where both coupling C species first deoxygenate before chain-growth. The CO insertion mechanism (b), inserts couples the C species with a CO species, prior to deoxygenation. Picture taken from reference.[4]

The most prominent difference is that in the carbide mechanism, the generation of the monomers is a different kinetic process that occurs alongside chain-propagation on the same catalytic surface, whereas in the CO-insertion mechanism, CO directly acts as the monomer. After C-O bond scission, the resulting oxygen atoms need to be removed from the surface. Oxygen can be either removed as

water by twofold hydrogenation or as CO<sub>2</sub> by coupling with CO. The preferred mechanism for oxygen removal highly depends on the metal(-carbide) and the exposed crystal facets of the catalyst.

### 1.5 Fischer-Tropsch catalysts

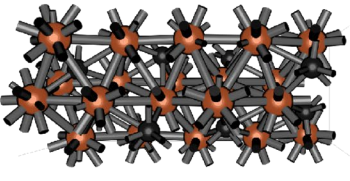
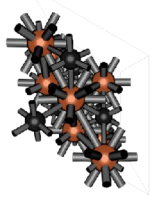
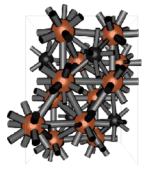
Fischer and Tropsch systematically explored the activity of various late transition metals under CO hydrogenation conditions.[16] Most late transition metals show appreciable activity towards CO hydrogenation, yet the reaction products differ widely. While Fe, Co and Ru mainly produce longer hydrocarbons, Ni produces mostly methane, Rh gives rise to some oxygenates (C<sub>1</sub>-C<sub>3</sub>) in addition to methane and metals such as Pt, Pd and Cu can also produce methanol. These selectivity differences are usually attributed to the propensity of the metal towards the CO bond scission reaction. Quantum chemical calculations have revealed that CO bond scission shows a relatively low barrier on metals such as Fe, Co and Ru, whereas it is difficult on metals such as Pd, Pt and Cu.[17]

### 1.6 Iron-based Fischer-Tropsch catalysts

The principle advantage of Fe as a Fischer-Tropsch catalyst compared to Ru and Co is the abundance and low price of this metal.[18] Compared to Co, Fe can be used in a wider temperature range. Fe can also deal with lower H<sub>2</sub>/CO ratios of the synthesis gas feedstock, because Fe-based FT catalysts are typically active in the water-gas shift (WGS) reaction. In this reaction, CO and H<sub>2</sub>O are converted into H<sub>2</sub> and CO<sub>2</sub>, raising the H<sub>2</sub>/CO ratio. Accordingly, it is usually argued that Fe-based FT catalysts can process synthesis gas derived from resources such as coal and biomass. Fe is also known to display a higher selectivity towards (lower) olefins than Co, which has led to the development of catalysts for a desirable, yet not commercialized Fischer-Tropsch to Olefins technology.[19, 20] Another advantage is that Fe-based catalysts are typically less sensitive to temperature and pressure, as compared to Co. [20]

A wide body of research has led to the conclusion that not metallic Fe but Fe-carbides are the active phase in the Fischer-Tropsch reaction. The conversion of iron oxide precursors into the active iron carbide phase is typically achieved by exposure to synthesis gas at elevated temperature.[21-23] Mostly, mixtures of different phases including remaining iron oxide are obtained in this manner. A recent protocol developed by Wang et al. showed that careful reduction of iron oxide to  $\alpha$ -Fe

followed by carburization can lead to high purity  $\varepsilon$ -Fe-carbide. A study of Smit et al. [24] showed that at moderate temperatures (around 250°C) and a high carbon chemical potential (low  $H_2/CO$ ),  $\chi$ - $Fe_5C_2$  is the thermodynamically most stable iron carbide phase. At low temperatures (below 200°C),  $\varepsilon'$ - $Fe_{2.2}C$  /  $\varepsilon$ - $Fe_2C$  is thermodynamically stable. At high temperatures (around 350°C) and a low carbon chemical potential (high  $H_2/CO$ ), or at very high temperatures (around 450°C) and a high carbon chemical potential,  $\theta$ - $Fe_3C$  is the preferred iron carbide phase. A recent protocol developed by Wang et al. showed that careful reduction of iron oxide to  $\alpha$ -Fe followed by carburization can lead to highly pure  $\varepsilon$ -Fe-carbide. The three main iron carbide phases, with their corresponding space group, unit cell parameters and typically observed Fe/C ratios, are shown in Figure 1.5.

	$\chi$ -Fe-Carbide	$\varepsilon$ -Fe-Carbide	$\theta$ -Fe-Carbide
			
<b>Space group</b>	C2/c (monoclinic)	P6 <sub>3</sub> 22 (hexagonal)	Pnma (orthorhombic)
<b>Unit cell parameters</b>	a = 11.504 Å, b = 4.524 Å, c = 5.012 Å $\alpha = \gamma = 90^\circ$ , $\beta = 97.75^\circ$	a = b = 4.760 Å, c = 8.667 Å $\alpha = \beta = 90^\circ$ , $\gamma = 120^\circ$	a = 5.082 Å, b = 6.733 Å, c = 4.514 Å $\alpha = \beta = \gamma = 90^\circ$
<b>Fe/C ratio</b>	2.5	2 / 2.2 / 3	3

**Figure 1.5:** Representation of the three main Fe-carbide phases. The three unit cells depicted for the  $\chi$ - $Fe_5C_2$ ,  $\varepsilon$ - $Fe_2C$ , and  $\theta$ - $Fe_3C$  are used as input for the DFT calculations in this thesis. The corresponding space group, unit cell parameters and most commonly observed Fe/C ratios are displayed below the unit cells.

For each Miller index plane for the Fe-carbides, more than one unique surface termination is possible, as cleaving the unit cell in the direction perpendicular to the Miller plane at fractional distances results in different surface terminations. This is due to the presence of interstitial C atoms. In this study, we adopted the notation introduced by Steynberg et al. to indicate the cut that generates the different surfaces.[25] In the case that a subscript is not specified, the surface was spanned at the origin of the two vectors composing the Miller index planes.

Hägg carbide ( $\chi$ - $Fe_5C_2$ ) is usually argued to be the most relevant carbide phase with respect to the FT reaction.[24] As a consequence, a large number of works have been devoted to understand this particular carbide.[26-33] Nevertheless, also the other  $\theta$ -Fe-carbide ( $\theta$ - $Fe_3C$ ) [33-39] and  $\varepsilon$ -Fe-

carbide [27, 40-43] phases have been observed in industrial FT catalysts. Therefore, it remains unclear to what extent  $\theta$ -Fe<sub>3</sub>C and  $\varepsilon$ -Fe<sub>2</sub>C contribute to the performance of commercial FT catalysts.

$\varepsilon$ -Fe carbides have been studied intensively in the middle of the past century because they were of interest to the steel industry.  $\varepsilon$ -Fe carbide is a transition iron carbide with a chemical formula between  $\varepsilon$ -Fe<sub>2</sub>C and  $\varepsilon$ -Fe<sub>3</sub>C, which was first identified by Hofer et al. [44]. Nagakura showed that below a temperature of 250 °C,  $\varepsilon$ -Fe carbide is produced by cementation, while if temperature exceeds 250 °C Hägg carbide is produced by cementation.[45] Manes et al. showed that  $\varepsilon$ -Fe carbide was the only carbide obtained at temperatures up to 250 °C.[46] Fang et al. confirmed the high stability of  $\varepsilon$ -Fe<sub>2</sub>C and also found stable configurations for  $\varepsilon$ -Fe<sub>2.4</sub>C. Under some conditions, they observed the conversion of the hexagonal  $\varepsilon$ -Fe<sub>2</sub>C phase to the orthorhombic  $\eta$ -Fe<sub>2</sub>C.[47]

The  $\theta$ -Fe<sub>3</sub>C phase is a meta-stable iron carbide, which is considered an intermediate in the transition from pure  $\alpha$ -Fe to the more carbon-rich  $\chi$ -phase. In addition, it is also identified as the most prevalent phase under high temperatures and low CO pressure.[24] The structure of  $\theta$ -Fe<sub>3</sub>C has been a topic of great interest, because  $\theta$ -Fe<sub>3</sub>C is the most stable phase in steel at high temperature. Its structure has been determined experimentally through X-ray, electron, and neutron diffraction measurements.[37, 48-59]

## 1.7 Fischer Tropsch to olefins

The product distribution of the FT process can be predicted by the Anderson-Schulz-Flory (ASF) distribution, which depends on the chain-growth probability. Iron carbide catalysts are known to predominantly yield either lower (C<sub>2</sub>-C<sub>4</sub>) or higher (C<sub>5</sub>+) olefins and paraffins, depending on the process conditions.[60] The high-boiling fractions can be used directly as fuels. Lower olefins are major chemical building blocks in the production of plastics. Fischer-Tropsch to olefins (FTO) refers to tailored processes that focus on direct conversion of CO and H<sub>2</sub> to lower olefins. High selectivity to C<sub>2</sub>-C<sub>4</sub> can be achieved by increasing the reaction temperature, because it generally is expected to lower the chain-growth probability. However, this typically goes together with increase of methane selectivity. Therefore, efforts have been made to suppress methane formation on these catalysts. An important example is the use of Na-S promoters for Fe-based catalysts [61, 62]. For Co catalysts, the use of Mn has been proposed.[63] Another way of tuning the product selectivity is to design bifunctional catalysts, e.g., combine a supported Fe-based catalyst with acidic zeolite catalysts for cracking such as a ZSM-5 zeolite[64]. Due to the shape selective and acidic nature of the zeolite

component, a certain fraction of the lower olefins is converted to aromatics, which are also very much desired as chemical building blocks. Recently, it was shown that selectivity to aromatics could be improved without decreasing the C<sub>2</sub>-C<sub>4</sub> selectivity by promoting bifunctional Fe-carbide/zeolite ZSM-5 catalysts with Na and S.[65] A general drawback of Fe-based Fischer-Tropsch and FTO processes in particular is the high selectivity to CO<sub>2</sub>, which impedes the economic viability. A recent experimental study has shown that pure iron-carbide catalysts predominantly form H<sub>2</sub>O instead of CO<sub>2</sub> at lower temperatures.[42]

### 1.8 Scope of the thesis

The aim of this thesis is to understand the dominant mechanisms of the Fischer-Tropsch synthesis reaction on relevant iron carbides ( $\chi$ -Fe<sub>5</sub>C<sub>2</sub>,  $\epsilon$ -Fe<sub>2</sub>C, and  $\theta$ -Fe<sub>3</sub>C). We make use of density functional theory to determine the energetics (stable states, transition states) of elementary reaction steps underlying the Fischer-Tropsch mechanism and use microkinetics simulations to predict catalytic performance in terms of rates, product distribution and other relevant parameters. The general approach of this study is to investigate different terminations of these iron carbides that give rise to a reasonable rate of CO dissociation. For these surfaces, a more detailed investigation of all relevant elementary reaction steps was undertaken and used as input to microkinetics simulations.

In Chapter 2, the computational methods used in this thesis are described. These include quantum chemical calculations based on density functional theory and microkinetics simulations.

Chapter 3 focuses on the CO dissociation mechanism on Hägg carbide ( $\chi$ -Fe<sub>5</sub>C<sub>2</sub>). We first determined surface free energies of different surface terminations and employed the Wulff construction to determine the most stable surfaces. The surface containing step-edge site configuration were further investigated for their rate of CO dissociation, involving different modes of CO dissociation such as direct CO bond scission and modes in which this step was assisted by hydrogenation or reaction with structural C atoms at the surface.

In Chapter 4, we expanded the dataset for the energetics of the Fischer-Tropsch synthesis reaction on Hägg carbide by involving the hydrogenation of adsorbed C to methane, oxygen removal as water and carbon dioxide, chain-growth and chain termination. Based on these energetics, a microkinetic model is formulated for the stepped (100)<sub>0.0</sub> surface. Microkinetics simulations were carried out to understand the main reaction pathways. A comparison is made to experimental data on pure Hägg carbide.

Chapter 5 deals with the  $\varepsilon$ -Fe<sub>2</sub>C phase. Using a combination of DFT and microkinetics simulations, we predict catalytic performance for a terrace surface (001) and a stepped (011) surface. Additionally these predictions are compared to experimental data.

In Chapter 6, we study CO dissociation on  $\theta$ -Fe<sub>3</sub>C. We investigate the stability of various surface terminations and establish their predominance on the basis of a Wulff construction. From the DFT calculations, a simple kinetic analysis was carried out to compare the rate of CO dissociation on different theta carbides.

## References

- [1] V. Smil, Energy transitions: global and national perspectives, ABC-CLIO, 2016.
- [2] I. Chorkendorff, J. Niemantsverdriet, Concepts of modern catalysis and kinetics. 2003, Wiley-VCH, 1997.
- [3] I.G. Pitt, R.G. Gilbert, K.R. Ryan, Application of transition-state theory to gas-surface reactions: barrierless adsorption on clean surfaces, *The Journal of Physical Chemistry* 98 (1994) 13001-13010.
- [4] I.A.W. Filot, Quantum chemical and microkinetic modeling of the Fischer-Tropsch reaction, Technische Universiteit Eindhoven, 2015.
- [5] A. Underwood, Industrial synthesis of hydrocarbons from hydrogen and carbon monoxide, *Industrial & Engineering Chemistry* 32 (1940) 449-454.
- [6] J. Sa, Fuel production with heterogeneous catalysis, CRC Press, 2014.
- [7] M.E. Dry, The Fischer-Tropsch process: 1950-2000, *Catalysis Today* 71 (2002) 227-241.
- [8] M.E. Dry, The production of hydrocarbons from coal, *Endeavour* 8 (1984) 2-4.
- [9] C. Smith, The Arab-Israeli Conflict, *International relations of the Middle East* (2013) 245-267.
- [10] O.O. Embargo, Embargo 1973-1974, US Department of State, Office of the Historian.
- [11] [http://www.petrosa.co.za/innovation\\_in\\_action/Pages/Operations-and-Refinery.aspx](http://www.petrosa.co.za/innovation_in_action/Pages/Operations-and-Refinery.aspx).
- [12] V. Van Wechem, M. Senden, Conversion of natural gas to transportation fuels via the Shell Middle Distillate Synthesis Process (SMDS), *Studies in Surface Science and Catalysis*, Elsevier, 1994, pp. 43-71.
- [13] J. Xu, Y. Yang, Y.-W. Li, Fischer-Tropsch synthesis process development: steps from fundamentals to industrial practices, *Current Opinion in Chemical Engineering* 2 (2013) 354-362.
- [14] P. Biloen, W. Sachtler, Mechanism of hydrocarbon synthesis over Fischer-Tropsch catalysts, *Advances in Catalysis*, Elsevier, 1981, pp. 165-216.
- [15] P. Biloen, J.N. Helle, W.M.H. Sachtler, Incorporation of surface carbon into hydrocarbons during Fischer-Tropsch synthesis: Mechanistic implications, *Journal of Catalysis* 58 (1979) 95-107.
- [16] F. Fischer, H. Tropsch, Über die direkte Synthese von Erdöl-Kohlenwasserstoffen bei gewöhnlichem Druck. (Erste Mitteilung), *Berichte der deutschen chemischen Gesellschaft (A and B Series)* 59 (1926) 830-831.
- [17] R.A. Van Santen, A. De Koster, T. Koerts, The quantum chemical basis of the Fischer-Tropsch reaction, *Catalysis Letters* 7 (1990) 1-14.
- [18] W. Haynes, *CRC Handbook of Chemistry and Physics*, revised ed, CRC Press, Boca Raton, Florida, 2016.
- [19] M.E. Dry, Fischer-Tropsch synthesis over iron catalysts, *Catalysis Letters* 7 (1990) 241-251.
- [20] H. Schulz, Comparing Fischer-Tropsch Synthesis on Iron- and Cobalt Catalysts: The dynamics of structure and function, in: B.H. Davis, M.L. Occelli, (Eds.), *Studies in Surface Science and Catalysis*, Elsevier, 2007, pp. 177-199.
- [21] D.B. Bukur, K. Okabe, M.P. Rosynek, C. Li, D. Wang, K. Rao, G. Huffman, Activation studies with a precipitated iron catalyst for Fischer-Tropsch synthesis: I. characterization studies, *Journal of Catalysis* 155 (1995) 353-365.
- [22] E. de Smit, A.M. Beale, S. Nikitenko, B.M. Weckhuysen, Local and long range order in promoted iron-based Fischer-Tropsch catalysts: a combined in situ X-ray absorption spectroscopy/wide angle X-ray scattering study, *Journal of Catalysis* 262 (2009) 244-256.
- [23] K. Sudsakorn, J.G. Goodwin Jr, A.A. Adeyiga, Effect of activation method on Fe FTS catalysts: investigation at the site level using SSITKA, *Journal of Catalysis* 213 (2003) 204-210.
- [24] E. de Smit, F. Cinquini, A.M. Beale, O.V. Safonova, W. van Beek, P. Sautet, B.M. Weckhuysen, Stability and reactivity of  $\epsilon$ - $\chi$ - $\theta$  iron carbide catalyst phases in Fischer-Tropsch synthesis: controlling  $\mu\text{C}$ , *Journal of the American Chemical Society* 132 (2010) 14928-14941.
- [25] P.J. Steynberg, J.A. Van den Berg, W.J. van Rensburg, Bulk and surface analysis of Hägg Fe carbide ( $\text{Fe}_5\text{C}_2$ ): a density functional theory study, *Journal of Physics: Condensed Matter* 20 (2008) 064238.
- [26] R.J.P. Broos, B. Zijlstra, I.A.W. Filot, E.J.M. Hensen, Quantum-Chemical DFT Study of Direct and H- and C-Assisted CO Dissociation on the  $\chi$ - $\text{Fe}_5\text{C}_2$  Hägg Carbide, *The Journal of Physical Chemistry C* 122 (2018) 9929-9938.
- [27] Q. Chang, C. Zhang, C. Liu, Y. Wei, A.V. Cheruvathur, A.I. Dugulan, J.W. Niemantsverdriet, X. Liu, Y. He, M. Qing, L. Zheng, Y. Yun, Y. Yang, Y. Li, Relationship between Iron Carbide Phases



- ( $\epsilon$ -Fe<sub>2</sub>C, Fe<sub>7</sub>C<sub>3</sub>, and  $\chi$ -Fe<sub>5</sub>C<sub>2</sub>) and Catalytic Performances of Fe/SiO<sub>2</sub> Fischer–Tropsch Catalysts, *ACS Catalysis* 8 (2018) 3304–3316.
- [28] B. Chen, D. Wang, X. Duan, W. Liu, Y. Li, G. Qian, W. Yuan, A. Holmen, X. Zhou, D. Chen, Charge-Tuned CO Activation over a  $\chi$ -Fe<sub>5</sub>C<sub>2</sub> Fischer–Tropsch Catalyst, *ACS Catalysis* 8 (2018) 2709–2714.
- [29] M.A. Petersen, J.-A. van den Berg, W.J. van Rensburg, Role of step sites and surface vacancies in the adsorption and activation of CO on  $\chi$ -Fe<sub>5</sub>C<sub>2</sub> surfaces, *The Journal of Physical Chemistry C* 114 (2010) 7863–7879.
- [30] M.O. Ozbek, J.H. Niemantsverdriet, Elementary reactions of CO and H<sub>2</sub> on C-terminated  $\chi$ -Fe<sub>5</sub>C<sub>2</sub> (001) surfaces, *Journal of Catalysis* 317 (2014) 158–166.
- [31] D.-B. Cao, Y.-W. Li, J. Wang, H. Jiao, Chain growth mechanism of Fischer–Tropsch synthesis on Fe<sub>5</sub>C<sub>2</sub> (0 0 1), *Journal of Molecular Catalysis A: Chemical* 346 (2011) 55–69.
- [32] J.M. Gracia, F.F. Prinsloo, J. Niemantsverdriet, Mars-van Krevelen-like mechanism of CO hydrogenation on an iron carbide surface, *Catalysis letters* 133 (2009) 257.
- [33] C.-F. Huo, Y.-W. Li, J. Wang, H. Jiao, Insight into CH<sub>4</sub> formation in iron-catalyzed Fischer–Tropsch synthesis, *Journal of the American Chemical Society* 131 (2009) 14713–14721.
- [34] A.C. B. Kniep, D. Niemeier, K.D. Becker, Eine in-situ Mössbauer-Untersuchung zur Bildung von Zementit, Fe<sub>3</sub>C, *Z. Anorg. Allg. Chem* 629 (2003) 1795–1804.
- [35] L.-J. Deng, C.-F. Huo, X.-W. Liu, X.-H. Zhao, Y.-W. Li, J. Wang, H. Jiao, Density Functional Theory Study on Surface C<sub>x</sub>H<sub>y</sub> Formation from CO Activation on Fe<sub>3</sub>C (100), *The Journal of Physical Chemistry C* 114 (2010) 21585–21592.
- [36] Y. Wang, Y. Li, S. Huang, J. Wang, H. Wang, J. Lv, X. Ma, Insight into CH<sub>4</sub> formation and chain growth mechanism of Fischer–Tropsch synthesis on  $\theta$ -Fe<sub>3</sub>C(031), *Chemical Physics Letters* 682 (2017) 115–121.
- [37] I. Wood, L. Vočadlo, K. Knight, D.P. Dobson, W. Marshall, G.D. Price, J. Brodholt, Thermal expansion and crystal structure of cementite, Fe<sub>3</sub>C, between 4 and 600 K determined by time-of-flight neutron powder diffraction, *Journal of Applied Crystallography* 37 (2004) 82–90.
- [38] R.J.P. Broos, B. Klumpers, B. Zijlstra, I.A.W. Pilot, E.J.M. Hensen, A quantum-chemical study of the CO dissociation mechanism on low-index Miller planes of  $\theta$ -Fe<sub>3</sub>C, *Catalysis Today* (2019).
- [39] W.C. Chiou, E.A. Carter, Structure and stability of Fe<sub>3</sub>C-cementite surfaces from first principles, *Surface Science* 530 (2003) 88–100.
- [40] L.-L. Bao, C.-F. Huo, C.-M. Deng, Y.-W. Li, Structure and stability of the crystal Fe<sub>2</sub>C and low index surfaces, *Journal of Fuel Chemistry and Technology* 37 (2009) 104–108.
- [41] X. Yu, X. Zhang, Y. Meng, Y. Zhao, Y. Li, W. Xu, Z. Liu, CO adsorption, dissociation and coupling formation mechanisms on Fe<sub>2</sub>C(001) surface, *Applied Surface Science* 434 (2018) 464–472.
- [42] P. Wang, W. Chen, F.-K. Chiang, A.I. Dugulan, Y. Song, R. Pestman, K. Zhang, J. Yao, B. Feng, P. Miao, W. Xu, E.J.M. Hensen, Synthesis of stable and low-CO<sub>2</sub> selective  $\epsilon$ -iron carbide Fischer–Tropsch catalysts, *Science Advances* 4 (2018) eaau2947.
- [43] K. Xu, B. Sun, J. Lin, W. Wen, Y. Pei, S. Yan, M. Qiao, X. Zhang, B. Zong,  $\epsilon$ -Iron carbide as a low-temperature Fischer–Tropsch synthesis catalyst, *Nature Communications* 5 (2014) 5783.
- [44] L.J.E. Hofer, E.M. Cohn, W.C. Peebles, The Modifications of the Carbide, Fe<sub>2</sub>C; Their Properties and Identification, *Journal of the American Chemical Society* 71 (1949) 189–195.
- [45] S. Nagakura, Study of Metallic Carbides by Electron Diffraction Part III. Iron Carbides, *Journal of the Physical Society of Japan* 14 (1959) 186–195.
- [46] M. Manes, A.D. Damick, M. Mentser, E.M. Cohn, L.J.E. Hofer, Hexagonal Iron Carbide as an Intermediate in the Carbiding of Iron Fischer–Tropsch Catalysts<sup>1,2</sup>, *Journal of the American Chemical Society* 74 (1952) 6207–6209.
- [47] C. Fang, M. van Huis, H. Zandbergen, Structure and stability of Fe<sub>2</sub>C phases from density-functional theory calculations, *Scripta Materialia* 63 (2010) 418–421.
- [48] E.C. Bain, X-ray data on cementite, *Chem. And Met. Eng.* 25 (1921).
- [49] A. Westgren, G. Phragmén, Zum Kristallbau des Eisens und Stahls. II, *Zeitschrift für Physikalische Chemie* 102 (1922) 1–25.
- [50] F.W. M. Polanyi, Röntgen-Emissionsspektren der Eisenmodifikationen, *Mitt. Kaiser-Wilhelm-Inst. Eisenforschung* 4 (1922).

- [51] S. SHIMURA, A Study on the Structure of Cementite, Proceedings of the Imperial Academy 6 (1930) 269-271.
- [52] S.B. Hendricks, XXXVI. The Crystal Structure of Cementite, Zeitschrift für Kristallographie-Crystalline Materials 74 (1930) 534-545.
- [53] H. Lipson, N. Petch, The crystal structure of cementite,  $\text{Fe}_3\text{C}$ , Iron and Steel Institute (London) 142 (1940).
- [54] H.A. Schwartz, Correspondence on the findings of H. Lipson and N.J. Petch regarding the crystal structure of cementite, J. Iron and Steel Institute 142 (1940).
- [55] O.K. D. Meinhardt, Strukturuntersuchungen an Karbiden des Eisens, Wolframs und Chroms mit thermischen Neutronen, Z. das Eisenhüttenwesen 77 (1962).
- [56] A.I. Gardin, An Electron-Diffraction Study of the Structure of Cementite Kristallografiya 7 (1963).
- [57] F. Herbstein, J. Smuts, Comparison of X-ray and neutron-diffraction refinements of the structure of cementite  $\text{Fe}_3\text{C}$ , Acta Crystallographica 17 (1964) 1331-1332.
- [58] E. Fasiska, G. Jeffrey, On the cementite structure, Acta Crystallographica 19 (1965) 463-471.
- [59] P.C. D. Fruchart, R. Fruchart, A. Rouault, J.P. Senateur, Études structurales de composés de type cémentite: Effet de l'hydrogène sur  $\text{Fe}_3\text{C}$  suivi par diffraction neutronique. Spectrométrie Mössbauer sur  $\text{FeCo}_2\text{B}$  et  $\text{Co}_3\text{B}$  dopés au  $^{57}\text{Fe}$ , J. Solid State Chemistry 51 (1984) 246-252.
- [60] A. Steynberg, Introduction to fischer-tropsch technology, Studies in surface science and catalysis, Elsevier, 2004, pp. 1-63.
- [61] H.M.T. Galvis, A.C. Koeken, J.H. Bitter, T. Davidian, M. Ruitenbeek, A.I. Dugulan, K.P. de Jong, Effects of sodium and sulfur on catalytic performance of supported iron catalysts for the Fischer–Tropsch synthesis of lower olefins, Journal of catalysis 303 (2013) 22-30.
- [62] H.M.T. Galvis, J.H. Bitter, C.B. Khare, M. Ruitenbeek, A.I. Dugulan, K.P. de Jong, Supported iron nanoparticles as catalysts for sustainable production of lower olefins, Science 335 (2012) 835-838.
- [63] L. Zhong, F. Yu, Y. An, Y. Zhao, Y. Sun, Z. Li, T. Lin, Y. Lin, X. Qi, Y. Dai, Cobalt carbide nanoprisms for direct production of lower olefins from syngas, Nature 538 (2016) 84.
- [64] A.V. Karre, A. Kababji, E.L. Kugler, D.B. Dadyburjor, Effect of addition of zeolite to iron-based activated-carbon-supported catalyst for Fischer–Tropsch synthesis in separate beds and mixed beds, Catalysis today 198 (2012) 280-288.
- [65] J.L. Weber, I. Dugulan, P.E. de Jongh, K.P. De Jong, Bifunctional catalysis for the conversion of synthesis gas to olefins and aromatics, ChemCatChem 10 (2018) 1107-1112.

## 2. Computational Methods

### 2.1 Introduction

In this chapter, a detailed description of the computational methods employed in this thesis is given. First, the basic principles, underlying assumptions and methods applied from electronic many-body calculations and density functional theory (DFT) are discussed. DFT allows us to calculate relevant kinetic parameters for the individual elementary reaction steps. Next, transition state theory is introduced as the framework to compute reaction rate constants for elementary reaction steps. The main aspects of microkinetics simulations are discussed as a method to simulate relevant kinetic parameters such as reaction rates, product distribution, reaction orders for a given chemo-kinetic network. Finally, the inclusion of such microkinetics in a continuously stirred tank reactor (CSTR) model is discussed.

### 2.2 Many-body calculations

Catalysts, like all matter, consist of nuclei and electrons. In order to model their chemical behaviour, quantum mechanical calculations should be employed. These calculations are based on solving the non-relativistic time-independent Schrödinger equation for a many-body system[1]:

$$\hat{H}\Psi_i(\vec{r}_1, \vec{r}_2, \dots, \vec{r}_N, \vec{R}_1, \vec{R}_2, \dots, \vec{R}_M) = [\hat{T} + \hat{V} + \hat{U}]\Psi_i = E_i\Psi_i(\vec{r}_1, \vec{r}_2, \dots, \vec{r}_N, \vec{R}_1, \vec{R}_2, \dots, \vec{R}_M)\Psi_i \quad (2.1)$$

Here,  $\hat{H}$  is the Hamiltonian for a system containing  $N$  electrons and  $M$  nuclei.  $R$  and  $r$  represent the positions of the nuclei and electrons, respectively. The Hamiltonian in atomic units [2] can be expressed as follows:

$$\hat{H} = - \sum_{i=1}^N \frac{1}{2} \nabla_i^2 - \sum_{A=1}^M \frac{1}{2M_A} \nabla_A^2 - \sum_{i=1}^N \sum_{A=1}^M \frac{Z_A}{r_{i,A}} + \sum_{i=1}^N \sum_{j>i}^N \frac{1}{r_{i,j}} + \sum_{A=1}^M \sum_{B>A}^M \frac{Z_A Z_B}{R_{AB}} \quad (2.2)$$

$M_A$  is the ratio of the mass of nucleus  $A$  to the mass of an electron and  $Z_A$  is the atomic number of nucleus  $A$ .  $\nabla_i^2$  and  $\nabla_A^2$  are the Laplacian operators involving the differentiation with respect to the coordinates of the  $i^{\text{th}}$  electron and  $A^{\text{th}}$  nucleus, respectively. The five terms in the equations are related to different operators for the energies for electrons and nuclei. The first and second term are the operators for the kinetic energy of the electrons and nuclei ( $\hat{T}$ ), respectively. The third term

represents the Coulomb attraction between electrons and nuclei ( $\hat{V}$ ). The fourth and fifth terms represent the repulsion between electrons and between nuclei ( $\hat{U}$ ), respectively.

The Born-Oppenheimer approximation is one of the basic concepts underlying the description of the quantum states of molecules. This approximation makes it possible to separate the motion of the nuclei and the motion of the electrons as the mass of the former is much larger than that of the latter.[3] As such, the terms for the kinetic energy of the nuclei and the repulsion between the nuclei can be treated as constants and can therefore be evaluated outside the Hamiltonian. The remaining Hamiltonian is usually called the electronic Hamiltonian,  $\hat{H}_{elec}$ :

$$\hat{H}_{elec} = - \sum_{i=1}^N \frac{1}{2} \nabla_i^2 - \sum_{i=1}^N \sum_{A=1}^M \frac{Z_A}{r_{i,A}} + \sum_{i=1}^N \sum_{j>i}^N \frac{1}{r_{i,j}} \quad (2.3)$$

Despite these simplifications, it remains impossible to solve the Schrödinger equation analytically.[2] We can further simplify the equation by replacing the complicated many-electron problem by a one-electron problem in which the electron-electron repulsion is treated using a mean-field approximation, which is in essence the Hartree-Fock approximation. Herein, the anti-symmetric wave function of the ground state can be modelled using a Slater determinant. The drawback of this method is that the electron correlation is only partially described. Methods to further improve the electron-electron description involve adding electron correlation; methods such as Coupled Cluster (CC), Configuration Interaction (CI) and Møller-Plesset Perturbation Theory (MPPT) can take this into account but are very costly.[2]

### 2.2.1 Density functional theory

Typical heterogeneous catalysts can only be properly modelled with many atoms. This makes electronic structure calculations at the Hartree-Fock or post-Hartree-Fock level of theory usually computationally intractable. Instead of directly calculating the exchange-correlation interactions from the wave functions, an alternative approach is to use density functional theory (DFT), which uses the electron density (i.e., the square of the absolute value of the electronic wave function) to calculate these interactions. This approach significantly reduces the computational cost as DFT typically scales with  $N^3$ , where  $N$  is the number of basis functions, which scales linearly with the number of atoms if they are from the same element (arising from the matrix diagonalization procedure), whereas wave function-based methods scale with  $N^4$  (arising from the evaluation of the

two-electron integrals). In this work, we utilize DFT to calculate the electronic properties of the catalytic materials under investigation.

### 2.2.2 Hohenberg-Kohn theorem

As the many-body wave function is too complicated to solve efficiently, Hohenberg and Kohn provided two theorems that allow using the electron density instead. The first theorem states[4] that the non-degenerate ground state wave function of a system of interacting electrons is a functional of the ground state density. In other words, the ground state density uniquely determines the potential and, thus, all properties of the system, including the many-body wave function. In this way, a universal functional of the electron density can be made. This universal functional,  $F[n]$ , is called the Hohenberg-Kohn or HK functional[4], and looks as follows:

$$F[n] = T[n] + U[n] \quad (2.4)$$

Here,  $T[n]$  is the kinetic energy operator and  $U[n]$  is the electron-electron interaction operator. The universality comes from the fact that the functional has the same dependence on the electron density for any system, independent of the external potential.

The second theorem states that there exists an energy functional of the electron density that is minimal for the ground state density. The ground state density is found by minimizing this functional with respect to all possible electron densities  $n(\vec{\rho})$ , obeying the following equation:

$$N[n] \equiv \int d\vec{\rho} n(\vec{\rho}) = N \quad (2.5)$$

where  $N$  is the number of particles and the integral is the sum of the electron densities. The functional for the ground state energy  $E[n]$  for a given external potential  $v(\vec{\rho})$  [5] will become:

$$E[n] = \int d\vec{\rho} n(\vec{\rho})v(\vec{\rho}) + F[n] \quad (2.6)$$

Although the energy functional as shown above is correct, the functional  $F[n]$  is not known. Because of the long range of the Coulomb interaction, it is often convenient to separate the  $F[n]$  into the classical Coulomb energy and a remaining functional  $G[n]$ , as described below:

$$F[n] = \frac{1}{2} \int \int d\vec{\rho} d\vec{\rho'} \frac{n(\vec{\rho}) n(\vec{\rho'})}{|\vec{\rho} - \vec{\rho'}|} + G[n] \quad (2.7)$$

The remaining functional  $G[n]$ , which is a universal functional of the density, is still an unknown functional. This remaining part can be described using the Kohn-Sham theory, which will be discussed in the next section.

### 2.2.3 Kohn-Sham theory

The theorems by Hohenberg and Kohn are exact, yet not very useful. Therefore, Kohn and Sham [6] came up with a theory to turn the theorems into a more practical perspective. In their theory, a fictional system of *non-interacting electrons* is considered in an external potential in such a way that the corresponding density is the same as the density of the system of the *interacting* electrons. This converts the multi-body problem into a series of one-body problems, as is the case in the Hartree-Fock method.[7-9] Considering the ground state wave function  $\Psi[n]$  of the non-interacting system and only the kinetic part  $T_s[n]$ , the new functional for  $T_s[n]$  will become:

$$T_s[n] = \langle \Psi_s | T | \Psi_s \rangle = F[n] \quad (2.8)$$

The functional for the interacting system can then be split into two separate functionals: the functional of the non-interacting system ( $T_s[n]$ ) and the exchange-correlation functional ( $E_{xc}[n]$ ).

It should be noted that we do not have a functional to calculate the kinetic part directly from the electron density and for this reason, the wave function is still used. This calculation however scales with  $N$ , where  $N$  is the number of basis functions, and therefore is not expensive in terms of computational cost.

### 2.2.4 Local Density Approximation (LDA)

The exchange-correlation functional, as introduced in the previous section, can be described by the local density approximation. In the local density approximation (LDA)[10], the exchange-correlation energy functional of an inhomogeneous system of interacting electrons is approximated as given in the following equation:

$$E_{xc}[n] \approx \int d\vec{\rho} \epsilon_{xc}[n(\vec{\rho})]n(\vec{\rho}) \quad (2.9)$$

where  $\epsilon_{xc}(n(\vec{\rho}))$  is the exchange-correlation energy per electron of a homogeneous electron gas, with a density equal to the local density that is denoted as  $n(\vec{\rho})$ . The downside of this approximation is that it cannot correctly describe the London dispersion interaction [11], which is approximately

proportional to  $\frac{1}{R^6}$  at large distances. In brief, two or more molecules or atoms only affect each other if they have overlap in their electron density. However, London dispersion interaction is caused by correlated movement of electrons in separate atoms or molecules because it is caused by mutually induced dipoles. This occurs without the overlapping electron densities. The LDA is only exact for a homogeneous electron gas as the gradient of the density is zero in this case. LDA has been used extensively to model bulk metallic systems, wherein the electron density does not change significantly. However, it proved to be relatively inaccurate in describing chemistry as typical systems studied in chemistry have a strongly varying electron density. Thus, as an improvement to LDA, a gradient-corrected method was envisioned. This approximation will be discussed in the next section.

### 2.2.5 Generalized Gradient Approximation (GGA)

In contrast to the local density approximation, where only the local electron density is included, the generalized gradient approximation[12] has an additional term which includes the gradient of the electron density. The GGA is in essence an expansion to the previously proposed LDA. The 0<sup>th</sup> order expansion of the GGA is exactly the LDA. The higher orders in this expansion are called GGAs. This approximation has the capability to predict binding energies of molecules within the required precision to model chemistry.

The specific GGA-XC functional used throughout this thesis is the Perdew-Burke-Ernzerhof functional, which is a functional not based on any parameters fitted using experimental data.[12]

Although, overbinding is a well-known issue using the PBE functional for the adsorption of CO, [13-15] using the RPBE functional[16] to mitigate this overbinding might introduce new and yet unknown errors in the calculations. Hence, we opted for the PBE functional. For energy calculations of elementary reaction steps on the catalytic surface, the particular choice of the exchange-correlation functional is less critical due to the principle of cancellation of error.[17]

### 2.2.6 Projector Augmented Wave (PAW) method

The projector augmented wave method is a technique which allows carrying out DFT calculations with high computational efficiency. As we are usually dealing with periodic systems in heterogeneous catalyst models, the electron density can be described using a set of plane waves. These plane waves are well suited for the cases in which wave functions do not have a sharp positional dependence. The wave functions of the core electrons vary on small length scales.

However, the difference between the wave functions for the core electrons and isolated atoms is rather small. Therefore, it makes sense to exclude these wave functions from our description, concentrating only on the valence electrons. Since the wave functions for the valence electrons should be orthogonal, these wave functions have sharp variations in the core region. This problem can be solved by replacing the potential by a pseudopotential and the all-electron wave function  $|\Psi\rangle$ , by a pseudo wave function  $|\tilde{\Psi}\rangle$ , which is smooth in the core region.

Blöchl[18] introduced a combination of pseudopotentials with the augmented wave method, as an extension of both methods. This method divides the all-electron wave function into a pseudo wave function consisting of two parts: (i) a part that approximates the free electrons in the solid using plane waves and (ii) a part that approximates the electron density near the core using pseudopotentials. An additional correction is needed because of the difference in overlap between the two regions. A linear transformation between the valence wave functions and the fictional pseudo wave functions leads to the following equation for the all-electron wave function:

$$|\Psi\rangle = |\tilde{\Psi}\rangle + \sum_i |\phi_i\rangle \langle \tilde{p}_i | \tilde{\Psi}\rangle - \sum_i |\tilde{\phi}_i\rangle \langle \tilde{p}_i | \tilde{\Psi}\rangle \quad (2.10)$$

Herein,  $\phi_i$  is the eigenstate of the one-electron Hamiltonian, which is obtained by radially integrating the Schrödinger equations of the atomic energy for a set of energies and orthogonalisation to the core states.  $|\tilde{\phi}_i\rangle$  is the pseudo partial wave, which coincides with the corresponding all-electron partial wave outside some augmentation region for each all-electron partial wave and  $\langle \tilde{p}_i |$  is the projector function.

Although there are many quantum chemical codes based on plane waves, not all of these codes implement the PAW method. Among these codes employing the PAW method, the Vienna-Ab Initio Simulation Package (VASP) is among the most popular DFT codes.

### 2.2.7 Nudged elastic band method

An elementary reaction step is defined as the minimum energy pathway over the potential energy surface (PES) that connects two stable states (termed initial and final state) separated by a dividing surface. The point on the dividing surface that is lowest in energy (i.e., the point with the highest crossing frequency) is termed the transition state. From the perspective of the PES, the transition state is characterized as a maximum in the direction of the reaction coordinate and being a minimum in all other directions. Such a position on the PES corresponds to a first-order saddle point. Note



that initial and final states in this definition can be readily exchanged by reversal of the direction of the reaction coordinate using the concept of microscopic reversibility.[19]

Whereas obtaining the geometries of the initial and final states is relatively simple using structure optimization routines such as conjugate-gradient, finding the transition state that connects these two stable states is less trivial. An algorithm specifically developed to search for the transition state is the nudged elastic band method.[20] This method works by optimizing a number of intermediate images along the reaction path. Each image finds the lowest energy possible while maintaining equal spacing (in the hyper dimensional sense) to the neighbouring images. This constrained optimization is done by adding spring forces along the band between images and by projecting out the component of the force due to the potential perpendicular to the band. A few improvements have been made to this approach, leading to the climbing image NEB (CI-NEB) method.[21] In this method, the highest energy image is driven up to the saddle point. This image does not feel the spring forces along the band, but instead the true force inverts along the tangent at this image. The energy of the image is thus maximized in the direction along the band and simultaneously minimized in all other directions, leading to convergence of the algorithm at the saddle point.

#### 2.2.8 Frequency analysis

To find the transition state, the CI-NEB is not required to complete to full convergence. If we can identify a point on the PES sufficiently close to the transition state, we can use an optimization routine that is computationally much cheaper (e.g. Newton-Raphson) in order to find the exact transition state. The assessment whether we are sufficiently close to the transition state is of paramount importance. A frequency analysis can be used to validate whether all vibrational frequencies calculated are real-valued numbers (i.e., correspond to a positive force constant), except for the frequency in the direction of the reaction coordinate, which should be imaginary (i.e., correspond to a negative force constant). Not only is this analysis used to assess (the close proximity to) the transition states, it is also used to determine the vibrational partition functions and in turn the pre-exponential factors for all of the elementary reaction steps (*vide infra*).

Within VASP, a frequency analysis is conducted using finite-difference discretization.[22] Using the finite difference method, the second-order derivatives can be calculated directly from the forces or from the energies. In VASP, the former approach is used. A Hessian matrix is built, which is the square matrix of second-order partial derivatives of the potential energy. By mass-weighting the Hessian matrix and performing a matrix diagonalization, one obtains the eigenmodes (i.e., direction

of the vibrational frequency) as well as the eigenvalues (i.e., the strength or force constant of the vibrational frequencies). Within VASP, it is only possible to calculate the frequencies numerically. Alternatively, one could calculate the frequencies in an analytical fashion. Other DFT codes (e.g. ADF[23, 24]) do have an option to calculate the frequencies in an analytical fashion, yet this approach is computationally significantly more expensive. Calculating the analytical frequencies in ADF requires the solution of the Coupled Perturbed Kohn-Sham equations[25], which is an iterative and expensive computational process. In most cases, analytical expressions are as accurate as the numerical frequencies for the same integration accuracy, but can be up to 3 to 5 times quicker to compute.[26] Hence, in most cases it makes sense to use a numerical method for determination of the frequencies.

### 2.3 Microkinetics simulations

Chemical kinetics deals with the kinetics of chemical reactions, i.e. it concerns how the rate of reactions depends on the conditions, which includes temperature, pressure and the concentrations of the reactants. In surface catalysis, two main mechanisms are considered. In the Langmuir-Hinshelwood mechanism, two surface species react from their adsorbed states with each other to form a new species. The alternative mechanism to be considered is the Eley-Rideal mechanism which refers to a reaction between one surface adsorbate with a gas phase species. Based on entropy considerations, the likelihood of the Eley-Rideal mechanism is very low. Therefore, most mechanisms for heterogeneous reactions are described in terms of Langmuir-Hinshelwood-type of reaction steps. While this mechanism deals with the reaction between two adsorbates originating from adsorption from the gas or liquid phase, reactions may also involve atoms belonging to the catalyst surface rather than an adsorbate. We call this the Mars-Van Krevelen mechanism.

#### 2.3.1 Transition state theory

The Eyring equation[27], as seen below, is used for the calculation of rate constants for the elementary reaction steps, which are taking place on the surface.

$$k = \frac{k_b T}{h} \frac{Q^\ddagger}{Q} e^{\left(\frac{-\Delta E_{\text{act}}^{\text{zpe}}}{k_b T}\right)} \quad (2.11)$$

Herein,  $k_b$  is Boltzmann's constant in J/K,  $k$  is the reaction rate of an elementary reaction step,  $T$  is the temperature in K,  $h$  is Planck's constant in J/s.  $\Delta E_{\text{act}}^{\text{zpe}}$  is the zero-point energy corrected activation energy in J per particle.  $Q^\ddagger$  and  $Q$  are the total partition functions of the transition state and initial state, respectively. It must be noted that (1) the single imaginary frequency corresponding to the movement over the transition state is not directly included in the total partition function for the transition state, yet is extracted to obtain the  $\frac{k_b T}{h}$  term in the Eyring equation and (2) that when using the ZPE corrected activation energy, all partition functions should be constructed with respect to the lowest vibrational energy level and not with respect to the electronic ground state.

The molecular partition function for a gas phase species is a product of contributions from translational, vibrational and rotational degrees of freedom. A detailed derivation of the translational, vibrational, and rotational partition functions can be found in the literature.[28]

The total partition function can be calculated as follows:

$$Q_i = q_{i,\text{trans}} q_{i,\text{vib}} q_{i,\text{rot}} \quad (2.12)$$

Here,  $Q_i$  is the molecular partition function, or in other words, the total number of states accessible to the atom or molecule.  $q_{i,\text{trans}}$  is the translational partition function,  $q_{i,\text{vib}}$  the molecular vibrational partition function and  $q_{i,\text{rot}}$  the molecular rotational partition function. All partition functions reported below are given for an atom or a molecule in three-dimensional space.

The translational kinetic energy ( $q_{i,\text{trans}}$ ) of a molecule in a three dimensional space becomes:

$$q_{i,\text{trans}} = \frac{V (2\pi m_i k_b T)^{\frac{3}{2}}}{h^3} \quad (2.13)$$

Here,  $V$  is the volume of the three-dimensional space,  $m_i$  is the mass of the particle,  $k_b$  is Boltzmann's constant,  $T$  is the temperature and  $h$  is the Planck constant.

To obtain a value for the vibrational partition function ( $q_{i,\text{vib}}$ ), the following equation is employed:

$$q_{i,\text{vib}} = \frac{1}{1 - e^{-\left(\frac{h\nu}{k_b T}\right)}}, \quad (2.14)$$

where  $h$  is the Planck constant,  $\nu$  stands for the frequency of the vibrational mode,  $k_b$  the Boltzmann constant, and  $T$  the temperature. As mentioned above, this partition function is constructed with respect to the lowest vibrational energy level and not with respect to the electronic ground state.

The general formula for the rotational partition function for an asymmetric polyatomic system ( $q_{\text{rot}}$ ) with 3 rotational degrees of freedom (i.e. the 3 principal axes of rotation, each with a different moment of inertia  $I$ ) looks as follows:

$$q_{\text{rot}} = \frac{\pi^2}{\sigma} \left( \frac{8\pi^2 I_a k_b T}{h^2} \right)^{\frac{1}{2}} \cdot \left( \frac{8\pi^2 I_b k_b T}{h^2} \right)^{\frac{1}{2}} \cdot \left( \frac{8\pi^2 I_c k_b T}{h^2} \right)^{\frac{1}{2}} = \frac{\pi^2}{\sigma} \sqrt{\frac{T^3}{\Theta_a \Theta_b \Theta_c}} \quad (2.15)$$

Here,  $T$  is the temperature,  $\Theta$  is the characteristic temperature of rotation,  $I$  is the moment of inertia,  $k_b$  is the Boltzmann constant,  $h$  is the Planck constant and  $\sigma$  is the symmetry number, which is defined as the number of different ways of achieving a given spatial orientation that differs only in labels on identical nuclei. If the point group of the molecule is known, the value for  $\sigma$  can be readily found from the corresponding character table by either summing the number of rotations ('C $x$ ') or from the symmetry number  $h$ . For example, the value for the symmetry number is 1 for a diatomic, heteronuclear system (Point group  $C_{\infty v}$ ). A homonuclear (diatomic) linear system (Point group  $D_{\infty v}$ ) has a symmetry number of 2. The rotational partition function ( $q_{i,\text{rot}}$ ) for diatomic molecules is given by the following equation:

$$q_{i,\text{rot}} = \frac{T}{\sigma \Theta_{\text{rot}}} = \frac{8\pi^2 I_i k_b T}{\sigma h^2} \quad (2.16)$$

### 2.3.2 Adsorption/Desorption

Adsorption on the surface is the first step in every heterogeneous catalytic reaction. Adsorption can occur either in a dissociative or associative fashion. During dissociative adsorption, a reactant molecule dissociates prior to adsorption, whereas via an associative adsorption the reactant adsorbs prior to reaction.

The rates for adsorption and desorption can be readily calculated from the Eyring equation by identification of the nature of the molecular degrees of freedom (i.e. rotational, vibrational and translational) and using these to establish the total molecular partition functions for the initial and transition state. Often, several assumptions (e.g. the ideal gas law) are made to further simplify the formulas. As an example, we report such a derivation for an adsorption and a desorption reaction.

When a molecule adsorbs from the gas phase, it undergoes a change in entropy, corresponding to a transformation in the nature of the molecular partition functions from rotational and translational to vibrational. In general, it is assumed that the molecule only has vibrational degrees of freedom upon chemisorption. A non-activated adsorption can be represented by the following formula, wherein we assumed that the adsorbent loses one translational degree of freedom corresponding to a motion parallel to the normal direction of the catalytic surface:

$$\begin{aligned}
 k &= \frac{k_b T}{h} \frac{Q^\ddagger}{Q} e^{\left(\frac{-\Delta E_{\text{ads}}^{\text{zpe}}}{k_b T}\right)} = \frac{k_b T}{h} \frac{q_{\text{trans}}^{\ddagger(2)} q_{\text{rot}}^{\ddagger(3)} q_{\text{vib}}^{\ddagger(3N-6)}}{q_{\text{trans}}^{(3)} q_{\text{rot}}^{(3)} q_{\text{vib}}^{(3N-6)}} e^{\left(\frac{-\Delta E_{\text{ads}}^{\text{zpe}}}{k_b T}\right)} = \dots \\
 &\dots = \frac{k_b T}{h} \frac{L^2 (2\pi m k_b T) h^3}{L^3 (2\pi m k_b T)^{\frac{3}{2}} h^2} e^{\left(\frac{-\Delta E_{\text{ads}}^{\text{zpe}}}{k_b T}\right)} = \frac{k_b T}{L \sqrt{2\pi m k_b T}} e^{\left(\frac{-\Delta E_{\text{ads}}^{\text{zpe}}}{k_b T}\right)} \quad (2.17)
 \end{aligned}$$

If we then assume the ideal gas law and define  $A$  as

$$A = \frac{V}{L} \quad (2.18)$$

we will get the following expression for the rate of adsorption:

$$k = \frac{PA}{\sqrt{2\pi m k_b T}} e^{\left(\frac{-\Delta E_{\text{act}}^{\text{zpe}}}{k_b T}\right)} \quad (2.19)$$

The expression is only valid using the following assumptions:

- The transition state is a loose transition state in which the molecule has several translational and rotational degrees of freedom left.
- Deviations from an ideal gas are negligible, i.e. we can readily use the ideal gas law.
- The molecule loses only one translational degree of freedom between the initial and the transition state.
- The vibrational degrees of freedom can be neglected as they approximate unity at low temperature.
- The number of rotational and translational microstates do not change appreciable upon adsorption.

Desorption is the reverse of adsorption, as the molecule migrates to the gas phase after being adsorbed on the surface. If we assume the adsorbed state to only have vibrational degrees of freedom, we obtain the following expression for a diatomic molecule:

$$\begin{aligned}
 k &= \frac{k_b T}{h} \frac{Q^\ddagger}{Q} e^{\left(\frac{-\Delta E_{\text{des}}^{\text{zpe}}}{k_b T}\right)} = \frac{k_b T}{h} \frac{q_{\text{trans}}^{\ddagger(2)} q_{\text{rot}}^{\ddagger(2)} q_{\text{vib}}^{\ddagger(3N-6)}}{q_{\text{vib}}^{(3N-6)}} e^{\left(\frac{-\Delta E_{\text{des}}^{\text{zpe}}}{k_b T}\right)} = \dots \\
 &\dots = \frac{k_b T}{h} \frac{A(2\pi m k_b T)}{h^2} \frac{8\pi^2 I_i k_b T}{\sigma h^2} e^{\left(\frac{-\Delta E_{\text{des}}^{\text{zpe}}}{k_b T}\right)} = \frac{k_b T^3}{h^3} \frac{A(2\pi m k_b)}{\sigma \theta_{\text{rot}}} e^{\left(\frac{-\Delta E_{\text{des}}^{\text{zpe}}}{k_b T}\right)} \quad (2.20)
 \end{aligned}$$

### 2.3.3 Microkinetic modelling

When all the elementary reactions and their corresponding kinetic parameters are calculated, the rates of those elementary reactions can be determined by microkinetic modelling. The microkinetic model is a collection of ordinary differential equations (ODE). The construction of the system of ODEs is straightforward. First, the rate equations ( $r_j$ ) for the elementary reaction steps should be constructed using the following formula:

$$r_j = \left( k^+ \prod_{\nu_i < 0} [X_i]^{\nu_i} - k^- \prod_{\nu_i > 0} [X_i]^{\nu_i} \right) \quad (2.21)$$

wherein  $k^+$  and  $k^-$  are the rate constants for the forward and backward reactions, respectively.  $\nu_i$  is the stoichiometric coefficient of component  $X_i$ , which has a negative value for the reactants and a positive value for the products. This gives a set of  $2R$  elementary reaction equations (forward and backward) for  $N$  compounds. For each unique compound, a single ODE is obtained as given by the following formula:

$$r_X = \frac{d[X]}{dt} = \nu_X \left( k^+ \prod_{\nu_i < 0} [X_i]^{\nu_i} - k^- \prod_{\nu_i > 0} [X_i]^{\nu_i} \right) \quad (2.22)$$

wherein  $r_X$  is the rate for component X and  $\frac{d[X]}{dt}$  is the change of the components as a function of time. The system of ODEs can be time-integrated using a so-called ODE solver. A discussion on the internal workings of ODE solvers can be found in the literature. [29-31] It should be noted that the system of ODEs typically encountered in chemical kinetics suffer from the concept of stiffness. Although there is no clear mathematical definition of what stiffness is, an important characteristic

of stiff equations is that numerical methods to solve them prove to be unstable unless a very small step size is taken. Dedicated solvers have been developed to deal with such systems. Probably the most well-known method is the *ode15s* routine as present in Matlab.[32]

Several programs have been developed in the past few years to study chemokinetic systems using microkinetics simulations.[33-35] A lot of research groups build their own dedicated-purpose programs that are tailored for a specific chemical system. Herein, often Matlab or Python is used as these packages come bundled with ODE-solver libraries. In this thesis, we have used the in-house developed general-purpose modelling suite entitled MKMCXX.[36, 37] The MKMCXX program is built upon the Sundials library[38] which uses the backward differentiation formula method to solve stiff systems of ODEs.[39] MKMCXX builds the system of ODEs based on a set of elementary reaction steps and their corresponding kinetic parameters. Given a set of system parameters (e.g. pressure and temperature) and initial conditions, the system of ODEs is time-integrated until steady-state is reached. Once a steady-state solution is found, kinetic parameters such as the apparent activation energy, reaction order or degree of rate control coefficient can be automatically calculated, which provides much insights into the inner workings of the catalytic mechanism.

#### 2.3.4 Degree of rate control

One important property of a catalytic system to assess is the propensity to which each of the elementary reaction steps control the overall activity of the chemokinetic network. The degree of rate control method as introduced by Campbell and co-workers is very useful here.[40] Within this method, a rate control coefficient ( $\chi_i$ ) is defined for each elementary reaction step in the following manner:

$$\chi_i = \frac{k_i}{r} \left( \frac{\partial r}{\partial k_i} \right)_{k_j \neq k_i, K_i} = \left( \frac{\partial \ln r}{\partial \ln k_i} \right)_{k_j \neq k_i, K_i} \quad (2.23)$$

In this formula,  $r$  represents the overall reaction rate,  $k_i$  the reaction rate constant for elementary reaction step  $i$  and  $K_i$  the equilibrium constant of elementary reaction step  $i$ , as defined by the following equation:

$$K_i = \frac{k_i^+}{k_i^-} \quad (2.24)$$

In this way, the effect of lowering or increasing the reaction barrier for each elementary reaction step on the overall reaction rate is probed relative to the current rate of chemical transformation. A

positive value represents a rate-controlling step, as decreasing the reaction barrier for such a reaction step results in an increase of the overall reaction rate. A negative rate control coefficient indicates that the corresponding elementary reaction step is rate inhibiting, meaning that decreasing the barrier for this elementary reaction step results in the lowering of the overall reaction rate. The sum of the degree of rate control coefficients for all elementary reaction steps under steady-state conditions and at zero conversion should be unity.[28]

### 2.3.5 Reactor modelling

For the reactor modelling, we have implemented an isobaric and isothermal CSTR model, assuming the gases to behave ideally. Gas phase concentrations ( $C_i$ ) were determined using the following design equation[41]:

$$V \frac{dC_i}{dt} = F_i^{\text{in}} - F_i^{\text{out}} + N_{\text{sites}} r_i \quad (2.25)$$

Here,  $V$  is the volume of the reactor,  $r_i$  is the production or consumption of species  $i$  as predicted by the microkinetic model,  $F_i^{\text{in}}$  and  $F_i^{\text{out}}$  are the molar flow rates at the reactor entrance and exit, respectively. To obtain different conversions at isobaric conditions, the number of sites ( $N_{\text{sites}}$ ) can be varied corresponding to changing the catalyst loading in the reactor. We have kept the number of sites constant in the reactor. We varied the residence time by flow rates ( $F_i^{\text{in}}$ ) so that the reactor operated at differential conditions (i.e. below 15% conversion). This conversion was chosen to allow a comparison between the calculated results and the experimental results as the kinetic experiments were conducted under differential conditions.



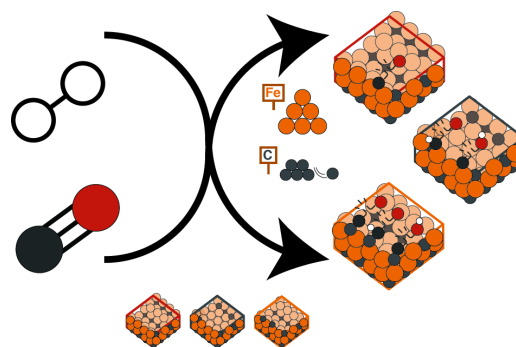
## References

- [1] E. Schrödinger, An undulatory theory of the mechanics of atoms and molecules, *Physical review* 28 (1926) 1049.
- [2] N.S. Ostlund, A. Szabo, *Modern Quantum Chemistry: Introduction to advanced electronic structure theory*, Dover Publications Inc New edition edn, 1996.
- [3] M. Born, R. Oppenheimer, Zur quantentheorie der molekeln, *Annalen der physik* 389 (1927) 457-484.
- [4] P. Hohenberg, W. Kohn, Inhomogeneous Electron Gas, *Physical Review* 136 (1964) B864-B871.
- [5] P. Hohenberg, W. Kohn, Inhomogeneous electron gas, *Physical review* 136 (1964) B864.
- [6] W. Kohn, L.J. Sham, Self-Consistent Equations Including Exchange and Correlation Effects, *Physical Review* 140 (1965) A1133-A1138.
- [7] V. Fock, Näherungsmethode zur Lösung des quantenmechanischen Mehrkörperproblems, *Zeitschrift für Physik* 61 (1930) 126-148.
- [8] V. Fock, „Selfconsistent field “mit Austausch für Natrium, *Zeitschrift für Physik* 62 (1930) 795-805.
- [9] D.R. Hartree, The wave mechanics of an atom with a non-Coulomb central field. Part I. Theory and methods, *Mathematical Proceedings of the Cambridge Philosophical Society*, Cambridge University Press, 1928, pp. 89-110.
- [10] J.W. Negele, Structure of Finite Nuclei in the Local-Density Approximation, *Physical Review C* 1 (1970) 1260-1321.
- [11] R. Eisenschitz, F. London, Über das Verhältnis der van der Waalsschen Kräfte zu den homöopolaren Bindungskräften, *Zeitschrift für Physik* 60 (1930) 491-527.
- [12] J.P. Perdew, K. Burke, M. Ernzerhof, Generalized gradient approximation made simple, *Physical review letters* 77 (1996) 3865.
- [13] F. Abild-Pedersen, M. Andersson, CO adsorption energies on metals with correction for high coordination adsorption sites—A density functional study, *Surface Science* 601 (2007) 1747-1753.
- [14] P.J. Feibelman, B. Hammer, J.K. Nørskov, F. Wagner, M. Scheffler, R. Stumpf, R. Watwe, J. Dumesic, The CO/Pt(111) Puzzle, *The Journal of Physical Chemistry B* 105 (2001) 4018-4025.
- [15] S.E. Mason, I. Grinberg, A.M. Rappe, First-principles extrapolation method for accurate CO adsorption energies on metal surfaces, *Physical Review B* 69 (2004) 161401.
- [16] B. Hammer, L.B. Hansen, J.K. Nørskov, Improved adsorption energetics within density-functional theory using revised Perdew-Burke-Ernzerhof functionals, *Physical Review B* 59 (1999) 7413-7421.
- [17] S. Shetty, A.P.J. Jansen, R.A. van Santen, Active Sites for N<sub>2</sub> Dissociation on Ruthenium, *The Journal of Physical Chemistry C* 112 (2008) 17768-17771.
- [18] P.E. Blöchl, Projector augmented-wave method, *Physical review B* 50 (1994) 17953.
- [19] T.L. Hill, *An introduction to statistical thermodynamics*, Courier Corporation, 1986.
- [20] H. Jónsson, G. Mills, K.W. Jacobsen, Nudged elastic band method for finding minimum energy paths of transitions, (1998).
- [21] G. Henkelman, B.P. Uberuaga, H. Jónsson, A climbing image nudged elastic band method for finding saddle points and minimum energy paths, *The Journal of chemical physics* 113 (2000) 9901-9904.
- [22] G.D. Smith, *Numerical solution of partial differential equations: finite difference methods*, Oxford university press, 1985.
- [23] C. Fonseca Guerra, J.G. Snijders, G. te Velde, E.J. Baerends, Towards an order-N DFT method, *Theoretical Chemistry Accounts* 99 (1998) 391-403.
- [24] G.t. Te Velde, F.M. Bickelhaupt, E.J. Baerends, C. Fonseca Guerra, S.J. van Gisbergen, J.G. Snijders, T. Ziegler, Chemistry with ADF, *Journal of Computational Chemistry* 22 (2001) 931-967.
- [25] A. Bérces, R.M. Dickson, L. Fan, H. Jacobsen, D. Swerhone, T. Ziegler, An implementation of the coupled perturbed Kohn-Sham equations: perturbation due to nuclear displacements, *Computer Physics Communications* 100 (1997) 247-262.
- [26] ADF Manual, <https://www.scm.com/doc/ADF/Input/Frequencies.html>, (2019).
- [27] H. Eyring, The Activated Complex and the Absolute Rate of Chemical Reactions, *Chemical Reviews* 17 (1935) 65-77.
- [28] I.A.W. Filot, *Introduction to Microkinetic modeling*, Technische Universiteit Eindhoven, Eindhoven, 2018.

- [29] P.N. Brown, G.D. Byrne, A.C. Hindmarsh, VODE: A variable-coefficient ODE solver, *SIAM journal on scientific and statistical computing* 10 (1989) 1038-1051.
- [30] G.D. Byrne, A.C. Hindmarsh, A polyalgorithm for the numerical solution of ordinary differential equations, *ACM Transactions on Mathematical Software (TOMS)* 1 (1975) 71-96.
- [31] G.D. Byrne, A.C. Hindmarsh, Stiff ODE solvers: A review of current and coming attractions, *Journal of Computational physics* 70 (1987) 1-62.
- [32] L.F. Shampine, M.W. Reichelt, The matlab ode suite, *SIAM journal on scientific computing* 18 (1997) 1-22.
- [33] E.D. Hermes, A.N. Janes, J.R. Schmidt, Mechanistic Insights into Solution-Phase Oxidative Esterification of Primary Alcohols on Pd(111) from First-Principles Microkinetic Modeling, *ACS Catalysis* 8 (2018) 272-282.
- [34] P. van Helden, J.-A. van den Berg, M.A. Petersen, W.J. van Rensburg, I.M. Ciobîcă, J. van de Loosdrecht, Computational investigation of the kinetics and mechanism of the initial steps of the Fischer–Tropsch synthesis on cobalt, *Faraday discussions* 197 (2017) 117-151.
- [35] A.J. Medford, C. Shi, M.J. Hoffmann, A.C. Lausche, S.R. Fitzgibbon, T. Bligaard, J.K. Nørskov, CatMAP: A Software Package for Descriptor-Based Microkinetic Mapping of Catalytic Trends, *Catalysis Letters* 145 (2015) 794-807.
- [36] I.A.W. Filot, R.A. van Santen, E.J.M. Hensen, The Optimally Performing Fischer–Tropsch Catalyst, *Angewandte Chemie International Edition* 53 (2014) 12746-12750.
- [37] I.A.W.Z. Filot, B.; Hensen, E. J. M., MKMCXX, a C++ program for constructing microkinetic models, <http://www.mkmcxx.nl>, (2019).
- [38] A.C. Hindmarsh, P.N. Brown, K.E. Grant, S.L. Lee, R. Serban, D.E. Shumaker, C.S. Woodward, SUNDIALS: Suite of nonlinear and differential/algebraic equation solvers, *ACM Trans. Math. Softw.* 31 (2005) 363-396.
- [39] C. Curtiss, J.O. Hirschfelder, Integration of stiff equations, *Proceedings of the National Academy of Sciences of the United States of America* 38 (1952) 235.
- [40] C.A. Wolcott, A.J. Medford, F. Studt, C.T. Campbell, Degree of rate control approach to computational catalyst screening, *Journal of Catalysis* 330 (2015) 197-207.
- [41] H.S. Fogler, *Essentials of Chemical Reaction Engineering: Essenti Chemica Reactio Engi*, Pearson Education, 2010.

### 3. A Quantum-Chemical DFT Study on the CO dissociation on various $\chi$ -Fe<sub>5</sub>C<sub>2</sub> Hägg Carbide surfaces

*This chapter has been published as: R.J.P. Broos, B. Zijlstra, I.A.W. Filot, E.J.M. Hensen, The Journal of Physical Chemistry C 122 (2018) 9929-9938.*



#### Abstract

The first step in the Fischer-Tropsch reaction is the production of C<sub>1</sub> monomers by dissociation of the C-O bond. While Fe is the active metal, it is well known that under typical reaction conditions, Fe changes into various carbide phases. The Hägg carbide ( $\chi$ -Fe<sub>5</sub>C<sub>2</sub>) phase is usually considered as the catalytically active phase. We carried out a comprehensive DFT study of CO dissociation on various surface terminations of the Hägg carbide, selected on their specific site topology and the presence of stepped sites. Based on the reaction energetics, we identified several feasible CO dissociation pathways over the Hägg-carbide. In this study, we have compared direct CO dissociation with H- and C-assisted CO dissociation mechanisms. We demonstrated that the reaction rate for CO dissociation critically depends on the presence and topology of interstitial C atoms close to the active site. Typically, CO dissociation proceeds via a direct C-O bond scission mechanism on the stepped sites on the Fe-carbide surface. We have shown a preference for direct CO dissociation on the surfaces with a stepped character. H-assisted CO dissociation, via a HCO intermediate, was preferred when the surface did not have a clear stepped character. We have also shown that activation barriers for dissociation are highly dependent on the surface termination. With a consistent dataset and including migration corrections, we then compared CO dissociation rates based on a simplified kinetic model. With this model, we not only showed the activation energy to be important, but the adsorption energy of the CO, the C, and the O species to be of relevance for the reaction rate as well. We found that the most active surface termination is a (11 $\bar{1}$ ) surface cut in such way that the surface exposes B<sub>5</sub> sites that are not occupied by C atoms. On these B<sub>5</sub> sites, direct CO dissociation presents the highest rate.

### 3.1 Introduction

Fischer-Tropsch (FT) synthesis has proven to be an economically attractive route for the conversion of natural gas and coal into synthetic fuels and chemicals in certain settings.[1] The products obtained from CO hydrogenation critically depend on the transition metal used. Ru and Co mainly produce long-chain hydrocarbons, while Fe-based catalysts find application in the production of long-chain hydrocarbons, gasoline or light olefins, depending on the process conditions. The active phase in commercial FT catalysts is typically based on Co or Fe. Fe catalysts are less expensive and more active in the water-gas shift reaction than Co. The latter is important when synthesis gas with a low  $H_2/CO$  ratio needs to be processed.[2] Fe-based FT catalysts are usually prepared by precipitation. Promoters such as Cu and K are used to improve the Fe reduction degree and increase FT activity and selectivity, respectively.

Similar to Co, the nature of the active sites in Fe-based FT catalysts and the mechanism by which CO is converted to hydrocarbons remain topics of considerable debate. It is well known that under FT conditions the Fe-oxide precursor is rapidly converted into Fe-carbide. Hägg carbide ( $\chi\text{-Fe}_5\text{C}_2$ ) has been identified as the most likely catalytically active phase.[3] Accordingly, besides studies on metallic Fe surfaces into FT mechanism, [4-7] most computational investigations have focused on Fe-carbide model surfaces.[4, 8-17] For the Hägg carbide, several surface terminations display comparable thermodynamic stability at FT conditions.[18] Therefore, it is important to involve these stable surfaces in mechanistic studies of the FT reaction. CO dissociation, which initiates the FT reaction, is one of the crucial elementary reaction steps and key to understanding structure-performance in FT catalysis. Until now, most studies have considered direct CO dissociation on Fe carbides.[4, 8-15] H-assisted CO dissociation involving HCO as an intermediate has been considered as an alternative way of activating CO on metallic[19] and Hägg carbide surfaces.[8-12, 14, 15, 20] Another relevant aspect is that Fe-carbides can expose C atoms at their surface, which can also be involved in the FT reaction. C-O bond scission via a CC-O intermediate has been only scarcely investigated[16, 21], and, when considered, has not been compared to H-assisted CO dissociation. Compared to these earlier studies, we have performed a migration correction to our data. In such a correction, we consider migration of the adsorbates before and after the elementary reaction step to and from the most stable adsorption state, respectively. These aspects are essential to properly compare different C-O bond scission pathways.

In the present work, we use quantum-chemical density functional theory (DFT) to determine the preferred CO dissociation pathways on Hägg carbide surfaces. We first computed surface free energies of various surface terminations of the Hägg carbide and established how CO adsorbs on these surfaces. Then, we determined activation energies for different CO dissociation pathways on the most stable surface terminations. These data are compared to literature data. We then compared CO dissociation rates based on a simplified kinetic model, with a consistent dataset while including migration corrections.

### 3.2 Method

All spin-polarized density functional theory (DFT) calculations were conducted using the projector augmented wave (PAW) method and the Perdew–Burke–Ernzerhof (PBE) functional implemented in the Vienna ab initio simulation package (VASP) code.[22]<sup>[23]</sup> Solutions of the Kohn-Sham equations were calculated using a plane-wave basis set with a cut-off energy of 400 eV. The sampling of the Brillouin zone was done using 5x5x1 *k*-points. Higher cut-off energy or finer Brillouin zone sampling did not lead to significant energy differences. Electron smearing was employed using a first-order Methfessel-Paxton technique[24], with a smearing width of 0.2 eV. The tetrahedron method with Blöchl corrections with a smearing width of 0.2 eV was used for the calculation of the bulk structure. All atoms were allowed to relax for the calculation of the bulk structure as well as the calculation of the empty surfaces. The thickness of the empty unit cells was taken between 6.4 and 10.3 Å, depending on the Miller index plane. We used a slab containing 40 Fe atoms and 16 C atoms for the (010)<sub>0.25</sub> surface, 60 Fe atoms and 24 C atoms for the (11 $\bar{1}$ )<sub>0.0</sub> and (11 $\bar{1}$ )<sub>0.5</sub> surfaces and 80 Fe and 32 C atoms for the (100)<sub>0.0</sub> and (100)<sub>0.287</sub> surfaces. Adsorption of adatoms was done on the top side of the slab while the lower half of the slab was frozen.

The adsorption energies of the gas phase molecules were determined by subtracting both energies of the empty surface and the free adsorbate from the adsorbed state. The energy of the adsorbate in the gas phase was performed by placing a molecule at the centre of a 10x10x10 Å<sup>3</sup> unit cell, using the  $\Gamma$ -point for *k*-point sampling. For the electron smearing, a Gaussian smearing width of 0.002 eV was used. The adsorption energies, after zero-point energy (ZPE) corrections, were in good agreement with tabulated thermodynamic data.[25]

For all calculations, the convergence criterion was set to 10<sup>-4</sup> eV for the ionic steps and to 10<sup>-5</sup> eV for the electronic convergence. All geometry optimizations were conducted using the conjugate-gradient algorithm. Transition states were acquired using the nudged elastic band (NEB)

method.[26] A frequency analysis was performed to confirm that all transition geometries corresponded to a first-order saddle point on the potential energy surface with an imaginary frequency in the direction of the reaction coordinate. The Hessian matrix was constructed using a finite difference approach with a step size of 0.02 Å for displacement of individual atoms along each Cartesian coordinate. The corresponding normal mode vibrations were also used to calculate the zero-point energy correction. We corrected the barriers for the migration of fragments after dissociation by considering the energy difference of the geometry directly after dissociation and their most stable adsorption positions at infinite distance.

The surface energies were calculated using

$$E_{surface} = \frac{(E_n - n * E_{bulk})}{2 * A} \quad (3.1)$$

where  $E_n$  refers to the total energy of the slab, containing  $n$  times the conventional monoclinic bulk cell ( $\text{Fe}_{20}\text{C}_8$ ),  $E_{bulk}$  to the bulk energy,  $A$  to the area of the surface, and  $E_{surface}$  to the surface energy of the surface, respectively. This procedure is valid for stoichiometric and symmetric surfaces (i.e., surfaces with equivalent top and bottom surfaces). In our study we have also used stoichiometric and asymmetric surfaces. An average surface energy was calculated for the asymmetric surfaces using the abovementioned procedure.

The rate constant ( $k$ ) of an elementary reaction step can be determined using the Eyring equation, which is defined as follows:

$$k = v \exp\left(\frac{-\Delta E_{act}}{k_b T}\right) \quad (3.2)$$

where  $\Delta E_{act}$  stands for the activation energy,  $k_b$  for the Boltzmann constant,  $T$  for temperature, and  $v$  for the pre-exponential factor. This pre-exponential factor can be calculated for the forward and backward reaction and is defined as follows:

$$v_{forward} = \frac{k_b T}{h} \left( \frac{q_{vib}^{TS}}{q_{vib}^{IS}} \right) \text{ and } v_{backward} = \frac{k_b T}{h} \left( \frac{q_{vib}^{TS}}{q_{vib}^{FS}} \right), \quad (3.3)$$

where  $v_{forward}$  and  $v_{backward}$  refer to the pre-exponential factors for the forward and the backward reaction, respectively,  $q_{vib}$  stands for the vibrational partition function of the initial state (IS) and the transition state (TS), and  $h$  for Planck's constant.

To compare the CO dissociation rates on the different surfaces, we employed a simplified kinetic model, similar to the one used by Liu et al.[27] For these calculations, we used a temperature of 500

K and a CO pressure of  $3 \cdot 10^{-5}$  Pa. The relatively low pressure was chosen to simulate conditions of low CO coverage, consistent with the low coverage used in the transition-state calculations. For more complex reaction pathways involving pre-hydrogenation to HCO and COH, we used the overall reaction barrier for C-O bond scission and a  $H_2$  pressure of  $6 \cdot 10^{-5}$  Pa. For C-assisted CO dissociation pathways, we took into account two separate steps, namely the adsorption of CO and the formation of CCO prior to cleavage of the C-O bond in CCO. The rate is described by the following rate equation:

$$r = \frac{k_3 K_1 K_2 P_{CO}}{1 + K_1 P_{CO} + K_1 K_2 P_{CO} + K_1^2 K_2 P_{CO}^2} \quad (3.3)$$

where  $K_1$  and  $K_2$  are the equilibrium rate constants for CO adsorption and C-CO coupling, respectively,  $k_3$  the rate constant for the rate-limiting step (the CO dissociation) and  $P_{CO}$  the partial pressure of CO. The derivation of this equation can be found in Appendix A.1.

### 3.3 Results and Discussion

DFT calculations were performed to investigate the energetics of CO dissociation on various Hägg carbide surfaces. First, we will present the bulk structure and surface energies of the candidate surface terminations of Hägg carbide. Then, we will discuss CO and H adsorption. Finally, we will discuss direct and assisted C-O bond scission pathways for the five most stable surfaces and employ simplified kinetic models to compare CO dissociation rate on these surfaces.

#### 3.3.1 Bulk and surface Hägg carbide models

Hägg carbide has a monoclinic unit cell with space group C2/c and cell dimensions  $a = 11.588$  Å,  $b = 4.579$ ,  $c = 5.059$  Å, and  $\beta = 97.75^\circ$ . [28] Optimized cell parameters determined by our DFT calculations are  $a = 11.504$  Å,  $b = 4.524$  Å,  $c = 5.012$  Å, and  $\beta = 97.75^\circ$  ( $\alpha = \gamma = 90^\circ$ ). Figure 3.1 shows orthographic representations of the top (green), front (blue) and side (red) views of the bulk structure of Hägg carbide. As described by Steynberg et al., [18] there are nine unique low Miller index planes for the Hägg carbide. For each of these planes, more than one unique surface termination is possible, as cleaving the unit cell in the direction perpendicular to the Miller plane at fractional distances results in different surface terminations. This is due to the presence of interstitial

C atoms present in the Hägg carbide. In this study, we adopted the notation introduced by Steynberg et al. to indicate the cut that generates the different surfaces.

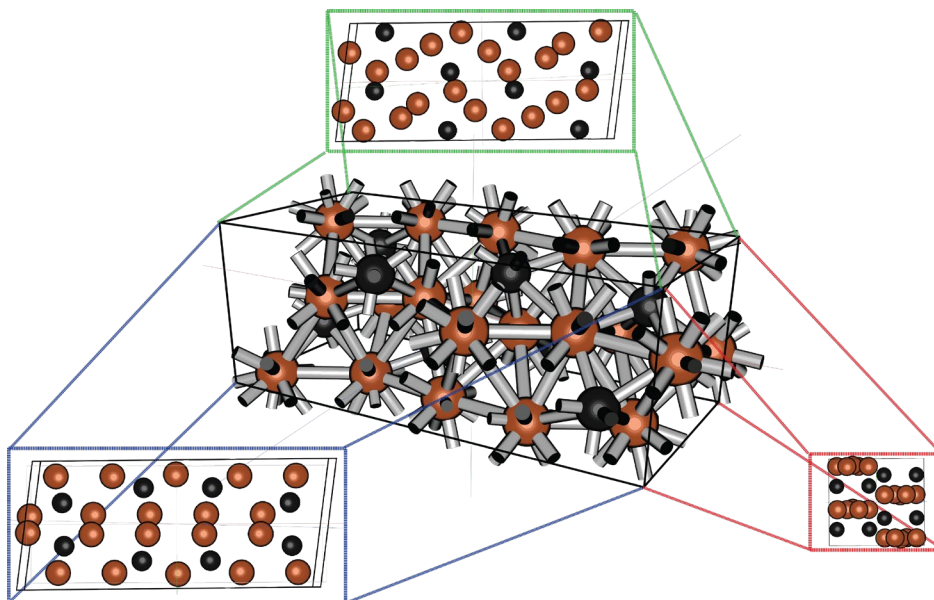


**Figure 3.1** Orthographic representations of the a-b plane (green), b-c plane (blue) and a-c plane (red) of the monoclinic (C2/c) unit cell for the bulk structure of Hägg carbide. The orange and black atoms represent the Fe and C atoms, respectively.

A guiding example can be found in Figure 3.2. Steynberg et al. only considered the 14 symmetric surfaces. Sorescu stressed the importance of including non-symmetric surfaces, as some have lower surface free energies than the symmetric ones.[16]

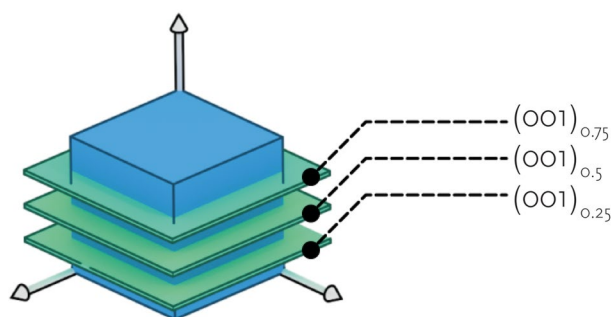


**Figure 3.2** Graphical depiction of the notation of the surface terminations. The surface orientation is denoted using Miller indices. For the surfaces spanned at the origin of the two vectors composing the Miller index planes, we use the subscript 0.0. A non-zero subscript refers to a translation of the plane in the direction of the surface normal indicated by the particular Miller index. This subscript is fractional; meaning that a subscript of 1.0 would indicate that the cutting plane is translated exactly by one unit cell.

In this work, we considered two such asymmetric surfaces, namely  $(100)_{0.0}$  and  $(100)_{0.287}$ , because they are among the most stable surface terminations and also because they contain surface topologies akin of  $B_5$  sites, i.e. adjacent 4- and threefold sites. The  $(100)_{0.287}$  surface does not contain C atoms in the surface and the sub-surface layer. The calculated surface energies of the various surfaces investigated herein are collected in Table 3.1.



**Table 3.1** Surface energies of the various Hägg carbide termination. The surface energies are calculated with respect to the monoclinic bulk unit cell  $\text{Fe}_{20}\text{C}_8$  (C2/c).

Surface Termination	Surface energy [J/m <sup>2</sup> ]	Surface Termination	Surface energy [J/m <sup>2</sup> ]
(100) <sub>0.0</sub>	2.19	(011) <sub>0.0</sub>	2.54
(010) <sub>0.25</sub>	2.24	(10 $\bar{1}$ ) <sub>0.0</sub>	2.65
(11 $\bar{1}$ ) <sub>0.0</sub>	2.24	(011) <sub>0.25</sub>	2.66
(100) <sub>0.287</sub>	2.42	(010) <sub>0.429</sub>	2.69
(11 $\bar{1}$ ) <sub>0.5</sub>	2.45	(111) <sub>0.5</sub>	2.70
(111) <sub>0.0</sub>	2.46	(010) <sub>0.0</sub>	2.76
(110) <sub>0.0</sub>	2.47	(101) <sub>0.0</sub>	2.90
(110) <sub>0.5</sub>	2.48	(100) <sub>0.25</sub>	3.01
(001) <sub>0.0</sub>	2.54		

The differences in surface free energies are consistent with literature reports.[16, 18]

On the basis of these surface free energies, we constructed a Wulff particle taking into account only the lowest surface free energy of a specific Miller index plane. For instance, for the (010) plane, the (010)<sub>0.25</sub> was included (i.e., the (010)<sub>0.0</sub> surface was excluded as the (010)<sub>0.25</sub> is more stable by 0.52 J/m<sup>2</sup>). The resulting Wulff particle is shown in Figure 3.3. Nearly two-thirds of the surface of the Wulff particle is made up of (010)<sub>0.25</sub>, (11 $\bar{1}$ )<sub>0.0</sub> and (100)<sub>0.0</sub> surfaces, as the Wulff particle consists of 10% of the (010) surfaces, 25% of the (100) surfaces and 30% of the (11 $\bar{1}$ ) surfaces. On the basis of this analysis, we selected the five surfaces with the lowest surface energies, i.e., the (010)<sub>0.25</sub>, (11 $\bar{1}$ )<sub>0.0</sub>, (100)<sub>0.0</sub>, (11 $\bar{1}$ )<sub>0.5</sub>, and (100)<sub>0.287</sub> surface terminations as models to study CO dissociation. For the Wulff construction, we only took the most stable Miller index plane into account.

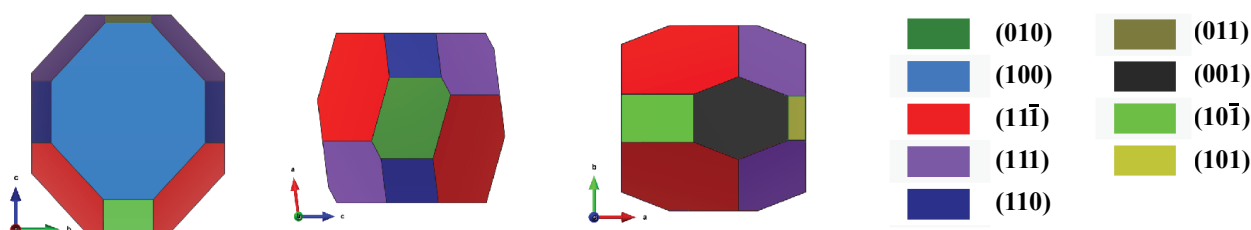


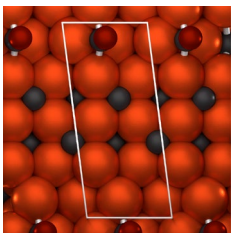
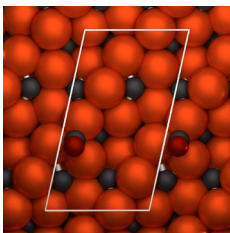
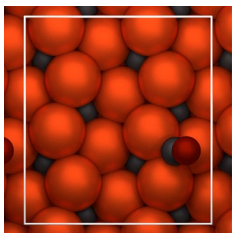
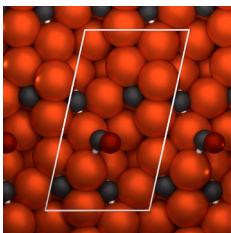
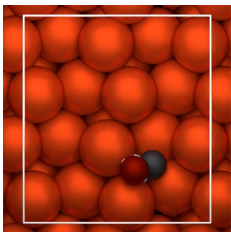
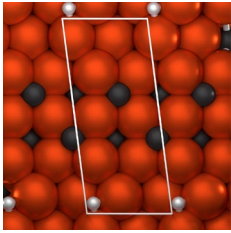
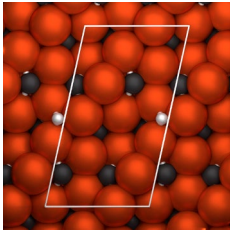
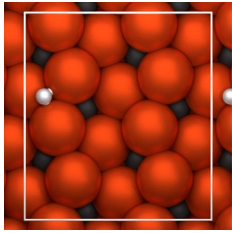
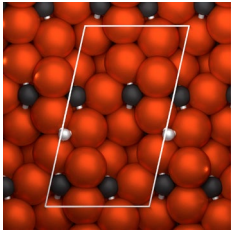
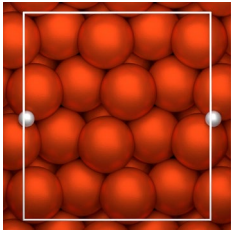
**Figure 3.3** Visualization of the Wulff particle, taking only the lowest surface free energy of a specific Miller index plane. The, b and c axes are represented by red, green and blue arrows, respectively. Nearly three-quarters of the surface of the Wulff particle is made up of (010)<sub>0.25</sub>, (11 $\bar{1}$ )<sub>0.0</sub> and (100)<sub>0.0</sub> surfaces.

However, the possibility remains that, depending on the reaction conditions, the (100)<sub>0.287</sub> surface is present instead of the (100)<sub>0.0</sub>. So, even though the (11 $\bar{1}$ )<sub>0.0</sub>, and the (100)<sub>0.0</sub> surfaces are more stable as compared to the (11 $\bar{1}$ )<sub>0.5</sub> and (100)<sub>0.287</sub> surface terminations, the latter terminations were also

taken into consideration. Here, we will show that the most active surface termination is a  $(11\bar{1})$  surface cut in such a way that the surface exposes  $B_5$  sites not occupied by C atoms.

### 3.3.2 CO adsorption and CO bond dissociation

To identify the preferred adsorption site for CO, we explored adsorption on top, bridge, threefold, fourfold, fivefold and sixfold sites. Moreover, we considered adsorption on pseudo  $B_5$ -sites, i.e. sites with a topology that resembles a  $B_5$  site. Figure 3.4 presents the most stable adsorption modes for CO and H on the selected surfaces.

CO on $(010)_{0.25}$	CO on $(11\bar{1})$	CO on $(100)$	CO on $(11\bar{1})_{0.5}$	CO on $(100)_{0.287}$
				
fourfold ( $2B_3$ site) 178 kJ/mol	threefold 184 kJ/mol	threefold 181 kJ/mol	bridged 191 kJ/mol	fourfold ( $B_5$ site) 221 kJ/mol
H on $(010)_{0.25}$	H on $(11\bar{1})$	H on $(100)$	H on $(11\bar{1})_{0.5}$	H on $(100)_{0.287}$
				
threefold 101 kJ/mol	threefold 105 kJ/mol	threefold 120 kJ/mol	threefold 151 kJ/mol	threefold 167 kJ/mol

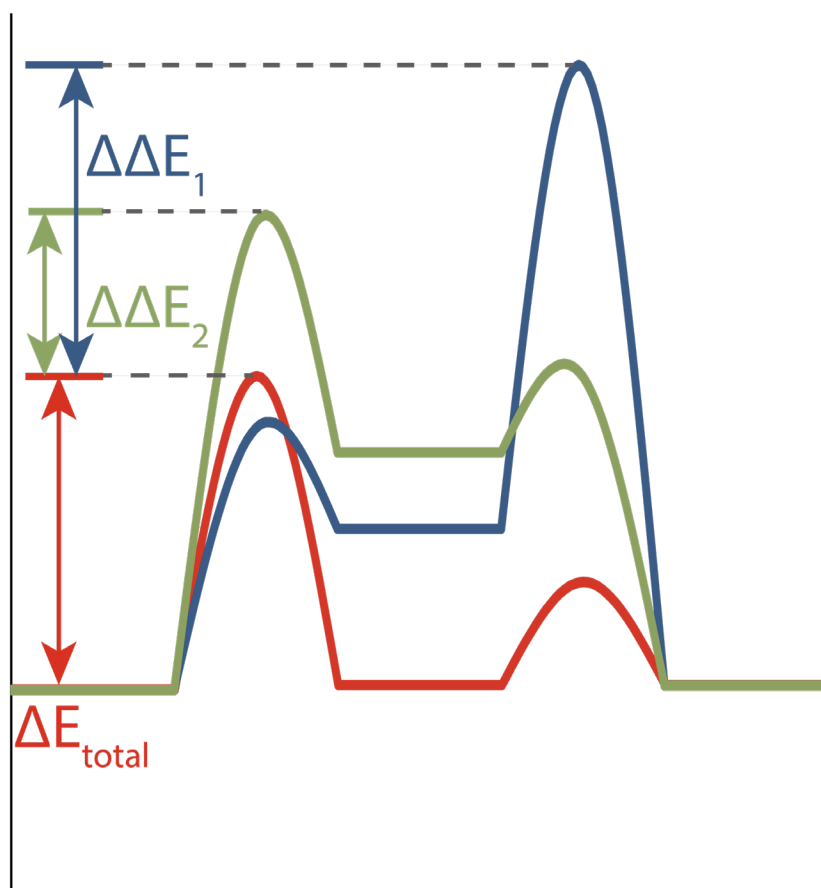
**Figure 3.4** Surface topology of the five most stable surface terminations of the Hägg carbide. The most stable adsorption configurations and the corresponding adsorption energies of CO and H are also shown. CO tends to adsorb on a fourfold site, unless this is hampered by interstitial C atoms. The notation  $2B_3$  indicates that CO is adsorbed in two adjacent threefold sites. H prefers to adsorb on a threefold site.

A complete overview of the configurations is given in Appendix A.2. Then, direct, H- and C-assisted C-O bond dissociation reactions were taken into account. For the H-assisted CO dissociation mechanism, we considered the pathways via COH and HCO intermediates. Activation barriers and corresponding pre-exponential factors for the calculated elementary reaction steps are listed in Table 3.2.

**Table 3.2** Forward activation energy ( $E_f$ ) and backward activation energy ( $E_b$ ) in kJ/mol, and forward ( $v_f$ ) and backward ( $v_b$ ) pre-exponential factors for direct and H-assisted CO dissociation on the five most stable  $\text{Fe}_5\text{C}_2$  surfaces. C\* indicates that a C atom from the surface is involved. The (010)<sub>0.25</sub> surface with a C-vacancy is noted as (010)\*<sub>0.25</sub>.

Surface	Dissociation site	Elementary Reaction step		$E_f$ (kJ/mol)	$v_f$	$E_b$ (kJ/mol)	$v_b$
(010) <sub>0.25</sub>	2B <sub>3</sub>	CO	$\rightleftharpoons$ C + O	166	$1.2 \cdot 10^{12}$	178	$1.1 \cdot 10^{13}$
(010) <sub>0.25</sub>	2B <sub>3</sub>	CO + H	$\rightleftharpoons$ HCO	119	$4.0 \cdot 10^{12}$	68	$4.6 \cdot 10^{13}$
(010) <sub>0.25</sub>	2B <sub>3</sub>	CO + H	$\rightleftharpoons$ COH	216	$2.3 \cdot 10^{13}$	134	$7.5 \cdot 10^{12}$
(010) <sub>0.25</sub>	2B <sub>3</sub>	HCO	$\rightleftharpoons$ CH + O	53	$7.6 \cdot 10^{12}$	143	$1.2 \cdot 10^{13}$
(010) <sub>0.25</sub>	2B <sub>3</sub>	COH	$\rightleftharpoons$ C + OH	133	$1.8 \cdot 10^{12}$	152	$3.1 \cdot 10^{12}$
(010)* <sub>0.25</sub>	B <sub>5</sub>	CO	$\rightleftharpoons$ C + O	137	$2.2 \cdot 10^{12}$	215	$5.3 \cdot 10^{12}$
(010)* <sub>0.25</sub>	B <sub>5</sub>	CO + H	$\rightleftharpoons$ HCO	120	$4.0 \cdot 10^{12}$	50	$1.2 \cdot 10^{13}$
(010)* <sub>0.25</sub>	B <sub>5</sub>	CO + H	$\rightleftharpoons$ COH	122	$1.3 \cdot 10^{13}$	71	$6.1 \cdot 10^{12}$
(010)* <sub>0.25</sub>	B <sub>5</sub>	HCO	$\rightleftharpoons$ CH + O	48	$1.1 \cdot 10^{12}$	186	$1.7 \cdot 10^{13}$
(010)* <sub>0.25</sub>	B <sub>5</sub>	COH	$\rightleftharpoons$ C + OH	2	$6.1 \cdot 10^{12}$	56	$7.2 \cdot 10^{12}$
(11 $\bar{1}$ ) <sub>0.0</sub>		CO	$\rightleftharpoons$ C + O	156	$8.6 \cdot 10^{11}$	144	$9.1 \cdot 10^{12}$
(11 $\bar{1}$ ) <sub>0.0</sub>	B <sub>3</sub>	CO + H	$\rightleftharpoons$ HCO	173	$1.1 \cdot 10^{12}$	4	$3.9 \cdot 10^{12}$
(11 $\bar{1}$ ) <sub>0.0</sub>		CO + H	$\rightleftharpoons$ COH	226	$6.2 \cdot 10^{12}$	60	$1.6 \cdot 10^{13}$
(11 $\bar{1}$ ) <sub>0.0</sub>	2B <sub>3</sub>	HCO	$\rightleftharpoons$ CH + O	10	$3.2 \cdot 10^{12}$	152	$9.4 \cdot 10^{12}$
(11 $\bar{1}$ ) <sub>0.0</sub>		COH	$\rightleftharpoons$ C + OH	67	$4.4 \cdot 10^{12}$	173	$6.6 \cdot 10^{12}$
(11 $\bar{1}$ ) <sub>0.0</sub>	B <sub>5</sub>	C* + CO	$\rightleftharpoons$ C*CO	80	$1.2 \cdot 10^{14}$	16	$6.0 \cdot 10^{13}$
(11 $\bar{1}$ ) <sub>0.0</sub>	B <sub>5</sub>	C*CO	$\rightleftharpoons$ C*C + O	98	$2.6 \cdot 10^{12}$	120	$1.1 \cdot 10^{13}$
(11 $\bar{1}$ ) <sub>0.0</sub>	B <sub>5</sub>	C*CO + H	$\rightleftharpoons$ C*HCO	97	$4.5 \cdot 10^{13}$	71	$3.9 \cdot 10^{13}$
(11 $\bar{1}$ ) <sub>0.0</sub>	B <sub>5</sub>	C*CO + H	$\rightleftharpoons$ C*COH	135	$5.5 \cdot 10^{12}$	85	$8.5 \cdot 10^{12}$
(11 $\bar{1}$ ) <sub>0.0</sub>	B <sub>5</sub>	C*HCO	$\rightleftharpoons$ C*CH + O	31	$1.7 \cdot 10^{13}$	167	$1.4 \cdot 10^{13}$
(11 $\bar{1}$ ) <sub>0.0</sub>	B <sub>5</sub>	C*COH	$\rightleftharpoons$ C*C + OH	63	$8.7 \cdot 10^{12}$	87	$1.5 \cdot 10^{12}$
(100) <sub>0.0</sub>	B <sub>5</sub>	CO	$\rightleftharpoons$ C + O	128	$7.9 \cdot 10^{11}$	108	$5.6 \cdot 10^{12}$
(100) <sub>0.0</sub>	B <sub>5</sub>	CO + H	$\rightleftharpoons$ HCO	97	$1.7 \cdot 10^{12}$	11	$1.5 \cdot 10^{13}$
(100) <sub>0.0</sub>	B <sub>5</sub>	CO + H	$\rightleftharpoons$ COH	136	$3.2 \cdot 10^{12}$	27	$7.0 \cdot 10^{12}$
(100) <sub>0.0</sub>	B <sub>5</sub>	HCO	$\rightleftharpoons$ CH + O	98	$5.7 \cdot 10^{13}$	183	$1.6 \cdot 10^{13}$
(100) <sub>0.0</sub>	B <sub>5</sub>	COH	$\rightleftharpoons$ C + OH	58	$6.0 \cdot 10^{12}$	129	$2.3 \cdot 10^{12}$
(11 $\bar{1}$ ) <sub>0.5</sub>	B <sub>5</sub>	CO	$\rightleftharpoons$ C + O	118	$1.2 \cdot 10^{12}$	139	$1.2 \cdot 10^{13}$
(11 $\bar{1}$ ) <sub>0.5</sub>	B <sub>3</sub>	CO + H	$\rightleftharpoons$ HCO	152	$2.2 \cdot 10^{12}$	89	$1.6 \cdot 10^{13}$
(11 $\bar{1}$ ) <sub>0.5</sub>	B <sub>5</sub>	CO + H	$\rightleftharpoons$ COH	224	$1.9 \cdot 10^{13}$	82	$1.9 \cdot 10^{13}$
(11 $\bar{1}$ ) <sub>0.5</sub>	2B <sub>3</sub>	HCO	$\rightleftharpoons$ CH + O	65	$1.2 \cdot 10^{13}$	94	$1.4 \cdot 10^{13}$
(11 $\bar{1}$ ) <sub>0.5</sub>	B <sub>5</sub>	COH	$\rightleftharpoons$ C + OH	47	$2.2 \cdot 10^{12}$	141	$7.4 \cdot 10^{12}$
(100) <sub>0.287</sub>	B <sub>5</sub>	CO	$\rightleftharpoons$ C + O	128	$5.1 \cdot 10^{12}$	220	$1.1 \cdot 10^{13}$
(100) <sub>0.287</sub>	B <sub>3</sub>	CO + H	$\rightleftharpoons$ HCO	139	$3.0 \cdot 10^{13}$	37	$3.7 \cdot 10^{13}$
(100) <sub>0.287</sub>	B <sub>3</sub>	CO + H	$\rightleftharpoons$ COH	192	$3.0 \cdot 10^{13}$	53	$2.9 \cdot 10^{13}$
(100) <sub>0.287</sub>	B <sub>5</sub>	HCO	$\rightleftharpoons$ CH + O	46	$9.2 \cdot 10^{12}$	182	$1.1 \cdot 10^{13}$
(100) <sub>0.287</sub>	B <sub>5</sub>	COH	$\rightleftharpoons$ C + OH	31	$1.3 \cdot 10^{13}$	179	$9.1 \cdot 10^{12}$

The most favourable reaction pathways for CO dissociation will be discussed for the five most stable surfaces. In order to have a quantitative approach to compare different pathways, we define an overall barrier for CO dissociation ( $\Delta E_{\text{total}}$ ) as the difference between the highest lying transition states along the potential energy surface that yields dissociated CO and the most stable adsorption state of CO. We also define  $\Delta\Delta E$  as the difference in  $\Delta E_{\text{total}}$  with the most favourable pathway characterized by the lowest  $\Delta E_{\text{total}}$  for a particular surface. Reaction pathways with relatively small  $\Delta\Delta E$  can still contribute to CO bond dissociation under practical conditions. This will be taken into account by a simplified kinetic model. Values for  $\Delta E_{\text{total}}$  and  $\Delta\Delta E$  for the different surfaces are given in Table 3.3. A graphical representation of  $\Delta E_{\text{total}}$  and  $\Delta\Delta E$  values is shown in Figure 3.5. The structures of the C-O scission steps are shown in Table 3.4.

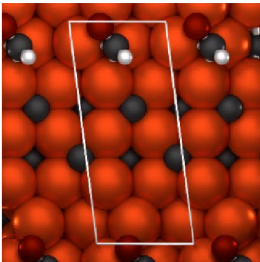
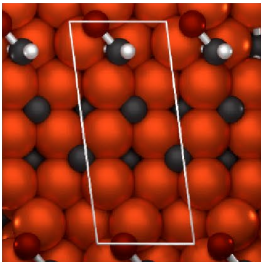
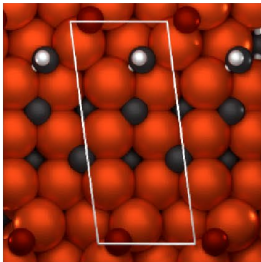
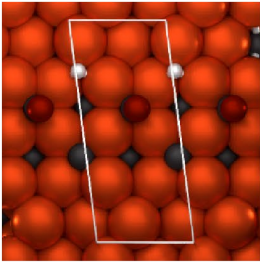
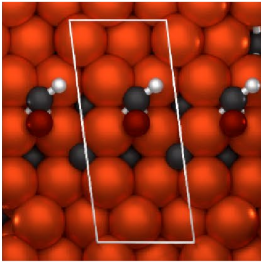
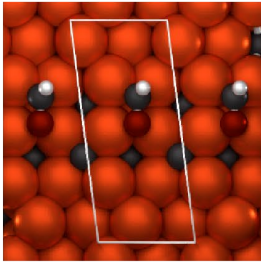
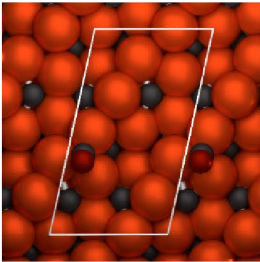
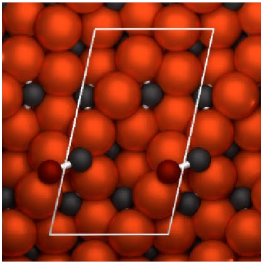
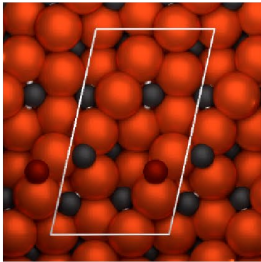
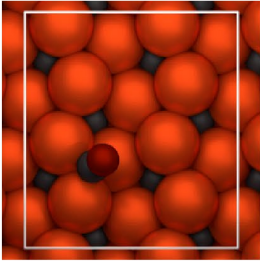
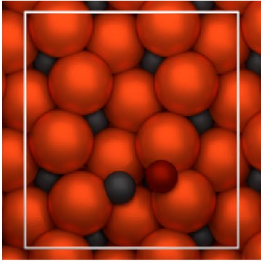
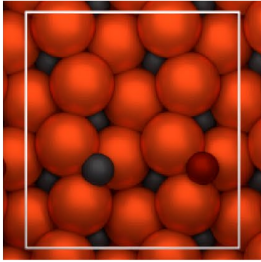
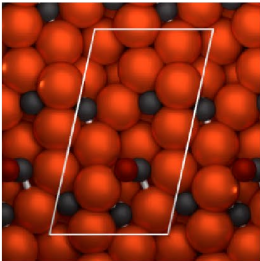
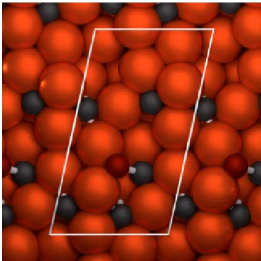
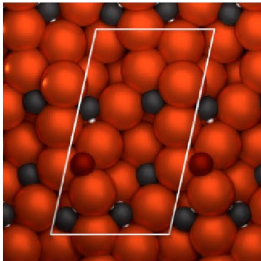
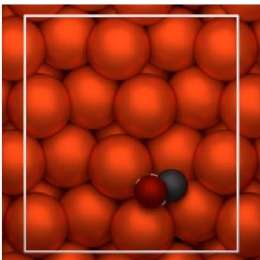
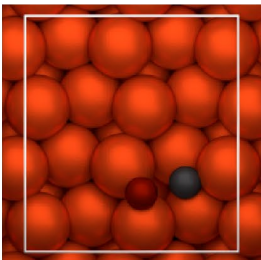
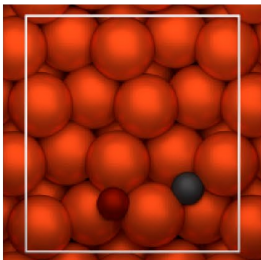


**Figure 3.5** Graphical representation of the  $\Delta E_{\text{total}}$  and the  $\Delta\Delta E$

**Table 3.3**  $\Delta E_{\text{total}}$  and  $\Delta \Delta E$  values for CO dissociation over the five most stable surfaces via the direct CO dissociation and the H-assisted pathways for CO dissociation.  $\Delta E_{\text{total}}$  is defined as the difference in energy between the energy of the adsorbed species and the energy of the energetically highest lying transition state of the energetically lowest pathway. The  $\Delta \Delta E$  is defined as the difference in the value for  $\Delta E_{\text{total}}$  for the energetically most favourable pathway and the  $\Delta E_{\text{total}}$  for a different pathway. The (010)<sub>0.25</sub> surface with a C-vacancy is noted as (010)\*<sub>0.25</sub>.

Surface	CO dissociation pathway	$\Delta E_{\text{total}}^*$ [kJ/mol]	$\Delta \Delta E$ [kJ/mol]	Rate limiting step
(010) <sub>0.25</sub>	Direct	166	55	$\text{CO} \rightarrow \text{C} + \text{O}$
	H-assisted via HCO	119	0	$\text{CO} + \text{H} \rightarrow \text{HCO}$
	H-assisted via COH	216	98	$\text{CO} + \text{H} \rightarrow \text{COH}$
(010)* <sub>0.25</sub>	Direct	141	15	$\text{CO} \rightarrow \text{C} + \text{O}$
	H-assisted via HCO	124	0	$\text{CO} + \text{H} \rightarrow \text{HCO}$
	H-assisted via COH	126	2	$\text{CO} + \text{H} \rightarrow \text{COH}$
(111) <sub>0.0</sub>	C-assisted via CCO	162	6	$\text{CCO} \rightarrow \text{CC} + \text{O}$
	Direct	156	0	$\text{CO} \rightarrow \text{C} + \text{O}$
	H-assisted via HCO	179	23	$\text{HCO} \rightarrow \text{CH} + \text{O}$
	H-assisted via COH	233	77	$\text{CO} + \text{H} \rightarrow \text{COH}$
	H/C-assisted via CHCO	161	5	$\text{CCO} + \text{H} \rightarrow \text{CHCO}$
	H/C-assisted via CCOH	199	43	$\text{CCO} + \text{H} \rightarrow \text{CCOH}$
(100) <sub>0.0</sub>	Direct	128	0	$\text{CO} \rightarrow \text{C} + \text{O}$
	H-assisted via HCO	184	56	$\text{HCO} \rightarrow \text{CH} + \text{O}$
	H-assisted via COH	167	39	$\text{COH} \rightarrow \text{C} + \text{OH}$
(111) <sub>0.5</sub>	Direct	118	0	$\text{CO} \rightarrow \text{C} + \text{O}$
	H-assisted via HCO	152	34	$\text{CO} + \text{H} \rightarrow \text{HCO}$
	H-assisted via COH	224	106	$\text{CO} + \text{H} \rightarrow \text{COH}$
(100) <sub>0.287</sub>	Direct	128	0	$\text{CO} \rightarrow \text{C} + \text{O}$
	H-assisted via HCO	148	20	$\text{HCO} \rightarrow \text{CH} + \text{O}$
	H-assisted via COH	192	64	$\text{CO} + \text{H} \rightarrow \text{COH}$

**Table 3.4** Modes for the rate limiting C-O scission steps. Depicted are the configurations of the CO or HCO molecule as the initial state with corresponding transition state and the configurations of C, CH, and O in the transition and final state.

Surface	Initial state	Transition state	Final state
$(010)_{0.25}$			
$(010)^*_{0.25}$			
$(11\bar{1})$			
$(100)$			
$(11\bar{1})_{0.5}$			
$(100)_{0.287}$			



### 3.3.3 The $(010)_{0.25}$ surface

The  $(010)_{0.25}$  surface contains two C atoms in fourfold positions, while two C atoms are located in interstitial locations below the surface. The surface exposes top, threefold and fourfold Fe sites for adsorption. Binding of CO to the fourfold site of the  $B_5$  ensemble is not possible because of the presence of the interstitial C atom below the adsorption site. No stable adsorption configuration of CO on top or threefold sites was identified and, in these cases, CO reverted to a fourfold adsorption mode involving binding to two adjacent threefold sites. This site is termed a  $2B_3$  site. CO adsorption on this site is slightly more stable than bridged adsorption on the edge of a threefold site. We also found that CO can adsorb on top of a surface C atom with an energy of 77 kJ/mol. Other adsorption modes involving simultaneous coordination to C and Fe atoms were found to be unstable. The dissociative adsorption energy of  $H_2$  is 101 kJ/mol and the H atoms prefer to bind to threefold Fe sites.

C-O bond dissociation may start from different adsorption modes. Direct dissociation from the  $2B_3$  site involves a barrier of 166 kJ/mol, close to the value reported by Sorescu for the same dissociation pathway.[16] In the transition state, the C atom remains in the  $2B_3$  site, while the O atom moves to a bridge position on one of the threefold sites of the  $2B_3$  site. Finally, repulsion is relieved by migration of the O atom to an adjacent threefold site. H-assisted pathways were considered as well. Hydrogenation of CO adsorbed in the  $2B_3$  site to COH has a barrier 209 kJ/mol. The barrier for HCO formation, on the other hand, is only 119 kJ/mol. In the initial state, the H atom is located at a threefold site adjacent to the CO, which is located in the  $2B_3$  site. Upon HCO formation, the C and O atoms in the final state are bound in a threefold and bridged manner to the surface, respectively. The transition state for HCO formation resembles the final state, with the exception of a slight rotation. The barrier for dissociating the HCO intermediate from this configuration is only 53 kJ/mol. From these data, it is clear that the H-assisted pathway via HCO is the preferred mode of CO dissociation on this surface. Huo et al.[10] compared direct and H-assisted mechanisms for CO dissociation on this surface and also concluded that H-assisted CO dissociation via HCO is the more favourable reaction pathway. On the other hand, Petersen and Janse van Rensburg reported similar barriers for direct and H-assisted CO dissociation on this surface.[14] The main difference is their choice to remove the C atoms from the surface, rendering the surface more reactive for direct CO bond dissociation. Therefore, we also explored CO dissociation in a vacancy site. This vacancy was created by removing a fourfold C atom from the surface and the resulting surface is denoted by  $(010)^*_{0.25}$ . The most stable CO adsorption site is the fourfold site, i.e. the vacancy obtained by C removal. Direct CO dissociation is more facile on the defective surface and shows an activation

energy of 141 kJ/mol, in good agreement with the value found by Petersen and Janse van Rensburg.[14] Dissociation via the COH intermediate is also more facile, as the activation energy is lowered from 216 kJ/mol to 126 kJ/mol. The pathway via HCO remains nearly unaffected, as the HCO intermediate is slightly less stable in the vacancy compared to the 2B<sub>3</sub> site. Overall, the dissociation of CO in a vacancy site most likely occurs via a H-assisted pathway, although direct CO dissociation is still possible. The difference between the overall barrier for direct CO and H-assisted C-O bond scission is only 15 kJ/mol ( $\Delta\Delta E = 15$  kJ/mol).

### 3.3.4 The $(11\bar{1})_{0.0}$ surface

The  $(11\bar{1})_{0.0}$  surface contains four C atoms in fivefold coordination and two C atoms in interstitial locations below the fourfold sites. At the surface, there are top, threefold, fourfold and B<sub>5</sub> sites available for CO adsorption. One of the two threefold sites is part of a B<sub>5</sub> site, the other is a B<sub>3</sub> site. Despite the presence of a B<sub>5</sub> site, CO adsorption is not possible because of the interstitial C atom below the fourfold site. When CO was adsorbed on either the threefold or the fourfold sites of the B<sub>5</sub> site, CO migrated to nearby top sites. The top adsorption energy is 88 kJ/mol. However, CO adsorption on the threefold site resulted in an adsorption energy of 184 kJ/mol. The adsorption energy of H<sub>2</sub> is 105 kJ/mol with the H atom preferring to bind to a threefold site.

We also explored CO adsorption on C atoms of the Fe-carbide, giving rise to Fe-C and C-C bonds. Adsorption of CO to threefold and fourfold sites resulted in coordination to one C atom and 2 or 3 Fe atoms (sites denoted as 2Fe1C and 3Fe1C), respectively. The CO adsorption energies on these sites are lower than on the other sites (112 kJ/mol and 103 kJ/mol for the 3Fe1C and 2Fe1C sites, respectively).

Direct C-O bond dissociation can occur from different adsorption states. Starting from a Fe-only adsorption site, the forward activation barrier is 156 kJ/mol. This barrier is relatively high, because the C-O bond scission proceeds over a terrace-like site. Direct CO dissociation starts from the most stable adsorption site, i.e. the threefold site. The final state holds the C atom in the same threefold position with the O atom located bridged in an adjacent threefold site. The transition state has a late character. C-O bond scission starting from a CCO intermediate has a forward activation barrier of 98 kJ/mol, which is 58 kJ/mol lower compared to direct CO dissociation. Sorescu reported values of 175 kJ/mol for direct CO dissociation and 66 kJ/mol for C-O dissociation in CCO.[16] It is important to use migration-corrected energies for these two pathways. Then, we find values of 156 kJ/mol for the direct CO dissociation pathway and 162 kJ/mol for the CCO pathway. These data



compare very well to migration-corrected Sorescu data of 156 kJ/mol and 154 kJ/mol, respectively. The important conclusion is that, although CO bond dissociation in CCO is facile, the overall barrier is nearly the same than for the direct CO bond dissociation. Zhao and co-workers[21] investigated direct CO dissociation and C-assisted CO dissociation pathways. For direct CO dissociation, a much higher barrier was reported than found by us. For C-assisted CO dissociation, a barrier of 70 kJ/mol was computed. The CCO pathway was not considered by these authors.

In addition to the C-assisted pathway, we also investigated H-assisted pathways. CO hydrogenation to either HCO or COH involve relatively high activation barriers because both CO and H are strongly bound compared to the intermediate hydrogenated species. However, the barrier for CCO hydrogenation to CCOH is considerably lower compared to the hydrogenation of CO to COH, which is due to the higher stability of the CCO species. This reduces the barrier for hydrogenation by approximately 91 kJ/mol and the overall barrier from 233 kJ/mol to 199 kJ/mol. The associated  $\Delta\Delta E$  for this pathway is 43 kJ/mol, suggesting that this pathway will not significantly contribute to the overall CO dissociation rate. The overall barrier for CCH-O bond scission is similar to the barrier for CC-O bond scission. Accordingly, both CC-O and CCH-O bond scission are likely candidates for direct C-assisted pathway. Furthermore, direct C-O bond scission remains a likely pathway.

### 3.3.5 The (100)<sub>0.0</sub> surface

The (100)<sub>0.0</sub> surface is completely made up of B<sub>5</sub> sites, without any exposed C atoms. The interstitial C atoms in the first subsurface layer are located below the fourfold sites. Consequently, CO adsorption on this surface is not possible on the fourfold sites. CO adsorption can occur on top, threefold, and fivefold sites. The fivefold adsorption is similar to adsorption on a B<sub>5</sub> site, with the exception of location of the C atom. In a regular B<sub>5</sub> site, the C atom is bound to the fourfold site of the B<sub>5</sub> site. Due to the interstitial C atom below the fourfold site, the C from CO is not bound to the fourfold site, but to the threefold site adjacent to it. The O atom of CO is located in a regular bridged fashion at the edge of the fourfold site of the B<sub>5</sub> site. Adsorption on a threefold site is comparable (181 kJ/mol) to adsorption on a top site (180 kJ/mol). Adsorption of CO in a fivefold site is slightly less favourable (166 kJ/mol). Bridged adsorption of CO led to migration to threefold adsorption. The energy of dissociative adsorption of H<sub>2</sub> is 120 kJ/mol, the H atoms are located in threefold sites.

Both direct and H-assisted pathways were considered for CO dissociation. Direct C-O bond scission starts from CO adsorbed in a fivefold site and has an activation energy of 128 kJ/mol. In the transition and final states, the C atom remains in the threefold site. The O atom proceeds via a

bridged position in the transition state to a threefold position in the final state. Sorescu reported a CO adsorption energy of 186 kJ/mol on the  $(100)_{0.0}$  surface, which is close to our value (181 kJ/mol).[16] For direct CO dissociation, a barrier of 113 kJ/mol was reported. Migration correction would increase this barrier to 129 kJ/mol, close to the value found by us. Sorescu[16] did not take the H-assisted CO dissociation pathways into account. Sorescu[16] did not take the H-assisted CO dissociation pathway into account.

The formation of the HCO intermediate has an activation barrier of 97 kJ/mol. However, due to the instability of the HCO intermediate, the  $\Delta\Delta E$  for this pathway is 56 kJ/mol, implying that direct CO dissociation is preferred. Whereas CO hydrogenation towards a COH intermediate is only approximately 8 kJ/mol higher in energy compared to direct CO dissociation, the COH intermediate is also less stable, resulting in an overall barrier of 167 kJ/mol ( $\Delta\Delta E = 39$  kJ/mol). Thus, direct CO dissociation on a  $B_5$ -site is the most likely pathway. A different conclusion was reached by Gracia et al.,[9] who compared direct and H-assisted CO dissociation via a COH intermediate for this surface, but did not consider the HCO pathway. It must be noted that the computations of Gracia et al. were done for the  $(100)_{0.05}$  surface which is similar to the  $(100)_{0.0}$  surface, yet slightly shifted downward, resulting in a carbon-terminated surface. This hampers direct CO dissociation, as the carbon atoms block the sites for direct CO dissociation. This is the main explanation for the difference between our results and those found by Gracia and co-workers. Another reason is their use of a relatively small unit cell, implying that lateral interactions will play an important role. Furthermore, Gracia et al. determined the mechanism solely on the basis of the stability of the intermediates. They did not mention activation barriers, which are needed, as they are the predominant parameter determining the pathway. Although they did not report activation barriers, based on the stabilities of the intermediates they contended that the COH pathway is preferred to direct CO dissociation, which is in contradiction to our findings.

### 3.3.6 The $(11\bar{1})_{0.5}$ surface

The  $(11\bar{1})_{0.5}$  surface contains four C atoms in fivefold coordination and two C atoms in interstitial locations below the fourfold Fe sites. The difference with the  $(11\bar{1})_{0.0}$  surface is the location of the interstitial C atoms, which are now located below threefold sites. However, CO adsorption on a fourfold site of a  $B_5$ -site is not stable and CO reverts to a threefold position due to the proximity of a surface C atom. CO preferably adsorbs in fourfold fashion on a  $2B_3$  site with an adsorption energy

of 191 kJ/mol. The adsorption energy of  $H_2$  is 151 kJ/mol and the preferred adsorption site is the threefold one.

Direct CO dissociation proceeds by adsorbing CO in the  $B_5$ -site in the initial state. In the transition state, the C atom remains in a fourfold position, while the O atom is located in a bridged mode. In the final state, the O atom proceeds to a threefold site, while the C atom remains in place. Sorescu compared direct CO and C-assisted CO dissociation pathways for the  $(11\bar{1})_{0.5}$  surface, but did not consider the CCO formation step.[16] As the difference between the values of CO and CCO dissociation are small and migration corrections were not taken into account, C-assisted CO dissociation is not likely on this surface. Sorescu's value for CO adsorption (202 kJ/mol) is close to our value (190 kJ/mol) for CO adsorption on a bridge site. The reported values for C-O and CC-O bond scission are 77 kJ/mol and 80 kJ/mol, respectively. By applying a migration correction to these data, the activation barriers increase to 131 kJ/mol and 205 kJ/mol, respectively. Sorescu's migration-corrected value for direct CO dissociation is thus close to our computed value of 118 kJ/mol. Sorescu[16] did not take the H-assisted CO dissociation pathway into account. Our calculations show that hydrogenation to either HCO or COH has  $\Delta\Delta E$  values of 34 kJ/mol and 106 kJ/mol, respectively. Therefore, C-O bond scission will most likely occur in a direct fashion over a  $B_5$ -site on this surface.

### 3.3.7 The $(100)_{0.287}$ surface

The  $(100)_{0.287}$  surface is similar to the  $(100)_{0.0}$ , apart from the absence of C atoms in the surface and the first subsurface layer. This results in substantially higher CO adsorption energies. CO can adsorb in top, threefold or fourfold modes. The most stable site for CO adsorption is the  $B_5$ -site, where the C atom is bound in a fourfold manner and the O atom is bound bridged. The CO adsorption energy is 221 kJ/mol. The dissociative adsorption energy of  $H_2$  is 167 kJ/mol with the H atoms ending up in a threefold site.

CO dissociation can proceed in a direct manner from the most stable adsorption site. In the transition state, the C atom moves to a threefold site, while the O atom remains in a bridged position. In the final state, the O atom moves to a threefold site, while the C atom remains in the threefold position. The activation energy for direct CO dissociation is 128 kJ/mol. Hydrogenation of the CO to form either a HCO or COH species has higher overall barriers ( $\Delta\Delta E = 20$  kJ/mol and  $\Delta\Delta E = 64$  kJ/mol, respectively), due to the strong adsorption of both CO and H. Therefore, CO dissociation will most

likely proceed on a B<sub>5</sub>-site in a direct manner. Cheng et al.[4] computed direct CO dissociation on this surface, but started their transition state search from gaseous CO.

### 3.3.8 Kinetic Model

To explore differences in CO dissociation rates on the investigated surfaces, we used simplified kinetic models.

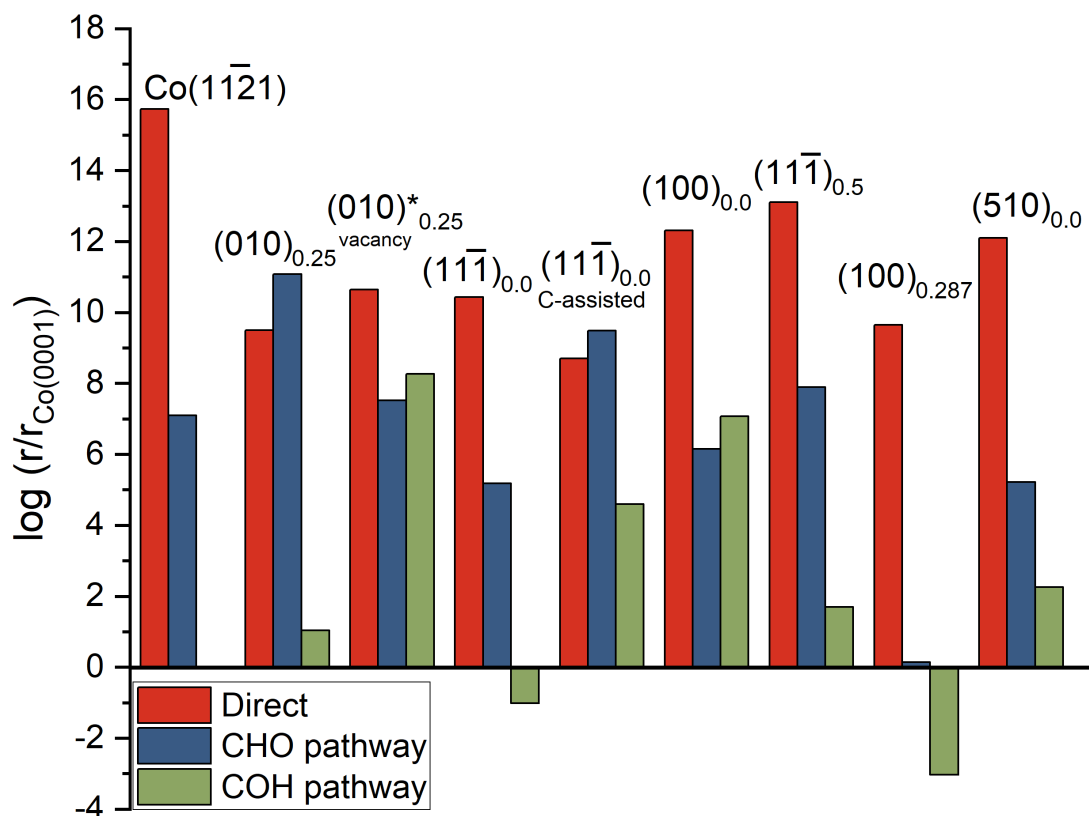


**Figure 3.6** Reaction rates for direct CO dissociation (red) and for CO dissociation involving H-assistance via HCO (blue) and COH (green). These rates are shown relative to the rate of direct CO dissociation on Co(0001). Positive values imply a higher reaction rate compared to the direct CO dissociation on the Co(0001) surface, whereas negative values imply a lower reaction rate. The rate for the Co(11 $\bar{2}$ 1) surface is given for comparison (data for Co surfaces taken from Liu et al.[27]). CO dissociation involving the (010)<sub>0.25</sub> surface with a C-vacancy is denoted by (010)<sup>\*</sup><sub>0.25</sub>, while data for the C-assisted pathway (CCO) on the (11 $\bar{1}$ )<sub>0.5</sub> are provided as well.

Figure 3.6 shows the reaction rates for CO dissociation involving direct and H-assisted (via HCO or COH) pathways. The site-based rates are shown relative to the rate of direct CO dissociation on the Co(0001) terrace. Positive values indicate a higher rate compared to the Co(0001) surface, negative values indicate a lower rate. Data for the Hägg carbide surfaces are compared to the stepped Co(11 $\bar{2}$ 1) surface. CO dissociation kinetic data for Co(11 $\bar{2}$ 1) and Co(0001) are taken from the literature.[27] For the (010)<sub>0.25</sub> surface, we also included data for the surface containing a C vacancy. For the (11 $\bar{1}$ )<sub>0.0</sub> surface, the pathway involving CCO was included.

For the  $(11\bar{1})_{0.0}$ ,  $(100)_{0.0}$ ,  $(11\bar{1})_{0.5}$  and  $(100)_{0.287}$  surfaces, direct CO dissociation is much faster than H-assisted pathways. C-assisted pathways involving CC-O and CCH-O bond cleavage reactions on the  $(11\bar{1})_{0.0}$  display comparable rates, whereas H-assisted CO dissociation on the  $(11\bar{1})_{0.0}$  surface proceeds at a lower rate compared to direct CO dissociation. The most active surface is the  $(11\bar{1})_{0.5}$  surface, followed by the  $(100)_{0.0}$  surface. On both of these surfaces, direct CO dissociation is preferred to the H-assisted CO dissociation. The  $(010)_{0.25}$  surface displays a preference for the HCO pathway, as the site for direct CO dissociation is blocked by C atoms. Removing a surface C atom from this surface changes the preferred mechanism to direct CO dissociation. The  $(11\bar{1})_{0.0}$  and  $(100)_{0.287}$  surfaces exhibit a lower rate for the COH pathway when compared to the direct CO dissociation on Co(0001). The rest of the surfaces are more active compared to direct CO dissociation on Co(0001). The  $(100)_{0.287}$  is the least reactive one. As follows from the literature[15, 29], higher Miller index surfaces with a terrace-like surface topology such as the  $(510)_{0.0}$  surface prefer a direct CO dissociation pathway instead of H-assisted CO dissociation.

Given the relatively small differences in computed energy barriers, we chose to base the comparison on some form of kinetics. Therefore, we added the data for the  $(510)_{0.0}$  surface based on the literature [15] (see Appendix A.3) to a comparison of reaction rates, as can be seen in Figure 3.6.

Figure 3.6 shows that direct CO dissociation is preferred on the  $(510)_{0.0}$  surface and that the rate for H-assisted CO dissociation via a COH intermediate is considerably lower, compared to the H-assisted CO dissociation via a HCO intermediate. Furthermore, it is also shown that the  $(510)_{0.0}$  surface is among the more active surfaces for direct CO dissociation. These results compare well to the relative rates for the step-like surfaces (the  $(100)$  and  $(11\bar{1})$  surfaces) within our calculations. However, comparing these results to our terrace-like  $(010)_{0.25}$  surface, it is clear that the preferred mechanism on both terrace-like surfaces is different, as the H-assisted CO dissociation via a HCO intermediate is the preferred mechanism on the  $(010)_{0.25}$  surface, while the direct CO dissociation is the preferred route on the  $(510)_{0.0}$  surface. We can therefore conclude that the mechanism for C-O bond scission is highly dependent on the local topology and hence the location of the surface- or interstitial C atoms.

### 3.3.9 General discussion

We have compared surface free energies of different terminations of the Hägg carbide and selected the five most stable surfaces on this basis for a detailed study of CO dissociation relevant to the Fischer-Tropsch reaction. A general trend observed is that CO binds more strongly to surfaces that

lack interstitial C atoms present in the first subsurface layer. CO prefers to adsorb on a fourfold site, unless this adsorption mode is hampered by interstitial C atoms. Adsorption of H atoms was also considered to be relevant to HCO and COH dissociation pathways. In all cases, H adsorbs on threefold sites. Adsorption energies increase with increasing surface free energies. Some of the explored surfaces contain stepped sites, which give rise to relatively low barriers for direct CO dissociation. The computed barriers for the different CO dissociation pathways on the Hägg carbide are higher than the barriers for the preferred (direct) CO dissociation pathways on stepped Co and Ru surfaces.

Overall, increasing occupancy of interstitial sites below the surface with C atoms results in a higher barrier for direct CO dissociation. This phenomenon was recently discussed by Chen et al.,[20] who also showed a strong correlation between the charge on the Fe atom and the CO activation barrier. They showed that more surface- and interstitial C atoms near the surface Fe atoms decreased the charge on the Fe atoms, as the C atoms withdraw electrons from the surface Fe atoms. This results in a weaker ability for CO activation. This interstitial C occupancy is highest for the  $(010)_{0.25}$  surface. In this case, the alternative pathway involving HCO shows a much lower overall activation barrier. This is at odds with the results obtained by Petersen and Janse van Rensburg[14], who found similar values for direct CO dissociation and H-assisted CO dissociation on the  $(010)_{0.25}$  surface. The main difference here is that they considered a surface from which the C atoms were removed. We verified that creating such vacancies indeed results in higher direct and COH dissociation rates, whereas the HCO pathway becomes less favourable. The reason is that on the surface with a vacancy, the C atoms of CO and COH are bound in a fourfold manner. However, the HCO intermediate is not stable when the C atom is bound in this site, requiring the migration from a bridged configuration of both the C and the O atom on this site. Overall, introduction of a vacancy results in a change of the preferred CO dissociation mechanism.

Summarising, one can state that CO dissociation proceeds via the direct pathway, when a  $B_5$ -type site is present on the surface. Otherwise, H-assisted mechanisms contribute to the overall rate of CO dissociation, usually due to the presence of (interstitial) C atoms. On the  $(11\bar{1})_{0.0}$ , a C-assisted mechanism is possible, as it presents comparable rates for direct and H-assisted CO dissociation. Taking into account the results of the Wulff construction and noting that Fe-carbide particles are usually relatively large[17] (making it reasonable that particles will adopt this shape) we observe that lowered free energy of a particular surface results in a lower reaction rate for CO dissociation. The  $(11\bar{1})$  and  $(010)$  surfaces enclose about 30% and 10% of the Wulff particle. The rate on the former surface is substantially lower than on the latter. However, it is clear that for a specific low

Miller-index surface, the rate for CO dissociation can vary substantially depending on the way the surface is cut. For instance, the  $(11\bar{1})_{0.5}$  surface presents a much higher CO dissociation rate than the  $(11\bar{1})_{0.0}$  surface. Moreover, these data show that, there is more competition between different modes of CO dissociation than for metallic Co surfaces, due to the complexity of the Fe carbide surface terminations.

### 3.4 Conclusions

We explored CO adsorption and dissociation on five stable surface terminations of the Hägg carbide, which were selected on the basis of the presence of stepped B<sub>5</sub>-type sites and low surface free energies. The strength of CO adsorption depends on the presence of interstitial C atoms in the first subsurface layer. CO adsorbs on a fourfold site unless hampered by interstitial C atoms. H atoms adsorb on threefold sites on all investigated surfaces. The H adsorption energy directly correlates with the surface free energy. In general, there is competition between direct and H-assisted pathways for CO dissociation on the considered surfaces. Direct CO dissociation becomes easier with increasing adsorption strength of CO (due to less subsurface interstitial C atoms). CO dissociation proceeds via the direct pathway, when a B<sub>5</sub>-type site is present on the surface. Otherwise, H-assisted mechanisms contribute to the overall rate of CO dissociation, usually due to the presence of (interstitial) C atoms. For instance, HCO dissociation is preferred to direct CO dissociation for the  $(010)_{0.25}$  surface with a large occupancy of subsurface C atoms. Direct CO dissociation on the  $(11\bar{1})_{0.5}$  surface presents the highest CO dissociation rate of all considered surfaces. These rates are typically lower than those observed for the stepped Co surface. We have also shown that C-assisted pathways can contribute to CO dissociation on a surface such as the  $(11\bar{1})_{0.0}$  surface. Whilst these calculations have all been performed at relatively low CO coverage, we expect that the contribution of C-assisted pathways may become more important under typical FT conditions.

## References

- [1] M.E. Dry, A.P. Steynberg, Commercial FT process applications, *Studies in Surface Science and Catalysis* 152 (2004) 406-481.
- [2] M.E. Dry, The fischer-tropsch synthesis, *Catalysis science and technology* 1 (1981) 159-255.
- [3] E. de Smit, F. Cinquini, A.M. Beale, O.V. Safonova, W. van Beek, P. Sautet, B.M. Weckhuysen, Stability and Reactivity of  $\epsilon$ - $\chi$ - $\theta$  Iron Carbide Catalyst Phases in Fischer–Tropsch Synthesis: Controlling  $\mu$ C, *Journal of the American Chemical Society* 132 (2010) 14928-14941.
- [4] J. Cheng, P. Hu, P. Ellis, S. French, G. Kelly, M.C. Lok, Density functional theory study of iron and cobalt carbides for Fischer–Tropsch synthesis, *The Journal of Physical Chemistry C* 114 (2009) 1085-1093.
- [5] A. Govender, D. Curulla Ferré, J.W. Niemantsverdriet, A density functional theory study on the effect of zero-point energy corrections on the methanation profile on Fe (100), *ChemPhysChem* 13 (2012) 1591-1596.
- [6] M. Ojeda, R. Nabar, A.U. Nilekar, A. Ishikawa, M. Mavrikakis, E. Iglesia, CO activation pathways and the mechanism of Fischer–Tropsch synthesis, *Journal of Catalysis* 272 (2010) 287-297.
- [7] D.C. Sorescu, First-principles calculations of the adsorption and hydrogenation reactions of CH<sub>x</sub> (x= 0, 4) species on a Fe (100) surface, *Physical Review B* 73 (2006) 155420.
- [8] D.-B. Cao, Y.-W. Li, J. Wang, H. Jiao, Chain growth mechanism of Fischer–Tropsch synthesis on Fe<sub>5</sub>C<sub>2</sub> (001), *Journal of Molecular Catalysis A: Chemical* 346 (2011) 55-69.
- [9] J.M. Gracia, F.F. Prinsloo, J.W. Niemantsverdriet, Mars-van Krevelen-like mechanism of CO hydrogenation on an iron carbide surface, *Catalysis letters* 133 (2009) 257-261.
- [10] C.-F. Huo, Y.-W. Li, J. Wang, H. Jiao, Insight into CH<sub>4</sub> formation in iron-catalyzed Fischer–Tropsch synthesis, *Journal of the American Chemical Society* 131 (2009) 14713-14721.
- [11] M.O. Ozbek, J.H. Niemantsverdriet, Elementary reactions of CO and H<sub>2</sub> on C-terminated  $\chi$ -Fe<sub>5</sub>C<sub>2</sub> (001) surfaces, *Journal of Catalysis* 317 (2014) 158-166.
- [12] M.O. Ozbek, J.W. Niemantsverdriet, Methane, formaldehyde and methanol formation pathways from carbon monoxide and hydrogen on the (001) surface of the iron carbide  $\chi$ -Fe<sub>5</sub>C<sub>2</sub>, *Journal of Catalysis* 325 (2015) 9-18.
- [13] M.A. Petersen, J.-A. van den Berg, W.J. van Rensburg, Role of step sites and surface vacancies in the adsorption and activation of CO on  $\chi$ -Fe<sub>5</sub>C<sub>2</sub> surfaces, *The Journal of Physical Chemistry C* 114 (2010) 7863-7879.
- [14] M.A. Petersen, W.J. van Rensburg, CO Dissociation at Vacancy Sites on Hägg Iron Carbide: Direct Versus Hydrogen-Assisted Routes Investigated with DFT, *Topics in Catalysis* 58 (2015) 665-674.
- [15] T.H. Pham, X. Duan, G. Qian, X. Zhou, D. Chen, CO activation pathways of Fischer–Tropsch synthesis on  $\chi$ -Fe<sub>5</sub>C<sub>2</sub> (510): direct versus hydrogen-assisted CO dissociation, *The Journal of Physical Chemistry C* 118 (2014) 10170-10176.
- [16] D.C. Sorescu, Plane-wave density functional theory investigations of the adsorption and activation of CO on Fe<sub>5</sub>C<sub>2</sub> surfaces, *The Journal of Physical Chemistry C* 113 (2009) 9256-9274.
- [17] J. Cheng, P. Hu, P. Ellis, S. French, G. Kelly, C.M. Lok, An Energy Descriptor To Quantify Methane Selectivity in Fischer–Tropsch Synthesis: A Density Functional Theory Study, *The Journal of Physical Chemistry C* 113 (2009) 8858-8863.
- [18] P.J. Steynberg, J.A. Van den Berg, W.J. van Rensburg, Bulk and surface analysis of Hägg Fe carbide (Fe<sub>5</sub>C<sub>2</sub>): a density functional theory study, *Journal of Physics: Condensed Matter* 20 (2008) 064238.
- [19] E. Shustorovich, A.T. Bell, Analysis of CO hydrogenation pathways using the bond-order-conservation method, *Journal of Catalysis* 113 (1988) 341-352.
- [20] B. Chen, D. Wang, X. Duan, W. Liu, Y. Li, G. Qian, W. Yuan, A. Holmen, X. Zhou, D. Chen, Charge-Tuned CO Activation over a  $\chi$ -Fe<sub>5</sub>C<sub>2</sub> Fischer–Tropsch Catalyst, *ACS Catalysis* (2018) 2709-2714.
- [21] S. Zhao, X.-W. Liu, C.-F. Huo, X.-D. Wen, W. Guo, D. Cao, Y. Yang, Y.-W. Li, J. Wang, H. Jiao, Morphology control of K<sub>2</sub>O promoter on Hägg carbide ( $\chi$ -Fe<sub>5</sub>C<sub>2</sub>) under Fischer–Tropsch synthesis condition, *Catalysis Today* 261 (2016) 93-100.
- [22] G. Kresse, J. Hafner, Ab initio molecular-dynamics simulation of the liquid-metal–amorphous-semiconductor transition in germanium, *Physical Review B* 49 (1994) 14251.



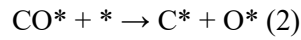
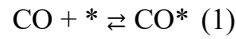
- [23] G. Kresse, J. Furthmüller, Efficiency of ab-initio total energy calculations for metals and semiconductors using a plane-wave basis set, *Computational Materials Science* 6 (1996) 15-50.
- [24] M.P.A.T. Methfessel, A.T. Paxton, High-precision sampling for Brillouin-zone integration in metals, *Physical Review B* 40 (1989) 3616.
- [25] K.P. Huber, G. Herzberg, NIST Chemistry WebBook, NIST Standard Reference Database Number 69. Eds. PJ Linstrom and WG Mallard. National Institute of Standards and Technology. Gaithersburg MD 20899, webbook. nist. gov (1997).
- [26] G. Henkelman, H. Jónsson, Improved tangent estimate in the nudged elastic band method for finding minimum energy paths and saddle points, *The Journal of chemical physics* 113 (2000) 9978-9985.
- [27] J.-X. Liu, H.-Y. Su, D.-P. Sun, B.-Y. Zhang, W.-X. Li, Crystallographic dependence of CO activation on cobalt catalysts: HCP versus FCC, *Journal of the American Chemical Society* 135 (2013) 16284-16287.
- [28] J.J. Retief, Powder diffraction data and Rietveld refinement of Hägg-Carbide,  $\chi$ -Fe<sub>5</sub>C<sub>2</sub>, *Powder Diffraction* 14 (1999) 130-132.
- [29] D. Wang, B. Chen, X. Duan, D. Chen, X. Zhou, Iron-based Fischer–Tropsch synthesis of lower olefins: The nature of  $\chi$ -Fe<sub>5</sub>C<sub>2</sub> catalyst and why and how to introduce promoters, *Journal of energy chemistry* 25 (2016) 911-916.

## Appendix A

### A.1 Derivation of the rate equations

#### Direct and H-assisted C-O bond scission

For the direct CO dissociation, we assume that the CO molecule obeys the Langmuir-Hinshelwood mechanism. Therefore, the first step in the mechanism is adsorption of the CO molecule. The second step is the dissociation of the CO molecule to C and O.



We assume that CO adsorption is in equilibrium and very fast compared to the CO dissociation, therefore, K is defined as:

$$K = \frac{k^{+1}}{k^{-1}} = \frac{\theta_{\text{CO}}}{\theta_* P_{\text{CO}}}, = \frac{K_0}{P_0}$$

where  $\theta_{\text{CO}}$  and  $\theta_*$  stand for the CO coverage and free sites, respectively, adding up to unity.

$\frac{k^{+1}}{k^{-1}}$  is the ratio between the forward and backward rate constants of the adsorption.

Therefore, we can write:

$$\theta_{\text{CO}} = \frac{KP_{\text{CO}}}{1+KP_{\text{CO}}} \text{ and } \theta_* = \frac{1}{1+KP_{\text{CO}}}$$

Meanwhile  $K^0$  can be calculated as follows:

$$K^0 = e^{\frac{-\Delta G^0}{k_b T}}$$

$$\Delta G^0 = E_{\text{ads}} - \Delta\mu(T, P_0)$$

Where  $\Delta G^0$  is the standard Gibbs free energy for CO adsorption,  $k_b$  is the Boltzmann constant, T the temperature and  $P_0$  the standard pressure.  $\Delta\mu(T, P_0)$  is the chemical potential of CO in the gas phase. Here, T = 500 K and P =  $3 \times 10^{-5}$  Pa, corresponding to low coverage of CO that were used in our study. To take changes in entropy (S) and enthalpy (H) into account,  $\Delta\mu_{\text{CO}}$  and  $\Delta\mu_{\text{H}}$  were determined using the NIST thermodynamic tables<sup>1</sup> and the abovementioned values for temperature and pressure in the following formula:

$$\Delta\mu_{CO/H}(T, P^0) = -TS(T, P^0) + (H(T, P^0) - H(0 K, P^0))$$

We have applied a value for  $\Delta\mu_{CO}$  of 91.59 kJ/mol and a value for  $\Delta\mu_H$  of 62 kJ/mol in our paper.

The rate for CO dissociation can be written as

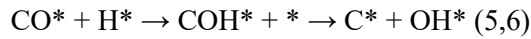
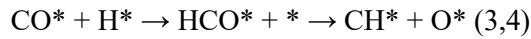
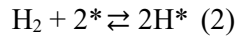
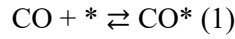
$$r = k_2 \theta_{CO} \theta_* = \frac{k_2 K P_{CO}}{(1 + K P_{CO})^2},$$

where

$$k_2 = \nu_f e^{\frac{E_f}{k_b T}}$$

In this formula,  $\nu_f$  and  $E_f$  stand for the pre-exponential factor and the forward reaction energy barrier for the CO dissociation reaction, as found in table 2.

For the H-assisted CO dissociation pathway, the following reactions have to be taken into account.



Reaction 3,4 and 5,6 are composed out of 2 lumped elementary reaction steps. The equations for the coverages are now as follows

$$\theta_{CO} = \frac{K_1 P_{CO}}{1 + K_1 P_{CO} + \sqrt{K_2 P_{H_2}}}, \theta_H = \frac{\sqrt{K_2 P_{H_2}}}{1 + K_1 P_{CO} + \sqrt{K_2 P_{H_2}}} \text{ and } \theta_* = \frac{1}{1 + K_1 P_{CO} + \sqrt{K_2 P_{H_2}}}$$

Now, the reaction rate can be defined as

$$r = k_{rls} \theta_{CO} \theta_H \hat{=} k_{rls} \theta_{CHO} \theta_* = \frac{k_{rls} K_1 P_{CO} \sqrt{K_2 P_{H_2}}}{(1 + K_1 P_{CO} + \sqrt{K_2 P_{H_2}})^2},$$

Where  $k_{rls}$  is the rate constant for the rate limiting step, which is defined as

$$k_{rls} = \nu_f e^{\left(\frac{E_{rls}}{k_b T}\right)}$$

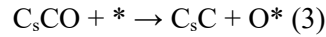
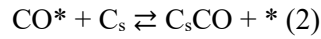
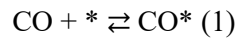
$E_{rls}$  is defined as the (lumped) reaction barrier, where the  $\Delta E$  of reaction 3 and 4 was taken for the HCO pathway and the  $\Delta E$  of reaction 5 and 6 was taken for the COH pathway.

$K_1$  is defined as

$$K_1 = \frac{e^{\left(\frac{\Delta G^0}{k_b T}\right)}}{P_0} = \frac{e^{\left(\frac{-E^{ads} - \Delta\mu_{CO}}{k_b T}\right)}}{P_0}$$

### Derivation rate equation for C-CO assisted C-O bond scission

For the direct C-CO dissociation, we assume that the CO molecule obeys the Langmuir-Hinshelwood mechanism. Therefore the first step in the mechanism is adsorption of the CO molecule. The second step is the reaction of the CO with a C from the surface, termed the  $C_s$ . After the formation of this intermediate species, dissociation of the CO molecule results in the formation of  $C_sC$  and O. It is necessary to introduce a dual site model, because we are using both regular empty sites and C from the surface. In this model, we denote the regular sites as  $\theta_*$  and the C from the surface as  $\theta_{C_s}$ .



$$\theta_* + \theta_{CO} = 1 \quad \& \quad \theta_{C_sCO} + \theta_{C_s} = 1$$

We get the following equations for the coverage for the regular sites:

$$\theta_{CO} = K_1 P_{CO} \theta_* = \frac{K_1 P_{CO}}{1 + K_1 P_{CO}}$$

$$\theta_* = \frac{1}{1 + K_1 P_{CO}}$$

We get the following equations for the coverage for the surface C sites:

$$\theta_{C_sCO} = \frac{K_2 \theta_{CO} \theta_{C_s}}{\theta_*} = K_2 K_1 P_{CO} \theta_{C_s} = \frac{K_1 K_2 P_{CO}}{1 + K_1 K_2 P_{CO}}$$

The rate for CO bond scission is expressed as:

$$r = k_3 \theta_{C_sCO} \theta_*$$

$$r = k_3 \theta_{C_sCO} \theta_* = k_3 \frac{K_1 K_2 P_{CO}}{1 + K_1 K_2 P_{CO}} \frac{1}{1 + K_1 P_{CO}} = \frac{k_3 K_1 K_2 P_{CO}}{1 + K_1 P_{CO} + K_1 K_2 P_{CO} + K_1^2 K_2 P_{CO}^2}$$

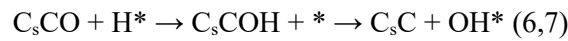
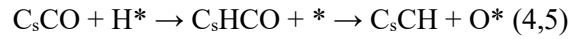
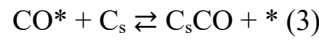
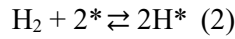
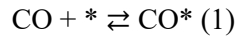
$K_1$ ,  $K_2$  and  $k_3$  are defined as follows:

$$K_1 = \frac{e\left(\frac{\Delta G^0}{k_b T}\right)}{P_0} = \frac{e\left(\frac{E^{ads} - \Delta \mu_{CO}}{k_b T}\right)}{P_0}$$

$$K_2 = \frac{e\left(\frac{\Delta G^0}{k_b T}\right)}{P_0} = \frac{e\left(\frac{\Delta H_{r_{ls}}}{k_b T}\right)}{P_0}$$

$$k_3 = 10^{13} e^{\left(\frac{\Delta E^{r_{ls}}}{RT}\right)}$$

The following reactions were used for the H-assisted CCO dissociation:



Reaction 4,5 and 6,7 are composed out of 2 lumped elementary reaction steps. The equations for the coverages are now as follows

$$\theta_{CO} = \frac{K_1 P_{CO}}{1 + K_1 P_{CO} + \sqrt{K_2 P_{H_2}}}, \theta_H = \frac{\sqrt{K_2 P_{H_2}}}{1 + K_1 P_{CO} + \sqrt{K_2 P_{H_2}}}, \theta_* = \frac{1}{1 + K_1 P_{CO} + \sqrt{K_2 P_{H_2}}},$$

$$\theta_{C_sCO} = \frac{K_3 K_{CO} P_{CO}}{1 + K_3 K_{CO} P_{CO} + K_3 K_4 K_{CO} P_{CO} \sqrt{K_2 P_{H_2}}}, \quad \text{and} \quad \theta_{C_s} = \frac{1}{1 + K_3 K_{CO} P_{CO} + K_3 K_4 K_{CO} P_{CO} \sqrt{K_2 P_{H_2}}}$$

Now, the reaction rate can be defined as

$$r = k_{r_{ls}} \theta_{C_sCO} \theta_H \hat{=} k_{r_{ls}} \theta_{C_sCHO} \theta_* \hat{=} k_{r_{ls}} \theta_{C_sCOH} \theta_* =$$

$$\frac{k_{r_{ls}} K_1 P_{CO} \sqrt{K_2 P_{H_2}}}{(1 + K_1 P_{CO} + \sqrt{K_2 P_{H_2}})(1 + (K_3 K_{CO} P_{CO} + K_3 K_4 K_{CO} P_{CO} \sqrt{K_2 P_{H_2}}))}$$

## A.2 Adsorption Energies for CO adsorption on Hägg carbide surfaces

**Table A.2.1:** CO adsorption on the five most stable Hägg carbide surfaces in various configurations and their corresponding adsorption energies. Adsorption modes found are Top (either on Fe or on C), Bridged, threefold (either on Fe-only or on 2Fe and 1C), fourfold (either on Fe-only, like 2B or on 3Fe and 1C), fivefold, and sixfold

<b>(010)<sub>0.25</sub></b>	<b>Bridged</b>	<b>fourfold (2B<sub>3</sub>)</b>	<b>Top (on 1 C)</b>
	<b>181 kJ/mol</b>	<b>194 kJ/mol</b>	<b>77 kJ/mol</b>
<b>(11<math>\bar{1}</math>)<sub>0.0</sub></b>	<b>Top</b>	<b>threefold (on 2 Fe and 1C)</b>	<b>fourfold (on 3Fe amd 1C)</b>
	92 kJ/mol	112 kJ/mol	121 kJ/mol
<b>(100)<sub>0.0</sub></b>	<b>Top</b>	<b>threefold</b>	<b>fivefold (B<sub>5</sub>)</b>
	189 kJ/mol	187 kJ/mol	174 kJ/mol
<b>(11<math>\bar{1}</math>)<sub>0.5</sub></b>	<b>Bridged</b>	<b>fourfold (2B<sub>3</sub>)</b>	<b>sixfold (B<sub>6</sub>)</b>
	202 kJ/mol	180 kJ/mol	147 kJ/mol
<b>(100)<sub>0.287</sub></b>	<b>Bridged</b>	<b>threefold</b>	<b>fivefold (B<sub>5</sub>)</b>
	186 kJ/mol	194 kJ/mol	230 kJ/mol

## A.3 Kinetic parameters for Direct and H-assisted CO dissociation on the (510)<sub>0.0</sub> surface

In order to compare our data with the data by Pham et al.[1], we have combined the data from Pham et al. with some of our own data (marked with \*). As the adsorption energy of H<sub>2</sub> was not included in the paper, we have calculated this using the values from Table A.3.1 We have determined the H<sub>2</sub> adsorption energy by using the reported total energy for an adsorbed H atom on a (510)<sub>0.0</sub> surface and subtracted the provided empty (510)<sub>0.0</sub> and our own H<sub>2</sub> gas phase energy. The adsorption energies used in our kinetic model are shown in Table A.3.2. Table A.3.3 shows the overall reaction energy for the C-O bond breaking and a fair estimation of the missing values for the pre-exponential factors for the forward reaction.

**Table A.3.1** Total energies from DFT in eV for the empty (510)<sub>0.0</sub>, the (510)<sub>0.0</sub> with H adsorbed and the gas phase H<sub>2</sub>

Total energy from DFT (eV)	
(510) <sub>0.0</sub> empty surface	-460.246610[1]
(510) <sub>0.0</sub> with H adsorbed	-464.393222[1]
H <sub>2</sub> gasphase	-6.7590177*

**Table A.3.2** Adsorption energies as used in the kinetic model

Adsorbate	Adsorption energy (kJ/mol)
H <sub>2</sub> on (510) <sub>0.0</sub>	148
H <sub>2</sub> on (100) <sub>0.0</sub>	144[2]
H <sub>2</sub> on (001) <sub>0.0</sub>	150[2]
H <sub>2</sub> on (110) <sub>0.0</sub>	139[2]
H <sub>2</sub> on (100) <sub>0.287</sub>	167*
CO on (510) <sub>0.0</sub>	202[1]

**Table A.3.3** Overall reaction energy barrier for the direct and H-assisted C-O bond breaking and corresponding estimates for the pre-exponential factors for the forward reaction ( $\nu_f$ )

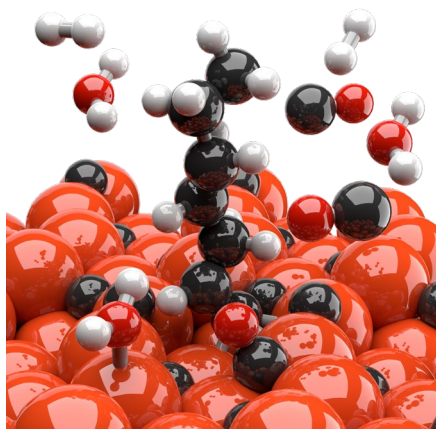
Reaction	(Overall) barrier for dissociation (kJ/mol)	$\nu_f$
CO → C + O	127[1]	1.0·10 <sup>13</sup>
CO + H → HCO → CH + O	149[1]	1.0·10 <sup>13</sup>
CO + H → COH → CO + H	184[1]	1.0·10 <sup>13</sup>

- [1] T.H. Pham, X. Duan, G. Qian, X. Zhou, D. Chen, CO activation pathways of Fischer–Tropsch synthesis on  $\chi$ -Fe<sub>5</sub>C<sub>2</sub> (510): direct versus hydrogen-assisted CO dissociation, The Journal of Physical Chemistry C 118 (2014) 10170-10176.
- [2] D.-B. Cao, F.-Q. Zhang, Y.-W. Li, J. Wang, H. Jiao, Density functional theory study of hydrogen adsorption on Fe<sub>5</sub>C<sub>2</sub> (001), Fe<sub>5</sub>C<sub>2</sub> (110), and Fe<sub>5</sub>C<sub>2</sub> (100), The Journal of Physical Chemistry B 109 (2005) 833-844.
- [3] H. Eyring, The Activated Complex and the Absolute Rate of Chemical Reactions, Chemical Reviews 17 (1935) 65-77.
- [4] Robin J.P. Broos, Bart Klumpers, Bart Zijlstra, Ivo A.W. Filot, and Emiel J.M. Hensen, <https://github.com/imc-codeteam/mkm-theta-carbide>, 2019.





## 4. First-principles based microkinetics simulations of the Fischer-Tropsch reaction on $\chi$ -Fe<sub>5</sub>C<sub>2</sub>



### Abstract

Iron carbides are generally considered to be the active phase in the iron-catalysed Fischer-Tropsch (FT) reaction. Among the different iron-carbide phases, the Hägg carbide ( $\chi$ -Fe<sub>5</sub>C<sub>2</sub>) phase is one of the most relevant phases for the conversion of synthesis gas into higher hydrocarbons. We expanded an earlier set of quantum-chemical data on CO bond dissociation with the reaction energetics for C hydrogenation, O removal, C-C coupling and C<sub>2</sub> hydrogenation steps. These reaction pathways are discussed for a low-reactive planar surface, i.e. a (010) surface, and a high-reactive step-edge surface, i.e. the (100) surface. Formation of C<sub>3+</sub> products was considered by extrapolation of data for C<sub>2</sub> formation. These resulting activation barriers and pre-exponential factors were used as input for a microkinetic model that describes the FT reaction on a stepped surface, given the lower barrier of CO dissociation compared to the planar surface. Microkinetics simulations show a kinetic preference for H<sub>2</sub>O over CO<sub>2</sub> formation. Both zero-conversion and finite conversion microkinetic modelling (in a CSTR) were performed. The results emphasize the importance of CO dissociation and O removal as rate-controlling steps, CH-CH coupling as the main mechanism for chain-growth and the formation of olefins as the primary hydrocarbon products. CO conversion rates are within one order of magnitude of experimental values, showing that step-edge sites are candidate sites for the FT reaction on Hägg carbide.

## 4.1 Introduction

Fischer-Tropsch (FT) synthesis technology is expected to become increasingly important for the production of transportation fuels and chemicals with the expected decrease of easily accessible oil supplies. In the FT process, a transition metal catalyst is used to convert synthesis gas (syngas), a mixture of CO and H<sub>2</sub>, to a variety of products. The versatility of the FT process derives in part from the possibility to obtain syngas feedstock from different carbonaceous sources such as natural gas and coal.[1] Depending on the process conditions, Fe-based catalysts find application in the production of long-chain paraffins (diesel), naphtha-range hydrocarbons (gasoline) and light olefins. The active phase in commercial FT synthesis catalysts is typically composed of Co or Fe. Fe catalysts are less expensive and more active in the water-gas shift (WGS) reaction than Co. High WGS activity can be important when processing synthesis gas with a low H<sub>2</sub>/CO ratio.[2]

It is well-established that under FT conditions the Fe-oxide precursor is converted into Fe-carbide, which is considered to be the main active phase. The active carbide phases of Fe and the mechanism by which syngas is converted to hydrocarbons on the surface of particles of these carbides remain topics of considerable debate. Hägg chi-carbide ( $\chi$ -Fe<sub>5</sub>C<sub>2</sub>), epsilon-carbide ( $\epsilon$ -Fe<sub>2</sub>C) and theta-carbide ( $\theta$ -Fe<sub>3</sub>C) were proposed as the active phase in Fe-based FT catalysts.[3] Besides the focus of some studies on metallic Fe surfaces, [4-7] most computational investigations dealt with Fe-carbide surfaces.[4, 8-17] For Hägg carbide, several surface terminations display comparable thermodynamic stability under FT conditions.[18] It is therefore important to involve these stable surfaces in mechanistic studies of the FT reaction.

The nature of CO dissociation on different low-(Miller)-index surfaces of Hägg carbide has been systematically studied in Chapter 3 of this thesis. The mechanism for CO dissociation depends on the surface termination. Generally, direct CO dissociation and H-assisted CO dissociation compete, which depends on the amount and location of interstitial C atoms that are close to the surface. For instance, on the (010)<sub>0.25</sub> surface, an H-assisted mechanism via HCO is preferred whereas the (100) surface follows a direct C-O bond scission pathway.

In this chapter, we carry out density functional theory (DFT) calculations to compute energetics of other elementary reaction steps relevant to the FT reaction in order to obtain a complete dataset sufficient to simulate the FT reaction using a microkinetics simulations approach. We focus on the (010)<sub>0.25</sub> and (100) surface, for which we have already computed the different pathways of CO dissociation. Methane formation, C-C coupling and hydrogenation and oxygen removal routes are the pathways of primary interest, as these steps play a critical role in the overall FT reaction

mechanism. The DFT calculations provide energies of stable states, transition states and information on entropy changes. Based on the resulting free energies, microkinetics simulations predict reaction rates, the product distribution, coverages and degree of rate control coefficients. Using this combined approach, we intend to gain an understanding of the reaction mechanism of chain-growth and oxygen removal in the FT reaction catalysed by Hägg carbide. These simulations also provide insight into the rate-controlling steps in the overall FT reaction.

## 4.2 Method

### 4.2.1 DFT calculations

All spin-polarized density functional theory (DFT) calculations were conducted using the projector augmented wave (PAW) method and the Perdew–Burke–Ernzerhof (PBE) exchange-correlation functional as implemented in the Vienna ab initio simulation package (VASP) code.[19, 20] Solutions of the Kohn-Sham equations were calculated using a plane-wave basis set with a cut-off energy of 400 eV. The sampling of the Brillouin zone was done using 5x5x1  $k$ -points. Higher cut-off energies or a finer Brillouin zone sampling did not lead to significant energy differences. Electron smearing was employed using a first-order Methfessel-Paxton technique[21], with a smearing width of 0.2 eV. All atoms were allowed to relax for the calculation of the empty surfaces. The layer thickness of the metal carbide slab in the empty unit cells was taken between 6.4 and 10.3 Å, depending on the miller index plane. We used a slab containing 40 Fe atoms and 16 C atoms for the (010)<sub>0.25</sub> surface, 40 Fe atoms and 15 C atoms for the (010)<sup>\*</sup><sub>0.25</sub> with a C vacancy and 80 Fe and 32 C atoms for the (100) surface, as described in our previous work.[22] Adsorption of adatoms was done on the top side of the slab while the lower half of the slab was frozen. A dipole correction was performed for all adsorbed states. A vacuum layer of 15 Å was added perpendicular to the surface in order to avoid spurious interactions between neighbouring system images.

The adsorption energies of the gas phase molecules were determined by subtracting both energies of the empty surface and the free adsorbate from the adsorbed state. The energy of the adsorbate in the gas phase was performed by placing a molecule at the centre of a 10 x 10 x 10 Å<sup>3</sup> unit cell, using only the  $\Gamma$ -point for the  $k$ -point sampling. For the electron smearing, a Gaussian smearing width of 0.002 eV was used. The adsorption energies, after zero-point energy (ZPE) corrections, are in good agreement with tabulated thermodynamic data.[23]

For all calculations, the convergence criterion was set to  $10^{-4}$  eV for the ionic steps and to  $10^5$  eV for the electronic convergence. All geometry optimizations were conducted using the conjugate-gradient algorithm. Transition states were acquired using the nudged elastic band (NEB) method.[24] A frequency analysis was performed to confirm that all transition geometries correspond to a first-order saddle point[25] on the potential energy surface with an imaginary frequency in the direction of the reaction coordinate. The Hessian matrix was constructed using a finite difference approach with a step size of 0.02 Å for displacement of individual atoms along each Cartesian coordinate. The corresponding normal mode vibrations were also used to calculate the zero-point energy correction. We furthermore corrected the barriers for the migration of fragments after dissociation by considering the energy difference of the geometry directly after dissociation and their most stable adsorption positions at infinite distance.

#### 4.2.2 Microkinetic modelling

For the construction of the microkinetic model, differential equations for all reaction intermediates on the catalytic surface were constructed using the rate constants of the relevant elementary reaction steps. Each adsorbate occupies exactly one active site. For adsorption, we assumed that the adsorbate loses one translational degree of freedom in the transition state with respect to the initial gas-phase state. Desorbing species were assumed to gain two translational degrees of freedom and three rotational degrees of freedom in the transition state with respect to the initial adsorbed state. From these two assumptions, the rate of adsorption and desorption are as follows[26]

$$k_{\text{ads}} = \frac{P \cdot A}{\sqrt{2\pi \cdot m \cdot k_b \cdot T}} \quad (4.1)$$

$$k_{\text{des}} = \frac{k_b \cdot T^3}{h^3} \cdot \frac{A \cdot (2\pi \cdot m \cdot k_b)}{\sigma \theta_{\text{rot}}} \cdot e^{\left(\frac{-E_{\text{des}}}{RT}\right)} \quad (4.2)$$

Herein,  $k_{\text{ads}}$  is the rate constant for the adsorption of the adsorbate,  $P$  is the pressure in Pa,  $A$  is surface area in  $\text{m}^2$ ,  $m$  is the mass of the reactant in kg,  $k_b$  is the Boltzmann constant in J/K,  $T$  is the temperature in K,  $k_{\text{des}}$  is the rate constant for the desorption of the adsorbate,  $h$  is the Planck constant in  $\text{m}^2\text{kg/s}$ ,  $\sigma$  is the symmetry number,  $\theta_{\text{rot}}$  the rotational temperature in K,  $E_{\text{des}}$  is the desorption energy in J/mol and  $R$  is the gas constant in J/mol K.

The rate constant ( $k$ ) of an elementary reaction step can be determined using the Eyring equation, which is defined as follows:

$$k = v \exp\left(\frac{-\Delta E_{\text{act}}}{k_{\text{b}}T}\right) \quad (4.3)$$

where  $\Delta E_{\text{act}}$  is activation energy in J/mol,  $k_{\text{b}}$  the Boltzmann constant,  $T$  the temperature in K and  $v$  the pre-exponential factor in  $\text{s}^{-1}$ . This pre-exponential factor can be calculated for the forward and backward reaction using the following equations:

$$v_{\text{forward}} = \frac{k_{\text{b}}T}{h} \left( \frac{q_{\text{vib}}^{\text{TS}}}{q_{\text{vib}}^{\text{IS}}} \right) \text{ and } v_{\text{backward}} = \frac{k_{\text{b}}T}{h} \left( \frac{q_{\text{vib}}^{\text{TS}}}{q_{\text{vib}}^{\text{FS}}} \right), \quad (4.4)$$

where  $v_{\text{forward}}$  and  $v_{\text{backward}}$  refer to the pre-exponential factors for the forward and the backward reaction, respectively,  $q_{\text{vib}}$  is the vibrational partition function of the initial state (IS) and the transition state (TS) and  $h$  denotes Planck's constant. For the  $q_{\text{vib}}$  in the transition state, the eigenmode corresponding to the direction of the reaction coordinate is explicitly not included but extracted to obtain the  $\frac{k_{\text{b}}T}{h}$  factor.[27]

All microkinetics simulations were performed using the MKMCXX software suite.[28] The set of differential equations was time-integrated using the backward differentiation formula (BDF) method [29, 30] until a steady-state solution was obtained.[31] From the steady-state coverages, the rates of the individual elementary reactions steps were computed. A standard set of conditions was a total pressure of 1 bar, a  $\text{H}_2/\text{CO}$  ratio of 2 and a temperature in the 510-545 K range.[32]

We studied the microkinetic models under two conditions, i.e. in the zero-conversion limit and at non-zero conversion in a CSTR model. In the zero-conversion limit, the gas-phase concentrations are constant, implying that no re-adsorption of products can take place. In the CSTR model, the gas-phase concentrations change with conversion allowing re-adsorption of products. Chain-growth was modelled via the coupling of two  $\text{C}_1$  species. Hydrocarbon chains with up to 20 C atoms were considered to estimate the chain-growth probability parameter and to avoid too large cut-off effects.[33] To achieve this, we extrapolated the data for  $\text{C}_2$  formation by treating a dangling chain  $((\text{CH}_2)_x\text{-CH}_3)$  as if it were an H atom. To validate this procedure, the energetics of some key reactions were computed for formation of  $\text{C}_3$  species and compared to corresponding energetics for the formation of  $\text{C}_2$  species. The underlying assumption of this approach is that the length of the side chain has a minor influence on the chain-growth rate. Following an approach developed by Zijlstra[34], we took lateral interactions for CO and H at the surface into account.

We added lateral interactions to our microkinetic model by adding a lateral correction term ( $E_{\text{lat}}$ ) to the desorption energy, which influences the rate of desorption through:

$$k_{\text{des}} = \frac{k_{\text{ads}}}{K_{\text{eq}}} = \frac{P \cdot A}{\sqrt{2\pi \cdot m \cdot k_b \cdot T}} \cdot \frac{\exp\left(\frac{S_{\text{gas}}}{R}\right)}{q_{\text{vib,ads}}} \cdot \exp\left(\frac{(E_{\text{des}} + E_{\text{lat}})}{RT}\right) \quad (4.5)$$

Here,  $S_{\text{gas}}$  was calculated from the thermodynamic tables using the Shomate equation.[36] The  $q_{\text{vib,ads}}$  term was introduced as not all gas-phase entropy is lost in the adsorption step. Vibrational entropy in the adsorbed state remains in the form of bond vibrations and hindered translations and rotations. The appropriate temperature corrections for the enthalpy was included in the desorption enthalpy ( $E_{\text{des}}$ ). For the implementation of the lateral interactions, we used the equations as proposed by Zijlstra et al. [34]:

$$E_x^{\text{lat}} = E_x^{\theta=1} \cdot \frac{(101^{\theta_{\text{lat}}}-1)}{100}, \quad (4.6)$$

where  $\theta_{\text{lat}}$  is computed via the following equation:

$$\theta_{\text{lat}} = \frac{(\theta_{\text{total}} - \theta_* - 0.5 \cdot \theta_{\text{H}}) - \theta_{\text{LB}}}{\theta_{\text{UB}} - \theta_{\text{LB}}} \quad (4.7)$$

Herein,  $E_x^{\text{lat}}$  is the lateral interaction penalty per species  $x$ ,  $E_x^{\theta=1}$  is the penalty for  $\theta_{\text{lat}} = 1$  while no lateral penalty was employed for  $\theta_{\text{lat}} = 0$ .  $\theta_{\text{LB}}$  and  $\theta_{\text{UB}}$  are the upper and lower bound, which were chosen at 0.25 and 0.75 monolayer, respectively. The overall thermodynamics of the microkinetic model were preserved by defining a lateral correction on a per-atom basis. The penalty for CO for instance, is sum of the lateral interactions of C and O. We assumed that all surface species contribute equally to the lateral interaction potential with the exception of hydrogen. Treating hydrogen lateral interactions in this way would overestimate the lateral repulsion considering its relatively small size. However, completely removing its contribution is likely to be an underestimation. In this study, we adopted the following lateral interaction parameters:  $E_{\text{C}}^{\theta=1} = E_{\text{O}}^{\theta=1} = 60$  kJ/mol and  $E_{\text{H}}^{\theta=1} = 30$  kJ/mol.

The entropy gain for desorption of hydrocarbons, which varies with chain length, was corrected due to its relevance for predicting more accurate adsorption and desorption rates.

To determine the influence of each elementary reactions step, we used the degree of rate control (DRC) method as introduced by Campbell and co-workers.[37] (cf. Chapter 2.3.4). On the basis of the DRC method, the degree of selectivity control (DCGC)[38] method was developed. Within this method, a chain-growth control coefficient ( $\chi_i$ ) is defined for each elementary reaction step in the following manner:

$$\chi_i = \left( \frac{\partial \alpha}{\partial \ln k_i} \right)_{k_j \neq k_i, K_i} \quad (4.8)$$

Here,  $\alpha$  is the chain-growth probability and  $k_i$  and  $K_i$  are the rate constant and equilibrium constant of the elementary reaction step  $i$ . In this way, the effect of lowering or increasing the reaction barrier for each elementary reaction step on the overall reaction rate is probed relative to the current chain-growth probability. A positive value implies that increasing the constant of a particular elementary reaction step leads to an increase in chain-growth probability. A negative indicates that the corresponding elementary reaction step has an inhibiting effect on chain-growth, meaning that decreasing the barrier for this elementary reaction step results in the lowering of chain-growth probability.

### 4.3 Results and discussion

#### 4.3.1 DFT calculations

DFT calculations were carried out to determine the energetics of the reaction network for the conversion of synthesis gas towards CH<sub>4</sub> and longer hydrocarbons, CO<sub>2</sub> and H<sub>2</sub>O. As surface models, we considered the (010)<sub>0.25</sub>, (010)<sup>\*</sup><sub>0.25</sub> and (100) surfaces, which are depicted in Figure 4.1 (a-c).

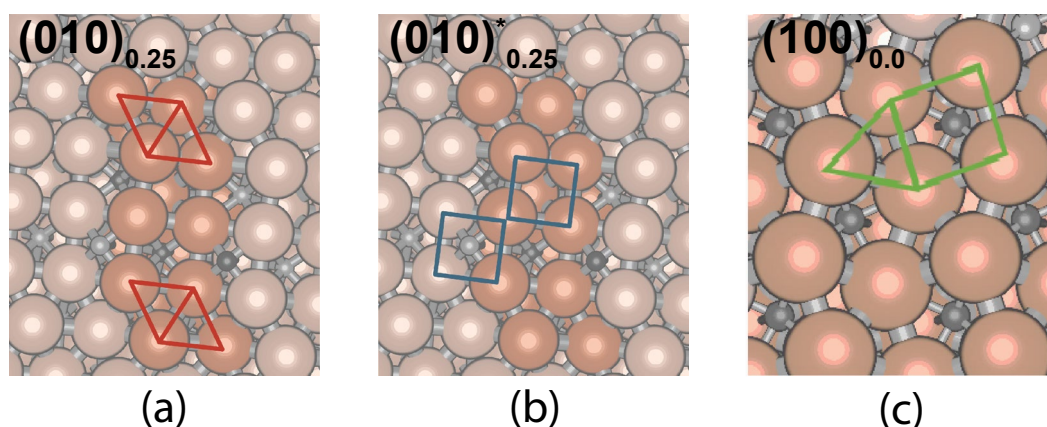


**Figure 4.1** Topology and active sites on the (010)<sub>0.25</sub> surface (a), the (010)<sup>\*</sup><sub>0.25</sub>, (b) and the (100) surface (c).

On the (010)<sub>0.25</sub> surface, we investigate surface reactions at two adjacent threefold sites (2B<sub>3</sub> site, marked with two adjacent red triangles in Figure 4.1a). The (010)<sup>\*</sup><sub>0.25</sub> surface contains two adjacent B<sub>4</sub> sites (marked with a blue square in Figure 4.1b) where a surface C atom belonging to the Hägg carbide structure is located on one of them. The (100) contains a B<sub>5</sub>-like step-edge site, which

consists of one B<sub>3</sub> and one B<sub>4</sub> site (marked with a green triangle adjacent to a green square in Figure 4.1c). Here, a C atom is located below the B<sub>4</sub> site. For these surfaces, we will first discuss the results for the hydrogenation of adsorbed C to CH<sub>4</sub>, followed by a discussion of pathways for adsorbed O removal. Then, we will present data on the various CH<sub>x</sub> + CH<sub>y</sub> coupling reactions and the hydrogenation of the resulting coupled products. Finally, we will discuss key reactions in the formation of C<sub>3</sub>-species in order to gauge the effect of a longer chain length on coupling and hydrogenation reactions.

#### 4.3.1.1 Methane formation

The forward and backward activation energies and the corresponding pre-exponential factors for the hydrogenation steps of adsorbed C to CH<sub>4</sub> are given in Table 4.1. The geometries for all elementary reaction steps are collected in Appendix B.1.

**Table 4.2:** Activation energies and pre-exponential factors (at 800K) for methane formation on (010)<sub>0.25</sub>, (010)<sup>\*</sup><sub>0.25</sub> and (100) surfaces.

Surface	Elementary Reaction step			E <sub>f</sub> (kJ/mol)	v <sub>f</sub> (s <sup>-1</sup> )	E <sub>b</sub> (kJ/mol)	v <sub>b</sub> (s <sup>-1</sup> )
(010) <sub>0.25</sub>	C + H	⇌	CH	83	1.7·10 <sup>13</sup>	109	1.4·10 <sup>13</sup>
(010) <sub>0.25</sub>	CH + H	⇌	CH <sub>2</sub>	53	1.1·10 <sup>13</sup>	2	7.2·10 <sup>12</sup>
(010) <sub>0.25</sub>	CH <sub>2</sub> + H	⇌	CH <sub>3</sub>	53	2.6·10 <sup>13</sup>	37	1.6·10 <sup>13</sup>
(010) <sub>0.25</sub>	CH <sub>3</sub> + H	⇌	CH <sub>4</sub>	91	1.1·10 <sup>14</sup>	48	6.9·10 <sup>13</sup>
(010) <sup>*</sup> <sub>0.25</sub>	C + H	⇌	CH	79	9.8·10 <sup>12</sup>	74	1.9·10 <sup>13</sup>
(010) <sup>*</sup> <sub>0.25</sub>	CH + H	⇌	CH <sub>2</sub>	70	1.1·10 <sup>13</sup>	1	9.4·10 <sup>12</sup>
(010) <sup>*</sup> <sub>0.25</sub>	CH <sub>2</sub> + H	⇌	CH <sub>3</sub>	88	2.3·10 <sup>13</sup>	13	5.4·10 <sup>11</sup>
(010) <sup>*</sup> <sub>0.25</sub>	CH <sub>3</sub> + H	⇌	CH <sub>4</sub>	41	1.6·10 <sup>12</sup>	36	3.2·10 <sup>11</sup>
(100)	C + H	⇌	CH	78	1.4·10 <sup>13</sup>	97	1.3·10 <sup>13</sup>
(100)	CH + H	⇌	CH <sub>2</sub>	53	5.8·10 <sup>13</sup>	12	8.9·10 <sup>12</sup>
(100)	CH <sub>2</sub> + H	⇌	CH <sub>3</sub>	49	9.1·10 <sup>13</sup>	45	3.0·10 <sup>12</sup>
(100)	CH <sub>3</sub> + H	⇌	CH <sub>4</sub>	109	1.7·10 <sup>13</sup>	49	1.3·10 <sup>11</sup>

C hydrogenation is relatively difficult on all three surfaces, as C is adsorbed in fourfold or threefold sites. The corresponding activation barriers for C hydrogenation are 83 kJ/mol, 79 kJ/mol and 78 kJ/mol on the (010)<sub>0.25</sub>, (010)<sup>\*</sup><sub>0.25</sub> and (100) surface. CH hydrogenation has a relatively low barrier on the (010)<sub>0.25</sub> and (100) surface (53 kJ/mol). The barrier on the (010)<sup>\*</sup><sub>0.25</sub> surface is higher (70 kJ/mol) because the CH species is more stable on this surface. The highest barrier for CH<sub>2</sub> hydrogenation is found for the (010)<sup>\*</sup><sub>0.25</sub> surface (88 kJ/mol). The considerably higher barrier compared to the other surface is due to the migration of the CH<sub>2</sub> species from a fourfold to a bridge



site on the  $(010)^*_{0.25}$  surface required before hydrogenation can take place.  $\text{CH}_3$  formation on the other surfaces is easier with activation barriers of 53 kJ/mol and 49 kJ/mol on the  $(010)_{0.25}$  and (100) surface, respectively.  $\text{CH}_2$  is most stable on the  $(010)^*_{0.25}$  with respect to the other surfaces, while the  $\text{CH}_3$  is more stable on the (100) and  $(010)_{0.25}$  surfaces. These differences can also be appreciated from the reaction energy diagram in Figure 4.2.  $\text{CH}_3$  hydrogenation to  $\text{CH}_4$  is the most difficult step with relatively high barriers on both the  $(010)_{0.25}$  and the (100) surface (91 kJ/mol and 109 kJ/mol, respectively). The formation of  $\text{CH}_4$  on the  $(010)^*_{0.25}$  is however much easier with a barrier of only 41 kJ/mol. These differences can be related to the stability of the  $\text{CH}_3$  species.  $\text{CH}_3$  is much more stable on the two (010) surfaces, which display higher barriers for  $\text{CH}_4$  formation. These differences can also be appreciated from Figure 4.2.

#### 4.3.1.2 Oxygen removal

The removal of O atoms from CO dissociation can occur via the formation of  $\text{CO}_2$  and  $\text{H}_2\text{O}$ . The formation of  $\text{CO}_2$  involves the recombination of O atoms with adsorbed CO.  $\text{H}_2\text{O}$  formation can either occur by direct O hydrogenation to OH followed by OH hydrogenation to  $\text{H}_2\text{O}$  or, for the latter step, via an H-transfer from one OH species to an adjacent OH species, forming  $\text{H}_2\text{O}$  and O (disproportionation). The forward and backward reaction energy barriers and corresponding pre-exponential factors for O removal are listed in Table 4.2. The geometries for all elementary reaction steps are collected in Appendix B.1.

$\text{CO}_2$  is adsorbed in a fourfold manner, while  $\text{H}_2\text{O}$  is adsorbed on top of a single surface Fe atom. OH is adsorbed in a bridged site in most cases, except on  $(010)^*_{0.25}$  where it is adsorbed fourfold. To minimize the distance between the two OH species for the OH+OH disproportionation reaction, the second OH species needs to be adsorbed in a threefold site on  $(010)_{0.25}$  and (100) and in a fourfold site on  $(010)^*_{0.25}$ .

Removal of O as  $\text{CO}_2$  via the CO+O reaction has the highest barrier on the (100) surface (181 kJ/mol). The barriers on  $(010)_{0.25}$  and  $(010)^*_{0.25}$  are 148 kJ/mol and 164 kJ/mol, respectively. The higher barrier on the stepped surface is due to the migration of CO out of the threefold site. The different barriers on the two (010) surface models is due to the different coordination of CO and O, which are adsorbed threefold on  $(010)_{0.25}$  and fourfold on  $(010)^*_{0.25}$ .

O hydrogenation to OH is most favourable on the (100) surface (65 kJ/mol), where O is adsorbed in a bridged site. On  $(010)_{0.25}$  and  $(010)^*_{0.25}$ , the barrier for OH formation is significantly higher (172

kJ/mol and 153 kJ/mol, respectively) compared to the (100) surface. The hydrogenation of OH to H<sub>2</sub>O has similar barriers on (010)<sub>0.25</sub> (129 kJ/mol) and on (100) (136 kJ/mol). On both surfaces, OH is adsorbed in a bridged site in the initial state. On the (010)<sup>\*</sup><sub>0.25</sub> surface, the activation energy is lower (103 kJ/mol) because of the weaker atop adsorption. This results in overall barriers for H<sub>2</sub>O formation (via OH hydrogenation) of 155 kJ/mol, 173 kJ/mol and 203 kJ/mol for (100), (010)<sup>\*</sup><sub>0.25</sub>, and (010)<sub>0.25</sub>, respectively. The barriers for the OH+OH disproportionation reaction on (010)<sub>0.25</sub> and (010)<sup>\*</sup><sub>0.25</sub> are significantly lower than on (100). However, due to the high OH formation energy, this reaction is unlikely on the (010)<sub>0.25</sub> and (010)<sup>\*</sup><sub>0.25</sub> surfaces. On the (100) surface, the overall energy barrier for H<sub>2</sub>O formation via direct hydrogenation of and disproportionation are almost the same, i.e. 155 kJ/mol and 156 kJ/mol, respectively.

From these calculations, we can infer that H<sub>2</sub>O formation is likely to be the preferred O removal pathway on the (100) surface, while CO<sub>2</sub> is the most likely O removal product on the other two surfaces. As the rates will not only depend on the activation barriers but also on the surface coverages of the intermediates, only microkinetics simulations can predict which O removal product is preferred.

**Table 4.3** Activation energies and pre-exponential factors (at 800K) for oxygen removal reactions on the (010)<sub>0.25</sub> surface, (010)<sup>\*</sup><sub>0.25</sub> surface and the (100) surface.

Surface	Elementary Reaction step			E <sub>r</sub> (kJ/mol)	v <sub>r</sub>	E <sub>b</sub> (kJ/mol)	v <sub>b</sub>
(010) <sub>0.25</sub>	CO + O	⇌	CO <sub>2</sub>	148	9.2·10 <sup>12</sup>	43	3.2·10 <sup>13</sup>
(010) <sub>0.25</sub>	O + H	⇌	OH	172	5.0·10 <sup>13</sup>	98	1.2·10 <sup>13</sup>
(010) <sub>0.25</sub>	OH + H	⇌	H <sub>2</sub> O	129	6.3·10 <sup>13</sup>	23	3.5·10 <sup>12</sup>
(010) <sub>0.25</sub>	OH + OH	⇌	H <sub>2</sub> O + O	95	1.5·10 <sup>12</sup>	64	3.5·10 <sup>13</sup>
(010) <sup>*</sup> <sub>0.25</sub>	CO + O	⇌	CO <sub>2</sub>	176	6.5·10 <sup>13</sup>	36	2.0·10 <sup>14</sup>
(010) <sup>*</sup> <sub>0.25</sub>	O + H	⇌	OH	153	1.4·10 <sup>13</sup>	83	1.0·10 <sup>13</sup>
(010) <sup>*</sup> <sub>0.25</sub>	OH + H	⇌	H <sub>2</sub> O	103	2.3·10 <sup>13</sup>	32	7.0·10 <sup>12</sup>
(010) <sup>*</sup> <sub>0.25</sub>	OH + OH	⇌	H <sub>2</sub> O + O	46	4.3·10 <sup>12</sup>	51	1.7·10 <sup>12</sup>
(100)	CO + O	⇌	CO <sub>2</sub>	181	4.3·10 <sup>13</sup>	142	7.6·10 <sup>13</sup>
(100)	O + H	⇌	OH	65	7.3·10 <sup>13</sup>	46	8.6·10 <sup>12</sup>
(100)	OH + H	⇌	H <sub>2</sub> O	136	1.6·10 <sup>13</sup>	1	1.5·10 <sup>12</sup>
(100)	OH + OH	⇌	H <sub>2</sub> O + O	118	6.4·10 <sup>12</sup>	1	5.1·10 <sup>12</sup>

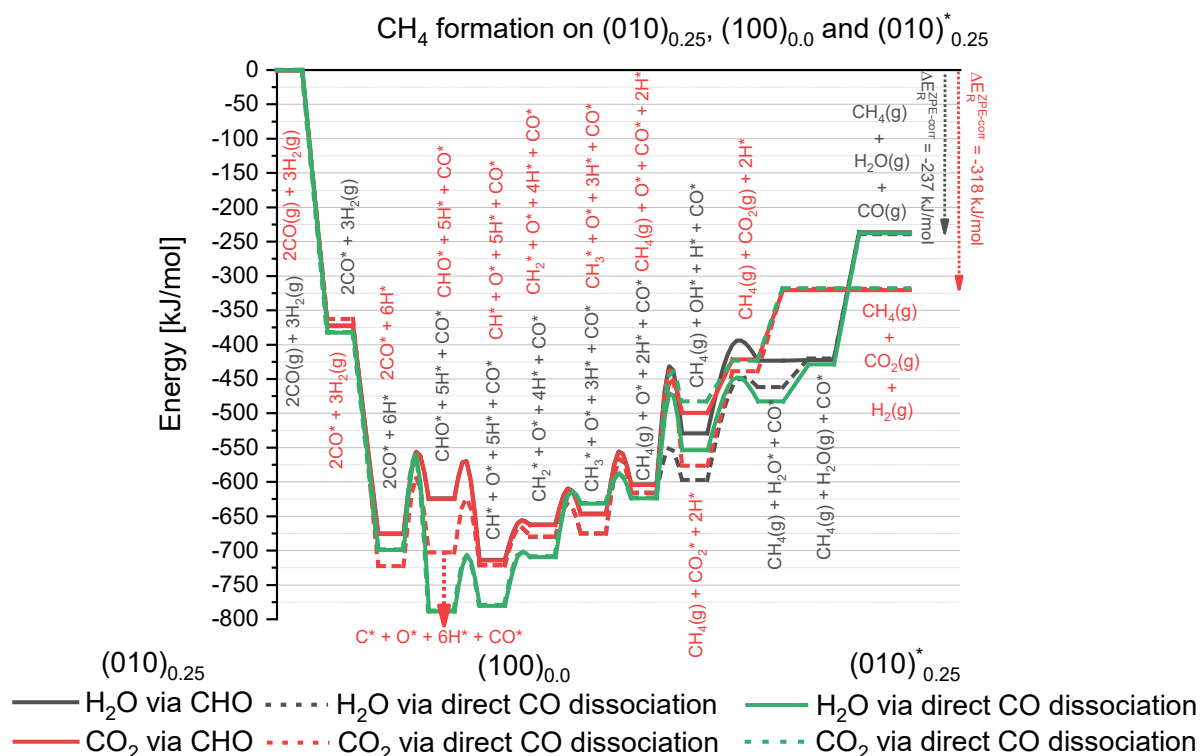


**Figure 4.2:** Reaction energy diagram for CH<sub>4</sub> formation on the (010)<sub>0.25</sub>, (100) and (010)<sup>\*</sup><sub>0.25</sub> surfaces. For the (010)<sub>0.25</sub>, the HCO mechanism is considered. For the (100) surface, the direct CO dissociation is followed.

The reaction energy diagrams for CH<sub>4</sub> formation and O removal as CO<sub>2</sub> and H<sub>2</sub>O on the (010)<sub>0.25</sub>, (010)<sup>\*</sup><sub>0.25</sub> and (100) surfaces are depicted in Figure 4.2. We chose the most dominant CO dissociation mechanism for each surface, as previously established.[22] CO dissociation proceeds via an H-assisted mechanism (HCO) on the (010)<sub>0.25</sub> surface and via a direct CO dissociation mechanism on the (100) and (010)<sup>\*</sup><sub>0.25</sub> surfaces. Figure 4.2 also shows that O removal is most likely to proceed via the formation of CO<sub>2</sub> on the (010)<sub>0.25</sub> surface, while oxygen is more likely to be removed as H<sub>2</sub>O on the other two surfaces. The preference for CO<sub>2</sub> formation on the (010)<sub>0.25</sub> surface can be explained by the high barrier for OH formation, which is 24 kJ/mol higher compared to the formation of CO<sub>2</sub>. The barrier for OH formation on the other two surfaces is lower compared to the formation of CO<sub>2</sub>. The overall formation of H<sub>2</sub>O on the (100) surface and the (010)<sup>\*</sup><sub>0.25</sub> surface are, 26 kJ/mol and 3 kJ/mol lower compared to the CO<sub>2</sub> formation.

#### 4.3.1.3 CH<sub>x</sub> - CH<sub>y</sub> coupling and C<sub>2</sub> hydrogenation

Out of the 10 possible elementary reaction steps for the coupling of two C<sub>1</sub> (CH<sub>x</sub>) species, we identified 8 transition states for the (010)<sub>0.25</sub> surface, 9 for the (100) surface and 9 for the (010)<sup>\*</sup><sub>0.25</sub>

surface. The energy barriers and the corresponding pre-exponential factors are listed in Table 4.3. For  $\text{CH}_2\text{-CH}_3$  coupling on  $(010)_{0.25}$  and  $\text{CH}_3\text{-CH}_3$  coupling on all three surfaces, we could not identify a transition state. This can be understood by the high Tolman angle of the  $\text{CH}_x$  adsorbates with respect to the metal atom [39], resulting in strong repulsion between the associating fragments. As the hydrogen atoms are directed away from the surface, this leads to a strong Pauli repulsion between the coupling  $\text{CH}_x$  ( $x = 2,3$ ) species meaning that they cannot come close enough to get sufficient overlap for the formation of a C-C bond. Consequently, there is no transition state for C-C bond formation because C-H bond cleavage will occur instead. This is especially the case for flat surfaces, where there is no possibility to alleviate the strong Pauli repulsion by reorientation of the surface intermediates. If, however, the Pauli repulsion is of moderate strength, we can still identify a transition state for C-C bond formation as for the  $(010)^*_{0.25}$  surface where the coupling is facilitated by the C-vacancy on the surface. The resulting barrier of this reaction is nevertheless very high (191 kJ/mol). A transition state for  $\text{CH}_2\text{-CH}_3$  coupling was also found for the stepped (100) surface. The relatively low barrier of 124 kJ/mol can be explained by the possibility for the  $\text{CH}_x$  intermediates to reorient, decreasing strong steric repulsion. CH-CH coupling is the most facile pathway for  $\text{C}_2$  formation on the  $(010)_{0.25}$  surface, while C-CH coupling is favoured on the (100) surface. The formation of ethylene and ethane can proceed via 12 unique hydrogenation steps, which were all identified for the three surfaces. The corresponding barriers and pre-exponential factors are collected in Table 4. The geometries for all elementary reaction steps are collected in Appendix B.1.

We found that the C species are preferentially adsorbed on fourfold sites. On the (100) surface, fourfold adsorption is however not possible because of the presence of a C atom in the first interstitial layer directly below the fourfold site. This leads to repulsion of surface adsorbates, explaining threefold adsorption. On the  $(010)_{0.25}$  and (100) surface, the CH species is mostly adsorbed in a threefold mode, with the exception of the initial state for C-CH on the  $(010)_{0.25}$  where CH is located in a fourfold  $2\text{B}_3$  site. On the  $(010)^*_{0.25}$  surface, CH and  $\text{CH}_2$  species are adsorbed in fourfold sites. On  $(010)_{0.25}$  and (100) surface,  $\text{CH}_2$  is adsorbed in a bridged site. Exceptions are the initial state for  $\text{CH}_2\text{-CH}_2$  coupling where one  $\text{CH}_2$  is adsorbed bridged on the (100) surface and both  $\text{CH}_2$  species are adsorbed in threefold sites on the  $(010)_{0.25}$  surface. On (100),  $\text{CH}_2$  is also adsorbed in a threefold site in the initial state for CH- $\text{CH}_2$  coupling.

In general, the (100) surface exhibits the lowest barriers for C-C coupling for the C-C(H) $_x$  ( $x = 0, 1$ , or 3) coupling reactions. The activation energies are all below 100 kJ/mol. The lowest activation barrier was found for C-CH coupling on the (100) surface (79 kJ/mol). Barriers for C-C (90 kJ/mol) and C- $\text{CH}_3$  coupling (96 kJ/mol) are slightly higher. The  $(010)_{0.25}$  surface has comparable barriers

for C-C coupling with respect to the (100) surface and lower activation energies compared to the (010)<sup>\*</sup><sub>0.25</sub> surface. The lowest barrier for C-C bond formation on the (010)<sub>0.25</sub> surface is CH-CH coupling (82 kJ/mol), followed by C-CH coupling and C-C coupling with respective barriers of 94 kJ/mol and 107 kJ/mol. C-CH<sub>3</sub> coupling (88 kJ/mol) has the only barrier for C-C coupling below 100 kJ/mol on the (010)<sup>\*</sup><sub>0.25</sub> surface. The activation energies of the other C-C coupling barriers on this surface are all higher than 120 kJ/mol, which is caused by the high stability of the C<sub>1</sub> species on the (010)<sup>\*</sup><sub>0.25</sub> surface relative to the other surfaces (Figure 4.3 a-c).

**Table 4.4** Activation energies and pre-exponential factors (at 800K) for  $\text{CH}_x\text{-CH}_y$  coupling on the  $(010)_{0.25}$  surface,  $(010)^*_{0.25}$  surface and the  $(100)$  surface.

Elementary Reaction step	$(010)_{0.25}$						$(010)^*_{0.25}$						$(100)$					
	$E_f$ (kJ/mol)	$\nu_f$	$E_b$ (kJ/mol)	$\nu_b$	$E_f$ (kJ/mol)	$\nu_f$	$E_f$ (kJ/mol)	$\nu_f$	$E_b$ (kJ/mol)	$\nu_b$	$E_f$ (kJ/mol)	$\nu_f$	$E_f$ (kJ/mol)	$\nu_f$	$E_b$ (kJ/mol)	$\nu_b$	$E_b$ (kJ/mol)	$\nu_b$
$\text{C} + \text{C} \rightleftharpoons \text{CC}$	107	$1.6 \cdot 10^{12}$	134	$4.9 \cdot 10^{12}$	201	$9.0 \cdot 10^{12}$	201	$9.0 \cdot 10^{12}$	27	$9.1 \cdot 10^{12}$	90	$4.6 \cdot 10^{11}$	90	$4.6 \cdot 10^{11}$	110	$7.9 \cdot 10^{12}$	110	$7.9 \cdot 10^{12}$
$\text{C} + \text{CH} \rightleftharpoons \text{CCH}$	94	$5.1 \cdot 10^{12}$	93	$5.0 \cdot 10^{12}$	146	$7.2 \cdot 10^{12}$	146	$7.2 \cdot 10^{12}$	49	$5.6 \cdot 10^{12}$	79	$1.9 \cdot 10^{12}$	79	$1.9 \cdot 10^{12}$	88	$7.9 \cdot 10^{12}$	88	$7.9 \cdot 10^{12}$
$\text{C} + \text{CH}_2 \rightleftharpoons \text{CCH}_2$	114	$8.5 \cdot 10^{12}$	131	$6.2 \cdot 10^{12}$	179	$9.3 \cdot 10^{12}$	179	$9.3 \cdot 10^{12}$	127	$3.0 \cdot 10^{12}$	122	$2.2 \cdot 10^{12}$	122	$2.2 \cdot 10^{12}$	174	$1.0 \cdot 10^{13}$	174	$1.0 \cdot 10^{13}$
$\text{C} + \text{CH}_3 \rightleftharpoons \text{CCH}_3$	121	$3.3 \cdot 10^{13}$	140	$9.3 \cdot 10^{12}$	88	$3.1 \cdot 10^{11}$	88	$3.1 \cdot 10^{11}$	120	$1.3 \cdot 10^{13}$	96	$1.1 \cdot 10^{13}$	96	$1.1 \cdot 10^{13}$	80	$1.3 \cdot 10^{13}$	80	$1.3 \cdot 10^{13}$
$\text{CH} + \text{CH} \rightleftharpoons \text{CHCH}$	82	$7.4 \cdot 10^{12}$	37	$8.3 \cdot 10^{12}$	147	$9.7 \cdot 10^{12}$	147	$9.7 \cdot 10^{12}$	1	$5.4 \cdot 10^{12}$	117	$2.0 \cdot 10^{11}$	117	$2.0 \cdot 10^{11}$	138	$6.6 \cdot 10^{11}$	138	$6.6 \cdot 10^{11}$
$\text{CH} + \text{CH}_2 \rightleftharpoons \text{CHCH}_2$	124	$9.6 \cdot 10^{12}$	87	$1.0 \cdot 10^{13}$	143	$4.6 \cdot 10^{13}$	143	$4.6 \cdot 10^{13}$	12	$2.1 \cdot 10^{13}$	111	$1.4 \cdot 10^{13}$	111	$1.4 \cdot 10^{13}$	88	$2.2 \cdot 10^{13}$	88	$2.2 \cdot 10^{13}$
$\text{CH} + \text{CH}_3 \rightleftharpoons \text{CHCH}_3$	188	$3.1 \cdot 10^{13}$	116	$1.4 \cdot 10^{13}$	121	$1.3 \cdot 10^{12}$	121	$1.3 \cdot 10^{12}$	75	$5.0 \cdot 10^{12}$	181	$2.5 \cdot 10^{12}$	181	$2.5 \cdot 10^{12}$	128	$4.5 \cdot 10^{12}$	128	$4.5 \cdot 10^{12}$
$\text{CH}_2 + \text{CH}_2 \rightleftharpoons \text{CH}_2\text{CH}_2$	126	$4.5 \cdot 10^{12}$	67	$5.5 \cdot 10^{12}$	185	$2.4 \cdot 10^{13}$	185	$2.4 \cdot 10^{13}$	87	$1.2 \cdot 10^{13}$	112	$1.1 \cdot 10^{13}$	112	$1.1 \cdot 10^{13}$	128	$1.6 \cdot 10^{12}$	128	$1.6 \cdot 10^{12}$
$\text{CH}_2 + \text{CH}_3 \rightleftharpoons \text{CH}_2\text{CH}_3$	-	-	-	-	191	$2.0 \cdot 10^{12}$	191	$2.0 \cdot 10^{12}$	132	$1.1 \cdot 10^{13}$	124	$8.0 \cdot 10^{12}$	124	$8.0 \cdot 10^{12}$	101	$7.6 \cdot 10^{13}$	101	$7.6 \cdot 10^{13}$

**Table 4.5** Activation energies and pre-exponential factors (at 800K) for C<sub>2</sub> hydrogenation reactions on the (010)<sub>0.25</sub> surface, (010)<sup>\*</sup><sub>0.25</sub> surface and the (100) surface.

Elementary Reaction step		(010) <sub>0.25</sub>						(010) <sup>*</sup> <sub>0.25</sub>						(100)					
		E <sub>f</sub> (kJ/mol)	v <sub>f</sub>	E <sub>b</sub> (kJ/mol)	v <sub>b</sub>	E <sub>f</sub> (kJ/mol)	v <sub>b</sub>	E <sub>f</sub> (kJ/mol)	v <sub>f</sub>	E <sub>b</sub> (kJ/mol)	v <sub>b</sub>	E <sub>f</sub> (kJ/mol)	v <sub>f</sub>	E <sub>f</sub> (kJ/mol)	v <sub>f</sub>	E <sub>b</sub> (kJ/mol)	v <sub>b</sub>	E <sub>f</sub> (kJ/mol)	v <sub>f</sub>
CC + H	⇌	84	1.6·10 <sup>13</sup>	84	1.5·10 <sup>13</sup>	81	1.5·10 <sup>13</sup>	81	2.7·10 <sup>12</sup>	150	1.1·10 <sup>13</sup>	70	1.6·10 <sup>13</sup>	77	1.6·10 <sup>13</sup>	77	1.4·10 <sup>13</sup>	77	1.6·10 <sup>13</sup>
CCH + H	⇌	80	1.4·10 <sup>13</sup>	47	7.0·10 <sup>12</sup>	41	7.0·10 <sup>12</sup>	41	8.4·10 <sup>11</sup>	15	3.6·10 <sup>12</sup>	45	1.9·10 <sup>13</sup>	47	1.9·10 <sup>13</sup>	47	1.2·10 <sup>13</sup>	47	1.2·10 <sup>13</sup>
CCH + H	⇌	89	1.2·10 <sup>13</sup>	70	1.1·10 <sup>13</sup>	164	1.1·10 <sup>13</sup>	164	8.5·10 <sup>11</sup>	108	7.6·10 <sup>12</sup>	67	1.8·10 <sup>13</sup>	61	1.8·10 <sup>13</sup>	61	1.8·10 <sup>13</sup>	61	1.8·10 <sup>13</sup>
CCH <sub>2</sub> + H	⇌	41	6.1·10 <sup>12</sup>	26	1.5·10 <sup>12</sup>	31	1.5·10 <sup>12</sup>	31	3.2·10 <sup>12</sup>	36	1.3·10 <sup>13</sup>	42	6.4·10 <sup>12</sup>	6	6.4·10 <sup>12</sup>	6	5.8·10 <sup>11</sup>	6	5.8·10 <sup>11</sup>
CCH <sub>2</sub> + H	⇌	105	4.2·10 <sup>13</sup>	77	5.2·10 <sup>13</sup>	95	5.2·10 <sup>13</sup>	95	4.2·10 <sup>12</sup>	8	8.3·10 <sup>12</sup>	142	5.6·10 <sup>13</sup>	85	5.6·10 <sup>13</sup>	85	6.8·10 <sup>13</sup>	85	6.8·10 <sup>13</sup>
CHCH + H	⇌	86	1.2·10 <sup>13</sup>	42	7.5·10 <sup>12</sup>	57	7.5·10 <sup>12</sup>	57	1.8·10 <sup>12</sup>	1	7.6·10 <sup>12</sup>	103	1.5·10 <sup>13</sup>	55	1.5·10 <sup>13</sup>	55	1.2·10 <sup>13</sup>	55	1.2·10 <sup>13</sup>
CCH <sub>3</sub> + H	⇌	90	7.4·10 <sup>12</sup>	26	9.8·10 <sup>12</sup>	111	9.8·10 <sup>12</sup>	111	1.1·10 <sup>14</sup>	26	1.6·10 <sup>13</sup>	56	2.8·10 <sup>12</sup>	1	2.8·10 <sup>12</sup>	1	2.0·10 <sup>12</sup>	1	2.0·10 <sup>12</sup>
CHCH <sub>2</sub> + H	⇌	102	7.4·10 <sup>12</sup>	28	5.5·10 <sup>12</sup>	68	5.5·10 <sup>12</sup>	68	4.1·10 <sup>11</sup>	29	7.5·10 <sup>12</sup>	38	3.3·10 <sup>13</sup>	36	3.3·10 <sup>13</sup>	36	4.7·10 <sup>12</sup>	36	4.7·10 <sup>12</sup>
CHCH <sub>2</sub> + H	⇌	72	8.0·10 <sup>12</sup>	21	2.1·10 <sup>12</sup>	41	2.1·10 <sup>12</sup>	41	6.6·10 <sup>11</sup>	48	2.8·10 <sup>12</sup>	200	1.3·10 <sup>14</sup>	165	1.3·10 <sup>14</sup>	165	6.6·10 <sup>12</sup>	165	6.6·10 <sup>12</sup>
CH <sub>2</sub> CH <sub>2</sub> + H	⇌	120	2.0·10 <sup>13</sup>	119	1.6·10 <sup>12</sup>	107	1.6·10 <sup>12</sup>	107	5.6·10 <sup>11</sup>	68	2.4·10 <sup>12</sup>	48	6.3·10 <sup>12</sup>	4	6.3·10 <sup>12</sup>	4	1.9·10 <sup>13</sup>	4	1.9·10 <sup>13</sup>
CHCH <sub>3</sub> + H	⇌	113	4.3·10 <sup>12</sup>	90	9.7·10 <sup>11</sup>	115	9.7·10 <sup>11</sup>	115	5.4·10 <sup>13</sup>	30	3.2·10 <sup>13</sup>	57	2.0·10 <sup>12</sup>	45	2.0·10 <sup>12</sup>	45	1.7·10 <sup>13</sup>	45	1.7·10 <sup>13</sup>
CH <sub>2</sub> CH <sub>3</sub> + H	⇌	84	2.1·10 <sup>12</sup>	153	2.3·10 <sup>13</sup>	50	2.3·10 <sup>13</sup>	50	2.4·10 <sup>10</sup>	147	1.0·10 <sup>11</sup>	94	2.5·10 <sup>14</sup>	139	2.5·10 <sup>14</sup>	139	7.5·10 <sup>13</sup>	139	7.5·10 <sup>13</sup>

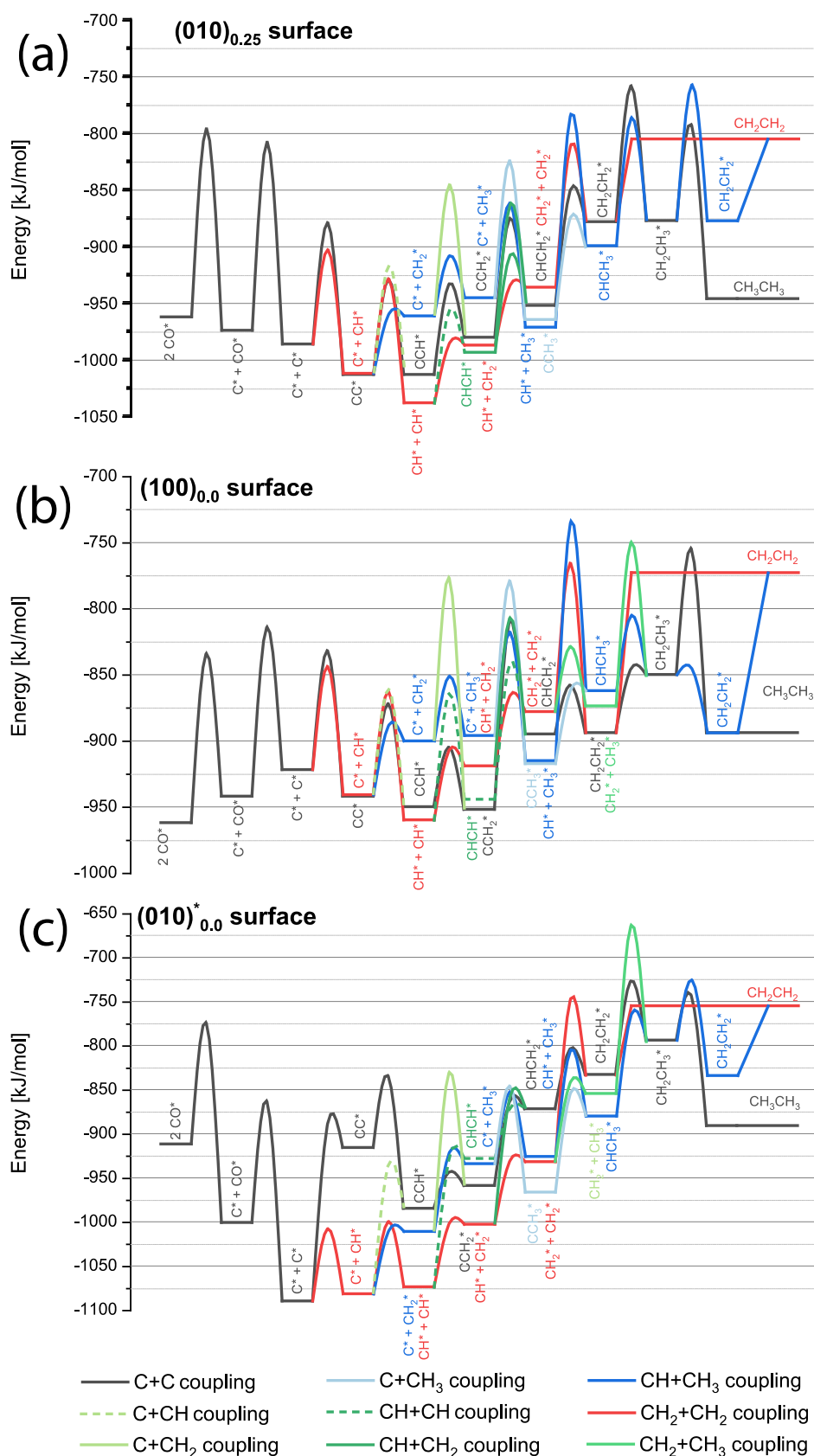


**Figure 4.3** Reaction energy diagrams for the C-C coupling reactions on a) the  $(010)_{0.25}$  surface, b) the  $(100)_{0.0}$  surface and c) the  $(010)^*_{0.25}$  surface. The most left state represents the surface with 2 CO and 5 H<sub>2</sub> molecules adsorbed. All energies are with respect to the empty surface and the reactants in the gas phase. The CO dissociation mechanism was considered for the two surfaces.



The reaction energy diagrams for the formation of ethylene and ethane from syngas on (010)<sub>0.25</sub> surface, the (100) surface and the (010)<sup>\*</sup><sub>0.25</sub> surface are shown in Figure 4.3. We employed the direct CO dissociation mechanism for both surfaces to directly compare C-C and C-CH<sub>x</sub> coupling with the other CH<sub>x</sub>-CH<sub>x</sub> coupling reactions. To identify the most plausible pathway from the energetics for each individual surface, we compared the pathway with the highest overall activation energy. On the basis of Figure 4.3a, we can expect C-CH and CH-CH coupling reactions (indicated by dashed lines) to be the dominant pathways for chain-growth on the (010)<sub>0.25</sub> surface. Furthermore, we can see that olefins formation are kinetically preferred over paraffins formation, because the transition states for formation of CH<sub>2</sub>CH<sub>3</sub> and CH<sub>3</sub>CH<sub>3</sub> are higher in energy than desorption of CH<sub>2</sub>CH<sub>2</sub>. Furthermore, the formation of CH<sub>2</sub>CH<sub>2</sub> is entropically preferred to CH<sub>3</sub>CH<sub>3</sub> on the free energy surface. Figure 4.3b shows the reaction energy diagram of C-C coupling reactions on the (100) surface. Again, olefins are preferred to paraffins. Dominant chain-growth steps are likely to be C-CH and CH-CH coupling reactions. The (100) surface is expected to be more active than the (010)<sub>0.25</sub> surface because most activation barriers, as well as the overall barrier for C<sub>2</sub> formation for the former, are lower. This hypothesis will be tested with the microkinetics simulations to be discussed below.

#### 4.3.1.4 C<sub>3</sub> formation

In order to obtain kinetic parameters for the formation of C<sub>3+</sub> hydrocarbons, we treated CH<sub>3</sub>-(CH<sub>2</sub>)<sub>n</sub>-fragments (n = 0, 1, 2, ...) as H atoms[31]. This approach is based on the assumption that the intrinsic chain-growth kinetics does not depend on the chain length. To assess the validity of this procedure, we explicitly calculated barriers for a selection of C<sub>2</sub> chain-growth steps and compared these barriers with those for C<sub>2</sub> formation. As we expect that the difference in the barriers for chain extension reactions is higher on terrace surfaces than on the more corrugated surfaces, we carried out such calculations for the (010)<sub>0.25</sub> and (010)<sup>\*</sup><sub>0.25</sub> surfaces. The energetics and pre-exponential factors for the selected reactions are collected in Table 4.5.

**Table 4.6** Activation energies and pre-exponential factors (at 800K) for C<sub>3</sub> formation on the (010)<sub>0.25</sub> surface and the (010)<sup>\*</sup><sub>0.25</sub> surface.

Surface	Elementary Reaction step			E <sub>f</sub> (kJ/mol)	v <sub>f</sub>	E <sub>b</sub> (kJ/mol)	v <sub>b</sub>
(010) <sub>0.25</sub>	C + CCH <sub>3</sub>	⇌	CCCH <sub>3</sub>	70	2.8·10 <sup>12</sup>	55	4.8·10 <sup>12</sup>
(010) <sub>0.25</sub>	CH + CCH <sub>3</sub>	⇌	CHCCH <sub>3</sub>	95	2.9·10 <sup>12</sup>	43	5.7·10 <sup>12</sup>
(010) <sub>0.25</sub>	CH <sub>3</sub> + CHCH <sub>3</sub>	⇌	CH <sub>3</sub> CHCH <sub>3</sub>	128	2.1·10 <sup>12</sup>	76	9.0·10 <sup>11</sup>
(010) <sub>0.25</sub>	CH <sub>2</sub> + CHCH <sub>3</sub>	⇌	CH <sub>2</sub> CHCH <sub>3</sub>	128	2.4·10 <sup>12</sup>	137	1.1·10 <sup>12</sup>
(010) <sup>*</sup> <sub>0.25</sub>	C + CCH <sub>3</sub>	⇌	CCCH <sub>3</sub>	142	7.5·10 <sup>13</sup>	59	5.5·10 <sup>11</sup>
(010) <sup>*</sup> <sub>0.25</sub>	CH + CCH <sub>3</sub>	⇌	CHCCH <sub>3</sub>	146	3.9·10 <sup>13</sup>	6	3.5·10 <sup>12</sup>

For the (010)<sub>0.25</sub> surface, two coupling reactions with CCH<sub>3</sub> and CHCH<sub>3</sub> species were considered. C and a CH species were coupled to CCH<sub>3</sub> leading to CCCH<sub>3</sub> and CHCCH<sub>3</sub>, respectively. These reactions are the equivalents of C-CH and CH-CH coupling. A comparison shows that the forward activation barriers are 24 kJ/mol lower for C<sub>3</sub> than for C<sub>2</sub> formation for C-CCH<sub>3</sub>/C-CH coupling and 13 kJ/mol lower for CH-CCH<sub>3</sub>/CH-CH coupling. The influence of chain length on the backward barriers were more significant, i.e. C<sub>3</sub> decoupling is much more favourable than C<sub>2</sub> decoupling. Furthermore, we considered coupling of CH<sub>2</sub> and CH<sub>3</sub> to CHCH<sub>3</sub>, resulting in CH<sub>2</sub>CHCH<sub>3</sub> and CH<sub>3</sub>CHCH<sub>3</sub>, respectively. Comparing the activation barriers for CH<sub>2</sub>-CH<sub>2</sub> coupling, the activation barriers for the forward and backward reactions differ by 2 kJ/mol and 70 kJ/mol (128 kJ/mol for C<sub>3</sub> and 126 kJ/mol for C<sub>2</sub> formation) and (137 kJ/mol for C<sub>3</sub> and 67 kJ/mol for C<sub>2</sub> formation). From these data, we can infer that substitution of a hydrogen atom with a methyl group results in lower barriers for C-C bond formation, although the resulting species become less stable. This electronic effect of alkyl substituents on the chain-growth has been previously described for Ru.[40] A comparison between CH<sub>2</sub>-CHCH<sub>3</sub> and CH<sub>2</sub>-CH<sub>2</sub> coupling is hampered by the absence of a transition state for CH<sub>2</sub>-CH<sub>3</sub> coupling on the (010)<sub>0.25</sub> surface. We also calculated barriers for C-CCH<sub>3</sub> and CH-CCH<sub>3</sub> coupling on the (010)<sup>\*</sup><sub>0.25</sub> surface with differences in all cases below 10 kJ/mol. These results imply that we can simply use the barriers obtained for the C<sub>2</sub> formation reactions as input for the C<sub>3+</sub> formation on the (010)<sup>\*</sup><sub>0.25</sub> surface. Carbonaceous species tend to bond slightly stronger, as this surface contains a vacancy on a position where a C atom is present on the (010)<sub>0.25</sub> surface. This may partially remove the beneficial effect of the methyl substituent group on the (010)<sup>\*</sup><sub>0.25</sub> surface. For the (010)<sub>0.25</sub> surface we see a relatively large effect of the methyl substituent on the C<sub>3</sub> formation energy when a C or a CH species is coupled to the growing chain. Coupling a CH<sub>2</sub> species to a CHCH<sub>3</sub> species did not result in a significant difference in the energy barrier when compared to the CH<sub>2</sub>-CH<sub>2</sub> coupling. This relates to the higher degree of hydrogenation of the C<sub>1</sub> and C<sub>2</sub> species,

resulting in stronger steric repulsion. Hence, we can extrapolate the barriers for the H-rich  $\text{CH}_x\text{-C}_n\text{H}_x$  ( $x = 2, 3, n \geq 2$ ) intermediates in  $\text{C}_2$  coupling reactions, whilst making a small correction for the other ( $x = 0, 1, n \geq 2$ )  $\text{C}_{3+}$  formation barriers.

### 4.3.2 Microkinetic modelling

Microkinetics simulations were used to predict the CO consumption rate and product distribution as a function of the reaction temperature. We employed the (100) surface as the most likely surface active in the FT reaction because of its low overall barrier for CO dissociation. The reaction energetics were based on the DFT-computed activation energies and pre-exponential factors discussed in previous sections. The pressure in our simulations was set to 1 bar, the  $\text{H}_2/\text{CO}$  ratio to unity. We explored the FT reaction in the temperature interval 510-545 K. We will present data in the zero-conversion limit as well as using a CSTR model.

#### 4.3.2.1 Microkinetic modelling on the (100) surface

Microkinetics simulations were performed using the DFT-computed energetics for the stepped (100) surface (Tables 4.1-4.5 and Table 3.2 of Chapter 3). Figure 4.4a shows the overall CO conversion rates into hydrocarbon products in the zero-conversion model. The total CO consumption rate increases from  $2.3 \cdot 10^{-3} \text{ s}^{-1}$  at 510 K to  $1.8 \cdot 10^{-2} \text{ s}^{-1}$  at 545 K. These rates are an order of magnitude higher than those reported in an experimental study of Chen et al.[41] For instance, Chen et al. measured experimental rates at 525 K to be in the range of  $1 \cdot 10^{-4} \text{ s}^{-1}$  to  $1 \cdot 10^{-3} \text{ s}^{-1}$  depending on the partial pressures. Our model predicts a CO consumption rate of  $5.8 \cdot 10^{-3} \text{ s}^{-1}$ . The difference can be due to the presence of other less reactive surface facets than the (100) facet on  $\chi$ -Fe-carbide particles. Moreover, we have to take into account the accuracy of DFT-computed activation barriers ( $\pm 10 \text{ kJ/mol}$ ). Another difference with experimental data is the dominance of olefins among the hydrocarbon reaction products in the simulations. The olefins-to-paraffins ratios (Appendix B.1) are several orders of magnitude higher than experimentally observed ratios in the range 1-10 considering hydrocarbons with 2 and 3 carbon atoms, respectively. In our simulations, we did not consider re-adsorption and hydrogenation of olefins. Thus, the different product distributions can be due to the fact that the simulations represent the case of zero conversion, which implies that we predict the formation of olefins to be preferred to that of paraffins. The C-based selectivity towards  $\text{C}_2\text{-C}_4$  species increases from 52.5% at 510 K to 58.9% at 545 K (Figure 4.4b), which is accompanied by

a decrease of the  $C_{5+}$  selectivity. The  $CH_4$  selectivity slightly decreases with increasing temperature. We can explain this behaviour by a decreased chain-growth probability due to an increased rate of hydrogenation to products as well as an increased rate of C-C coupling reactions, which should be relatively difficult on iron surfaces.[31] At 525 K, the  $CH_4$  selectivity is 21%, which is slightly lower than the experimental value of 26.5%. Oxygen removal reactions proceed primarily via the formation of  $H_2O$  (99.4% at 525 K) instead of  $CO_2$  (0.6% at 525 K; Figure 4.4c). The low  $CO_2$  selectivity ( $< 1\%$ ) is in good agreement with the experimentally determined selectivity of  $\chi$ -Fe-carbide at low conversion.

Figure 4.4d shows the Anderson-Schulz-Flory (ASF) distribution at three different temperatures, considering hydrocarbon products with 1-20 carbon atoms, within the chosen temperature range. At each temperature, we determined the corresponding chain-growth probability ( $\alpha$ ) based on the slope of the ASF distribution. These chain-growth probabilities are plotted in Figure 4.4e, which also included the reaction orders with respect to CO and  $H_2$  between 510 K and 545 K. The chain-growth probability decreases from 0.52 to 0.48 with increasing temperature. The predicted chain-growth probability at 525 K corresponds well to the experimental value of 0.5 reported by Chen et al. The simulations also predict the lower than expected  $C_2$  selectivity in the ASF distribution, which is typically observed for Co [42, 43] and Fe [44, 45] FT catalysts. The reaction network (Figure 4.5a) shows that ethylene is formed via hydrogenation of CHCH ( $CHCH \rightarrow CHCH_2 \rightarrow CH_2CH_2$ ), whereas CHCH is also involved (indirectly) in the coupling to CH-CCH<sub>3</sub>. ( $CHCH \rightarrow CCH \rightarrow CCH_2 \rightarrow CCH_3 \rightarrow CHCCH_3$ ) As the dehydrogenation rate of CHCH is higher than the hydrogenation rate of  $CHCH_2$ , more  $C_3$  is produced than  $C_2$ . The reaction order in CO is negative (-0.10 at 525 K) and compares reasonably well with the reaction order from experiments (-0.06) while it does not vary much with temperature. This indicates that the overall rate for CO consumption will decrease with an increase of the CO partial pressure. Experimentally, a reaction order of -0.05 was found at 525 K, indicating a lower dependence on the CO partial pressure. The value of -0.10 is higher than in the zero-conversion simulations, which might be explained by the relatively difficult removal of oxygen, leading to a higher O coverage. The reaction order in  $H_2$  is positive ( $\sim 0.21$  at 525 K) and is lower than the experimental value (close to 0.9). A possible explanation is that the lateral interactions on H assumed in the model are not entirely accurate. Another possible explanation can be sought in the hydrogenation of C atoms belonging to the Fe-carbide surface. Under experimental conditions, some of those C atoms might be hydrogenated, leading to the formation of additional  $CH_4$ . The rate-limiting step in  $CH_4$  formation is often the final hydrogenation step, as is the case on the (100) surface (see Figure 4.5b), leading to a higher order in  $H_2$ . However, the empty (100) surface does

not have any surface C atoms, which might explain the lower order in  $H_2$  compared to the experimental values.

The composition of the adsorbed layer is given in Figure 4.4f. CO is the most abundant surface species (0.38 ML) and its coverage does not vary significantly with temperature. The H coverage decreases slightly from 0.24 ML to 0.21 ML over the temperature as observed above. The fraction of empty sites increases from 0.18 ML to 0.20 ML and the O coverage increases by 0.01 ML. The surface coverage for the other surface species remains roughly the same. At 525 K, approximately 19% of the surface is covered by O species (17% O and 2% OH, respectively), indicating the presence of a substantial amount of O on the surface.

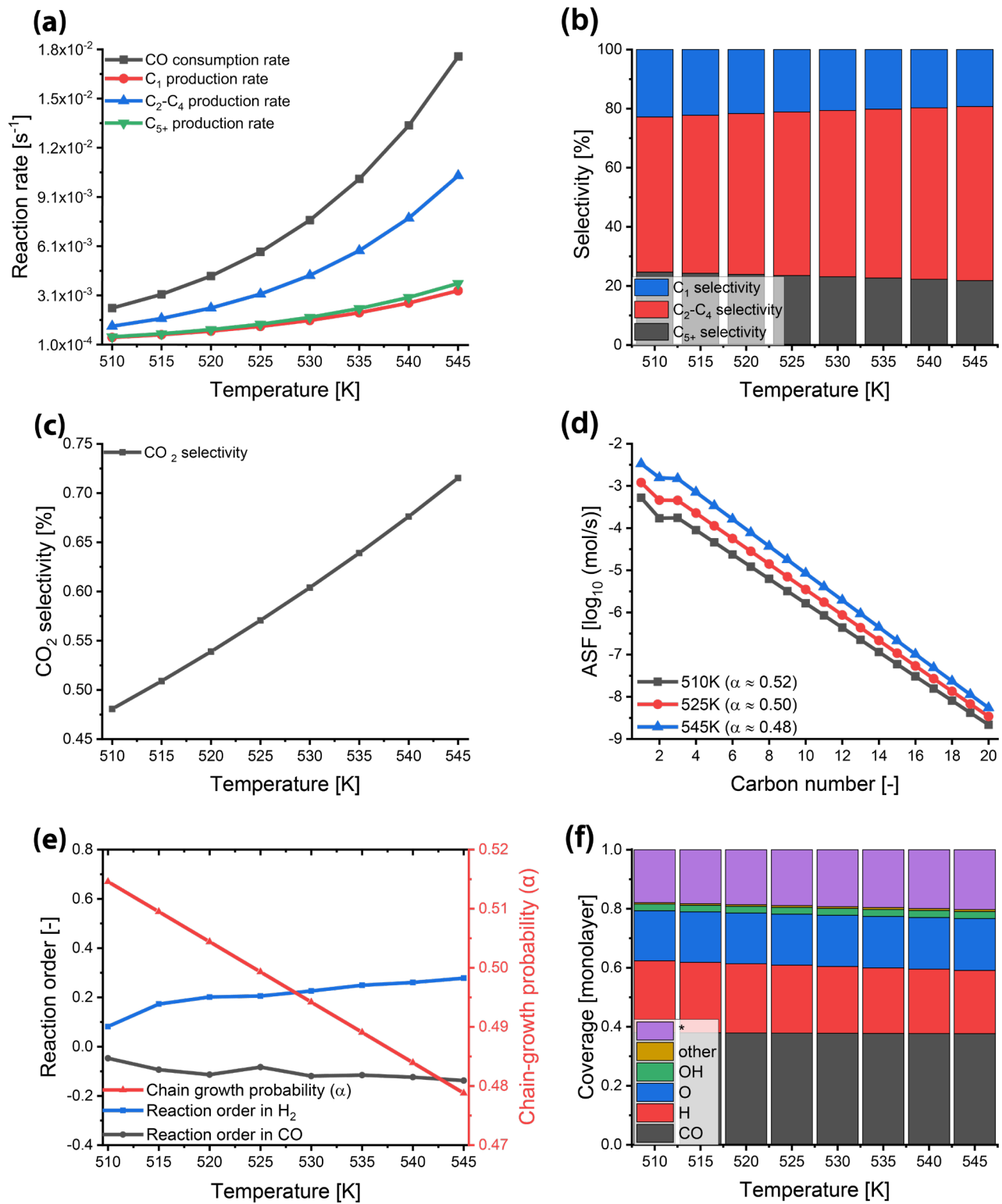


**Figure 4.4:** Microkinetics simulations of the FT reaction on the  $\text{Fe}_5\text{C}_2$ -(100) surface between 510 K and 545 K at 1 bar in the zero-conversion limit. (a) Reaction rate for the  $\text{C}_1$  species (red),  $\text{C}_2\text{-C}_4$  species (blue),  $\text{C}_{5+}$  species (green) and the CO consumption rate (dark grey). (b) Selectivities as a function of the temperature on the (100) surface for  $\text{C}_1$  species (blue bar),  $\text{C}_2\text{-C}_4$  species (red bar) and  $\text{C}_{5+}$  species (dark grey bar). (c)  $\text{CO}_2$  selectivity. (d) ASF distribution at 510 K (dark grey), 525 K (red) and 545 K (blue). (e) Reaction order in CO (dark grey) and  $\text{H}_2$  (blue) and chain-growth probability (red). (f) Surface coverages.

We also determined the relative rates of the elementary reaction steps in the reaction network. For clarification reasons, a simplified network diagram including the rates of the individual reaction steps is shown in Figure 4.5a. A complete network diagram is shown in Appendix B.2. The reaction network shows that H<sub>2</sub>O formation proceeds primarily via OH disproportionation, the rate of H<sub>2</sub>O formation in this way being more than two times higher than that of direct OH hydrogenation. Chain-growth proceeds primarily *via* CH-CH coupling, as also predicted for Ru[31] and Rh.[46] CCH formation species also proceeds *via* C-CH coupling and is further hydrogenated to the CCH<sub>3</sub> species. CCH<sub>3</sub> is either coupled to a C or a CH species, resulting in CCCH<sub>3</sub> and CHCCH<sub>3</sub>, respectively. The latter species can then either be dehydrogenated to CCCH<sub>3</sub> or hydrogenated to form C<sub>3</sub> olefin or paraffin. There is no preference in the sequence of hydrogenation steps for the CHCCH<sub>3</sub> species because the relative rate for C<sub>α</sub> hydrogenation followed by C<sub>β</sub> hydrogenation is identical to the relative rate for C<sub>β</sub> hydrogenation followed by C<sub>α</sub> hydrogenation. C<sub>4+</sub> formation occurs by hydrogenation of CC(CH<sub>2</sub>)<sub>n</sub>CH<sub>3</sub> (where  $0 \leq n \leq 16$ ) to CCH<sub>2</sub>(CH<sub>2</sub>)<sub>n</sub>CH<sub>3</sub>, followed by a CH-CCH<sub>2</sub>(CH<sub>2</sub>)<sub>n</sub>CH<sub>3</sub> coupling, which is the equivalent of CH-CH coupling.

The results of DRC and DCGC analyses are shown in Figure 4.5b and 4.5c, respectively. The DRC analysis for the simulations at 525 K shows that direct CO dissociation is the dominant rate-controlling step, followed by the removal of OH. CO dissociation becomes less controlling with increasing temperature, while the contribution of OH removal to the DRC increases. Consistent with the finding that both direct OH hydrogenation and OH disproportionation contribute to H<sub>2</sub>O formation, we observe that both steps are rate-controlling to some extent. The higher DRC value for OH disproportionation corresponds to the higher relative rate, which is consistent with the relative rates (*vide supra*). From the DCGC analysis, we conclude that chain-growth is mainly controlled by direct CO dissociation because this step generates the monomeric species needed in the coupling reactions. The contribution of O removal steps to DCGC can be explained by the formation of empty sites in this reaction step, which are needed for CO dissociation. The DCGC is mainly inhibited by hydrogenation of CHC(CH<sub>2</sub>)<sub>n</sub>CH<sub>3</sub> as this reaction terminates chain-growth. A similar effect, although smaller, is observed for CH<sub>3</sub> and CHCH hydrogenation.

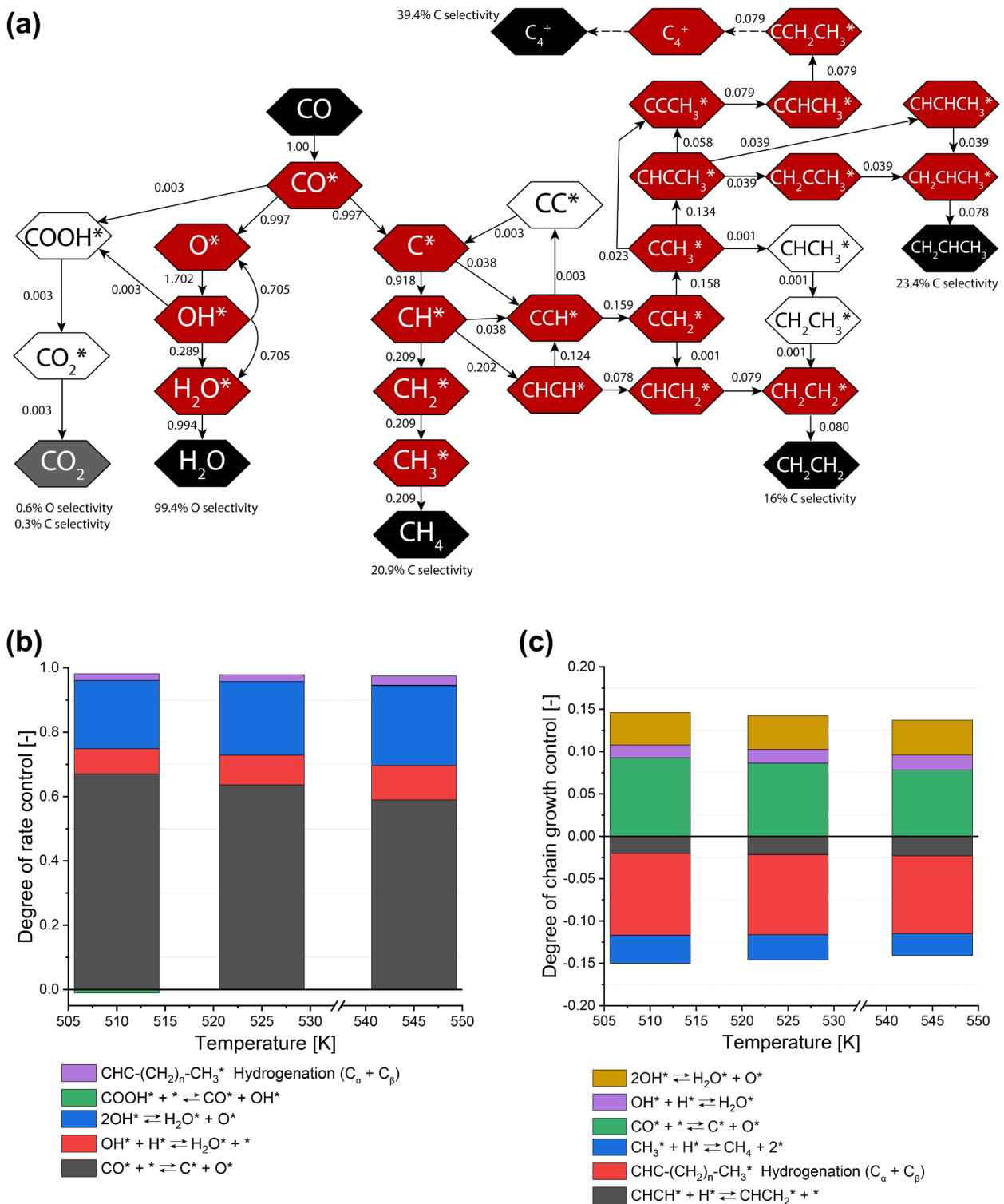


**Figure 4.5:** (a) Reaction network analysis at 525 K and 1 bar at the zero-conversion limit. The red hexagons represent the major intermediate species, the black hexagons represent the major gaseous components, the grey hexagons represent the minor gaseous components and the white hexagons represent minor intermediate species. The remainder of the intermediate species and products are omitted as their values were lower than the limit ( $10^{-4}$ ) relative to the flux of CO adsorption. (b) DRC analysis at 510 K, 525 K and 545 K. (c) DCGC analysis at 510 K, 525 K and 545 K.



### 4.3.2.2 Microkinetic modelling in a CSTR

We integrated the microkinetic model in a CSTR model to describe the effect of a non-zero conversion on the simulation kinetics. Amongst others, this provides insight into the influence of re-adsorption of reactant products on the catalyst surface. We kept all model parameters the same as the zero-conversion microkinetics simulations. The residence time of the CSTR was chosen so that the CO conversion was below 15% in the explored temperature range. Olefin re-adsorption was also taken into account. The main results of these simulations are shown in Figure 4.6.

The data for the zero-conversion and the CSTR model (see Figure 4.6 and Appendix B3) are very similar in terms of reaction rates, product distribution, chain-growth probability, reaction orders and surface coverages. Nevertheless, the olefins-to-paraffins ratio for  $C_2$  species, which is  $\sim 10^5$  in the zero-conversion limit, is lower than  $10^3$  at a finite conversion. This shows that re-adsorption of  $C_2$  species has a significant contribution to the formation of paraffins. The difference in olefins-to-paraffins ratios for  $C_{3+}$  species is significantly smaller. The much lower olefins-to-paraffins ratio observed in the experiment then suggests that olefins re-adsorption and hydrogenation to paraffins likely occurs on different sites such as planar sites, which typically bind these olefins weaker. Finally, we note that the  $CO_2$  selectivity at finite conversion is almost the same as in the zero conversion limit. This suggests that formation of secondary  $CO_2$  through reactions of CO with product  $H_2O$  does not take place at this surface. It is likely that other surface terminations are involved in the formation of extra  $CO_2$  with increasing conversion, which is a distinct feature of Fe-based catalysts.

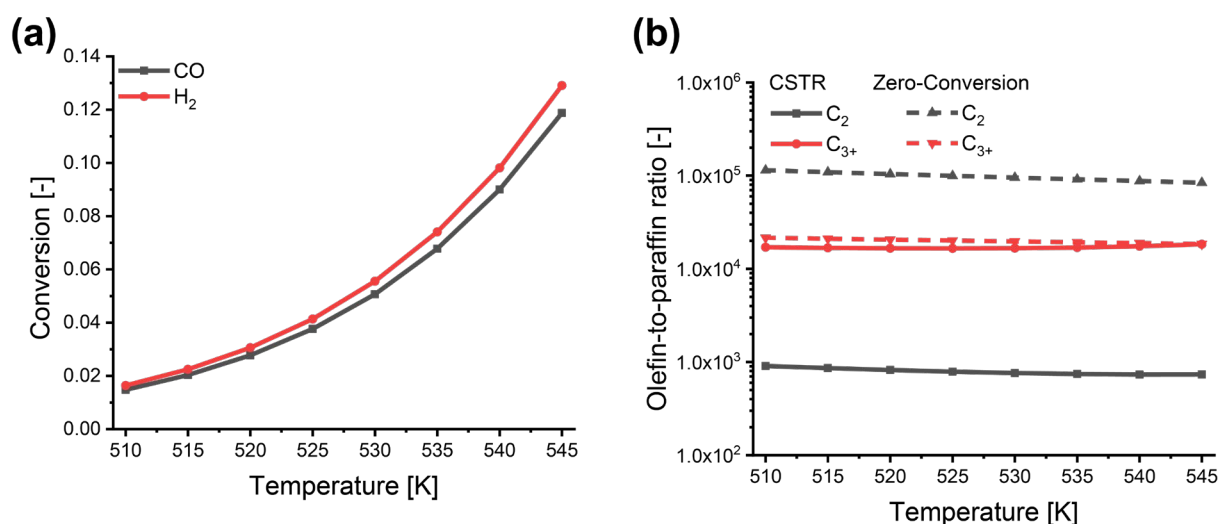


**Figure 4.6:** (a) CO (dark grey) and H<sub>2</sub> (red) conversion as a function of the temperature at 1 bar. (b) Olefin-to-paraffin ratio for  $C_2$  species (dark grey) and  $C_{3+}$  species (red). The solid lines indicate the olefin-to-paraffin ratios from the CSTR model, while the dashed lines show the olefin-to-paraffin ratios in the zero-conversion limit.

#### 4.4. Conclusions

We explored the FT reaction on  $\chi$ -Fe<sub>5</sub>C<sub>2</sub> by a combination of DFT calculations and microkinetic modelling. We chose the planar (010)<sub>0.25</sub> and the corrugated (100) surface to describe the reactions on the terrace and step-edge sites. DFT showed that oxygen removal has the lowest barriers to H<sub>2</sub>O, while CO<sub>2</sub> formation exhibits the lowest barriers for formation on the (010)<sub>0.25</sub> surface. C-C coupling proceeds easiest through C-CH coupling on the (100) surface, while CH-CH coupling has the lowest barrier on the (010)<sub>0.25</sub> surface. Microkinetic modelling was performed for the (100) surface in the zero-conversion limit and at finite conversion in a CSTR model. There are no substantial differences between both models except for the re-adsorption and hydrogenation of olefins, which significantly lowers the olefins-to-paraffins ratio. The chosen surface has an intermediate chain-growth probability of 0.5 (525 K, 1 bar, H<sub>2</sub>/CO = 1), meaning that C<sub>2</sub>-C<sub>4</sub> olefins are the main reaction products. With increasing temperature, the lower-olefins selectivity increases at the expense of the C<sub>5</sub>+ selectivity. H<sub>2</sub>O is the main O removal product, suggesting that this carbide phase does not make primary CO<sub>2</sub>. Both OH+OH disproportionation and direct OH hydrogenation contribute to H<sub>2</sub>O formation. CH-CH coupling is the preferred pathway for C<sub>2</sub> formation. CHCH is either hydrogenated further to CH<sub>2</sub>CH<sub>2</sub> or dehydrogenated to CCH. C<sub>3</sub> formation proceeds by hydrogenation CCH to CCH<sub>3</sub> and CH insertion to CHCCH<sub>3</sub>. Higher hydrocarbon chains are produced by CH insertion into the C(CH<sub>2</sub>)<sub>n</sub>CH<sub>3</sub> species. Chain termination proceeds by hydrogenation of CHC(CH<sub>2</sub>)<sub>n</sub>CH<sub>3</sub> species. The reaction rate is predominantly limited by CO dissociation, followed by O removal reactions. Chain-growth is limited by CO dissociation, while hydrogenation of CHC(CH<sub>2</sub>)<sub>n</sub>CH<sub>3</sub> species inhibits chain-growth.

## References

- [1] M.E. Dry, A.P. Steynberg, Commercial FT process applications, *Studies in Surface Science and Catalysis* 152 (2004) 406-481.
- [2] M.E. Dry, The fischer-tropsch synthesis, *Catalysis science and technology* 1 (1981) 159-255.
- [3] E. de Smit, F. Cinquini, A.M. Beale, O.V. Safonova, W. van Beek, P. Sautet, B.M. Weckhuysen, Stability and Reactivity of  $\epsilon$ - $\chi$ - $\theta$  Iron Carbide Catalyst Phases in Fischer–Tropsch Synthesis: Controlling  $\mu$ C, *Journal of the American Chemical Society* 132 (2010) 14928-14941.
- [4] J. Cheng, P. Hu, P. Ellis, S. French, G. Kelly, M.C. Lok, Density functional theory study of iron and cobalt carbides for Fischer–Tropsch synthesis, *The Journal of Physical Chemistry C* 114 (2009) 1085-1093.
- [5] A. Govender, D. Curulla Ferré, J.W. Niemantsverdriet, A density functional theory study on the effect of zero-point energy corrections on the methanation profile on Fe (100), *ChemPhysChem* 13 (2012) 1591-1596.
- [6] M. Ojeda, R. Nabar, A.U. Nilekar, A. Ishikawa, M. Mavrikakis, E. Iglesia, CO activation pathways and the mechanism of Fischer–Tropsch synthesis, *Journal of Catalysis* 272 (2010) 287-297.
- [7] D.C. Sorescu, First-principles calculations of the adsorption and hydrogenation reactions of CH<sub>x</sub> (x= 0, 4) species on a Fe (100) surface, *Physical Review B* 73 (2006) 155420.
- [8] D.-B. Cao, Y.-W. Li, J. Wang, H. Jiao, Chain growth mechanism of Fischer–Tropsch synthesis on Fe<sub>5</sub>C<sub>2</sub> (001), *Journal of Molecular Catalysis A: Chemical* 346 (2011) 55-69.
- [9] J.M. Gracia, F.F. Prinsloo, J.W. Niemantsverdriet, Mars-van Krevelen-like mechanism of CO hydrogenation on an iron carbide surface, *Catalysis letters* 133 (2009) 257-261.
- [10] C.-F. Huo, Y.-W. Li, J. Wang, H. Jiao, Insight into CH<sub>4</sub> formation in iron-catalyzed Fischer–Tropsch synthesis, *Journal of the American Chemical Society* 131 (2009) 14713-14721.
- [11] M.O. Ozbek, J.H. Niemantsverdriet, Elementary reactions of CO and H<sub>2</sub> on C-terminated  $\chi$ -Fe<sub>5</sub>C<sub>2</sub> (001) surfaces, *Journal of Catalysis* 317 (2014) 158-166.
- [12] M.O. Ozbek, J.W. Niemantsverdriet, Methane, formaldehyde and methanol formation pathways from carbon monoxide and hydrogen on the (001) surface of the iron carbide  $\chi$ -Fe<sub>5</sub>C<sub>2</sub>, *Journal of Catalysis* 325 (2015) 9-18.
- [13] M.A. Petersen, J.-A. van den Berg, W.J. van Rensburg, Role of step sites and surface vacancies in the adsorption and activation of CO on  $\chi$ -Fe<sub>5</sub>C<sub>2</sub> surfaces, *The Journal of Physical Chemistry C* 114 (2010) 7863-7879.
- [14] M.A. Petersen, W.J. van Rensburg, CO Dissociation at Vacancy Sites on Hägg Iron Carbide: Direct Versus Hydrogen-Assisted Routes Investigated with DFT, *Topics in Catalysis* 58 (2015) 665-674.
- [15] T.H. Pham, X. Duan, G. Qian, X. Zhou, D. Chen, CO activation pathways of Fischer–Tropsch synthesis on  $\chi$ -Fe<sub>5</sub>C<sub>2</sub> (510): direct versus hydrogen-assisted CO dissociation, *The Journal of Physical Chemistry C* 118 (2014) 10170-10176.
- [16] D.C. Sorescu, Plane-wave density functional theory investigations of the adsorption and activation of CO on Fe<sub>5</sub>C<sub>2</sub> surfaces, *The Journal of Physical Chemistry C* 113 (2009) 9256-9274.
- [17] J. Cheng, P. Hu, P. Ellis, S. French, G. Kelly, C.M. Lok, An Energy Descriptor To Quantify Methane Selectivity in Fischer–Tropsch Synthesis: A Density Functional Theory Study, *The Journal of Physical Chemistry C* 113 (2009) 8858-8863.
- [18] P.J. Steynberg, J.A. Van den Berg, W.J. van Rensburg, Bulk and surface analysis of Hägg Fe carbide (Fe<sub>5</sub>C<sub>2</sub>): a density functional theory study, *Journal of Physics: Condensed Matter* 20 (2008) 064238.
- [19] G. Kresse, J. Furthmüller, Efficiency of ab-initio total energy calculations for metals and semiconductors using a plane-wave basis set, *Computational materials science* 6 (1996) 15-50.
- [20] G. Kresse, J. Hafner, Ab initio molecular-dynamics simulation of the liquid-metal–amorphous-semiconductor transition in germanium, *Physical Review B* 49 (1994) 14251.
- [21] M.P.A.T. Methfessel, A.T. Paxton, High-precision sampling for Brillouin-zone integration in metals, *Physical Review B* 40 (1989) 3616.
- [22] R.J.P. Broos, B. Zijlstra, I.A.W. Filot, E.J.M. Hensen, Quantum-Chemical DFT Study of Direct and H- and C-Assisted CO Dissociation on the  $\chi$ -Fe<sub>5</sub>C<sub>2</sub> Hägg Carbide, *The Journal of Physical Chemistry C* 122 (2018) 9929-9938.

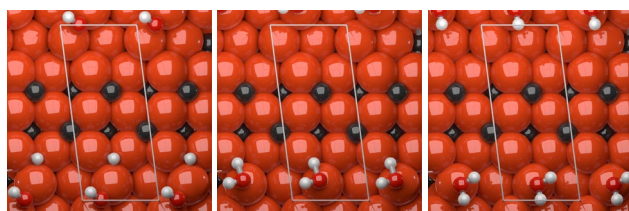
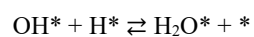
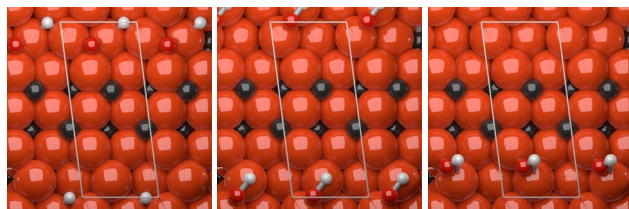
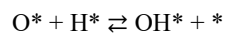
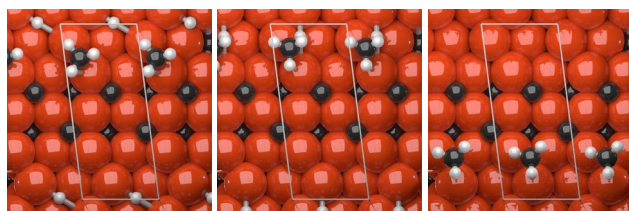
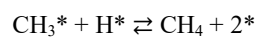
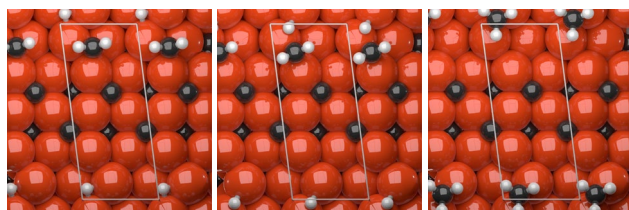
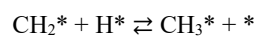
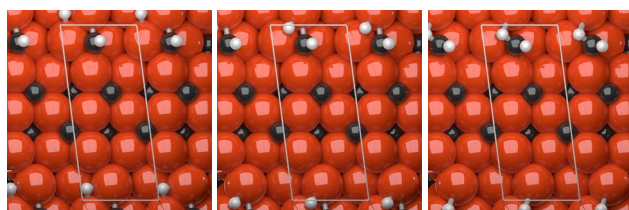
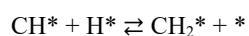
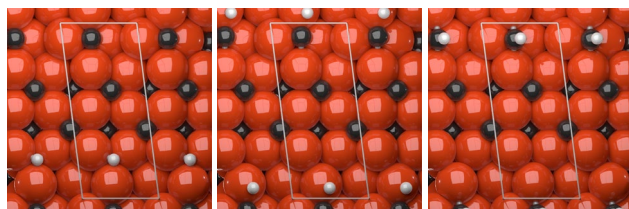
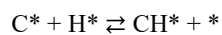
- [23] K.P. Huber, G. Herzberg, NIST Chemistry WebBook, NIST Standard Reference Database Number 69. Eds. PJ Linstrom and WG Mallard. National Institute of Standards and Technology. Gaithersburg MD 20899, webbook. nist. gov (1997).
- [24] G. Henkelman, H. Jónsson, Improved tangent estimate in the nudged elastic band method for finding minimum energy paths and saddle points, *The Journal of chemical physics* 113 (2000) 9978-9985.
- [25] D. Heidrich, W. Quapp, Saddle points of index 2 on potential energy surfaces and their role in theoretical reactivity investigations, *Theoretica chimica acta* 70 (1986) 89-98.
- [26] I.A.W. Filot, Introduction to Microkinetic modeling, Technische Universiteit Eindhoven, Eindhoven, 2018.
- [27] I.A.W. Filot, Introduction to microkinetic modeling, 2 ed., Technische Universiteit Eindhoven, Eindhoven, 2018.
- [28] I.A.W.Z. Filot, B.; Hensen, E. J. M., MKMCXX, a C++ program for constructing microkinetic models, <http://www.mkmcxx.nl>, (2019).
- [29] U.M. Ascher, L.R. Petzold, Computer methods for ordinary differential equations and differential-algebraic equations, Siam, 1998.
- [30] C. Curtiss, J.O. Hirschfelder, Integration of stiff equations, *Proceedings of the National Academy of Sciences of the United States of America* 38 (1952) 235.
- [31] I.A.W. Filot, R.A. van Santen, E.J.M. Hensen, The Optimally Performing Fischer–Tropsch Catalyst, *Angewandte Chemie International Edition* 53 (2014) 12746-12750.
- [32] P. Wang, W. Chen, F.-K. Chiang, A.I. Dugulan, Y. Song, R. Pestman, K. Zhang, J. Yao, B. Feng, P. Miao, W. Xu, E.J.M. Hensen, Synthesis of stable and low-CO<sub>2</sub> selective  $\epsilon$ -iron carbide Fischer–Tropsch catalysts, *Science Advances* 4 (2018) eaau2947.
- [33] P. van Helden, J.-A. van den Berg, M.A. Petersen, W.J. van Rensburg, I.M. Ciobîcă, J. van de Loosdrecht, Computational investigation of the kinetics and mechanism of the initial steps of the Fischer–Tropsch synthesis on cobalt, *Faraday discussions* 197 (2017) 117-151.
- [34] B. Zijlstra, R.J.P. Broos, W. Chen, I.A.W. Filot, E.J.M. Hensen, First-principles based microkinetic modeling of transient kinetics of CO hydrogenation on cobalt catalysts, *Catalysis Today* (2019).
- [35] M. Chase Jr, J. Curnutt, J. Downey Jr, R. McDonald, A. Syverud, E. Valenzuela, JANAF thermochemical tables, 1982 supplement, *Journal of Physical and Chemical Reference Data* 11 (1982) 695-940.
- [36] C.H. Shomate, A method for evaluating and correlating thermodynamic data, *The Journal of Physical Chemistry* 58 (1954) 368-372.
- [37] C.A. Wolcott, A.J. Medford, F. Studt, C.T. Campbell, Degree of rate control approach to computational catalyst screening, *Journal of Catalysis* 330 (2015) 197-207.
- [38] I.A.W. Filot, B. Zijlstra, R.J.P. Broos, W. Chen, R. Pestman, E.J.M. Hensen, Kinetic aspects of chain growth in Fischer–Tropsch synthesis, *Faraday Discussions* 197 (2017) 153-164.
- [39] C.A. Tolman, Steric effects of phosphorus ligands in organometallic chemistry and homogeneous catalysis, *Chemical Reviews* 77 (1977) 313-348.
- [40] I. Filot, R. van Santen, E. Hensen, Quantum chemistry of the Fischer–Tropsch reaction catalysed by a stepped ruthenium surface, *Catalysis Science & Technology* 4 (2014) 3129-3140.
- [41] W. Chen, J. Chai, P. Wang, E.J.M. Hensen, Unpublished results.
- [42] P. Chaumette, C. Verdon, P. Boucot, Influence of the hydrocarbons distribution on the heat produced during Fischer–Tropsch synthesis, *Topics in Catalysis* 2 (1995) 301-311.
- [43] E.W. Kuipers, C. Scheper, J.H. Wilson, I.H. Vinkenburg, H. Oosterbeek, Non-ASF Product Distributions Due to Secondary Reactions during Fischer–Tropsch Synthesis, *Journal of Catalysis* 158 (1996) 288-300.
- [44] N. Egiebor, W. Cooper, B. Wojciechowski, Carbon number distribution of fischer–Tropsch CO-hydrogenation products from precipitated iron catalysts, *The Canadian Journal of Chemical Engineering* 63 (1985) 826-834.
- [45] N. Rice, C. Hsu, B. Wojciechowski, The effects of catalyst surface heterogeneity on the fischer–Tropsch synthesis, *The Canadian Journal of Chemical Engineering* 66 (1988) 694-696.
- [46] J. Cheng, P. Hu, P. Ellis, S. French, G. Kelly, C.M. Lok, Chain Growth Mechanism in Fischer–Tropsch Synthesis: A DFT Study of C–C Coupling over Ru, Fe, Rh, and Re Surfaces, *The Journal of Physical Chemistry C* 112 (2008) 6082-6086.



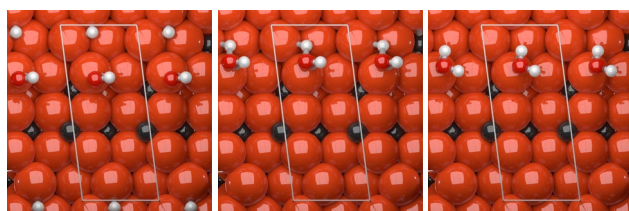
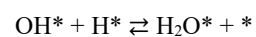
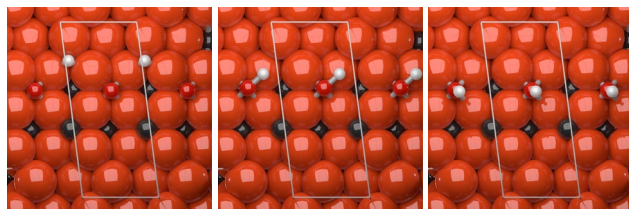
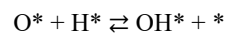
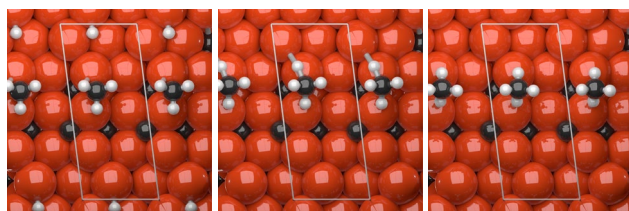
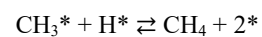
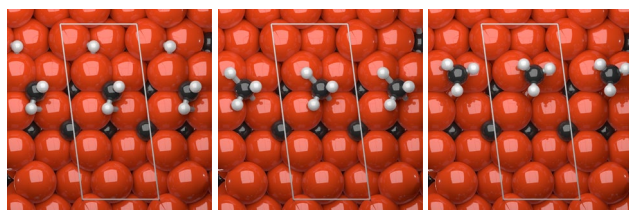
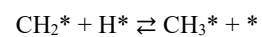
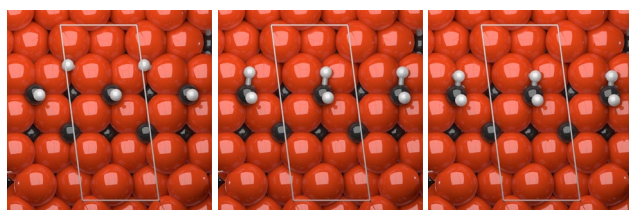
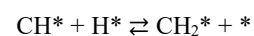
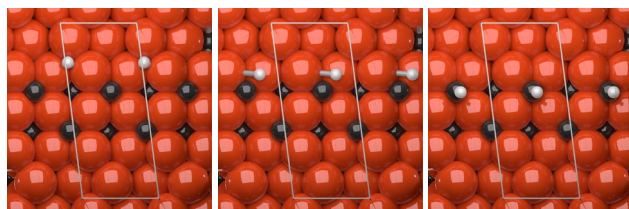
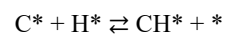
# Appendix B

## Appendix B.1 Geometries from DFT

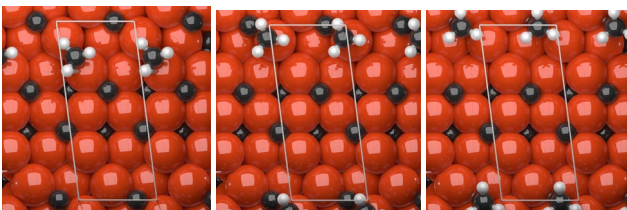
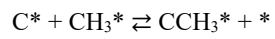
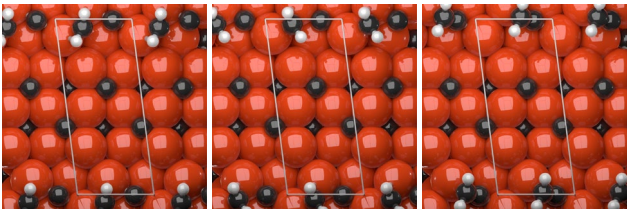
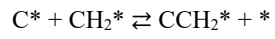
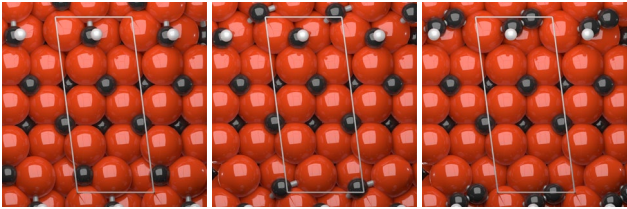
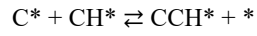
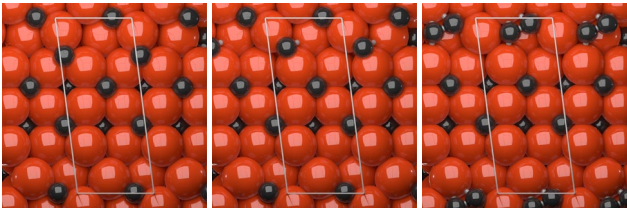
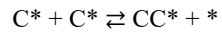
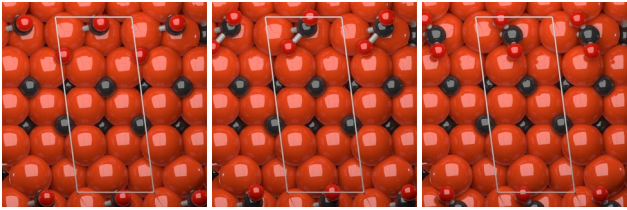
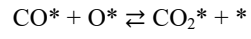
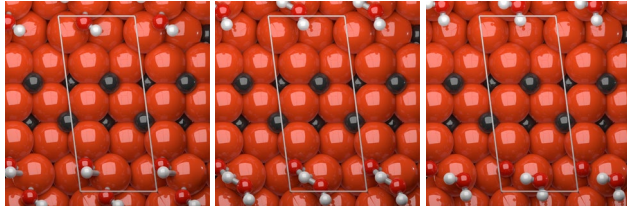
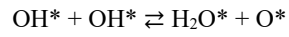
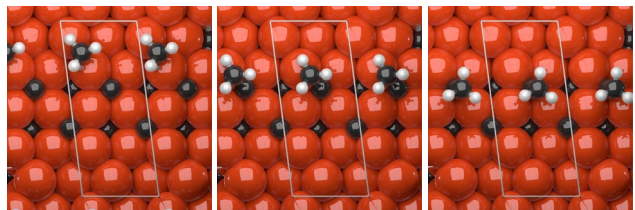
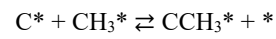
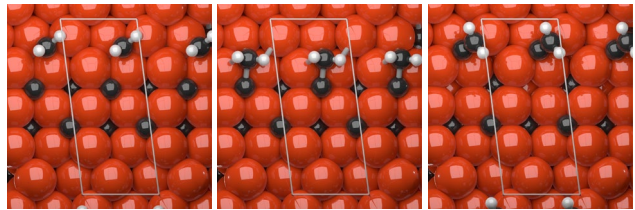
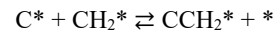
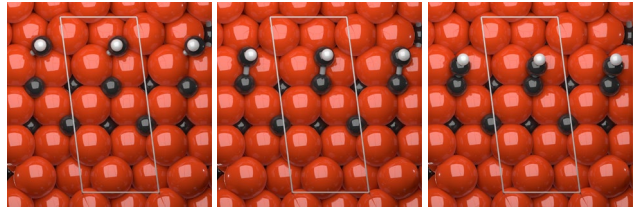
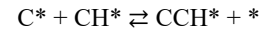
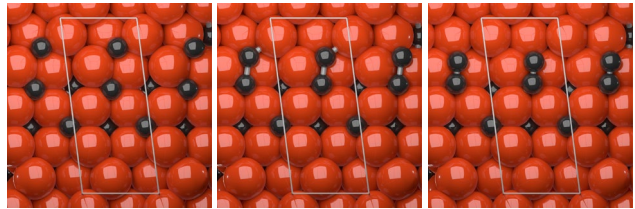
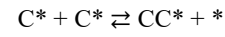
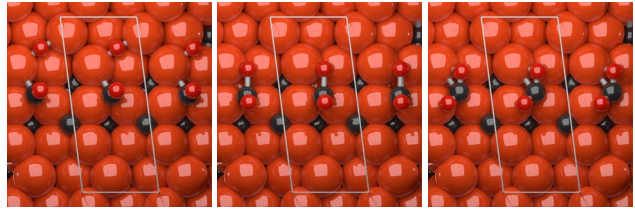
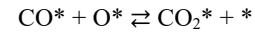
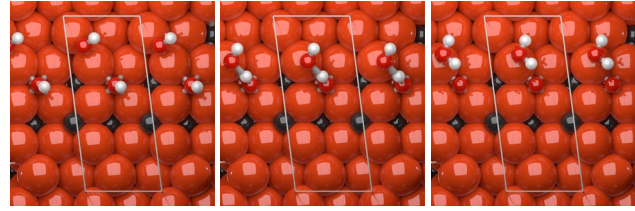
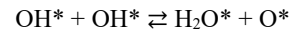
(010)<sub>0.25</sub>  $\chi$ -Fe<sub>5</sub>C<sub>2</sub>



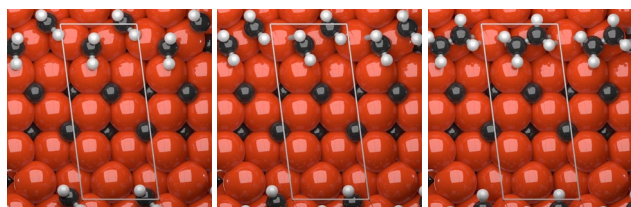
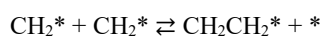
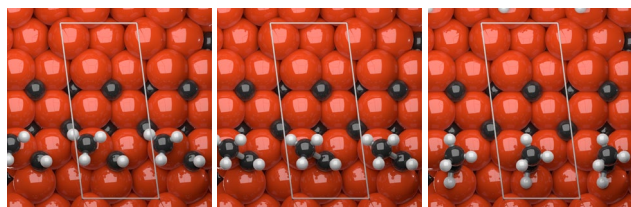
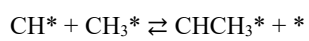
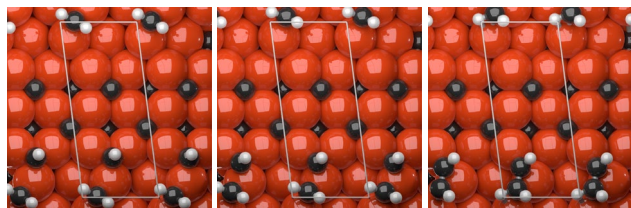
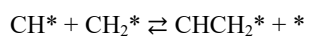
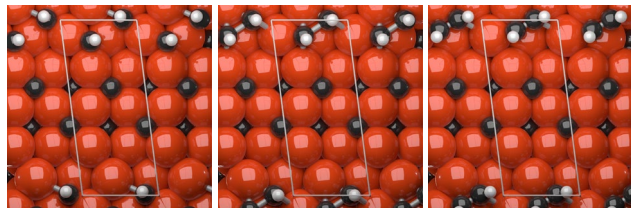
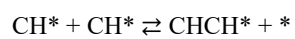
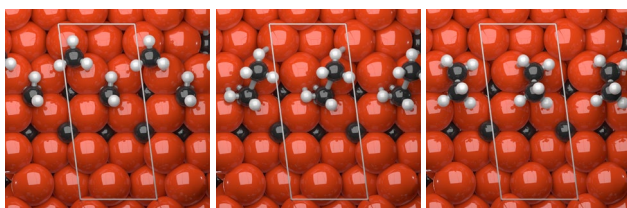
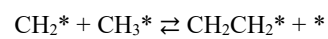
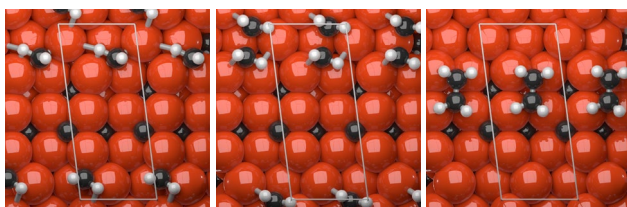
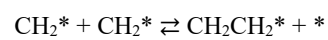
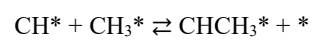
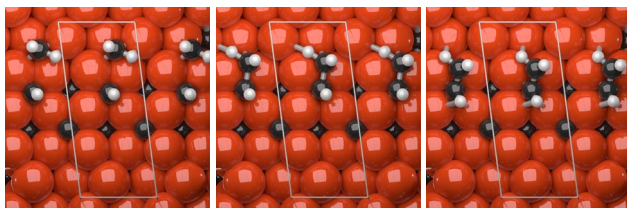
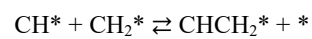
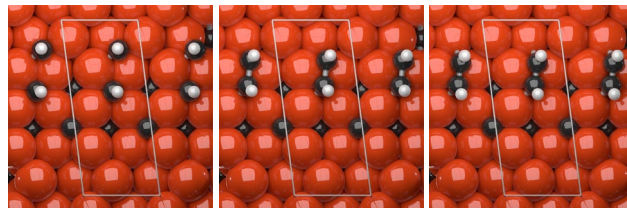
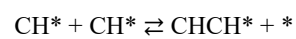
(010)\*<sub>0.25</sub>  $\chi$ -Fe<sub>5</sub>C<sub>2</sub>



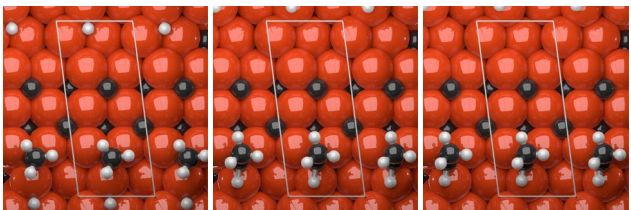
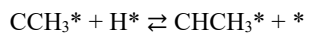
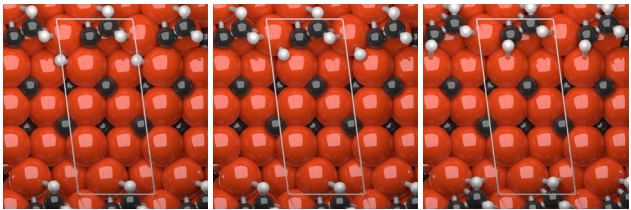
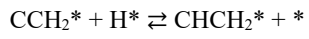
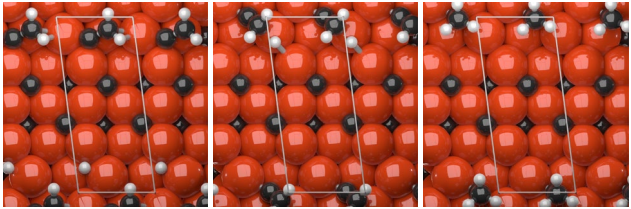
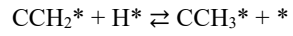
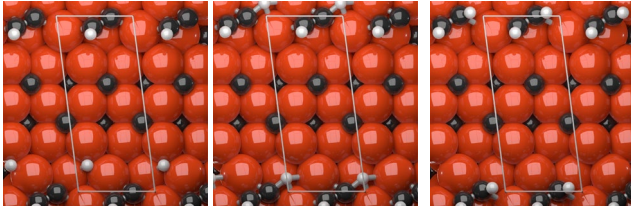
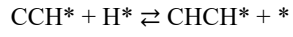
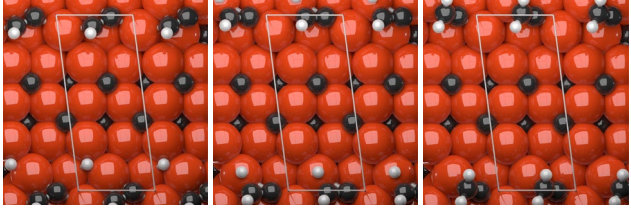
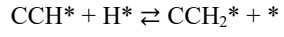
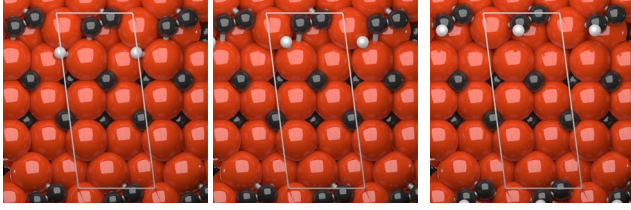
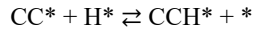
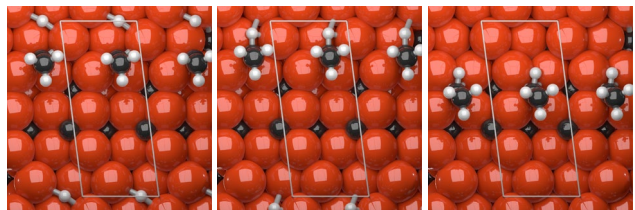
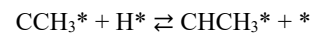
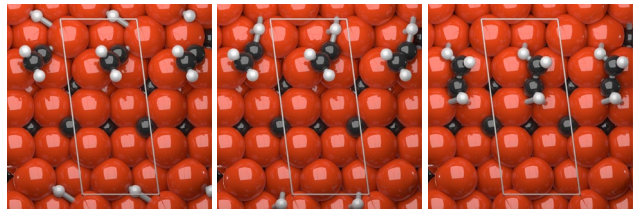
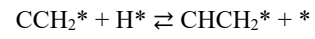
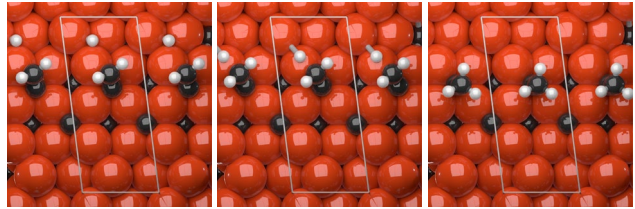
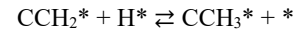
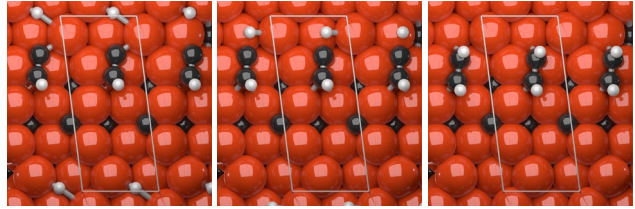
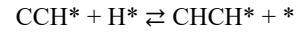
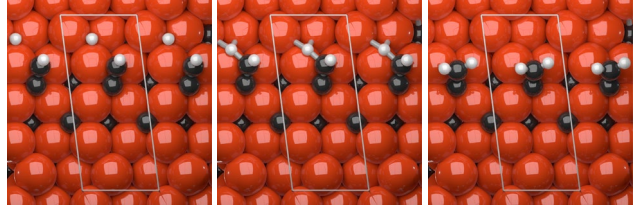
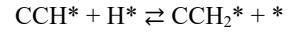
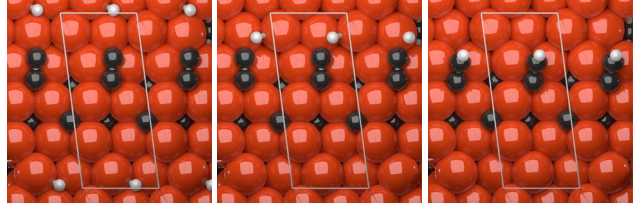
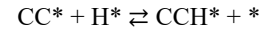


$(010)_{0.25} \chi\text{-Fe}_5\text{C}_2$  $(010)^*_{0.25} \chi\text{-Fe}_5\text{C}_2$ 

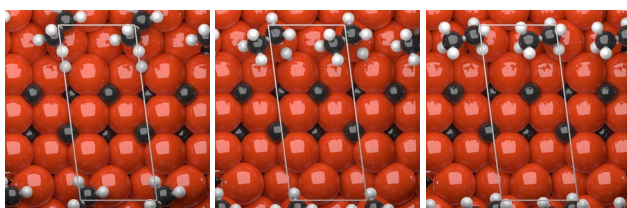
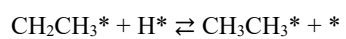
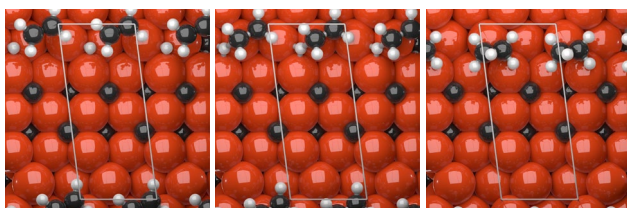
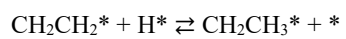
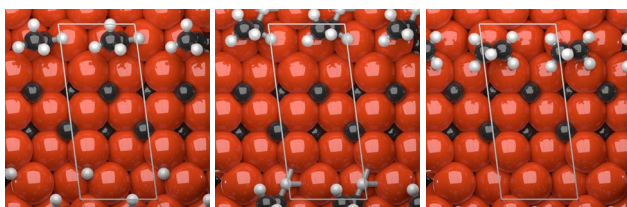
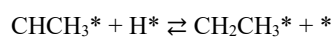
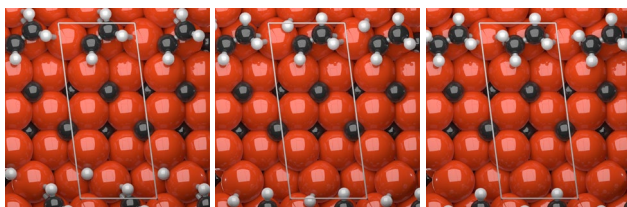
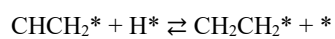
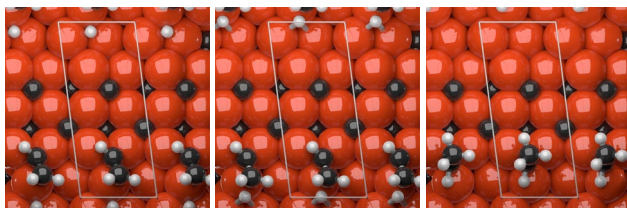
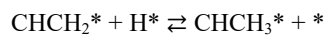
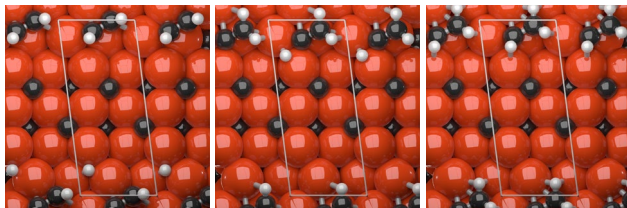
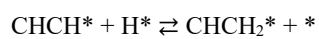
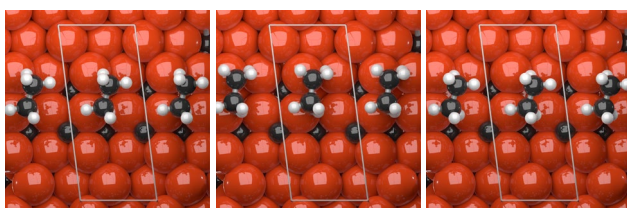
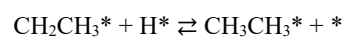
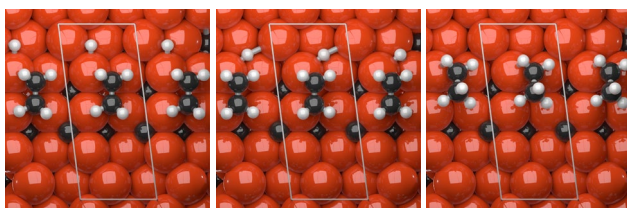
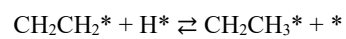
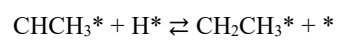
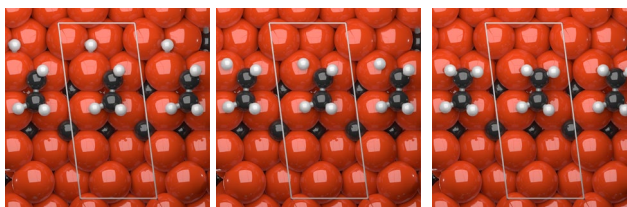
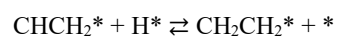
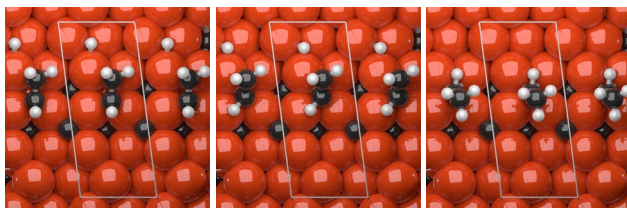
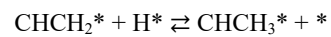
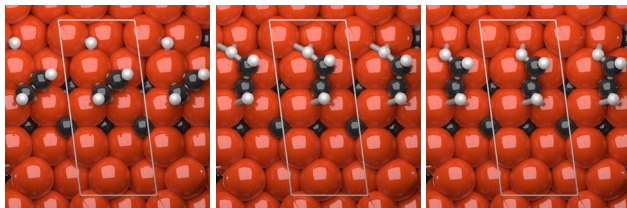
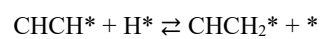


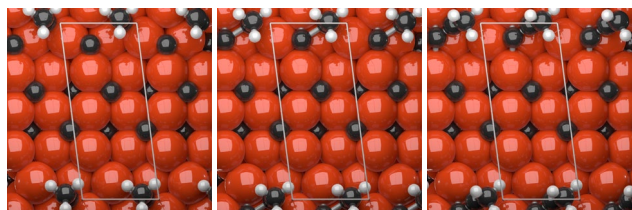
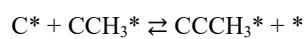
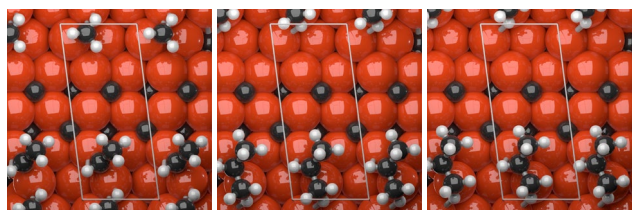
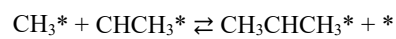
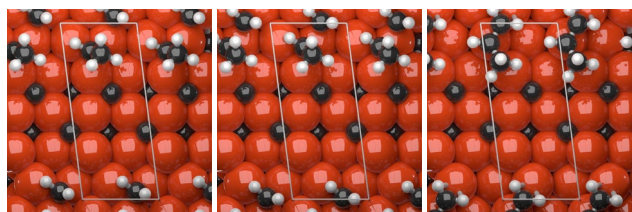
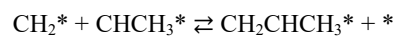
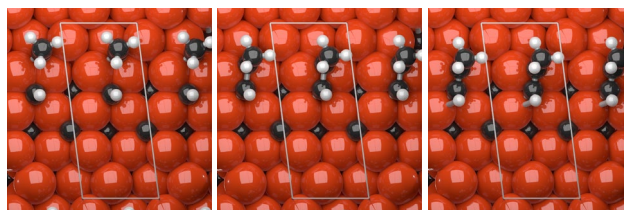
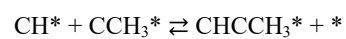
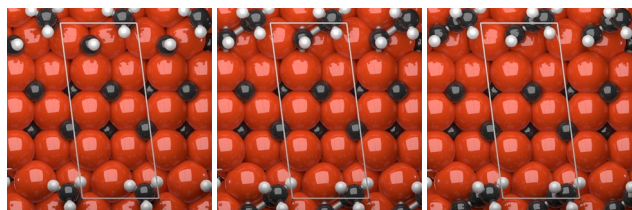
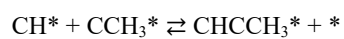
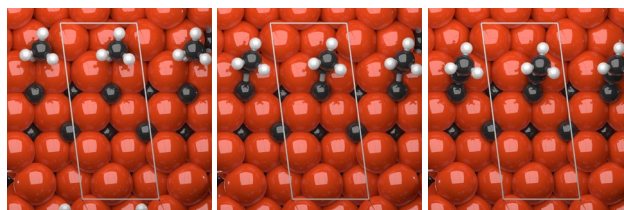
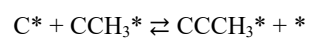
$(010)_{0.25} \chi\text{-Fe}_5\text{C}_2$  $(010)^*_{0.25} \chi\text{-Fe}_5\text{C}_2$ 



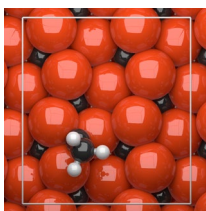
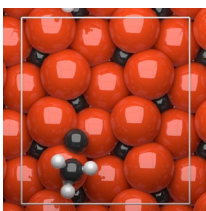
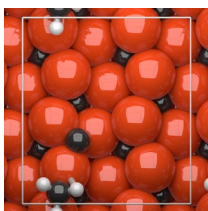
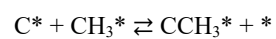
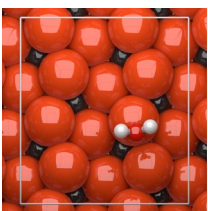
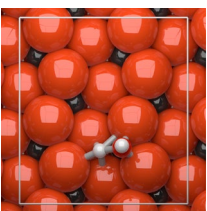
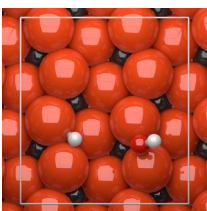
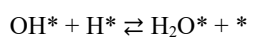
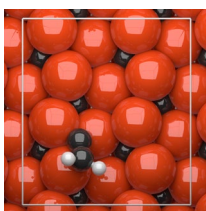
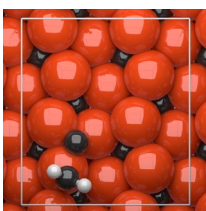
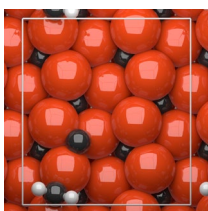
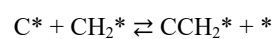
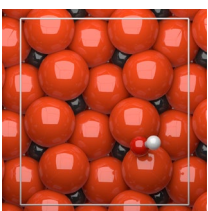
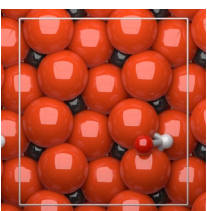
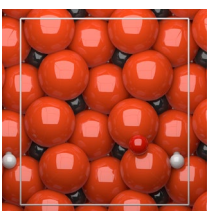
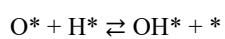
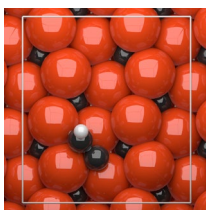
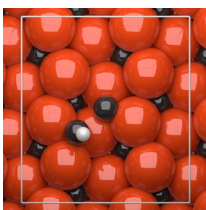
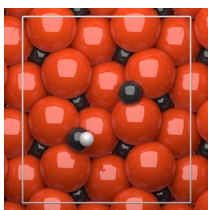
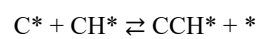
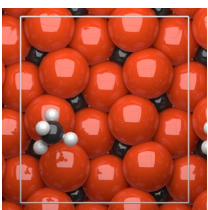
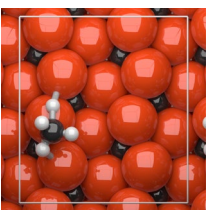
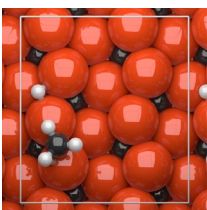
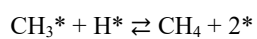
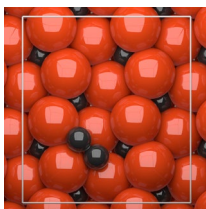
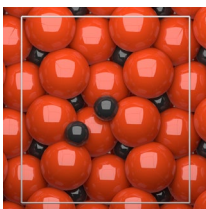
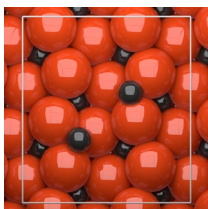
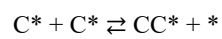
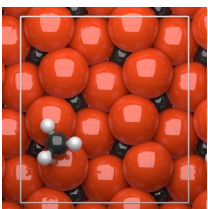
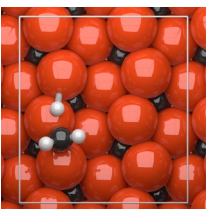
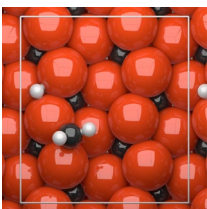
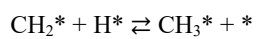
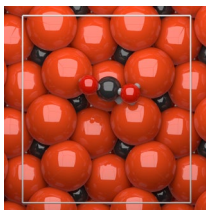
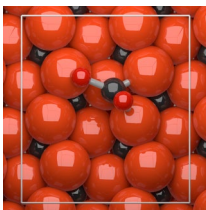
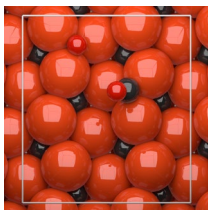
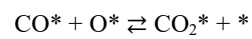
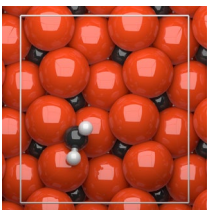
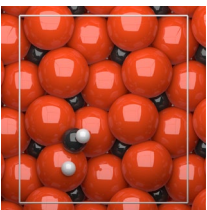
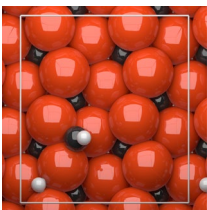
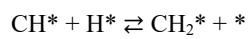
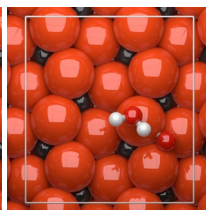
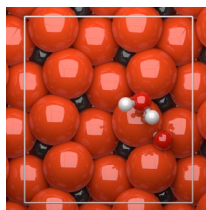
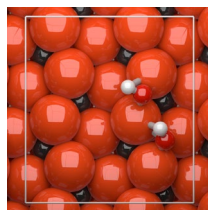
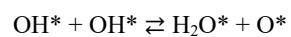
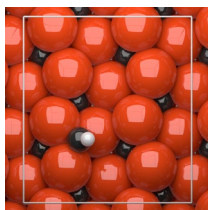
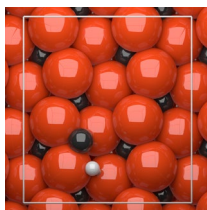
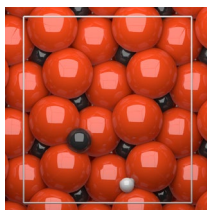
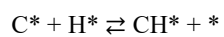
$(010)_{0.25} \chi\text{-Fe}_5\text{C}_2$  $(010)^*_{0.25} \chi\text{-Fe}_5\text{C}_2$ 



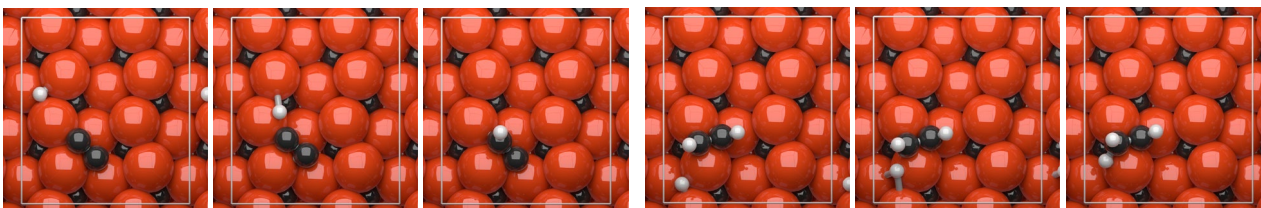
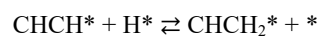
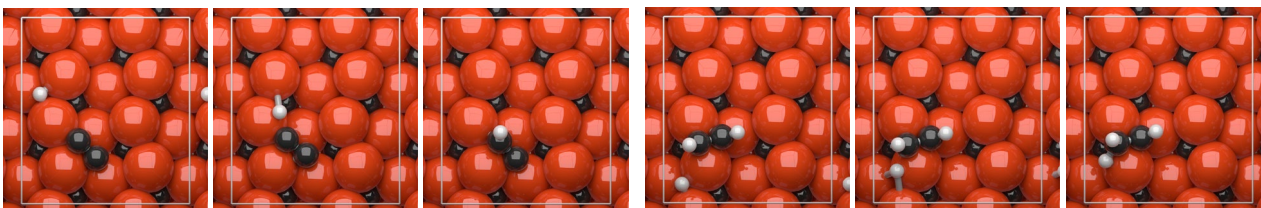
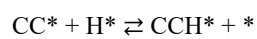
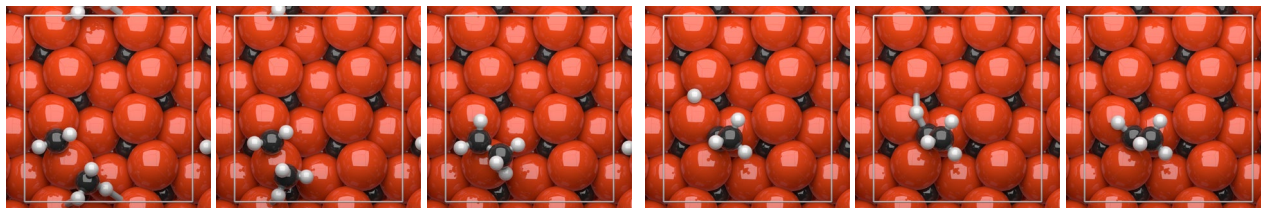
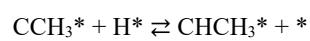
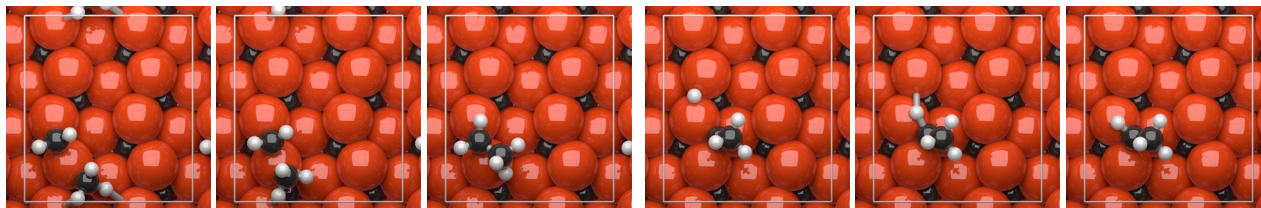
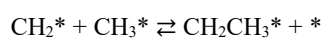
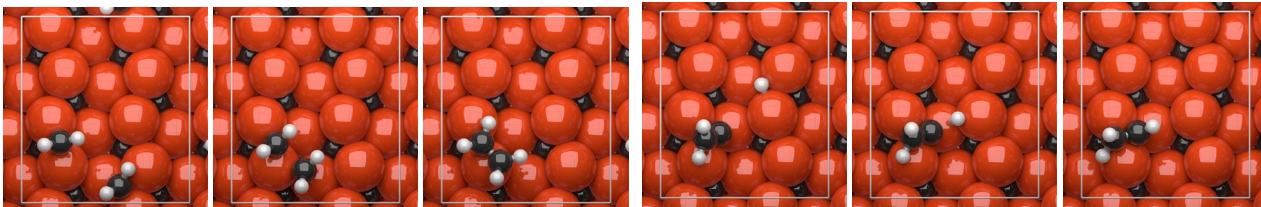
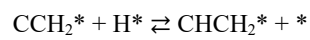
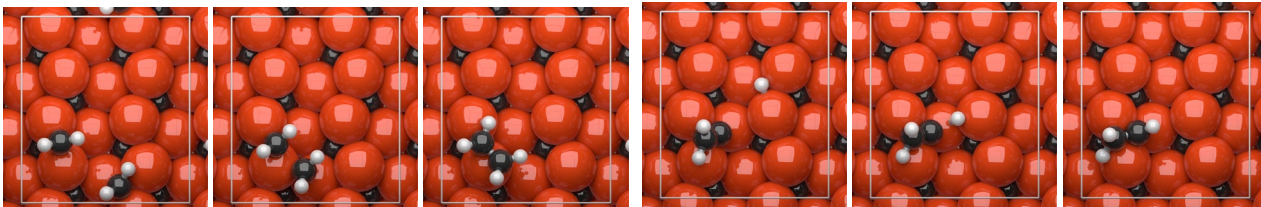
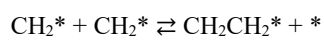
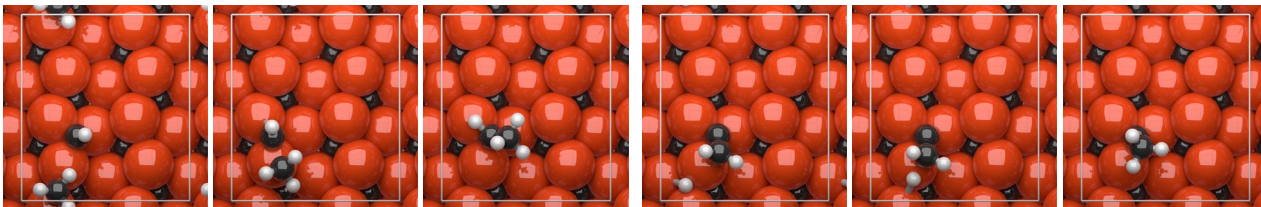
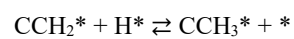
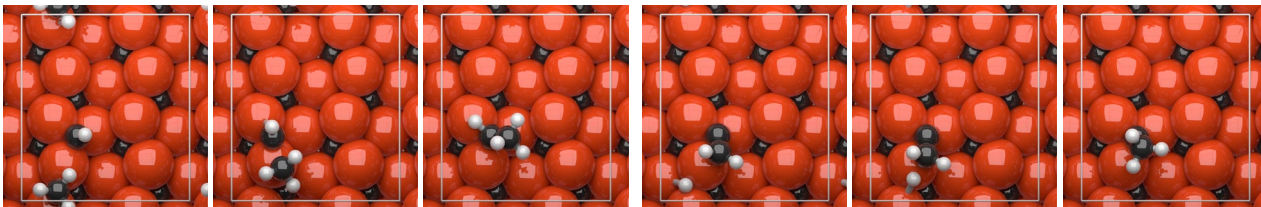
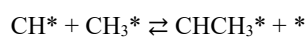
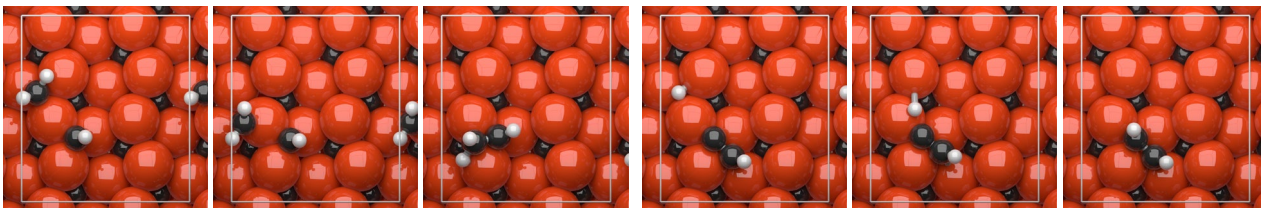
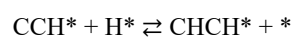
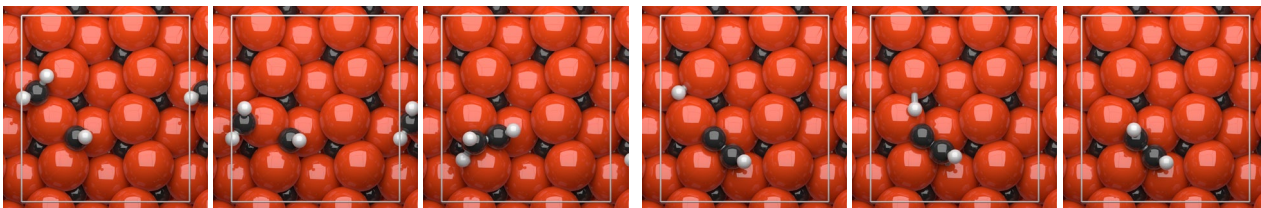
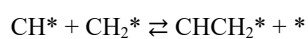
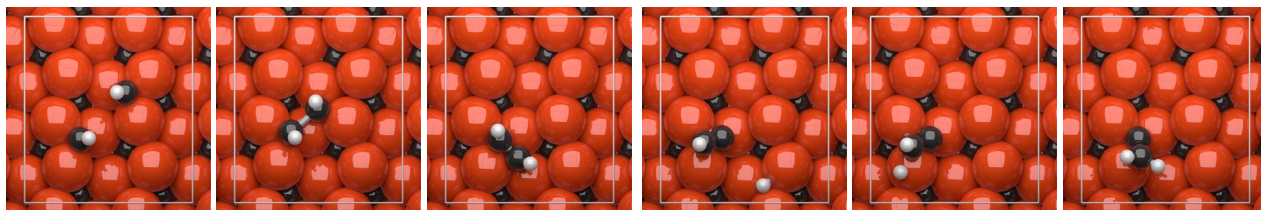
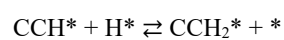
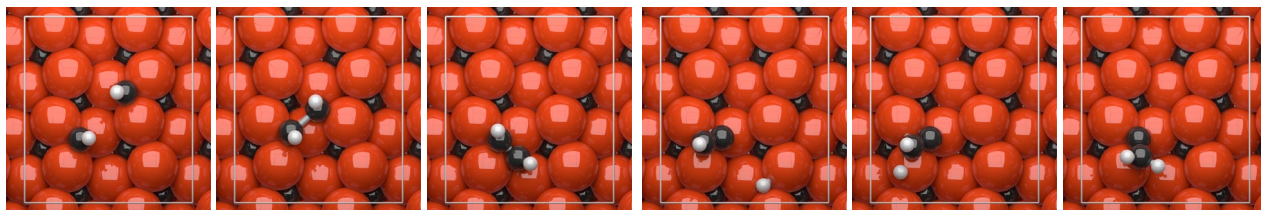
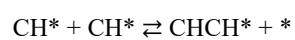
$(010)_{0.25} \chi\text{-Fe}_5\text{C}_2$  $(010)^*_{0.25} \chi\text{-Fe}_5\text{C}_2$ 

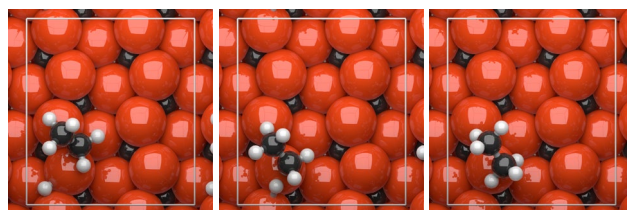
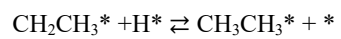
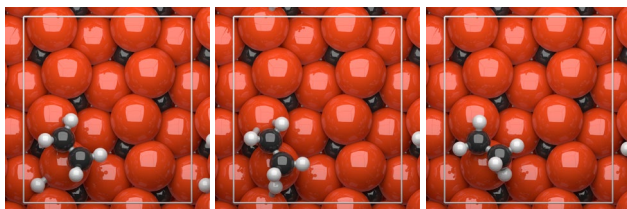
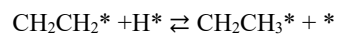
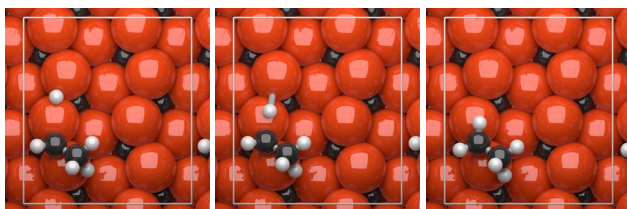
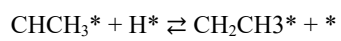
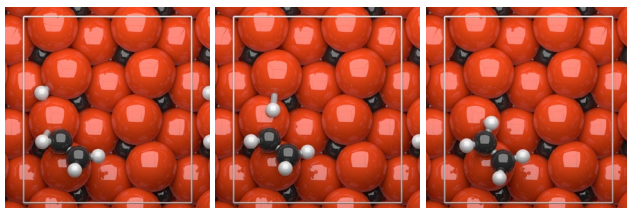
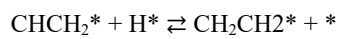
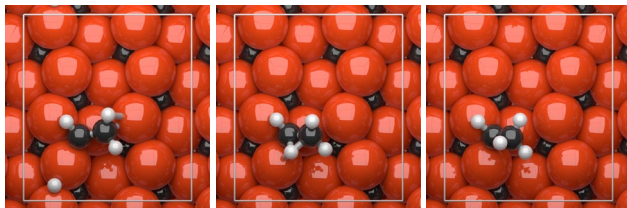
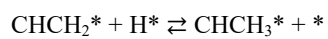
$(010)_{0.25} \gamma\text{-Fe}_5\text{C}_2$  $(010)^*_{0.25} \gamma\text{-Fe}_5\text{C}_2$ 



(100)  $\chi$ -FeC<sub>2</sub>



(100)  $\chi$ -Fe<sub>3</sub>C<sub>2</sub>

**(100)  $\chi$ -Fe<sub>5</sub>C<sub>2</sub>**

## Appendix B.2 Microkinetics simulations at the zero-conversion limit

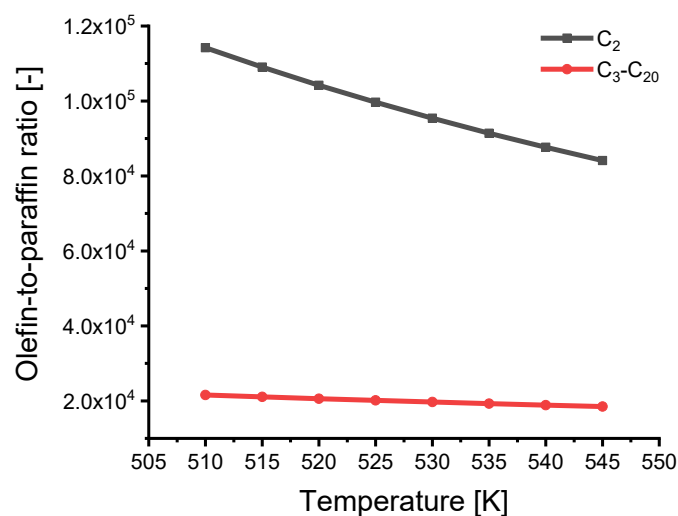


**Figure B.2.1:** Olefin-to-paraffin ratio for the zero-conversion limit for C<sub>2</sub> and C<sub>3+</sub> species between 510 K and 545 K on the (100)<sub>0,0</sub> surface at 1 bar.

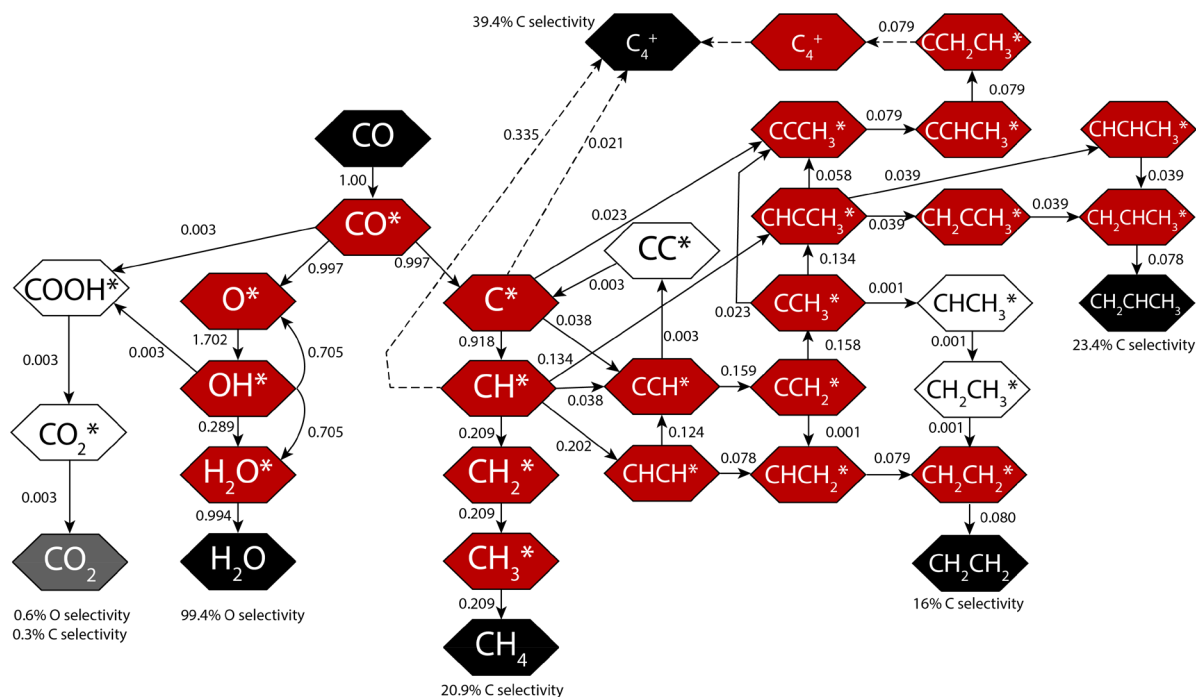


**Figure B.2.2:** Flux analysis at 525 K and 1 bar in the zero-conversion limit. The red hexagons represent the major intermediate species, the black hexagons represent the major gaseous components, the grey hexagons represent the minor gaseous components and the white hexagons represent minor intermediate species. The remainder of the intermediate species and products are omitted, as their values were lower than the limit ( $10^{-4}$ ) relative to the flux of CO adsorption.



### Appendix B.3 Microkinetics simulations in the CSTR model

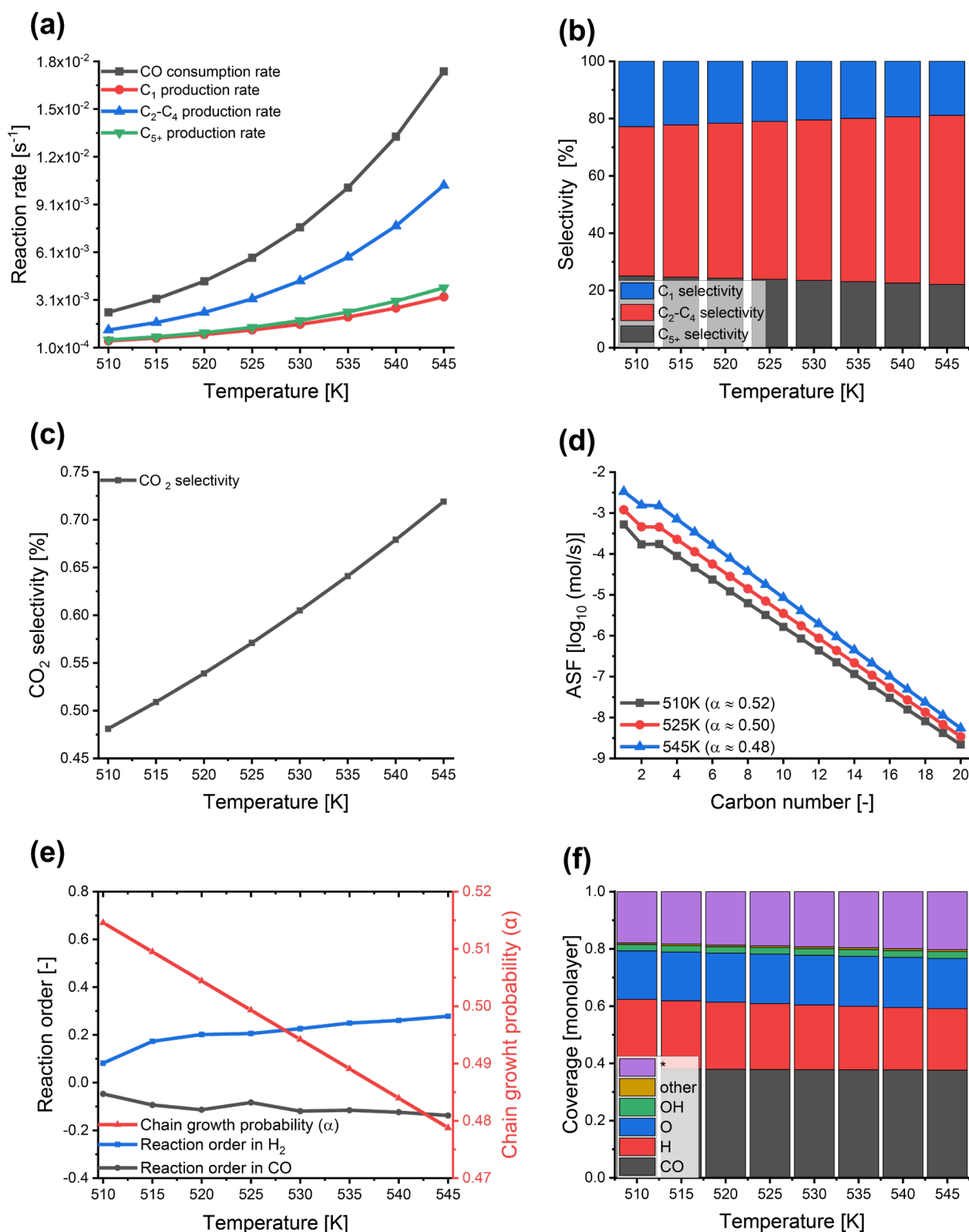


**Figure B.3.1:** Microkinetics simulations of the FT reaction on the  $\text{Fe}_5\text{C}_2\text{-(100)}_{0.0}$  surface between 510 K and 545 K at 1 bar in the CSTR model. (a) Reaction rate for the  $\text{C}_1$  species (red),  $\text{C}_2\text{-C}_4$  species (blue),  $\text{C}_{5+}$  species (green) and the CO consumption rate (dark grey) per second. (b) Selectivities as a function of the temperature on the  $(100)_{0.0}$  surface for  $\text{C}_1$  species (blue bar),  $\text{C}_2\text{-C}_4$  species (red bar) and  $\text{C}_{5+}$  species (dark grey bar). (c)  $\text{CO}_2$  selectivity. (d) ASF distribution function at 510 K (dark grey), 525 K (red) and 545 K (blue). (e) Reaction order in CO (dark grey) and  $\text{H}_2$  (blue) and chain-growth probability (red). (f) Composition of the adsorbed catalyst layer.

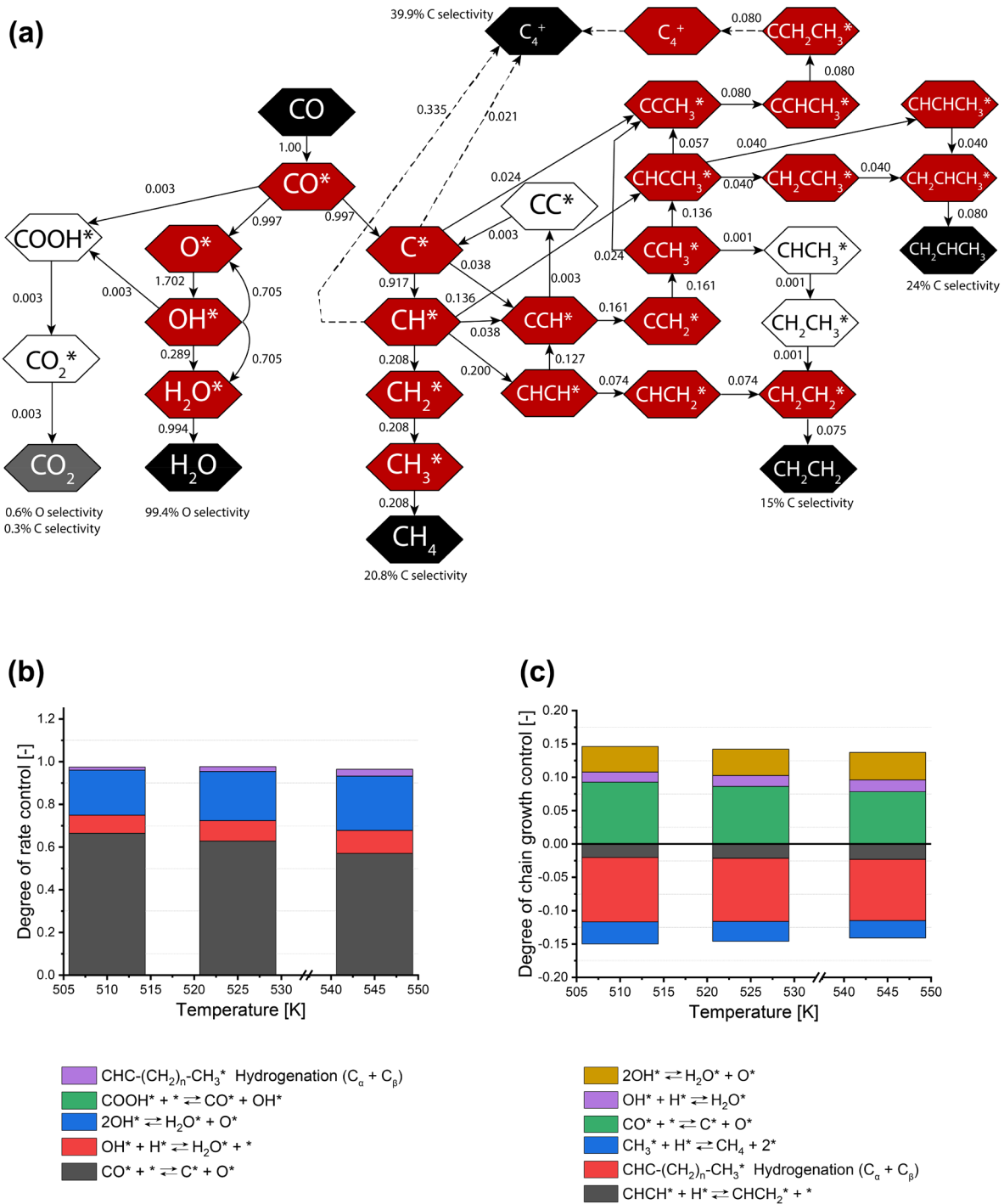
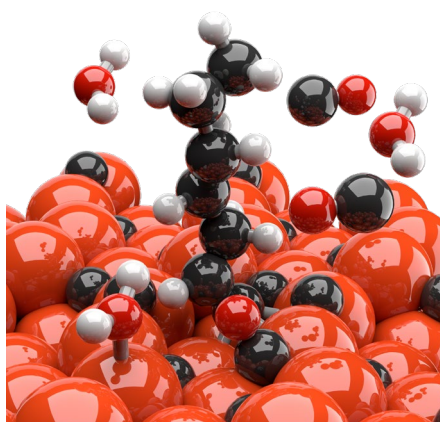


**Figure B.3.2:** (a) Flux analysis at 525 K and 1 bar in the CSTR model. The red hexagons represent the major intermediate species, the black hexagons represent the major gaseous components, the grey hexagons represent the minor gaseous components, and the white hexagons represent minor intermediate species. The remainder of the intermediate species and products are omitted, as their values were lower than the limit ( $10^{-4}$ ) relative to the flux of CO adsorption. (b) DRC analysis at 510 K, 525 K, and 545 K. (c) DCGC analysis at 510 K, 525 K, and 545 K.



## 5. A Quantum-Chemical DFT and Microkinetic Modelling Study of the Fischer-Tropsch Reaction on $\epsilon$ -Fe<sub>2</sub>C



### Abstract

Iron carbides are the active phase in the Fe-catalysed Fischer-Tropsch (FT) reaction. Recent experimental work shows that  $\epsilon$ -Fe<sub>2</sub>C carbide is an active and stable catalyst for the FT reaction (P. Wang, W. Chen, F.-K. Chiang, A.I. Dugulan, Y. Song, R. Pestman, K. Zhang, J. Yao, B. Feng, P. Miao, W. Xu, E.J.M. Hensen, *Sci. Adv.* 2018; 4 : eaau2947). Using density functional theory, we determined energy barriers and pre-exponential factors for all relevant elementary reaction steps underlying FT chemistry on several  $\epsilon$ -Fe-carbide surfaces. These parameters were used to simulate microkinetics of a step-edge (011) surface of  $\epsilon$ -Fe<sub>2</sub>C. These microkinetics are in line with experimental data for a pure  $\epsilon$ -Fe-carbide catalyst. The data indicate that H-assisted CO dissociation via HCO is the preferred pathway for formation of the chain-growth monomer. CH is the main chain-growth monomer inserting in CH<sub>3</sub> and CR (R = alkyl) fragments and H<sub>2</sub>O is the main product of O removal. While Co catalysts operate in the monomer formation limit with CO dissociation being rate controlling,  $\epsilon$ -Fe-carbide works in the chain-growth limit with coupling reactions being rate-limiting.

## 5.1 Introduction

Fischer-Tropsch (FT) synthesis is an established chemical process for the conversion of natural gas and coal into synthetic fuels and chemicals.[1] The active phase in commercial FT catalysts is typically based on Co or Fe. Fe-based catalysts are less expensive and more active in the water-gas shift reaction than Co-based ones. The latter is important during processing of synthesis gas with a low  $H_2/CO$  ratio as derived from coal. Promoters such as Cu and K are used to improve the Fe reduction degree and increase FT activity and long hydrocarbons selectivity, respectively. Fe catalysts find utility mainly in coal-to-liquids processes such as developed in the past in South-Africa by Sasol[2] and, more recently, in China.[3]

Similar to Co, the nature of the active sites in Fe-based catalysts and the mechanism by which CO is converted to hydrocarbons remain topics of considerable debate. It is well known that under FT conditions the Fe-oxide precursor is converted into Fe-carbide. Among such carbide phases, Hägg carbide ( $\chi$ -Fe<sub>5</sub>C<sub>2</sub>) is usually argued to be the most important one with respect to FT catalysis.[4] As a consequence, a large number of works have focused on this carbide.[5-12] Besides  $\chi$ -Fe-carbide,  $\theta$ -Fe-carbide ( $\theta$ -Fe<sub>3</sub>C) [12-18] and  $\epsilon$ -Fe-carbide ( $\epsilon$ -Fe<sub>2</sub>C) [6, 19-22] have also been observed in industrial catalysts. This leads to the question to what extent  $\theta$ -Fe<sub>3</sub>C and  $\epsilon$ -Fe<sub>2</sub>C contribute to the overall activity and selectivity. In this contribution, we aim to understand the mechanism of the FT reaction on  $\epsilon$ -Fe<sub>2</sub>C.

$\epsilon$ -Fe-carbides have been studied intensively in the late 40's and 50's of the previous century, as they are of interest in the steel industry.  $\epsilon$ -Fe carbide is a transition iron carbide with the chemical formula of  $\epsilon$ -Fe<sub>x</sub>C with  $x$  between 2 and 3, which was first identified by Hofer et. al [23]. They reported that  $\epsilon$ -Fe-carbides are the first product in the precipitation of quenched steels. Nagakura showed that  $\epsilon$ -Fe carbide is produced by cementation below a temperature of 250 °C, while Hägg carbide is produced by cementation above this temperature.[24] Manes et al. showed that the  $\epsilon$ -Fe carbide was the only carbide being formed up to 250 °C.[25] Fang et al. confirmed the high stability of the  $\epsilon$ -Fe<sub>2</sub>C and also found stable configurations for a  $\epsilon$ -Fe<sub>2.4</sub>C composition. Under some conditions, the hexagonal  $\epsilon$ -Fe<sub>2</sub>C phase can be converted into orthorhombic  $\eta$ -Fe<sub>2</sub>C.[26]

As widely accepted, the initial step in the FT mechanism is CO dissociation. CO dissociation can follow different routes: direct dissociation and hydrogen-assisted dissociation involving the hydrogenation of the C or O atom prior to C-O bond scission. Understanding CO dissociation is a crucial step because it provides the monomers for chain-growth and thus determines the activity and selectivity to a large extent.[27] Previous computational studies focusing on metallic Fe surfaces

[28-31] have demonstrated that the direct dissociation mechanism is the most important pathway for CO activation. In a recent work, we investigated the mode of CO dissociation on different Hägg carbide [5] and  $\theta$ -Fe<sub>3</sub>C surfaces.[17] We showed that the mode of CO dissociation strongly depends on the local surface topology. After C-O bond scission, the C atom can either be used to form CH<sub>4</sub> or in the formation of longer hydrocarbons. O atoms originating from CO dissociation can be removed as H<sub>2</sub>O or CO<sub>2</sub>. This reaction was shown to strongly influence activity and selectivity patterns.[32] H<sub>2</sub>O is formed by the twofold hydrogenation of surface O or by a disproportionation step wherein two hydroxyl (OH) species react to form water and a surface O atom.[33] CO<sub>2</sub> is formed by direct recombination with CO. One can therefore expect that the selectivity of the O removal product will depend not only on the barriers but also on the CO and H coverages. Fe-based FT catalysts typically show a high selectivity to CO<sub>2</sub>. [21] This can be seen as a benefit in case a feed with a low H<sub>2</sub>/CO ratio needs to be converted. However, in commercial practice the H<sub>2</sub>/CO ratio is preferably adjusted by a water-gas shift (WGS) section, which typically presents higher activity and catalyst lifetime allowing for easier removal of CO<sub>2</sub> than relying on WGS activity of the FT catalyst. Moreover, limiting the CO<sub>2</sub> selectivity in the FT section of a plant brings an additional cost benefit because less CO<sub>2</sub> will be recycled. It has recently been shown that pure  $\epsilon$ -Fe-carbide is not only active in the FT reaction but is also a stable catalyst under industrial conditions.[21] Unlike most other reports [34-36], it was found that a catalyst based on pure  $\epsilon$ -Fe-carbide did not produce CO<sub>2</sub> as the initial product. This suggests that the primary pathway of O removal on  $\epsilon$ -Fe-carbide is O hydrogenation to H<sub>2</sub>O.

In this study, we explore the FT mechanism over  $\epsilon$ -Fe-carbide using a combination of density functional theory (DFT) and microkinetic modelling. The surface abundance of the six unique low Miller index planes of  $\epsilon$ -Fe-carbide was studied using a Wulff construction based on surface free energies. We will check the stepped surface terminations for the presence of (vacant) B<sub>5</sub>-like sites, as those sites proved to be active in C-O bond scission on other metals by Van Hardeveld and Hartog.[37, 38] From the most abundant surfaces, we will use one terrace and one stepped surface. All elementary reaction steps relevant to the FT reaction over these surfaces are considered. Previous microkinetic studies of the FT reaction on a Co step-edge demonstrated that terrace and step-edge sites can be kinetically linked via migration processes. [39] We explored this aspect in our microkinetics simulations as well.

## 5.2 Methods

### 5.2.1 DFT calculations

All spin-polarized density functional theory (DFT) calculations were conducted using the projector-augmented wave (PAW) method and the Perdew–Burke–Ernzerhof (PBE) exchange-correlation functional as implemented in the Vienna Ab Initio Simulation Package (VASP) code.[40, 41] Solutions of the Kohn-Sham equations were calculated using a plane-wave basis set with a cut-off energy of 400 eV. The sampling of the Brillouin zone was done using a 5x5x1  $k$ -point mesh. A higher cut-off energy or finer Brillouin zone sampling did not lead to significant energy differences. Electron smearing was employed using a first-order Methfessel-Paxton technique [42] with a smearing width of 0.2 eV. All atoms were allowed to relax for the calculation of the empty surfaces. We employed the terrace (001) and the stepped (011) and (101) surfaces as representative surfaces for CO activation. For the total reaction mechanism, we employed the terrace (001) and the stepped (011) surfaces. The terrace surface is free of surface C-atoms and consists of FCC-hollow (free of sub-surface C) and HCP-hollow (with a subsurface C) sites. The height of the unit cell was 11.03 Å and 16.27 Å for the (011) and (001) surfaces, respectively. We used a slab containing 36 Fe atoms and 18 C atoms for the (011) surface and one containing 24 Fe atoms and 12 C atoms for the (001) surface. Adsorption of adatoms was simulated on the upper half of the slab, whereas the atomic positions corresponding to the lower half of the slab were frozen. A dipole correction was performed for all adsorbed states. A vacuum layer of at least 15 Å was added perpendicular to the surface in order to avoid spurious interactions between neighbouring system images. Adsorption energies were calculated by subtracting the gas phase energy and the total energy of the empty surface from the total energy of the adsorbed state.

Surface energies were obtained in the following manner:

$$E_{\text{surface}} = \frac{(E_n - n * E_{\text{bulk}})}{2 * A} \quad (5.1)$$

where  $E_n$  refers to the total energy of the slab, containing  $n$  times the bulk cell,  $E_b$  to the bulk energy,  $A$  to the area of the surface and  $E_{\text{surface}}$  to the surface energy of the surface.

The energy of the adsorbate in the gas phase was performed by placing a molecule at the centre of a 10 x 10 x 10 Å<sup>3</sup> unit cell, using the  $\Gamma$ -point for the  $k$ -point sampling. For electron smearing, a Gaussian smearing width of 0.002 eV was used. The adsorption energies, after zero-point energy (ZPE) corrections, are in good agreement with tabulated thermodynamic data.[43]

For all calculations, the convergence criterion was set to  $10^{-4}$  eV for the ionic steps and to  $10^{-5}$  eV for the electronic convergence. All geometry optimizations were conducted using the conjugate-gradient algorithm. Transition states were acquired using the climbing image nudged elastic band (CI-NEB) method.[44] A frequency analysis was performed to confirm that all transition geometries corresponded to a first-order saddle point on the potential energy surface with an imaginary frequency in the direction of the reaction coordinate. The Hessian matrix was constructed using a finite difference approach with a step size of 0.02 Å for the displacement of individual atoms along each Cartesian direction. The corresponding normal mode vibrations were also used to calculate the ZPE correction. We corrected the barriers for the migration of fragments after dissociation by considering the energy difference of the geometry directly after dissociation and their most stable adsorption positions at infinite distance.

The rate constant ( $k$ ) of an elementary reaction step was determined using the Eyring equation:

$$k = \nu \exp\left(\frac{-\Delta E_{\text{act}}}{k_{\text{b}}T}\right) \quad (5.2)$$

where  $\Delta E_{\text{act}}$  is activation energy in J/mol,  $k_{\text{b}}$  the Boltzmann constant in J/K,  $T$  the temperature in K, and  $\nu$  for the pre-exponential factor in  $\text{s}^{-1}$ . The pre-exponential factor can be evaluated for the forward and backward reaction using the following equations:

$$\nu_{\text{forward}} = \frac{k_{\text{b}}T}{h} \left( \frac{q_{\text{vib}}^{\text{TS}}}{q_{\text{vib}}^{\text{IS}}} \right) \text{ and } \nu_{\text{backward}} = \frac{k_{\text{b}}T}{h} \left( \frac{q_{\text{vib}}^{\text{TS}}}{q_{\text{vib}}^{\text{FS}}} \right) \quad (5.3)$$

where  $\nu_{\text{forward}}$  and  $\nu_{\text{backward}}$  refer to the pre-exponential factors for the forward and the backward reaction, respectively,  $q_{\text{vib}}$  is the vibrational partition function of the initial state (IS) or the transition state (TS) and  $h$  denotes Planck's constant. Note that we neglected other entropic contributions because we are mostly dealing with immobile surface adsorbates involved in dissociation or association reactions. Adsorption and desorption steps were treated in a different manner as discussed in the following section.

### 5.2.2 Microkinetic modelling

For the construction of the microkinetic model, differential equations for all surface reaction intermediates were constructed using the rate constants of all relevant elementary reaction steps. Each adsorbate occupies exactly one active site and is assumed to lose one translational degree of freedom in the transition state with respect to the initial gas-phase state. Desorbing species were

assumed to gain two translational degrees of freedom and three rotational degrees of freedom in the transition state with respect to the initial adsorbed state. From these two assumptions, the rate of adsorption and desorption are as follows[45]:

$$k_{\text{ads}} = \frac{P \cdot A}{\sqrt{2\pi \cdot m \cdot k_b \cdot T}} \quad (5.4)$$

$$k_{\text{des}} = \frac{k_b \cdot T^3}{h^3} \cdot \frac{A \cdot (2\pi \cdot m \cdot k_b)}{\sigma \theta_{\text{rot}}} \cdot e^{\left(\frac{-E_{\text{des}}}{RT}\right)} \quad (5.5)$$

Herein,  $k_{\text{ads}}$  is the rate constant for the adsorption of the adsorbate,  $P$  is the pressure in Pa,  $A$  is surface area in  $\text{m}^2$ ,  $m$  is the mass of the reactant in kg,  $k_b$  is the Boltzmann constant in J/K,  $T$  is the temperature in K,  $k_{\text{des}}$  is the rate constant for the desorption of the adsorbate,  $h$  is the Planck constant in  $\text{m}^2 \text{kg/s}$ ,  $\sigma$  is the symmetry number,  $\theta_{\text{rot}}$  the rotational temperature in K,  $E_{\text{des}}$  is the desorption energy in J/mol and  $R$  is the gas constant in J/mol K. We introduced a lateral correction ( $E_{\text{lat}}$ ) and in the following manner:

$$k_{\text{des}} = \frac{P \cdot A}{\sqrt{2\pi \cdot m \cdot k_b \cdot T}} \cdot \frac{\exp\left(\frac{S_{\text{gas}}}{R}\right)}{q_{\text{vib,ads}}} \cdot \exp\left(\frac{(E_{\text{des}} + E_{\text{lat}})}{RT}\right) \quad (5.6)$$

The lateral correction applied here reflects the qualitative effect of lateral interactions on the differential adsorption energies. The most important aspect is that the adsorption energy is relatively constant at low coverage and that the lateral repulsion increases steeply at high coverage. The overall thermodynamics of the microkinetic model are preserved by defining a lateral correction on a per-atom basis [39] with the penalty of species  $x$ .  $E_{\text{lat}}$  is computed as follows:

$$E_x^{\text{lat}} = E_x^{\theta=1} \times \frac{(101^{\theta_{\text{lat}}}-1)}{100}, \quad (5.7)$$

where  $\theta_{\text{lat}}$  is computed via the following equation:

$$\theta_{\text{lat}} = \frac{(\theta_{\text{total}} - \theta_* - 0.5 \cdot \theta_H) - \theta_{\text{LB}}}{\theta_{\text{UB}} - \theta_{\text{LB}}} \text{ with } \theta_{\text{lat}} \geq 0 \quad (5.7)$$

We used lateral interaction parameters of  $E_C^{\theta=1} = E_O^{\theta=1} = 4 \times E_H^{\theta=1} = 60 \text{ kJ/mol}$ ,  $\theta_{\text{LB}} = 0.25 \text{ ML}$ , and  $\theta_{\text{UB}} = 0.75 \text{ ML}$ . These parameters prevent surface coverages in our simulations that are physically unrealistic (e.g. CO coverages above 0.6 ML at 525K) We assumed that all surface species contribute equally to the lateral interaction potential with the exception of hydrogen. We considered that treating hydrogen equally would overestimate the lateral repulsion considering its

relatively small size. However, completely removing its contribution is likely to be an underestimation.

All microkinetics simulations were performed using the MKMCXX software suite.[46] The set of differential equations were time-integrated using the backward differentiation formula (BDF) method until a steady-state solution was obtained.[32] From the steady-state coverages, the rates of the individual elementary reactions steps were obtained using a so-called flux analysis, as readily available in the MKMCXX software. To mimic realistic conditions, we used an isobaric CSTR model for reactor modelling, over a temperature range between 510K and 545K. Furthermore, we performed the microkinetics simulates at a fixed H<sub>2</sub>/CO ratio of 1 at different pressures, varying from 0.1 bar to 5 bar. We implemented an isobaric and isothermal CSTR model, assuming the gases to behave ideally. Gas phase concentrations ( $C_i$ ) were determined using the following design equation [47]:

$$V \frac{dC_i}{dt} = F_i^{\text{in}} - F_i^{\text{out}} + N_{\text{sites}} r_i \quad (5.8)$$

Here,  $V$  is the volume of the reactor,  $r_i$  is the production or consumption of species  $i$  as predicted by the microkinetic model, while  $F_i^{\text{in}}$  and  $F_i^{\text{out}}$  are the molar flow rates at the reactor entrance and exit, respectively. To obtain different conversions at isobaric conditions, the number of sites ( $N_{\text{sites}}$ ) can be varied corresponding to changes in the catalyst loading in the reactor. The influence of the individual elementary reactions steps was determined using the Campbell's DRC method [48] and the DCGC[49] method (see also Chapter 4.2.2)

## 5.3 Results and Discussion

### 5.3.1 Wulff construction

First, the bulk  $\epsilon$ -Fe<sub>2</sub>C structure was optimized at the DFT level. The initial geometry was obtained from the structure reported by Nagakura and co-workers.[24] The unit cell corresponds to the hexagonal lattice of the P6<sub>3</sub>22 space group. We named this bulk structure  $\epsilon$ -Fe<sub>2</sub>C-025C, because it contains two additional non-symmetry conforming carbon layers at  $c = 0$  and  $c = 0.25$ , where  $c$  denotes the height with respect to the unit cell and is given in crystal coordinates such that  $c \in [0,1)$ . These layers are higher in carbon-density in comparison to the other layers, which are located at  $c = 0.5$  and  $c = 0.75$ . Another possible bulk structure could be constructed in which the additional non-

symmetric carbon layer is shifted by half a unit-cell in the  $c$ -direction ( $\epsilon$ -Fe<sub>2</sub>C-075C). Figure 5.1 depicts the bulk structures of  $\epsilon$ -Fe<sub>2</sub>C-025C and  $\epsilon$ -Fe<sub>2</sub>C-075C. The characteristics of  $\epsilon$ -Fe<sub>2</sub>C-025 match experimental observations of both high- and low-carbon-density regions embedded in the bulk as previously observed by Niemantsverdriet et al.[50]

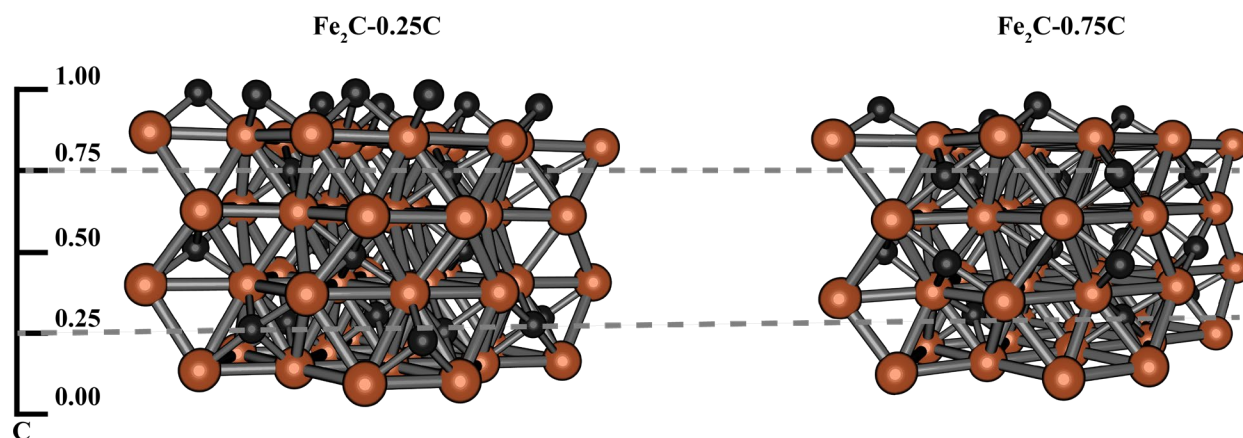


**Figure 5.1:** Representation of the  $\epsilon$ -Fe<sub>2</sub>C-025 (left) and the  $\epsilon$ -Fe<sub>2</sub>C-075 (right) bulk structures of  $\epsilon$ -Fe-carbide.

To investigate the exposed surface facets, a Wulff construction was made based on the set of low-index surface terminations as shown in Table 5.1. The surface energies of these unique low-index Miller surfaces as well as their relative exposed surface contributions following from the Wulff construction are given. The corresponding shape of the nanoparticle is depicted in Figure 5.2. The terrace (001) surface was found to be the most stable surface with a surface energy of 1.58 J/m<sup>2</sup>. The more corrugated (111), (101) and (011) surfaces are higher in energy but contribute, due to their favourable orientation, significantly to the exposed surface of the Wulff particle. Finally, the (110) and (100) surface with respective surface energies of 2.23 J/m<sup>2</sup> and 2.35 J/m<sup>2</sup> are expected to have minor contributions on a Wulff particle.

The catalytic activity and selectivity of close-packed terrace surfaces can differ substantially from more corrugated step-edge surfaces containing surface defects.[51] As a representative model for terrace sites, the (001) surface was chosen because it was the most abundant surface on the Wulff particle. As step-edge sites with a B5 geometry are usually considered to be important for low-barrier CO dissociation, we also selected a surface that contains such sites. As can be seen from Figure 5.2, out of the three corrugated low Miller index surfaces (011), (101) and (111), only the (011) and (101) surfaces contain B<sub>5</sub> sites. On the basis of direct CO dissociation barriers (*vide infra*), we chose the (011) as the surface model for the stepped surface. To determine the influence of each elementary reactions step, we used the degree of rate control (DRC) method as introduced by



Campbell and co-workers.[48] (cf. Chapter 2.3.4). The influence of each elementary reaction on the chain-growth probability was determined using the degree of chain-growth control (DCGC) method, as introduced by Filot et. al [49] (cf. Chapter 4.2.2).

**Table 5.1** Surface energies of the different unique low Miller-index surfaces in J/m<sup>2</sup> and the contributions of the surface facets to a Wulff particle.

Termination	Identical	Surface Energy (J/m <sup>2</sup> )	Total Amount of exposed surface (%)
Step-edge like (100)	( $\bar{1}00$ )(010)(0 $\bar{1}0$ )( $\bar{1}10$ )( $1\bar{1}0$ )	2.35	0.0
Terrace-like (001)	(00 $\bar{1}$ )	1.58	25.5
Step-edge like (110)	( $\bar{1}\bar{1}0$ )	2.23	0.0
Step-edge like (011)	(0 $\bar{1}\bar{1}$ )( $\bar{1}01$ )(10 $\bar{1}$ )( $1\bar{1}1$ )( $\bar{1}1\bar{1}$ )	2.05	24.1
Step-edge like (101)	(01 $\bar{1}$ )(0 $\bar{1}1$ )( $\bar{1}0\bar{1}$ )( $1\bar{1}\bar{1}$ )( $\bar{1}11$ )	1.95	35.4
Step-edge like (111)	( $\bar{1}\bar{1}\bar{1}$ )(11 $\bar{1}$ )( $\bar{1}\bar{1}1$ )	1.89	15.0

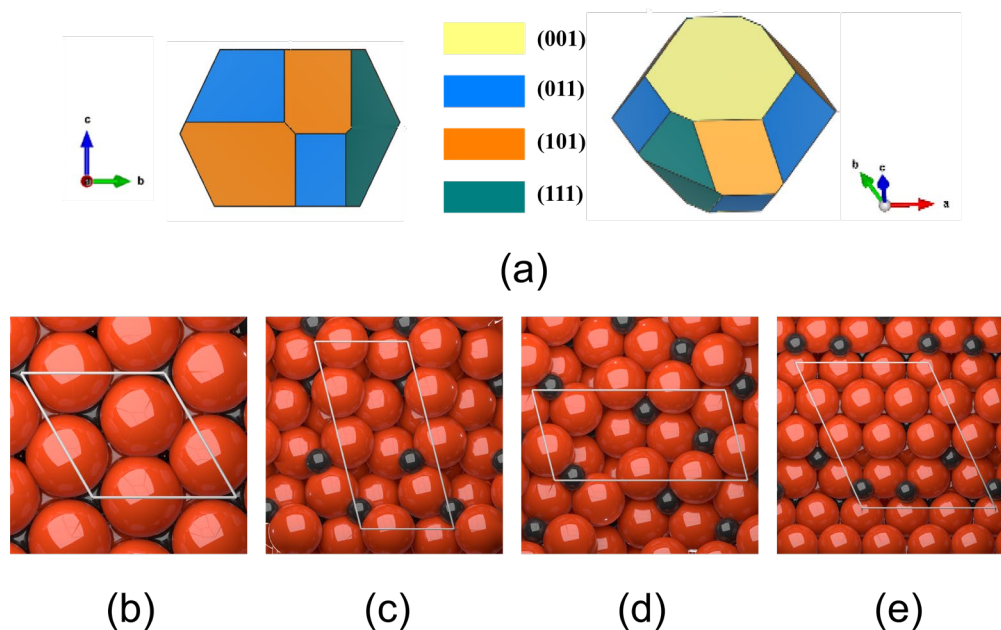


**Figure 5.2:** (a) Wulff construction of  $\epsilon$ -Fe-carbide and (b-e) the corresponding geometries of the exposed surfaces of (b) the (001) surface, (c) the (011) surface, (d) the (101) surface and (e) the (111) surface, respectively.

### 5.3.2 Reaction energetics

DFT calculations were performed to compute the reaction energetics of the elementary reaction steps leading up to and including C<sub>2</sub>-hydrocarbons. These reactions include CO dissociation, chain-growth via the carbide mechanism and hydrogenation of the C-containing intermediates as well as O removal steps. As explained above, the two surfaces considered in this study are the terrace (001) surface and the stepped (011) and (101) surfaces. For CO dissociation, we evaluated both direct and

H-assisted pathways. Based on these energetics, we proceeded with computing other relevant barriers for the (001) terrace and the (011) step. Reaction energetics for the hydrogenation of C to  $\text{CH}_x$  ( $x = 1-4$ ),  $\text{CH}_x + \text{CH}_y$  coupling and further hydrogenation of  $\text{CH}_x\text{CH}_y$  ( $x, y = 1-3$ ) were determined. The O removal pathways leading to  $\text{H}_2\text{O}$  and  $\text{CO}_2$  formation were also considered. The computed barriers for direct CO dissociation are collected in Table 5.2, while the rest of the computed barriers can be found in Table 5.3

### 5.3.2.1 CO dissociation

Although direct and H-assisted CO dissociation pathways on  $\varepsilon\text{-Fe}_2\text{C}$  were investigated before by other groups [12, 20], we computed the barriers to obtain a database of kinetic parameters at the same level of theory and using the same exchange-correlation functional. The geometries of the initial, transition and final states corresponding to the minimum energy pathways for direct CO dissociation are provided in Appendix C.1 whereas the corresponding barriers are provided in Table 5.2.

**Table 5.2:** Direct CO dissociation on terrace (001) and stepped (011) and (101) surfaces.

Direct CO dissociation								
Terrace (001)			Step (011)			Step (101)		
$E_a$ [kJ/mol]	$E_b$	$E_{\text{reac}}$	$E_a$	$E_b$	$E_{\text{reac}}$	$E_a$	$E_b$	$E_{\text{reac}}$
	[kJ/mol]	[kJ/mol]	[kJ/mol]	[kJ/mol]	[kJ/mol]	[kJ/mol]	[kJ/mol]	[kJ/mol]
<b>208</b>	133	76	146	237	-91	168	15	153

As expected, direct CO bond scission on the terrace (001) has a high activation energy barrier (208 kJ/mol) compared to the more corrugated (011) and (101) surfaces with activation energies of 146 kJ/mol and 168 kJ/mol, respectively. On the (011) and (101) surface, CO dissociation can proceed with a low activation barrier at the  $B_5$  site, similar to what has been found for Co [52] and Ru [33] surfaces. On the (011) surface, CO is adsorbed directly at the  $B_5$  site in a fourfold position, leading to a final state, where C remains adsorbed in the fourfold site, whereas the O is adsorbed in the adjacent threefold site. The slightly higher activation energy on the (101) originates from the surface C atom, adjacent to the  $B_5$  site, which causes strong lateral interactions in the transition state.

We compare our computed values to literature data. The direct CO dissociation barrier on the (001) surface is 38 kJ/mol higher compared to the value of 170 kJ/mol reported by Yu et al.[20] These authors used a different orthorhombic  $\eta\text{-Fe}_2\text{C}$  bulk structure following a proposal of Li and co-

workers[19] in contrast to the hexagonal  $\varepsilon$ -Fe<sub>2</sub>C structure used in this work. Although Li and co-workers showed that orthorhombic  $\eta$ -Fe<sub>2</sub>C is slightly more stable than the hexagonal  $\varepsilon$ -Fe<sub>2</sub>C unit cell, experiments demonstrated that  $\varepsilon$ -Fe<sub>2</sub>C predominantly adopts the hexagonal crystal structure.[4, 21, 53] Huo et al. used a similar structure to construct the (011) surface [12]. Unlike the structure that we used, the B<sub>5</sub> site used by Huo et al. is blocked by a surface C atom, precluding CO dissociation on the B<sub>5</sub> site, resulting in a preference for CO dissociation on the (011) surface. This difference stems from the different surface termination relative to the *c*-axis. As CO dissociation is more facile on the (011) surface than on the (101) surface, we focused on the former surface for a full kinetic model.

CO hydrogenation on the (001) surface proceeds on a threefold site with an activation energy of 146 kJ/mol. HC-O bond scission has an activation energy of 66 kJ/mol and occurs at the same site, after which CH remains at the threefold site and oxygen migrates to an adjacent threefold site. On the (011) surface, CO hydrogenation has an activation energy of 104 kJ/mol, whereas HCO dissociation has an activation energy of 41 kJ/mol. CO hydrogenation and HCO dissociation both proceed on the B<sub>5</sub> site.

Comparing the overall barriers for the hydrogen-assisted mechanism *via* HCO, we find that the H-assisted pathway is preferred to direct CO dissociation on both surfaces. The overall barrier for the (001) surface is lower by 13 kJ/mol, while the barrier for the (011) surface is lower by 32 kJ/mol via the HCO intermediate. This implies that on both surfaces, the H-assisted CO dissociation mechanism will probably be the most dominant pathway for dissociating the C-O bond.

### 5.3.2.2 CH<sub>4</sub> formation

We computed the activation energies for the hydrogenation reactions of all adsorbed CH<sub>x</sub> species with  $x = 0-3$  on the terrace (001) and (011) stepped surfaces. On the (011) surface, we did not take surface C hydrogenation into account. The geometries of the initial, transition and final states (IS, TS and FS) are displayed in Appendix C.1. For the terrace (001) surface, the hydrogenation steps of adsorbed C to CH<sub>3</sub> proceed at a threefold site on the (001) surface by recombination of the CH<sub>x</sub> species with a H atom, which is located at an adjacent threefold site in the IS. The final hydrogenation step towards CH<sub>4</sub> occurs over a single Fe atom. In the TS, a single metal atom is shared between the CH<sub>x</sub> moiety and the H atom. After hydrogenation of a surface CH<sub>3</sub>, the resulting CH<sub>4</sub> in the FS is no longer chemisorbed on the surface. CH hydrogenation has the lowest activation energy (60 kJ/mol), followed by the CH<sub>2</sub> hydrogenation (71 kJ/mol). C hydrogenation to CH and

CH<sub>3</sub> hydrogenation to CH<sub>4</sub> have the highest barriers, i.e., 89 kJ/mol and 101 kJ/mol, respectively. Methylidyne (CH) formation is exothermic, while all other hydrogenation steps are endothermic. It can be reasonably expected that the CH intermediate prefers the threefold site in contrast to the other, as the topology of this surface is most suitable for orbital hybridisation of this fragment, which has been discussed before for other transition metals.[54] Similar to other transition metal surfaces [33, 39], the highest barrier found in the C hydrogenation sequence is CH<sub>4</sub> formation.

C hydrogenation over the stepped (011) surface proceeds initially at the fourfold site. C is bonded strongest on the fourfold site. These sites are absent on the (001) surface. The H atom resides in an adjacent threefold site prior to C hydrogenation to CH. In the TS, two metal atoms are shared by the H atom. Consistent with the bond-order conservation principle, the corresponding activation energy for C hydrogenation is higher on the stepped surface (102 kJ/mol) with respect to the terrace surface (89 kJ/mol). After CH formation, the resulting CH<sub>2</sub> intermediate migrates to an adjacent threefold site, where it can be hydrogenated to CH<sub>3</sub>. The H atom involved in the hydrogenation step resides on an adjacent bridge position and in the TS, only a single metal atom is shared by the forming product. CH<sub>3</sub> formation proceeds in a similar manner. CH<sub>4</sub> formation proceeds from a bridged site configuration. Typically, the final hydrogenation step towards CH<sub>4</sub> occurs over a single metal atom.[55] Here, this step occurs using an H atom initially adsorbed on a fourfold site, which is inserted via a threefold site into the CH<sub>3</sub> moiety to form CH<sub>4</sub>. All hydrogenation steps are endothermic as can be expected as they correspond to removing a C atom from its very stable fourfold position. Similar to the (001) surface, C hydrogenation to CH and CH<sub>3</sub> hydrogenation to CH<sub>4</sub> have the highest barriers, i.e., respectively 102 kJ/mol and 127 kJ/mol on the (011) surface among the C hydrogenation steps. Hydrogenation of CH<sub>2</sub> to CH<sub>3</sub> requires overcoming a barrier around 70 kJ/mol. The barrier for the hydrogenation from CH to CH<sub>2</sub> has a barrier of 77 kJ/mol.

### 5.3.2.3 Oxygen removal

The removal of O can occur via CO<sub>2</sub> or H<sub>2</sub>O formation. The first step in the formation of H<sub>2</sub>O is the hydrogenation of an O atom to an OH species. This OH species can then either be directly hydrogenated to H<sub>2</sub>O or react with another OH, leading to H<sub>2</sub>O and O in a disproportionation reaction. This reaction was already shown to be relevant on the Hägg carbide of Fe (Chapter 4) and on other surfaces.[56] The formation of CO<sub>2</sub> involves the oxidation of a CO with an O atom. The forward and backward reaction energies for the removal of O on the terrace (001) and the stepped (011) surface are listed in Table 5.3. The corresponding geometries are shown in Appendix C.1.

The O atom is adsorbed threefold on both (001) and (011) surfaces. On the (001) surface, the OH group stays adsorbed on the threefold site after reaction. This is in contrast to the (011) surface, where the OH group assumes a bridged position after its formation. H<sub>2</sub>O is adsorbed atop on both surfaces. CO<sub>2</sub> is adsorbed on a threefold site on the (001) surface, whereas it assumes a bridged adsorption configuration on the (011) surface.

O hydrogenation has similar barriers on the (001) and (011) surfaces with activation energies of 140 kJ/mol and 146 kJ/mol, respectively. OH hydrogenation has a higher barrier on the (001) surface (142 kJ/mol) compared to the barrier on the (011) surface (128 kJ/mol). The OH+OH disproportionation reaction shows a significantly lower activation barrier (35 kJ/mol) on the (001) surface compared to the activation barrier of 133 kJ/mol on the (011) surface.

On the stepped (011) surface, H<sub>2</sub>O formation *via* a direct hydroxyl hydrogenation has the lowest overall energy barrier for the removal of O, whereas the most favourable O removal product on the terrace (001) surface is CO<sub>2</sub>.

#### 5.3.2.4 C-C coupling and CH<sub>x</sub>CH<sub>y</sub> hydrogenation

Of the 10 different ways to couple two CH<sub>x</sub> species to form a C<sub>2</sub> species, we identified 9 transition states. The energy barriers and corresponding geometries can be found in Table 5.3 and Appendix C.1, respectively. A general trend is that the C-C coupling steps on the terrace are easier than those on the corrugated surface. No transition state was identified for CH<sub>3</sub>-CH<sub>3</sub> coupling due to reasons discussed in Chapter 4.

As the (001) surface does not contain fourfold sites, most CH<sub>x</sub> species (except for the CH<sub>3</sub> species) adopt a threefold adsorption. On the (011) surface, C adsorbs on a fourfold site, except in the IS of C-CH coupling. In the IS of C-C coupling, one of the C atoms is adsorbed in a threefold site. CH generally adsorbs on a threefold site, except in the C-CH coupling where CH is adsorbed in a fourfold site. One of the CH species in the CH-CH coupling is also adsorbed on a fourfold site. CH<sub>2</sub> is generally adsorbed in a bridged site, except for the initial state of the C-CH<sub>2</sub> coupling, where it is adsorbed atop. All CH<sub>3</sub> species are adsorbed atop a single Fe atom.

In general, the C-C coupling reactions have a significantly lower activation barrier on the (001) surface than on the (011) surface. This is due to the higher stability of CH<sub>x</sub> ( $x = 0-2$ ) species on the stepped (011) surface, CH<sub>3</sub> species however being less stable on this surface. All coupling reactions

are endothermic on the stepped (011) surface, while most are exothermic on the (001) surface with the exception of CH-CH<sub>2</sub> and CH<sub>2</sub>-CH<sub>3</sub> formation.

On the (001) surface, all C-C coupling exhibit activation barriers below 100 kJ/mol, except for the C-CH<sub>3</sub> and the CH<sub>2</sub>-CH<sub>3</sub> coupling reactions. C-CH<sub>2</sub> coupling has the lowest activation barrier (40 kJ/mol), followed by CH-CH (45 kJ/mol) and C-CH coupling (46 kJ/mol). On the (011) surface, CH<sub>2</sub>-CH<sub>3</sub> coupling has the lowest activation energy (131 kJ/mol), followed by CH-CH<sub>3</sub> (138 kJ/mol) and C-CH<sub>3</sub> (146 kJ/mol) coupling. The other C-C coupling pathways exhibit an activation barrier above 150 kJ/mol. Coupling reactions involving one or two C(H) species are very high in activation energy because those species are adsorbed more strongly to the surface compared to the CH<sub>2</sub> or CH<sub>3</sub> species. As all reactions are migration corrected (*vide supra*), the strong adsorption energies cause a higher barrier for coupling. More hydrogenated species have a weaker interaction with the (011) surface and, therefore, a lower barrier for migration.

We considered 12 different hydrogenation reactions on both the (001) and the (011) surfaces. All hydrogenation reactions of the C<sub>2</sub> species, except for the termination step towards the paraffin, have a significantly lower activation energy on the (011) surface than on the (001) surface. Most hydrogenation reactions on the (001) surface have activation barriers higher than 100 kJ/mol, although CCH<sub>3</sub> and CH<sub>2</sub>CH<sub>3</sub> hydrogenation are easier with barriers of 96 kJ/mol and 52 kJ/mol, respectively. In contrast to the (001) surface, most activation energies on the (011) surface are lower than 100 kJ/mol with the exception of CHCH hydrogenation and CH<sub>2</sub>CH<sub>3</sub> hydrogenation. Most of the reactions on the (001) surface are endothermic, except for CC hydrogenation to CCH, and the C<sub>α</sub> and C<sub>β</sub> hydrogenation of CHCH<sub>2</sub> to CH<sub>2</sub>CH<sub>2</sub> or CHCH<sub>3</sub>, respectively. On contrary, hydrogenation reactions on the (011) surface are mostly endothermic. Only CC hydrogenation proceeds without a change in enthalpy.

We investigated the influence of the migration correction on the C-C coupling barriers on the (011) surface. Due to the high adsorption energies for C and CH on the fourfold site, it can be reasonably expected that this site is occupied under reaction conditions. Therefore, chain-growth will most likely occur between C<sub>1</sub> species from other, less favourable adsorption sites. In order to determine such C-C coupling reactions, we used the following approach. First, we computed the new reference states (adsorption in the threefold site) for the C and CH species. These adsorption energies were subsequently used to determine the corrected reaction barriers, which are indicated in brackets in Table 5.3. The corrected reaction barriers are lower by 64.6 kJ/mol per C fragment and by 24.3 kJ/mol per CH fragment involved in the coupling reaction.

**Table 5.3** Energy barriers for all reactions up to and including C<sub>2</sub> formation on the terrace (001) and the corrugated (011) surface termination of hexagonal ε-Fe<sub>2</sub>C. Values between brackets correspond to the corrected barriers for an occupied fourfold site.

			Terrace (001)			Step (011)		
H-assisted CO dissociation			E <sub>f</sub>	E <sub>b</sub>	ΔH	E <sub>f</sub>	E <sub>b</sub>	ΔH
			[kJ/mol]	[kJ/mol]	[kJ/mol]	[kJ/mol]	[kJ/mol]	[kJ/mol]
CO + H	⇌	HCO	146	17	129	104	31	73
HCO	⇌	CH + O	66	147	-81	41	175	-134
			Terrace (001)			Step (011)		
Methanation			E <sub>f</sub>	E <sub>b</sub>	ΔH	E <sub>f</sub>	E <sub>b</sub>	ΔH
			[kJ/mol]	[kJ/mol]	[kJ/mol]	[kJ/mol]	[kJ/mol]	[kJ/mol]
C + H	⇌	CH	89	117	-28	102	72	30
CH + H	⇌	CH <sub>2</sub>	60	18	41	77	7	70
CH <sub>2</sub> + H	⇌	CH <sub>3</sub>	71	52	18	70	26	44
CH <sub>3</sub> + H	⇌	CH <sub>4</sub>	101	49	52	127	68	59
			Terrace (001)			Step (011)		
Oxygen removal via H <sub>2</sub> O/CO <sub>2</sub>			E <sub>f</sub>	E <sub>b</sub>	ΔH	E <sub>f</sub>	E <sub>b</sub>	ΔH
			[kJ/mol]	[kJ/mol]	[kJ/mol]	[kJ/mol]	[kJ/mol]	[kJ/mol]
O + H	⇌	OH	140	74	65	146	72	75
OH + H	⇌	H <sub>2</sub> O	142	47	95	128	1	127
OH + OH	⇌	H <sub>2</sub> O + O	35	6	30	133	81	52
CO + O	⇌	CO <sub>2</sub>	144	3	141	228	134	95
			Terrace (001)			Step (011)		
C-C coupling			E <sub>f</sub>	E <sub>b</sub>	ΔH	E <sub>f</sub>	E <sub>b</sub>	ΔH
			[kJ/mol]	[kJ/mol]	[kJ/mol]	[kJ/mol]	[kJ/mol]	[kJ/mol]
C + C	⇌	CC	80	194	-114	292 (163)	175	116
C + CH	⇌	CCH	46	160	-114	244 (155)	158	86
C + CH <sub>2</sub>	⇌	CCH <sub>2</sub>	40	107	-67	217 (153)	182	36
C + CH <sub>3</sub>	⇌	CCH <sub>3</sub>	107	173	-66	146 (81)	144	2
CH + CH	⇌	CHCH	45	101	-56	188 (134)	97	91
CH + CH <sub>2</sub>	⇌	CHCH <sub>2</sub>	72	1	72	183 (158)	122	60
CH + CH <sub>3</sub>	⇌	CHCH <sub>3</sub>	89	97	-8	138 (114)	81	57
CH <sub>2</sub> + CH <sub>2</sub>	⇌	CH <sub>2</sub> CH <sub>2</sub>	88	98	-10	172	148	24
CH <sub>2</sub> + CH <sub>3</sub>	⇌	CH <sub>2</sub> CH <sub>3</sub>	181	119	63	131	95	36
			Terrace (001)			Step (011)		
C <sub>2</sub> hydrogenation			E <sub>f</sub>	E <sub>b</sub>	ΔH	E <sub>f</sub>	E <sub>b</sub>	ΔH
			[kJ/mol]	[kJ/mol]	[kJ/mol]	[kJ/mol]	[kJ/mol]	[kJ/mol]
CC + H	⇌	CCH	107	135	-28	90	91	-1
CCH + H	⇌	CCH <sub>2</sub>	186	97	88	89	69	20
CCH + H	⇌	CHCH	99	68	31	60	25	35
CCH <sub>2</sub> + H	⇌	CCH <sub>3</sub>	189	169	20	77	66	11
CCH <sub>2</sub> + H	⇌	CHCH <sub>2</sub>	228	117	111	60	6	54
CHCH + H	⇌	CHCH <sub>2</sub>	194	25	169	107	68	39
CCH <sub>3</sub> + H	⇌	CHCH <sub>3</sub>	96	65	30	86	1	85
CHCH <sub>2</sub> + H	⇌	CH <sub>2</sub> CH <sub>2</sub>	114	154	-41	61	27	34
CHCH <sub>2</sub> + H	⇌	CHCH <sub>3</sub>	111	172	-61	80	38	42
CH <sub>2</sub> CH <sub>2</sub> + H	⇌	CH <sub>2</sub> CH <sub>3</sub>	106	14	91	71	15	56
CHCH <sub>3</sub> + H	⇌	CH <sub>2</sub> CH <sub>3</sub>	187	75	112	69	20	48
CH <sub>2</sub> CH <sub>3</sub> + H	⇌	CH <sub>3</sub> CH <sub>3</sub>	52	50	2	118	75	43

### 5.3.3 Microkinetic modelling

To predict reaction rates and the product distribution in the FT reaction on  $\epsilon$ -Fe-carbide, microkinetics simulations were carried out. Given the high overall barrier of CO dissociation on the terrace surface, we focused on the stepped (011) surface. We employed a CSTR model for these simulations. First, we will present results at a pressure of 1 bar and a  $H_2/CO$  ratio of 1. Then, we describe the influence of pressure in the range 0.1-5 bar. The kinetic parameters used as input for the microkinetic model can be found in Table 5.2 and Table 5.3 and Appendix C.2. We used the corrected activation barriers for C-C coupling as shown in Table 5.3.

The FT reaction was first modelled in the temperature range 510-545 K at a pressure of 1 bar. The residence time of the CSTR was chosen so that the CO conversion was below 10% in this temperature range (Figure 5.3a). The microkinetic results will be compared to recent experimental kinetic data determined by Chen et al.[57] for a pure  $\epsilon$ -Fe-carbide.[21] A summary is given of these experimental data obtained at a total pressure 1 bar in Table 5.4.

Figure 5.3b shows the overall CO conversion rate into hydrocarbon products. The CO consumption rate increases from  $1.6 \cdot 10^{-3} \text{ s}^{-1}$  at 510 K to  $3.5 \cdot 10^{-3} \text{ s}^{-1}$  at 545 K. These values are very close to the experimental rates determined in Chen's work ( $TOF = 1.7 \cdot 10^{-3} \text{ s}^{-1}$ ). The C-based selectivity towards  $C_2$ - $C_4$  species decreases from 56.7% at 510 K to 52.2% at 545 K (Figure 5.3c) with a concomitant increase of the  $CH_4$  selectivity (21.4% to 24%). The  $C_{5+}$  selectivity increases slightly with rising temperature. These trends are due to an increasing rate of hydrogenation. O atoms are removed as  $H_2O$ , the selectivity to  $CO_2$  being negligible (see Appendix C2). Thus, together with the results presented in Chapter 4, we can conclude that  $H_2O$  is the primary product of O removal reactions on  $\chi$ - and  $\epsilon$ -Fe-carbide.

Anderson-Schulz-Flory (ASF) plots for the considered hydrocarbons up to 20 C atoms are shown for three different temperatures in Figure 5.3d. Although olefins can re-adsorb and be hydrogenated, we observe negligible amounts of paraffins (Appendix C2). In experiments, much lower olefins-to-paraffins ratios were observed. The most likely explanation is that olefin re-adsorption and hydrogenation can take place on less-reactive surfaces. For instance, the overall hydrogenation barriers on the terrace (001) surface are lower than on the corrugated surface. The ASF plots also show a  $C_2$  selectivity below the ASF trend, which was earlier observed for  $\chi$ -Fe-carbide (Chapter 4) and for Co [58, 59] and Fe [60, 61] catalysts. At each temperature, we determined the corresponding chain-growth probability ( $\alpha$ ) based on the slope of the ASF distribution. The chain-growth probabilities for all temperatures are shown in Figure



5.4f. The chain-growth probability is approximately 0.5 and varies only slightly with temperature going through a maximum. The experimental chain-growth probability is close to the predicted value.

The step-edge surface is fully covered under the simulated conditions as can be seen from Figure 5.4e. H, C and CH are the predominant species at the catalytic surface. Figure 5.4f depicts the reaction orders with respect to CO and H<sub>2</sub> in the same temperature range. The CO reaction order is close to zero, slightly lower than the unexpected positive experimental reaction order of 0.21. We speculate that this is due to the formation of CO<sub>2</sub> under experimental conditions, which is much more substantial in terms of CO<sub>2</sub> selectivity in the experiment (21%) than in the simulations (<0.01%). We attribute this difference to the water-gas shift reaction, likely taking place on other surface facets with a higher CO coverage. The higher than unity reaction order in H<sub>2</sub> indicates the importance of hydrogenation reactions. With increasing H<sub>2</sub> pressure, the chain-growth probability decreases at nearly constant CH<sub>4</sub> selectivity. This will lead to a higher H coverage because the C and CH coverage decreases. The reaction order in H<sub>2</sub> is however substantially higher than the experimental reaction order of 0.6. This can be linked to the high coverages of C and CH, which can be hydrogenated by more H at the surface. We refer to the work of Zijlstra et al. [62], who showed that inclusion of less-reactive surfaces in a microkinetic model can result in migration of CH<sub>x</sub> species from the high-reactive step-edge to a less-reactive terrace, decreasing the CH<sub>x</sub> coverage.

The reaction network containing the C- and O-based rates with respect to the rate of CO dissociation at a temperature of 525 K and 1 bar is shown in Figure 5.4a. CO dissociation preferentially occurs via H-assisted CO dissociation with a very small contribution of direct CO dissociation. CH is involved in the growth of longer hydrocarbons via coupling with CH and CR equivalents. For instance, C<sub>3</sub> species are formed by CH-CCH<sub>3</sub> coupling. Formation of CH<sub>2</sub>CH<sub>2</sub> involves reaction of CH with CH<sub>3</sub> followed by a series of (de)hydrogenation reactions (CHCH<sub>3</sub> → CCH<sub>3</sub> → CCH<sub>2</sub> → CHCH<sub>2</sub> → CH<sub>2</sub>CH<sub>2</sub>). As the rate of CH-CCH<sub>3</sub> coupling is higher than the rate of dehydrogenation of CCH<sub>3</sub>, the selectivity to C<sub>3</sub> is higher than that of CH<sub>2</sub>CH<sub>2</sub>. O atoms are preferentially removed via direct hydrogenation in two steps to H<sub>2</sub>O.

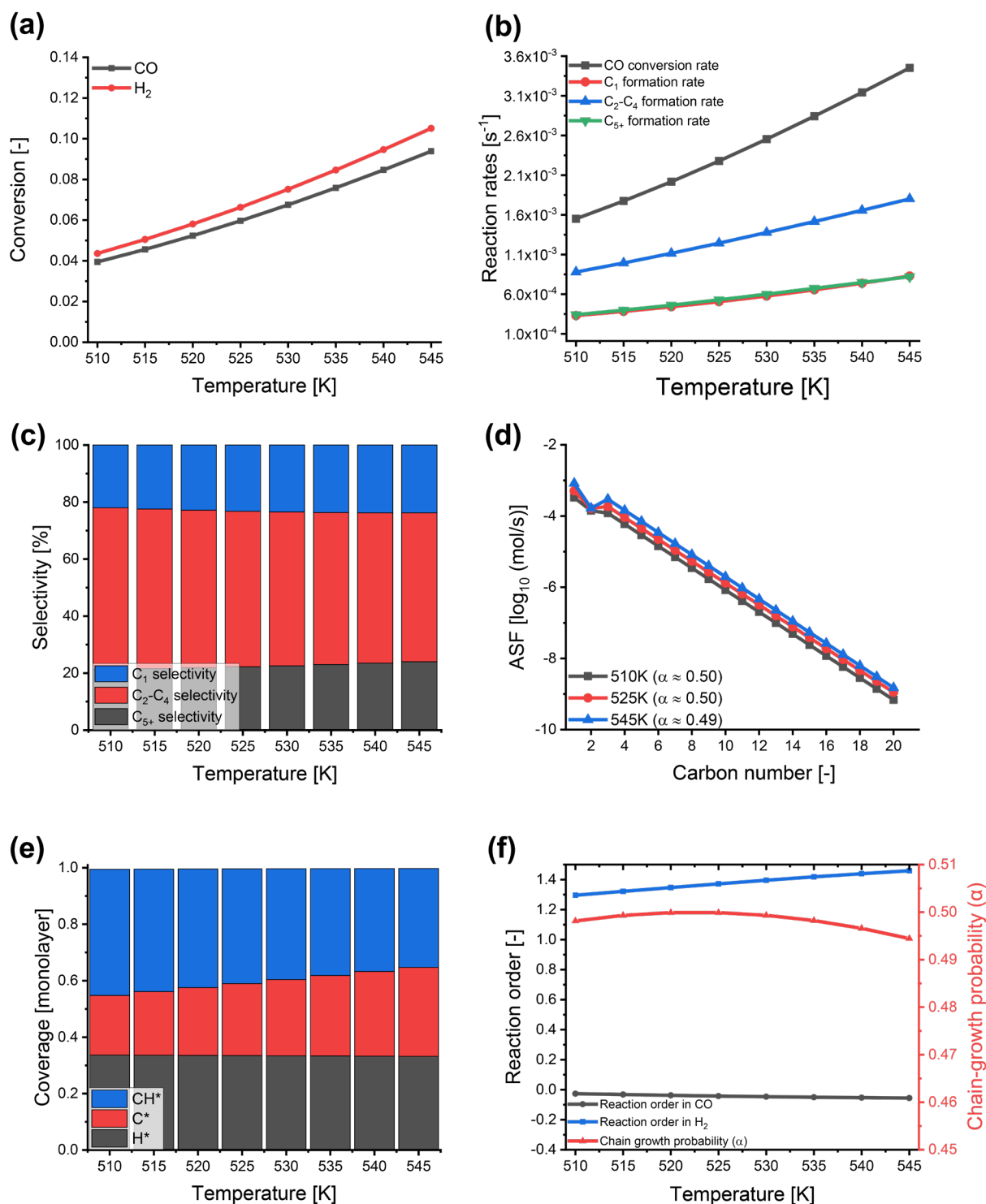


**Figure 5.3:** Microkinetics simulations of the FT reaction on the  $\text{Fe}_2\text{C}-(011)$  surface between 510 K and 545 K at 1 bar in the zero-conversion limit. (a) CO and  $\text{H}_2$  conversion. (b) Reaction rate for the  $\text{C}_1$  species (red),  $\text{C}_2\text{-C}_4$  species (blue),  $\text{C}_{5+}$  species (green) and the CO consumption rate (dark grey). (c) Selectivities as a function of the temperature on the (011) surface for  $\text{C}_1$  species (blue bar),  $\text{C}_2\text{-C}_4$  species (red bar) and  $\text{C}_{5+}$  species (dark grey bar). (d) ASF distribution at 510 K (dark grey), 525 K (red) and 545 K (blue). (e) Surface coverages. (f) Reaction order in CO (dark grey) and  $\text{H}_2$  (blue) and chain-growth probability (red).

Figure 5.4b and Figure 5.4c show the DRC and DCGC analysis, at 525 K and 1 bar. CO dissociation is not significantly contributing to the rate control, which is very different for Co [39] and Ru [63]. Instead, the dominant rate-controlling steps are the chain-growth steps, in particular CH-CH<sub>3</sub> coupling and CH-C(CH<sub>2</sub>)<sub>n</sub>CH<sub>3</sub> (where  $0 \leq n \leq 17$ ). CH<sub>3</sub> hydrogenation also contributes to the rate control, while HCO dissociation is slightly rate-inhibiting. Formation of olefins on the surface also inhibits the rate. The high DRC value for CH-CH<sub>3</sub> coupling can be explained by the relatively high barriers for C-C coupling. The DCGC analysis shows that CH-C(CH<sub>2</sub>)<sub>n</sub>CH<sub>3</sub> coupling controls chain-growth, while hydrogenation of CCH(CH<sub>2</sub>)<sub>n</sub>CH<sub>3</sub> intermediates inhibits chain-growth. The latter reaction leads to formation of olefins, which can desorb. These two reactions completely control the chain-growth vs. termination. This also explains the strong dependence of the kinetics on the H<sub>2</sub> partial pressure.

**Table 5.4:** Experimental kinetic data for a pure  $\epsilon$ -Fe-carbide catalyst [57] and simulated kinetic data for the (011) surface of  $\epsilon$ -Fe-carbide for the FT reaction at 1 bar.

Parameter	Experiment (1 bar)	Simulations (1 bar)
Temperature range (K)	525	510 – 545
Turnover frequency (mol/mol s)	$1.7 \cdot 10^{-3}$	$1.6 \cdot 10^{-3}$ - $3.5 \cdot 10^{-3}$
Reaction order CO & H <sub>2</sub> (-)	0.21 & 0.6	-0.05 & 1.37
Chain-growth probability ( $\alpha$ ) (-)	0.50	0.50-0.49
C <sub>1</sub> selectivity (%)	25	21 - 24
C <sub>2+</sub> selectivity (%)	75	79 - 76
CO <sub>2</sub> selectivity (%)	<< 0.01	<< 0.01
Residence time (s)	1-100 (s)	100 (s)
CO Conversion (%)	< 10	3.9 - 9.4

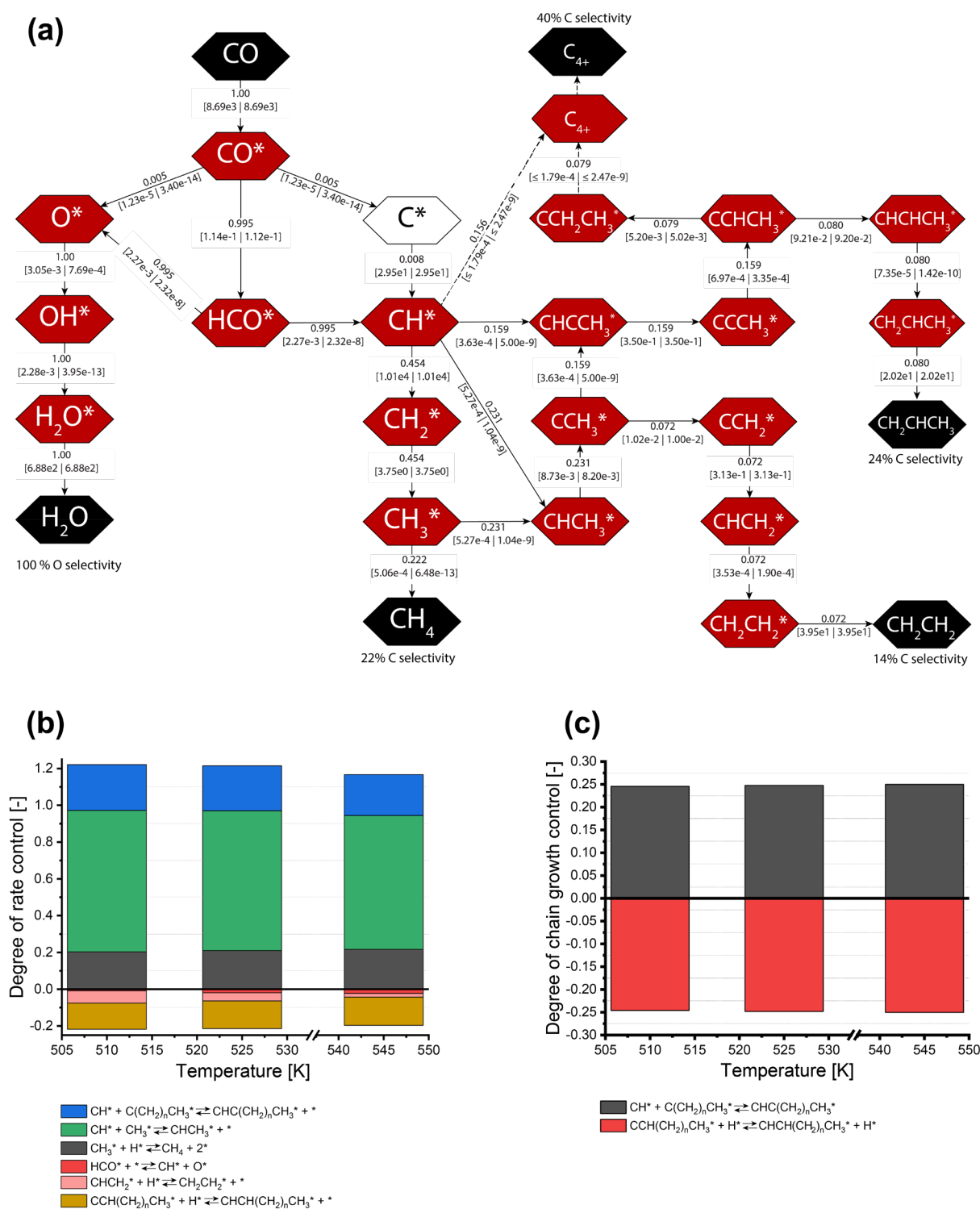


**Figure 5.4:** (a) Reaction network analysis at 525 K and 1 bar. The red hexagons represent the major intermediate species, the black hexagons represent the major gaseous components, the grey hexagons represent the minor gaseous components and the white hexagon represents minor intermediate species. The remainder of the intermediate species and products are omitted, as their values were lower than the limit ( $10^{-4}$ ) relative to the flux of CO adsorption. (b) DRC analysis at 510 K, 525 K and 545 K. (c) DCGC analysis at 510 K, 525 K and 545 K.

We next determined the influence of the total reaction pressure on the modelled kinetics for the (011) surface of  $\epsilon$ -Fe-carbide. The total pressure was varied between 0.1 bar and 5 bar, while keeping the  $H_2/CO$  ratio unity. The predicted kinetics are again compared to experimental data collected in Table 5.5 [57]. The temperature was varied between 510 K and 545 K. The main results for these simulations are shown in Figure 5.5.

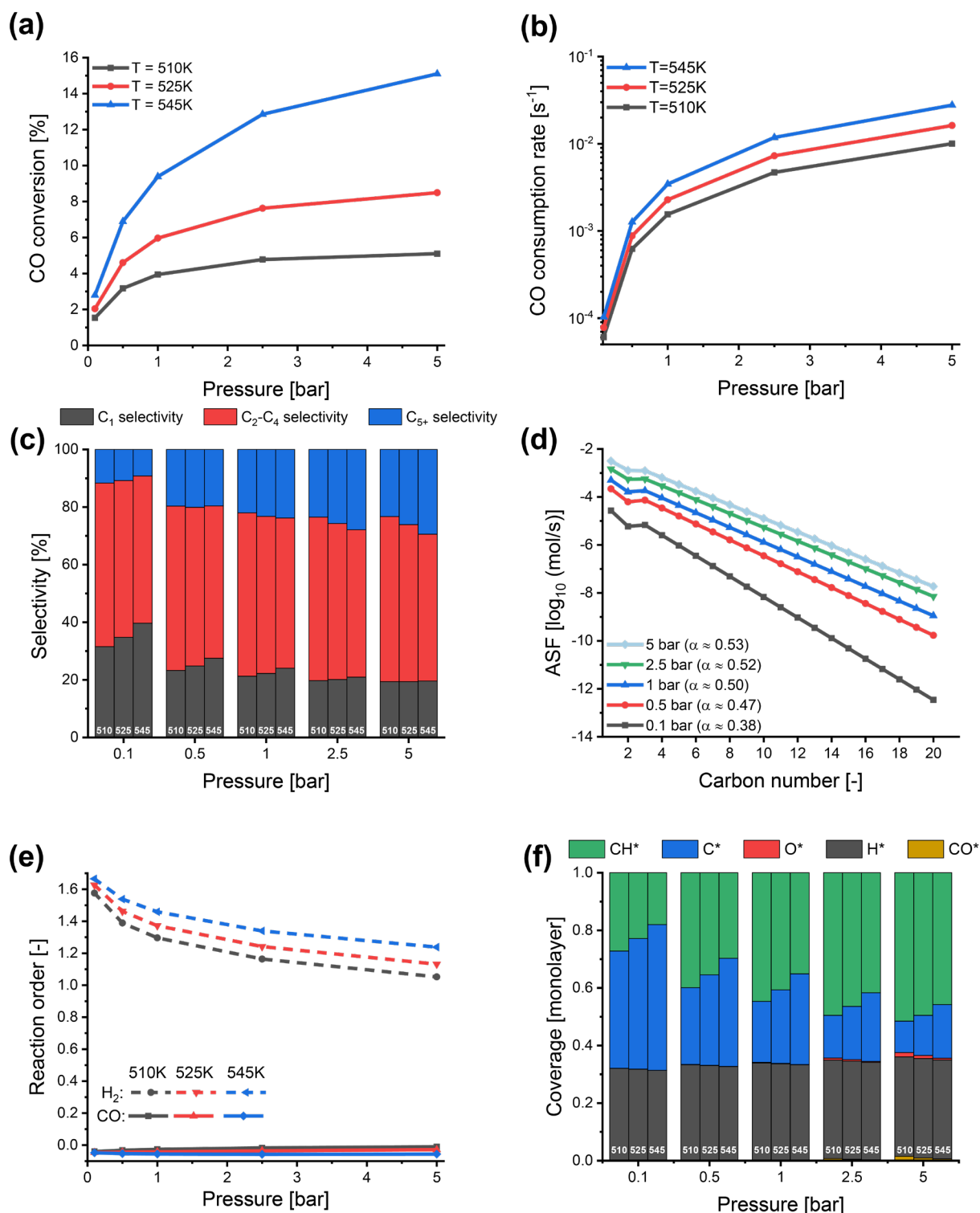
Figure 5.5a shows the CO conversion as a function of the pressure. CO conversion increases with total reaction pressure in a way that resembles an adsorption isotherm. The conversion shown in the chosen pressure and temperature range is below 15%. The CO conversion dependency on pressure correlates well with the CH trend with pressure. This is expected because the FT reaction operates in the chain-growth limited regime at this surface. CH is the main chain-growth monomer for this case. Figure 5.5b shows the CO consumption rates at 510 K, 525 K and 545 K as a function of the total pressure. The CO consumption rates increase with total pressure. For instance, at 525 K the CO consumption rate increases from  $7.8 \cdot 10^{-5} \text{ s}^{-1}$  at 0.1 bar to  $1.6 \cdot 10^{-2} \text{ s}^{-1}$  at 5 bar. The CO consumption rate scales nearly linear with pressure in the range 0.5-5 bar, in good correspondence with the experimental data.[57] In Figure 5.5c, we show the selectivity towards  $C_1$ ,  $C_2$ - $C_4$ , and  $C_{5+}$  species as a function of the total pressure for the three chosen temperatures. The  $C_2$ - $C_4$  selectivity is around 55% at 525 K and remains relatively constant within the chosen pressure range. The trends at the two other temperatures are similar. An increase in the total pressure leads to an increase in  $C_{5+}$  selectivity from 11% to 26% at 525 K at the expense of the  $CH_4$  selectivity from 35% to 19%. At 0.1 bar,  $CH_4$  selectivity increases from 32% to 40% with increasing temperature. This can be explained by a decrease in surface coverage of CH (see Figure 5.5f), which is a key component in chain growth. The lower CH surface coverage results in a lower rate for chain-growth, explaining the increased  $CH_4$  selectivity. At 5 bar,  $CH_4$  selectivity is relatively stable with increasing temperature. While  $C_{5+}$  selectivity increases,  $C_2$ - $C_4$  selectivity decreases due to an increase in the chain-growth rate. Oxygen removal is not influenced over the chosen pressure range and  $H_2O$  remains the main product of O removal.

Figure 5.5d shows the ASF distribution at 525 K for five different total pressures in the studied range. Corresponding with the experimental data, the chain-growth probability increases significantly at low pressures, from 0.38 at 0.1 bar to 0.50 at 1 bar. An increase of the pressure from 1 bar to 5 bar results in an increase in the chain-growth probability to 0.53. In the experiments, the chain-growth probability increased from 0.46 at 0.45 bar to 0.5 at 1 bar, and from  $\sim 0.50$  to  $\sim 0.52$  going from 1 bar to 3.6 bar.

The reaction orders for CO and H<sub>2</sub> are shown in Figure 5.5e. Microkinetics simulations predict that the reaction order in CO is roughly -0.05 and slightly increases to 0 at 5 bar. The reaction order in CO is lower compared to experiments (~0.21). This discrepancy was explained above by considering the water-gas shift reaction, which would lead to enhanced CO<sub>2</sub> formation. The reaction order in H<sub>2</sub> decreases with increasing pressure, from 1.6 at 0.1 bar to 1.1 at 5 bar. This decrease can be explained by the increasing CH coverage at the expense of C coverage concomitant with a slight increase in H coverage, as follows from Figure 5.5f. Likely, the increased H adsorption rate with increasing pressure leads to a higher ratio of CH/C at the surface, facilitating chain-growth and making the reaction less hydrogen dependent.

**Table 5.5:** Experimental kinetic data for a pure  $\epsilon$ -Fe-carbide catalyst [57] and simulated kinetic data for the (011) surface of  $\epsilon$ -Fe-carbide for the FT reaction at 525 K.

Parameter	Experiment (0.45 bar)	Simulations (0.5 bar)	Experiment (2.7 bar)	Simulations (2.5 bar)	Experiment (3.6 bar)	Simulations (5 bar)
Turnover frequency (mol/mol s)	$8.3 \cdot 10^{-4}$	$8.8 \cdot 10^{-4}$	$2.7 \cdot 10^{-3}$	$7.3 \cdot 10^{-3}$	$3.2 \cdot 10^{-3}$	$1.6 \cdot 10^{-2}$
Chain-growth probability ( $\alpha$ ) (-)	0.46	0.48	0.51	0.51	0.52	0.51
C <sub>1</sub> selectivity (%)	27	25	25	20	24	19
C <sub>2+</sub> selectivity (%)	73	75	75	80	76	81
CO <sub>2</sub> selectivity (%)	<< 0.01		<< 0.01		<< 0.01	



**Figure 5.5:** Microkinetics simulations of the FT reaction on the  $\text{Fe}_2\text{C}-(011)$  surface between 0.1 bar and 5 bar, and between 510 K and 545 K in the CSTR model. (a) CO conversion at 510 K (dark grey), 525 K (red) and 545 K (blue). (b) CO consumption rate at 510 K (dark grey), 525 K (red) and 545 K (blue). (c) C-based selectivities between 0.1 bar and 5 bar (at 510 K, 525 K and 545 K from left to right), for C<sub>1</sub> species (dark grey bar), C<sub>2</sub>-C<sub>4</sub> species (red bar) and C<sub>5</sub>+ species (blue bar). (d) ASF distribution at 525 K at 0.1 bar (dark grey), 0.5 bar (red), 1 bar (blue), 2.5 bar (dark green) and 5 bar (light green). (e) Reaction order in CO (solid lines) and H<sub>2</sub> (dashed lines) at 510 K (dark grey), 525 K (red) and 545 K (blue). (f) Surface coverages between 0.1 bar and 5 bar (at 510 K, 525 K and 545 K from left to right).

The dominant reaction pathways in the FT reaction are not substantially influenced by the total reaction pressure (Appendix C2). As expected, there is a difference in the relative reaction rates, since the selectivity is dependent on the pressure. DRC and DCGC analyses at 510 K, 525 K and 545 K are shown in Figure 5.6a and 5.6b, respectively. The  $\text{CH}_3$  hydrogenation step at 0.1 bar has a higher DRC than at higher pressures. This is likely caused by the higher  $\text{CH}_4$  selectivity at the lowest pressure. Interestingly, at higher pressure, O removal and HCO dissociation start contributing to the rate control. Thus, chain-growth rates increase with pressure due to a higher H coverage and higher CH/C coverage at the surface. As a consequence, chain-growth itself becomes less rate-controlling and formation of the chain-growth monomer through HCO dissociation starts contributing to the DRC. O hydrogenation also contributes to the rate control at low temperature. In line with this finding, chain-growth is controlling the chain-growth probability in the whole temperature and pressure range, while only at the highest pressures there is a slight contribution of HCO dissociation controlling chain-growth. Formation of ethylene via CH- $\text{CH}_3$  coupling inhibits chain-growth.

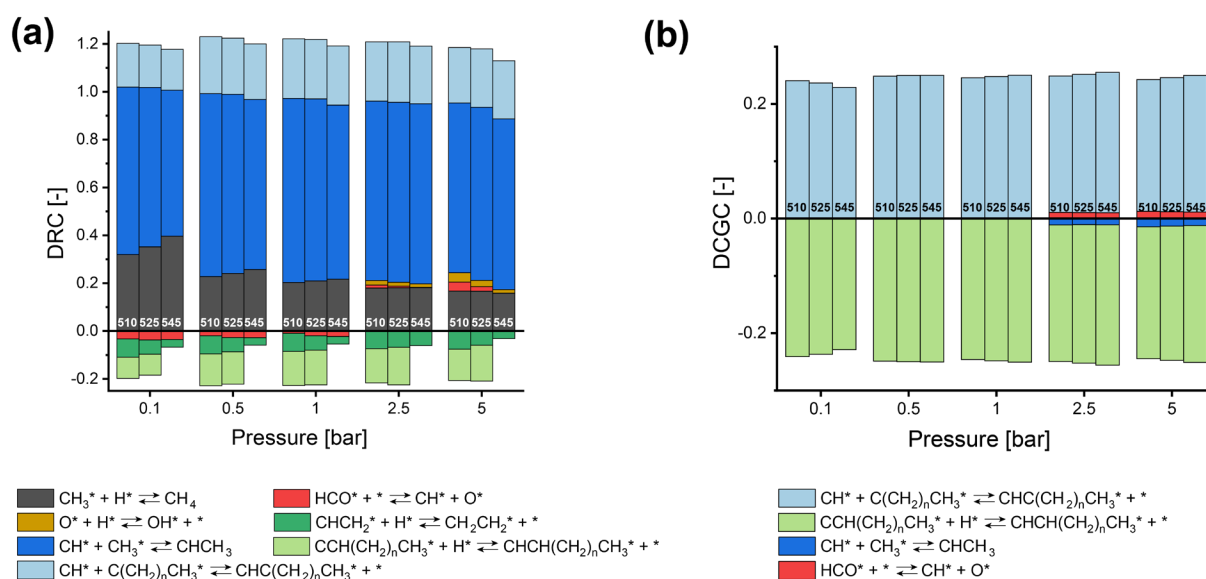


**Figure 5.6:** Rate and chain-growth control analysis between 0.1 bar and 5 bar (at 510 K, 525 K, and 545 K from left to right). (a) DRC analysis. (b) DCGC analysis.



### 5.3.4 Dual surface microkinetic modelling

We also considered the combination of the stepped (011) surface with the less reactive terrace (001) surface in one model in which migration of surface adsorbates between the two surfaces was allowed. For these simulations, we set the ratio of the two surfaces to unity, which is in reasonable agreement with the Wulff predictions shown in Table 5.1. The migration barriers and corresponding vibrational partition function for all surface species are listed in Appendix C.3. We employed again a CSTR model for these simulations at 1 bar, keeping the temperature range and H<sub>2</sub>/CO ratio the same as the microkinetics simulations described above for the single surface models. The kinetic parameters used as input for the microkinetic model can be found in Table 5.2-5.3 and Appendix C.2-C3. The residence time of the CSTR was chosen so that the CO conversion was below 10% in this temperature range (Figure 5.7a).

The CO consumption rate increases from  $1.3 \cdot 10^{-2} \text{ s}^{-1}$  at 510 K to  $6.6 \cdot 10^{-2} \text{ s}^{-1}$  at 545 K, which is approximately one order of magnitude higher as compared to the CO consumption rate on the stepped surface. Given that the rate on the stepped surface is limited by coupling reactions, the higher overall rate is mainly due to faster CH removal via the terrace surface. Note that the CO dissociation rate on the terrace surface is negligible.

The C-based selectivities for the terrace and the step-edge surface are shown in Figure 5.7c. CH<sub>4</sub> is predominantly produced on the terrace, while both surfaces are involved in the formation of C<sub>2+</sub> hydrocarbons. The C<sub>2</sub>-C<sub>4</sub> selectivity increases by approximately 8% when the temperature is raised from 510 K and 545 K at the expense of the CH<sub>4</sub> and the C<sub>5+</sub> selectivity. The CO<sub>2</sub> selectivity is not affected by using a dual surface model. There are two reasons for this. First, CO dissociation does not occur on the terrace surface due to the high overall barrier of CO dissociation. Second, O and OH are much more stable on the stepped surface than on the terrace surface. Therefore, migration of these species is negligible and the dominant O removal pathway remains H<sub>2</sub>O formation.

Figure 5.7d shows the ASF plot for these simulations at three different temperatures. At 525 K, the chain growth probability is around 0.5, which is very similar to the predictions made with the single surface model. Different from the single surface model, the chain-growth probability decreases slightly (from 0.52 at 510 K to 0.47 at 545 K), which is discussed in more detail below. Similar to the single surface model, olefins are the primary products with negligible paraffins formation (see Appendix C.3). The finding that also on terrace sites no paraffins are formed can be explained by the relatively high barrier for CH<sub>2</sub>CH<sub>2</sub> hydrogenation on this

surface. We earlier found that the barrier for  $\text{CH}_2\text{CH}_3$  hydrogenation on the stepped surface is so high that olefins are the dominant products on this surface as well.

The surface coverages on the individual stepped and terrace surfaces are shown in Figure 5.7e. The step-edge surface is nearly completely covered by predominantly H and O species. There are also some C and CH adsorbates, much lower than observed in the step-edge simulations in which also appreciable amounts of C and CH were present. The reason is the migration of C and CH species to the terrace on which coupling reaction are facile. The relatively high O coverage points to a change in the rate-limiting step to O removal. The terrace surface is approximately half covered by H and half by CO.

The reaction orders with respect to CO and  $\text{H}_2$  are shown in Figure 5.7f. The CO reaction order is -0.2, which is lower as compared to the (slightly positive) CO reaction order determined for the single surface microkinetics simulations. The slightly negative reaction order can be linked to the high surface coverage of CO on the terrace surface. The reaction order in  $\text{H}_2$  for these dual surface simulations is nearly the same as determined by the single surface simulations.

Figure 5.8a shows the reaction network for the formation of the different products for simulations carried out at a temperature of 525 K and at 1 bar. As expected, the mechanism for CO dissociation and O removal are unchanged by the inclusion of the terrace surface, because they mainly occur on the step-edge surface. CO dissociation proceeds via an HCO intermediate and O removal via two consecutive hydrogenation steps. The mechanism for chain growth changes for the dual surface model as compared to the single surface model. After HC-O bond scission, the CH species migrates to the terrace surface. The dominant mechanism for chain growth on the terrace is CH-CH coupling. The reaction network involves then dehydrogenation to CCH, after which the CCH species migrates to the step-edge. On the step-edge site, the CCH is hydrogenated twice, forming a  $\text{CCH}_3$  species.  $\text{CCH}_3$  migrates back to the terrace, where it is coupled to a CH, forming a CH- $\text{CCH}_3$  coupling.  $\text{CHCCH}_3$  is dehydrogenated on the terrace and hydrogenates on the step-edge to  $\text{CCHCH}_3$ .  $\text{C}_\alpha$  hydrogenation of the  $\text{CCHCH}_3$  followed by  $\text{C}_\beta$  hydrogenation leads to chain termination, while  $\text{C}_\beta$  hydrogenation followed by migration to the terrace leads to chain growth.

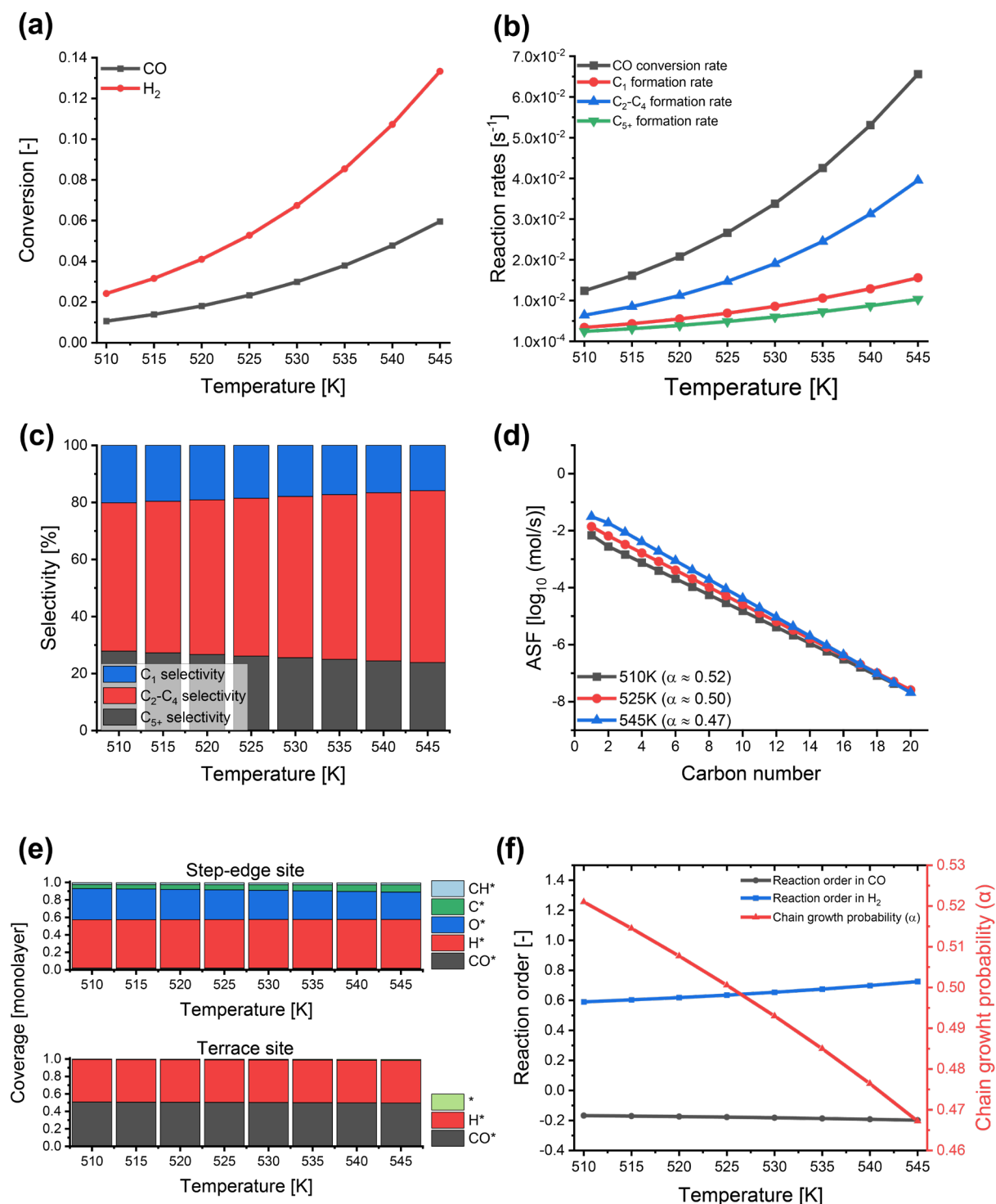


**Figure 5.7:** Microkinetics simulations of the FT reaction on the  $\text{Fe}_2\text{C}-(011)$  surface between 510 K and 545 K at 1 bar in the CSTR model. (a) CO and  $\text{H}_2$  conversion. (b) Reaction rate for the  $\text{C}_1$  species (red),  $\text{C}_2\text{-C}_4$  species (blue),  $\text{C}_{5+}$  species (green) and the CO consumption rate (dark grey). (c) Selectivities as a function of the temperature for  $\text{C}_1$  species (blue bar),  $\text{C}_2\text{-C}_4$  species (red bar) and  $\text{C}_{5+}$  species (dark grey bar). (d) ASF distribution at 510 K (dark grey), 525 K (red) and 545 K (blue). (e) Surface coverages for the stepped (011) (top) and the terrace (001) (bottom) surfaces. (f) Reaction order in CO (dark grey) and  $\text{H}_2$  (blue) and chain-growth probability (red).

The DRC and DCGC analyses for the dual surface model at 1 bar and 525 K are shown in Figure 5.8b and Figure 5.8c, respectively. O removal on the stepped surface is controlling to a significant extent the overall CO consumption rate with contributions from O and OH hydrogenation. This is different from the single surface model, for which chain growth was the dominant rate-controlling step. Overall, this is due to the lower Fe-carbon binding energy on the terrace sites, which leads to lower barriers for coupling reactions. Although O removal steps are more rate-controlling, CH-CH coupling and CH-C(CH<sub>2</sub>)<sub>n</sub>CH<sub>3</sub> coupling reactions on the terrace show a significant contribution to the DRC as well. HCO dissociation on the step is slightly rate-inhibiting, because this reaction leads to more O on the stepped surface. CH migration is slightly rate-limiting, as CH is adsorbed more favourable on the step than on the terrace. Hydrogenation of CHCH<sub>2</sub> and CHCH(CH<sub>2</sub>)<sub>n</sub>CH<sub>3</sub> species is slightly rate inhibiting.

The DCGC analysis shows that CH-C(CH<sub>2</sub>)<sub>n</sub>CH<sub>3</sub> coupling on the terrace predominantly controls chain growth, followed by O removal on the stepped surface. O removal has a positive effect on chain growth, as this leads to more sites for CO dissociation. Hydrogenation of CHCH(CH<sub>2</sub>)<sub>n</sub>CH<sub>3</sub> on the step intermediates inhibits chain growth, because this reaction leads to formation of olefins, which can desorb. A smaller inhibiting effect is found for the CH-CH and CH-CCH<sub>3</sub> coupling on the terrace surface.

Overall, the microkinetics for the dual surface model show that the chain-growth limitations observed for the more reactive stepped surface can be alleviated by the availability of a less reactive (terrace) surface on which coupling reactions are more facile. The microkinetics simulations using only the stepped surface are in much better agreement with the experimental kinetics than those obtained with the dual surface microkinetic model. This can indicate that migration of surface species is less important on Fe-carbides than on Co catalysts. Besides the strong bonding of C-containing species, another explanation to be mentioned is the larger size of Fe-carbide particles in experimental studies in comparison with Co particles.

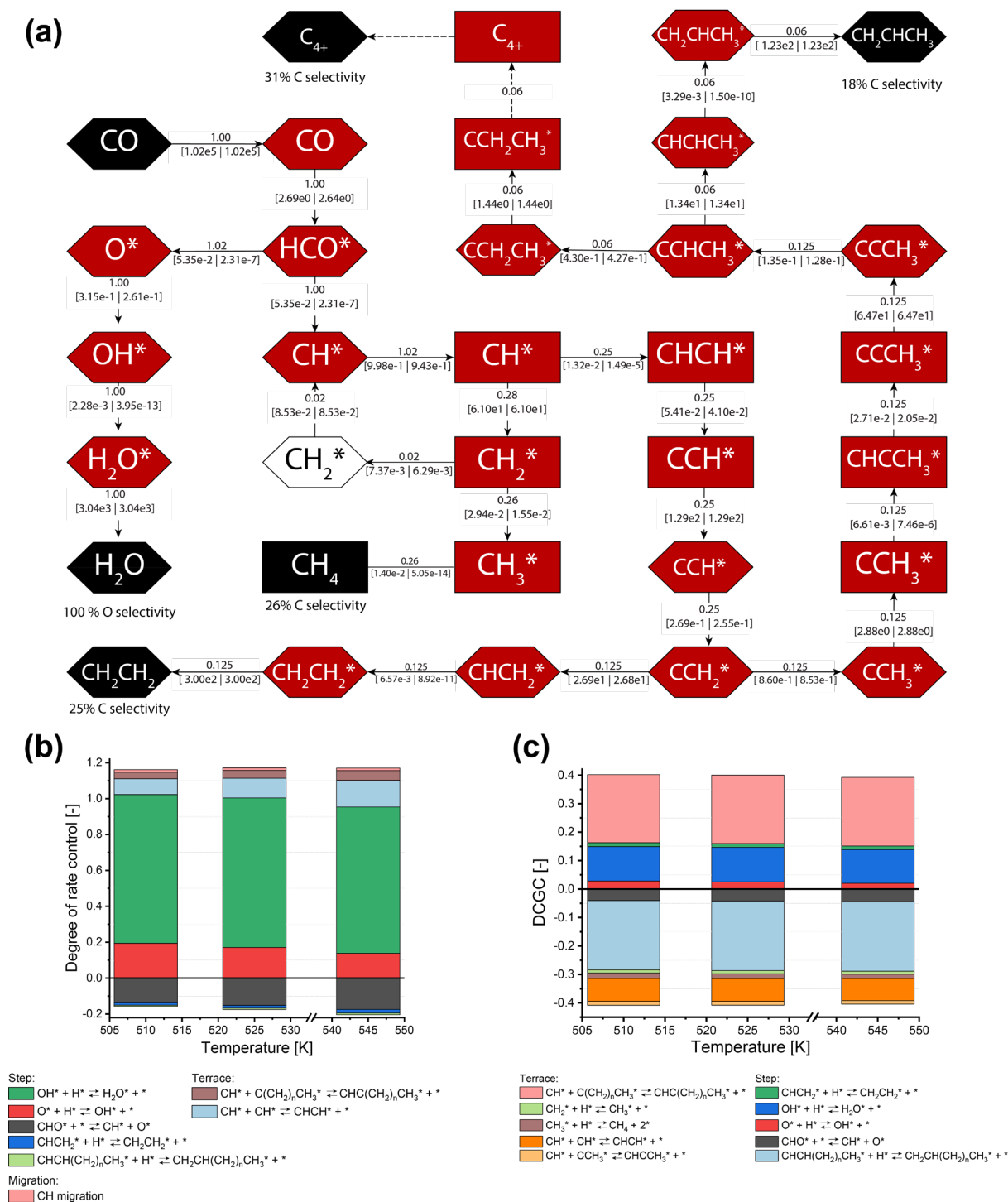


**Figure 5.8** (a) Reaction network analysis at 525 K and 1 bar. The hexagons represent the step-edge surface and the rectangles represent the terrace surface. The red shapes represent the major intermediate species, the black shapes represent the major gaseous components and the white hexagon represents minor intermediate species. The remainder of the intermediate species and products are omitted, as their values were lower than the limit ( $10^{-4}$ ) relative to the flux of CO adsorption. (b) DRC analysis (c) DCGC analysis

### 5.5 Operation regime $\epsilon$ -Fe-carbide

The simulated kinetic data for the stepped (011) surface of  $\epsilon$ -Fe-carbide are in good agreement with experimental data for a pure  $\epsilon$ -Fe-carbide catalyst. Clearly, the kinetics for this phase are very different from those observed for Co and Ru metal catalysts. In the work of Filot et al. [32], it was established that the FT reaction can proceed in three different operating regimes. The activity and selectivity can be described by carbon and oxygen binding energies based on scaling laws. Too low carbon and oxygen binding energy result in a slow rate of CO dissociation, resulting in a monomer formation limit where CO dissociation is the rate-controlling step (e.g., Ni(110)). Figure 5.9 shows the reaction rate as a function of the metal-carbon (M-C) and metal-oxygen (M-O) interaction energies for Hägg carbide and  $\epsilon$ -Fe-carbide are shown with respect to the interaction energies on Ru(11 $\bar{2}$ 1). For comparative reasons, we also show the M-C and M-O interaction energies for Ni(110), Co(11 $\bar{2}$ 1), and Fe(110).

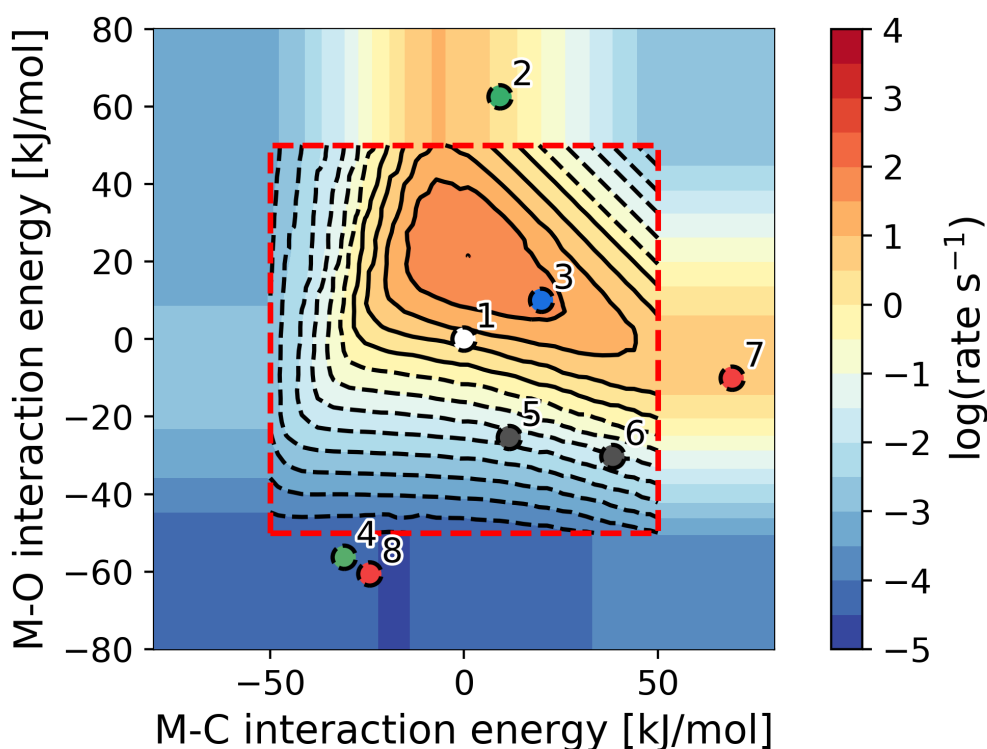


**Figure 5.9:** CO consumption rates as a function of the metal-carbon and metal-oxygen bond strengths ( $T = 500$  K;  $p = 20$  bar;  $H_2/CO = 2$ ) relative to the interaction energies on Ru(11 $\bar{2}$ 1) (1). The activation barriers for all elementary reaction steps were scaled to the metal-carbon and metal-oxygen bond strengths.[32] The positions of Co, Ni, Fe and Fe-carbide surfaces are indicated on the basis of computed strengths of their metal-carbon and metal-oxygen bonds: Ni(110) (2), Co(11 $\bar{2}$ 1) (3), Fe(110) (4), Fe<sub>5</sub>C<sub>2</sub>(010)<sub>0.25</sub> (5), Fe<sub>5</sub>C<sub>2</sub>(100) (6), Fe<sub>2</sub>C(001) (7) and Fe<sub>2</sub>C(011) (8). Note that the area outside of the red box is extrapolated. The colour scale bar at the right represents the logarithmic turnover rates in s<sup>-1</sup>.

A catalyst such as Ni works in the monomer formation limit and CH<sub>4</sub> is the dominant product, as the rate of hydrogenation is higher than the rate of CO dissociation. Especially, weak Ni-O bonding leads to a high barrier for CO dissociation, the slow supply of carbon building blocks

resulting in preferential  $\text{CH}_4$  formation. With increasing carbon and oxygen binding energies, the FT reaction chemistry shifts to a regime in which O removal reactions are controlling the overall rate. Ru operates in the O removal limit, however with chain-growth also contributing to the overall rate control.[32] Co presents a case in which both CO dissociation and O removal are controlling the rate to some degree, in agreement with the lower Co-C interaction energy. This kinetic regime agrees with kinetic modelling of experimental SSITKA data.[64, 65] and is characterized by a relatively high CO coverage and a negative CO reaction order. Microkinetics simulations of the Fischer-Tropsch reaction on a stepped Co surface confirm these aspects.[66] A third regime is the chain-growth limit operation, which corresponds to a strong carbon binding energy (and strong oxygen binding energy). Then, CO dissociation is fast and the rate is limiting by the growth of the chain at the surface. Typically, Fe-carbide surfaces interact strongly with both C and O and are expected to operate in this regime. The M-C and M-O interaction energies for  $(010)_{0.25}$  and  $(100)$  Hägg carbide surfaces are closer to those of Ru in comparison to the interaction energies for the  $(001)$  and  $(011)$  termination of  $\epsilon$ -Fe carbide. Microkinetics simulations for the stepped  $\text{Fe}_5\text{C}_2(100)$  surface predicted CO dissociation to be the most rate limiting step followed by the removal of oxygen, which indicates that the Hägg carbide operates in the same regime as  $\text{Co}(11\bar{2}1)$ . The stepped  $\epsilon$ -Fe-carbide surface investigated here by first-principles microkinetic theory simulations operates in the chain-growth limit. This can be explained by the much stronger Fe-C binding energy. The M-C and M-O interaction energies of the  $(110)$  surface of Fe are very similar to those of the stepped  $\epsilon$ -Fe-carbide surface. That is to say, despite the presence of C atoms in the surface and subsurface the reactivity of a stepped Fe-carbide surface is similar to that of a metallic Fe surface. We should not however that a stepped  $\text{Fe}(111)$  surface has even stronger Fe-C and Fe-O binding energies. Such a surface can dissociate CO but would exhibit a very low activity because of the low rate of (rate-limiting) chain growth. Obviously, metallic Fe is not stable under these conditions due to the favourable diffusion of C atoms in the Fe lattice.

The kinetic differences between the monomer formation and the chain-growth limited models were discussed in more detail in the work of Markvoort et al.[67] Consistent with the kinetic considerations therein, we find that the CO coverage in the chain-growth limit is very low, because CO dissociation is not limiting the overall reaction rate. Instead, the surface contains a large amount of the chain-growth monomer. Indeed, the surface contains mainly CH, the chain-growth monomer, C and H atoms and small amounts of the growing chains. The dominant rate-controlling step is the insertion of CH in growing chains. As outlined by Markvoort et al. [67],

the maximum in CO consumption rate corresponds to a catalyst with a high rate of CO dissociation and low enough carbon binding energy, so that the surface is not poisoned by carbon-containing species. The low CO consumption rate, intermediate chain-growth probability and relatively high CH<sub>4</sub> selectivity are inherent to the operation of  $\epsilon$ -Fe<sub>2</sub>C in the chain-growth limit.

## 5.6 Conclusions

We investigated the kinetics and mechanism of the FT reaction on  $\epsilon$ -Fe<sub>2</sub>C by DFT calculations and microkinetic modelling. We evaluated the planar (001) and the corrugated (011) surface to describe the reactions on the terrace and step-edge sites, respectively. DFT showed that CO dissociation on both surfaces proceeds via the HCO intermediate. Oxygen removal involves H<sub>2</sub>O formation on the stepped (011) surface, while CO<sub>2</sub> is the preferred O removal product on (001). The preferred C-C coupling mechanism proceeds via C-CH<sub>2</sub> coupling on (001) and CH-CH<sub>3</sub> coupling on (011). As only the barrier for CO dissociation on the stepped (011) surface is low enough to correspond to experimental rates, microkinetics simulations focused on this surface in a CSTR model. Kinetic parameters such as the reaction rate, reaction orders, CH<sub>4</sub> selectivity and chain-growth probability correspond well with experimental data for a pure  $\epsilon$ -Fe<sub>2</sub>C catalyst. The stepped surface has an intermediate chain-growth probability of 0.5 (525 K, 1 bar, H<sub>2</sub>/CO = 1), meaning that C<sub>2</sub>-C<sub>4</sub> olefins are the main reaction products. Hydrogenation to paraffins is limited on the investigated surface. CO consumption rates are of the order 10<sup>-3</sup> s<sup>-1</sup>. CO dissociation proceeds via HCO formation and dissociation. H<sub>2</sub>O is the main O removal product, suggesting that this carbide phase does not make CO<sub>2</sub> as a primary product, consistent with experiments. CH is the chain-growth monomer and chain-growth occurs via CH-CH<sub>3</sub> and CH-CR coupling. Chain termination involves hydrogenation of CHC(CH<sub>2</sub>)<sub>n</sub>CH<sub>3</sub> species. The overall CO consumption rate is mostly limited by coupling reactions with the CH chain-growth monomer. CO dissociation is intrinsically fast compared to chain-growth, which implies a different operating regime of this catalyst in comparison to Co FT catalysts. The intrinsically high rate of CO dissociation explains why the CO coverage is very low. The surface is mainly covered by C and CH species. As C needs to be hydrogenated to CH before coupling can occur, the total pressure affects the rate mainly due to a shift to more CH species involved in the rate-controlling chain-growth step. The low CO consumption rate, intermediate chain-growth probability and relatively high CH<sub>4</sub> selectivity are inherent to the operation of  $\epsilon$ -Fe<sub>2</sub>C in the chain-growth limit.



## References

- [1] M.E. Dry, A.P. Steynberg, Commercial FT process applications, *Studies in Surface Science and Catalysis* 152 (2004) 406-481.
- [2] M. Dry, A. Steynberg, *Fischer-Tropsch Technology*, Elsevier, 2004.
- [3] L. Yong-Wang, Clean Diesel Production from Coal Based Syngas via Fischer-Tropsch Synthesis: Technology Status and Demands in China, *Chinese Academy* (2014) 1-13.
- [4] E. de Smit, F. Cinquini, A.M. Beale, O.V. Safonova, W. van Beek, P. Sautet, B.M. Weckhuysen, Stability and Reactivity of  $\epsilon$ - $\chi$ - $\theta$  Iron Carbide Catalyst Phases in Fischer-Tropsch Synthesis: Controlling  $\mu$ C, *Journal of the American Chemical Society* 132 (2010) 14928-14941.
- [5] R.J.P. Broos, B. Zijlstra, I.A.W. Filot, E.J.M. Hensen, Quantum-Chemical DFT Study of Direct and H- and C-Assisted CO Dissociation on the  $\chi$ -Fe<sub>5</sub>C<sub>2</sub> Hägg Carbide, *The Journal of Physical Chemistry C* 122 (2018) 9929-9938.
- [6] Q. Chang, C. Zhang, C. Liu, Y. Wei, A.V. Cheruvathur, A.I. Dugulan, J.W. Niemantsverdriet, X. Liu, Y. He, M. Qing, L. Zheng, Y. Yun, Y. Yang, Y. Li, Relationship between Iron Carbide Phases ( $\epsilon$ -Fe<sub>2</sub>C, Fe<sub>7</sub>C<sub>3</sub>, and  $\chi$ -Fe<sub>5</sub>C<sub>2</sub>) and Catalytic Performances of Fe/SiO<sub>2</sub> Fischer-Tropsch Catalysts, *ACS Catalysis* 8 (2018) 3304-3316.
- [7] B. Chen, D. Wang, X. Duan, W. Liu, Y. Li, G. Qian, W. Yuan, A. Holmen, X. Zhou, D. Chen, Charge-Tuned CO Activation over a  $\chi$ -Fe<sub>5</sub>C<sub>2</sub> Fischer-Tropsch Catalyst, *ACS Catalysis* 8 (2018) 2709-2714.
- [8] M.A. Petersen, J.-A. van den Berg, W.J. van Rensburg, Role of step sites and surface vacancies in the adsorption and activation of CO on  $\chi$ -Fe<sub>5</sub>C<sub>2</sub> surfaces, *The Journal of Physical Chemistry C* 114 (2010) 7863-7879.
- [9] M.O. Ozbek, J.H. Niemantsverdriet, Elementary reactions of CO and H<sub>2</sub> on C-terminated  $\chi$ -Fe<sub>5</sub>C<sub>2</sub> (001) surfaces, *Journal of Catalysis* 317 (2014) 158-166.
- [10] D.-B. Cao, Y.-W. Li, J. Wang, H. Jiao, Chain growth mechanism of Fischer-Tropsch synthesis on Fe<sub>5</sub>C<sub>2</sub> (0 0 1), *Journal of Molecular Catalysis A: Chemical* 346 (2011) 55-69.
- [11] J.M. Gracia, F.F. Prinsloo, J. Niemantsverdriet, Mars-van Krevelen-like mechanism of CO hydrogenation on an iron carbide surface, *Catalysis letters* 133 (2009) 257.
- [12] C.-F. Huo, Y.-W. Li, J. Wang, H. Jiao, Insight into CH<sub>4</sub> formation in iron-catalyzed Fischer-Tropsch synthesis, *Journal of the American Chemical Society* 131 (2009) 14713-14721.
- [13] A.C. B. Kniep, D. Niemeier, K.D. Becker, Eine in-situ Mössbauer-Untersuchung zur Bildung von Zementit, Fe<sub>3</sub>C, *Z. Anorg. Allg. Chem* 629 (2003) 1795-1804.
- [14] L.-J. Deng, C.-F. Huo, X.-W. Liu, X.-H. Zhao, Y.-W. Li, J. Wang, H. Jiao, Density Functional Theory Study on Surface C<sub>x</sub>H<sub>y</sub> Formation from CO Activation on Fe<sub>3</sub>C (100), *The Journal of Physical Chemistry C* 114 (2010) 21585-21592.
- [15] Y. Wang, Y. Li, S. Huang, J. Wang, H. Wang, J. Lv, X. Ma, Insight into CH<sub>4</sub> formation and chain growth mechanism of Fischer-Tropsch synthesis on  $\theta$ -Fe<sub>3</sub>C(031), *Chemical Physics Letters* 682 (2017) 115-121.
- [16] I. Wood, L. Vočadlo, K. Knight, D.P. Dobson, W. Marshall, G.D. Price, J. Brodholt, Thermal expansion and crystal structure of cementite, Fe<sub>3</sub>C, between 4 and 600 K determined by time-of-flight neutron powder diffraction, *Journal of Applied Crystallography* 37 (2004) 82-90.
- [17] R.J.P. Broos, B. Klumpers, B. Zijlstra, I.A.W. Filot, E.J.M. Hensen, A quantum-chemical study of the CO dissociation mechanism on low-index Miller planes of  $\theta$ -Fe<sub>3</sub>C, *Catalysis Today* (2019).
- [18] W.C. Chiou, E.A. Carter, Structure and stability of Fe<sub>3</sub>C-cementite surfaces from first principles, *Surface Science* 530 (2003) 88-100.
- [19] L.-L. Bao, C.-F. Huo, C.-M. Deng, Y.-W. Li, Structure and stability of the crystal Fe<sub>2</sub>C and low index surfaces, *Journal of Fuel Chemistry and Technology* 37 (2009) 104-108.
- [20] X. Yu, X. Zhang, Y. Meng, Y. Zhao, Y. Li, W. Xu, Z. Liu, CO adsorption, dissociation and coupling formation mechanisms on Fe<sub>2</sub>C(001) surface, *Applied Surface Science* 434 (2018) 464-472.
- [21] P. Wang, W. Chen, F.-K. Chiang, A.I. Dugulan, Y. Song, R. Pestman, K. Zhang, J. Yao, B. Feng, P. Miao, W. Xu, E.J.M. Hensen, Synthesis of stable and low-CO<sub>2</sub> selective  $\epsilon$ -iron carbide Fischer-Tropsch catalysts, *Science Advances* 4 (2018) eaau2947.

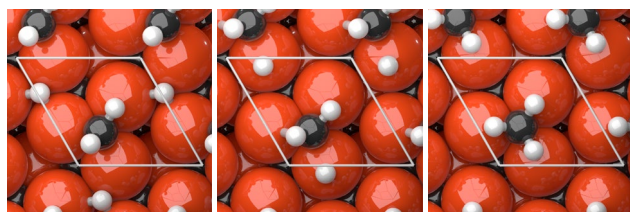
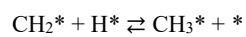
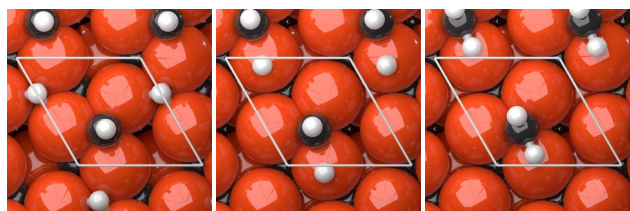
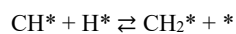
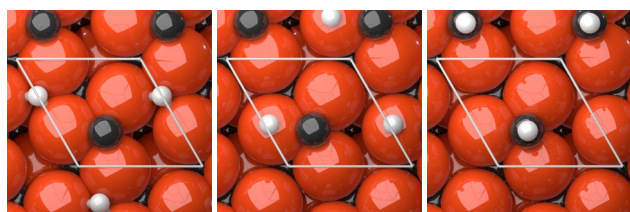
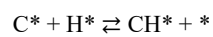
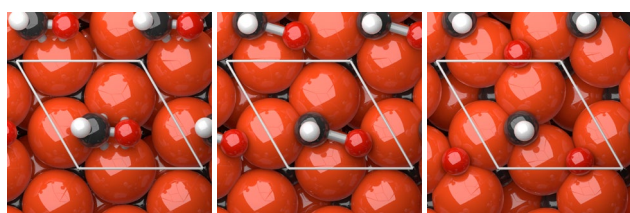
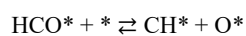
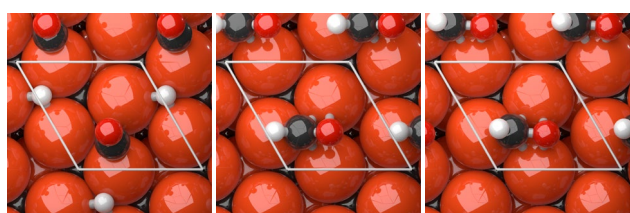
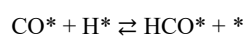
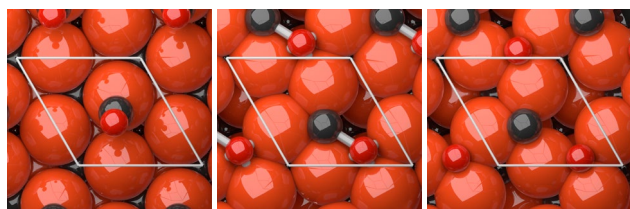
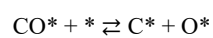
- [22] K. Xu, B. Sun, J. Lin, W. Wen, Y. Pei, S. Yan, M. Qiao, X. Zhang, B. Zong,  $\epsilon$ -Iron carbide as a low-temperature Fischer–Tropsch synthesis catalyst, *Nature Communications* 5 (2014) 5783.
- [23] L.J.E. Hofer, E.M. Cohn, W.C. Peebles, The Modifications of the Carbide,  $\text{Fe}_2\text{C}$ ; Their Properties and Identification, *Journal of the American Chemical Society* 71 (1949) 189-195.
- [24] S. Nagakura, Study of Metallic Carbides by Electron Diffraction Part III. Iron Carbides, *Journal of the Physical Society of Japan* 14 (1959) 186-195.
- [25] M. Manes, A.D. Damick, M. Mentser, E.M. Cohn, L.J.E. Hofer, Hexagonal Iron Carbide as an Intermediate in the Carbiding of Iron Fischer–Tropsch Catalysts<sup>1,2</sup>, *Journal of the American Chemical Society* 74 (1952) 6207-6209.
- [26] C. Fang, M. van Huis, H. Zandbergen, Structure and stability of  $\text{Fe}_2\text{C}$  phases from density-functional theory calculations, *Scripta Materialia* 63 (2010) 418-421.
- [27] R.A. van Santen, A.J. Markvoort, I.A.W. Filot, M.M. Ghouri, E.J.M. Hensen, Mechanism and microkinetics of the Fischer–Tropsch reaction, *Physical Chemistry Chemical Physics* 15 (2013) 17038-17063.
- [28] J. Cheng, P. Hu, P. Ellis, S. French, G. Kelly, M.C. Lok, Density functional theory study of iron and cobalt carbides for Fischer–Tropsch synthesis, *The Journal of Physical Chemistry C* 114 (2009) 1085-1093.
- [29] A. Govender, D. Curulla Ferré, J.W. Niemantsverdriet, A density functional theory study on the effect of zero-point energy corrections on the methanation profile on  $\text{Fe}$  (100), *ChemPhysChem* 13 (2012) 1591-1596.
- [30] M. Ojeda, R. Nabar, A.U. Nilekar, A. Ishikawa, M. Mavrikakis, E. Iglesia, CO activation pathways and the mechanism of Fischer–Tropsch synthesis, *Journal of Catalysis* 272 (2010) 287-297.
- [31] D.C. Sorescu, First-principles calculations of the adsorption and hydrogenation reactions of  $\text{CH}_x$  ( $x = 0, 4$ ) species on a  $\text{Fe}$  (100) surface, *Physical Review B* 73 (2006) 155420.
- [32] I.A.W. Filot, R.A. van Santen, E.J.M. Hensen, The Optimally Performing Fischer–Tropsch Catalyst, *Angewandte Chemie International Edition* 53 (2014) 12746-12750.
- [33] I.A.W. Filot, R.A. van Santen, E.J.M. Hensen, Quantum chemistry of the Fischer–Tropsch reaction catalysed by a stepped ruthenium surface, *Catalysis Science & Technology* 4 (2014) 3129-3140.
- [34] R. Anderson, H. Kölbels, M. Rálek, *The Fischer-Tropsch, Synthesis*, Academic Press, Inc (1984).
- [35] M. Dry, *The fischer-tropsch synthesis*, *Catalysis science and technology* 1 (1981) 159-255.
- [36] A. Steynberg, M. Dry, Steynberg, *AP Fischer–Tropsch Technology*, Elsevier Amsterdam, 2004.
- [37] R. Van Hardeveld, F. Hartog, The statistics of surface atoms and surface sites on metal crystals, *Surface Science* 15 (1969) 189-230.
- [38] R. Van Hardeveld, F. Hartog, Influence of metal particle size in nickel-on-aerosil catalysts on surface site distribution, catalytic activity, and selectivity, *Advances in Catalysis*, Elsevier, 1972, pp. 75-113.
- [39] B. Zijlstra, R.J.P. Broos, W. Chen, I.A.W. Filot, E.J.M. Hensen, First-principles based microkinetic modeling of transient kinetics of CO hydrogenation on cobalt catalysts, *Catalysis Today* (2019).
- [40] G. Kresse, J. Furthmüller, Efficiency of ab-initio total energy calculations for metals and semiconductors using a plane-wave basis set, *Computational materials science* 6 (1996) 15-50.
- [41] G. Kresse, J. Hafner, Ab initio molecular-dynamics simulation of the liquid-metal–amorphous-semiconductor transition in germanium, *Physical Review B* 49 (1994) 14251.
- [42] M.P.A.T. Methfessel, A.T. Paxton, High-precision sampling for Brillouin-zone integration in metals, *Physical Review B* 40 (1989) 3616.
- [43] K.P. Huber, G. Herzberg, *NIST Chemistry WebBook*, NIST Standard Reference Database Number 69. Eds. PJ Linstrom and WG Mallard. National Institute of Standards and Technology. Gaithersburg MD 20899, webbook. nist. gov (1997).
- [44] G. Henkelman, H. Jónsson, Improved tangent estimate in the nudged elastic band method for finding minimum energy paths and saddle points, *The Journal of chemical physics* 113 (2000) 9978-9985.

- [45] I.A.W. Filot, Introduction to Microkinetic modeling, Technische Universiteit Eindhoven, Eindhoven, 2018.
- [46] I.A.W.Z. Filot, B.; Hensen, E. J. M., MKMCXX, a C++ program for constructing microkinetic models, <http://www.mkmcxx.nl>, (2019).
- [47] H.S. Fogler, Essentials of Chemical Reaction Engineering: Essenti Chemica Reactio Engi, Pearson Education, 2010.
- [48] C.A. Wolcott, A.J. Medford, F. Studt, C.T. Campbell, Degree of rate control approach to computational catalyst screening, *Journal of Catalysis* 330 (2015) 197-207.
- [49] I.A.W. Filot, B. Zijlstra, R.J.P. Broos, W. Chen, R. Pestman, E.J.M. Hensen, Kinetic aspects of chain growth in Fischer–Tropsch synthesis, *Faraday Discussions* 197 (2017) 153-164.
- [50] J.W. Niemantsverdriet, A.M. Van der Kraan, W.L. Van Dijk, H.S. Van der Baan, Behavior of metallic iron catalysts during Fischer-Tropsch synthesis studied with Moessbauer spectroscopy, x-ray diffraction, carbon content determination, and reaction kinetic measurements, *The Journal of Physical Chemistry* 84 (1980) 3363-3370.
- [51] R.A. Van Santen, Modern heterogeneous catalysis: an introduction, John Wiley & Sons, 2017.
- [52] J.-X. Liu, H.-Y. Su, D.-P. Sun, B.-Y. Zhang, W.-X. Li, Crystallographic dependence of CO activation on cobalt catalysts: HCP versus FCC, *Journal of the American Chemical Society* 135 (2013) 16284-16287.
- [53] T.A. Wezendonk, V.P. Santos, M.A. Nasalevich, Q.S.E. Warringa, A.I. Dugulan, A. Chojecki, A.C.J. Koeken, M. Ruitenbeek, G. Meima, H.-U. Islam, G. Sankar, M. Makkee, F. Kapteijn, J. Gascon, Elucidating the Nature of Fe Species during Pyrolysis of the Fe-BTC MOF into Highly Active and Stable Fischer–Tropsch Catalysts, *ACS Catalysis* 6 (2016) 3236-3247.
- [54] A. De Koster, R.A. Van Santen, Molecular orbital studies of the adsorption of CH<sub>3</sub>, CH<sub>2</sub>, and ch on Rh(111) and Ni(111) surfaces, *Journal of Catalysis* 127 (1991) 141-166.
- [55] T. Zhu, P.W. van Grootel, I.A.W. Filot, S.-G. Sun, R.A. van Santen, E.J.M. Hensen, Microkinetics of steam methane reforming on platinum and rhodium metal surfaces, *Journal of Catalysis* 297 (2013) 227-235.
- [56] I.A.W. Filot, R.J.P. Broos, J.P.M. van Rijn, G.J.H.A. van Heugten, R.A. van Santen, E.J.M. Hensen, First-principles-based microkinetics simulations of synthesis gas conversion on a stepped rhodium surface, *ACS Catalysis* 5 (2015) 5453-5467.
- [57] W. Chen, J. Chai, P. Wang, E.J.M. Hensen, Unpublished results.
- [58] P. Chaumette, C. Verdon, P. Boucot, Influence of the hydrocarbons distribution on the heat produced during Fischer-Tropsch synthesis, *Topics in Catalysis* 2 (1995) 301-311.
- [59] E.W. Kuipers, C. Scheper, J.H. Wilson, I.H. Vinkenburg, H. Oosterbeek, Non-ASF Product Distributions Due to Secondary Reactions during Fischer–Tropsch Synthesis, *Journal of Catalysis* 158 (1996) 288-300.
- [60] N. Egiebor, W. Cooper, B. Wojciechowski, Carbon number distribution of fischer—Tropsch CO-hydrogenation products from precipitated iron catalysts, *The Canadian Journal of Chemical Engineering* 63 (1985) 826-834.
- [61] N. Rice, C. Hsu, B. Wojciechowski, The effects of catalyst surface heterogeneity on the fischer-tropsch synthesis, *The Canadian Journal of Chemical Engineering* 66 (1988) 694-696.
- [62] B. Zijlstra, R.J.P. Broos, W. Chen, H. Oosterbeek, I.A.W. Filot, E.J.M. Hensen, Coverage Effects in CO Dissociation on Metallic Cobalt Nanoparticles, *ACS Catalysis* 9 (2019) 7365-7372.
- [63] I.A.W. Filot, Quantum chemical and microkinetic modeling of the Fischer-Tropsch reaction, Technische Universiteit Eindhoven, 2015.
- [64] W. Chen, I.A.W. Filot, R. Pestman, E.J.M. Hensen, Mechanism of Cobalt-Catalyzed CO Hydrogenation: 2. Fischer–Tropsch Synthesis, *ACS Catalysis* 7 (2017) 8061-8071.
- [65] W. Chen, R. Pestman, B. Zijlstra, I.A. Filot, E.J. Hensen, Mechanism of cobalt-catalyzed CO hydrogenation: 1. Methanation, *ACS catalysis* 7 (2017) 8050-8060.
- [66] B. Zijlstra, Microkinetic modeling of Fischer-Tropsch synthesis on cobalt, (2020).
- [67] R.A. van Santen, A.J. Markvoort, M.M. Ghouri, P.A.J. Hilbers, E.J.M. Hensen, Monomer Formation Model versus Chain Growth Model of the Fischer–Tropsch Reaction, *The Journal of Physical Chemistry C* 117 (2013) 4488-4504.

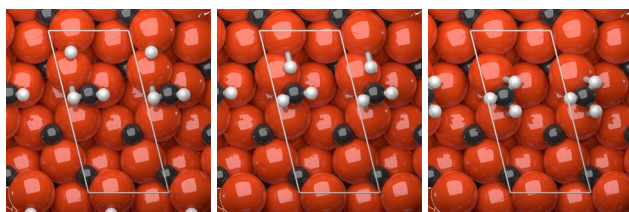
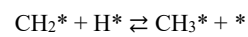
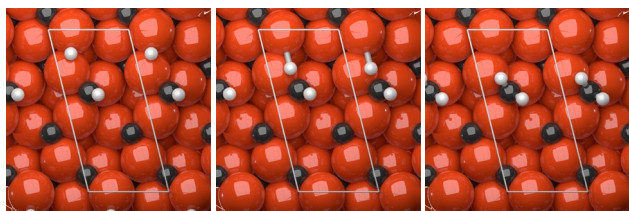
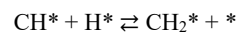
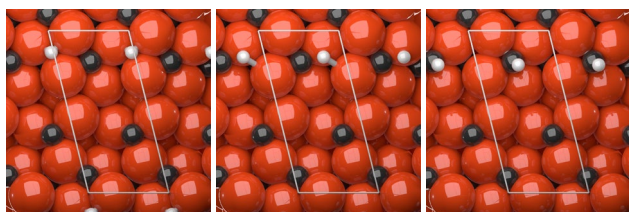
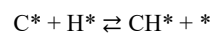
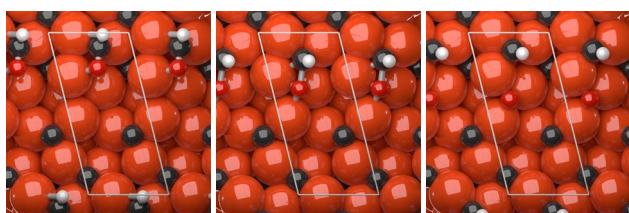
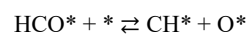
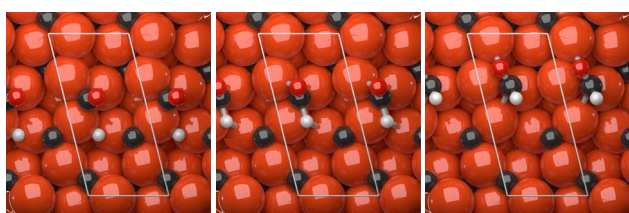
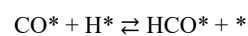
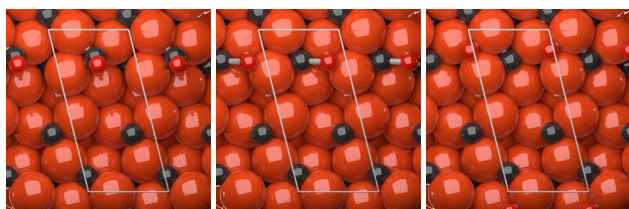
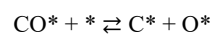
## Appendix C

## Appendix C.1 Geometries from DFT

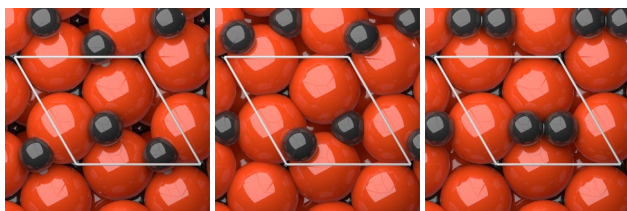
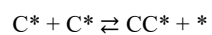
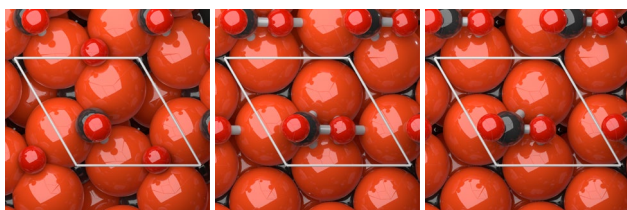
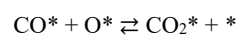
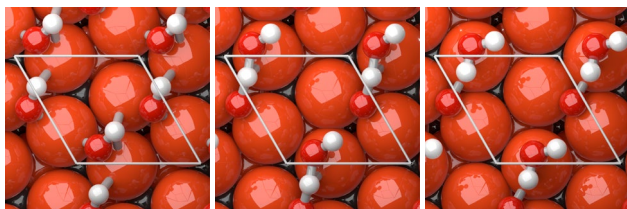
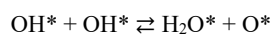
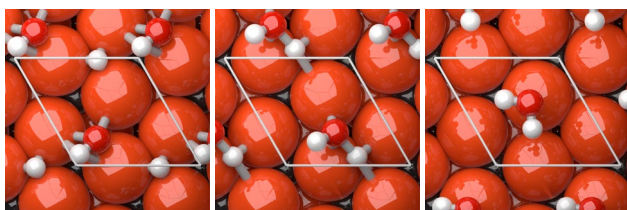
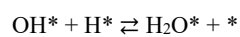
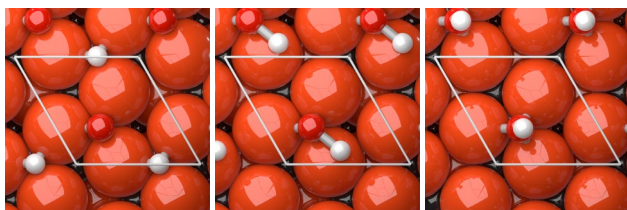
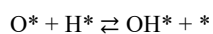
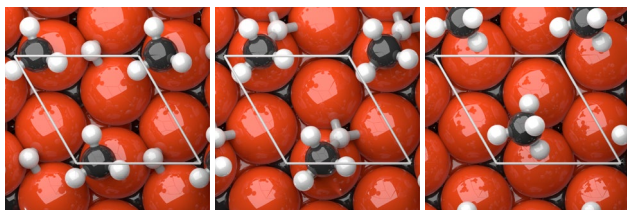
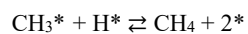
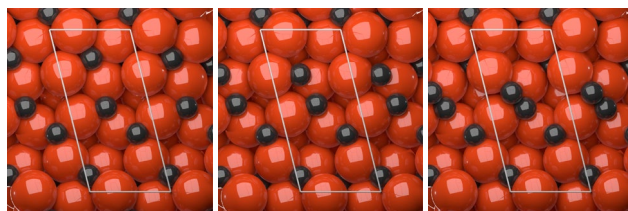
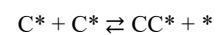
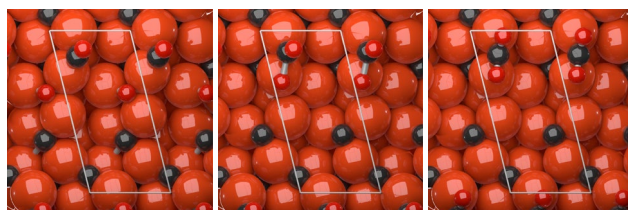
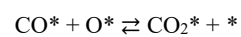
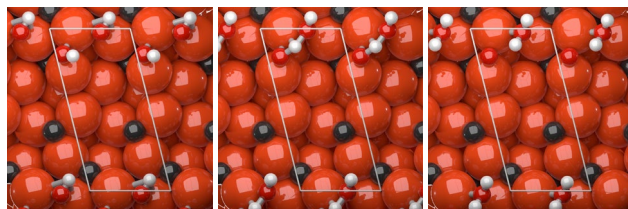
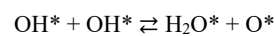
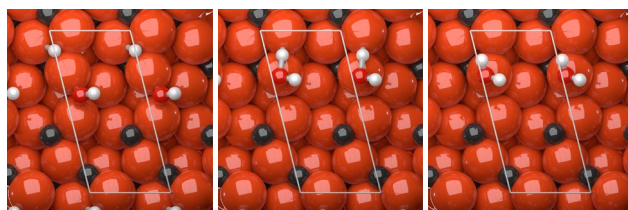
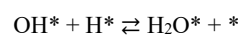
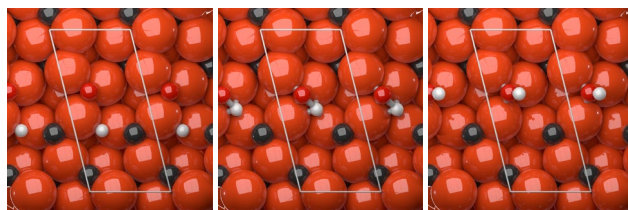
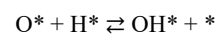
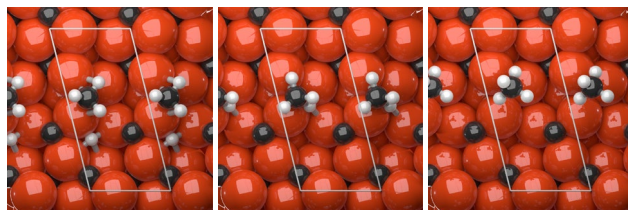
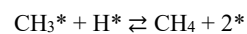
(001)  $\epsilon$ -Fe<sub>2</sub>C



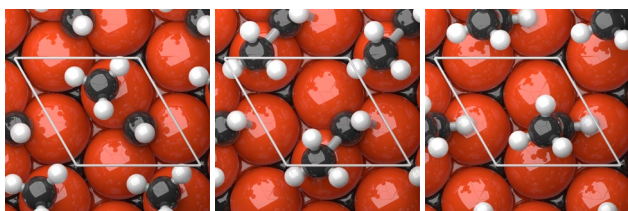
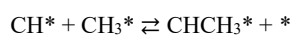
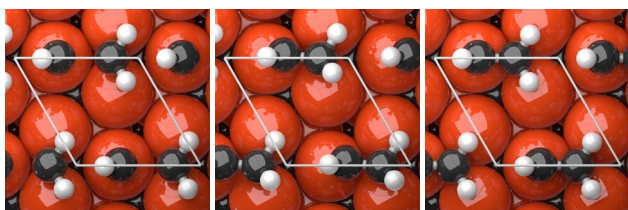
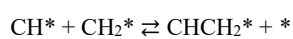
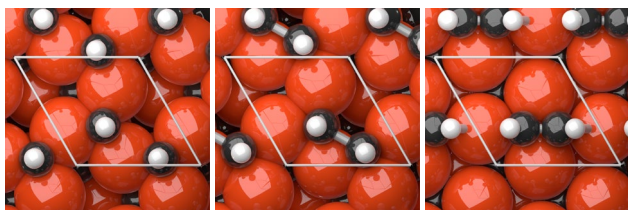
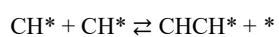
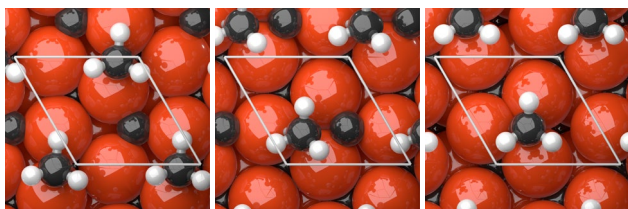
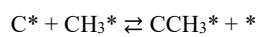
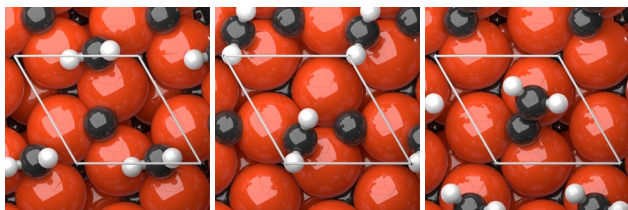
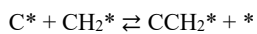
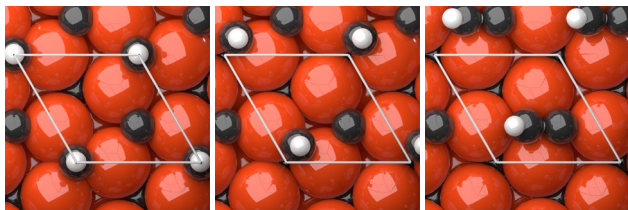
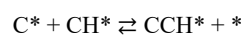
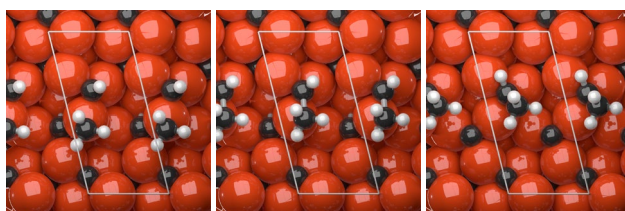
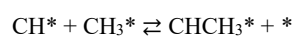
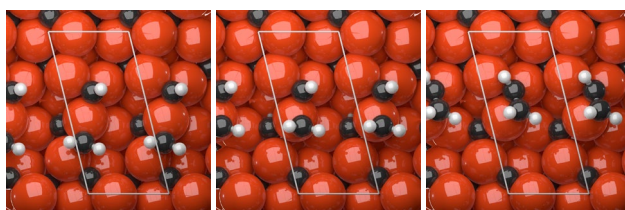
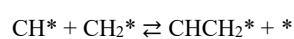
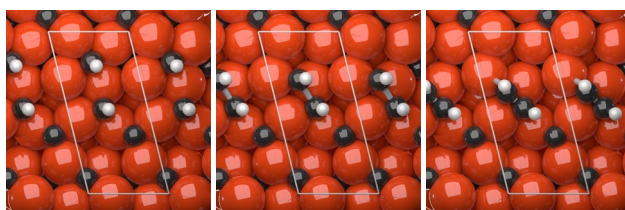
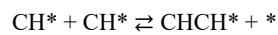
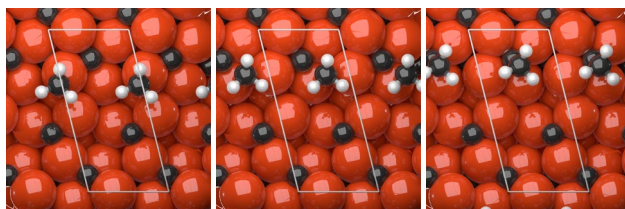
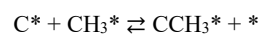
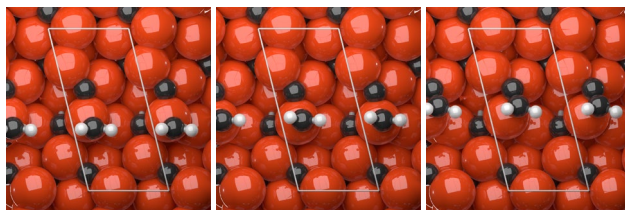
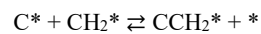
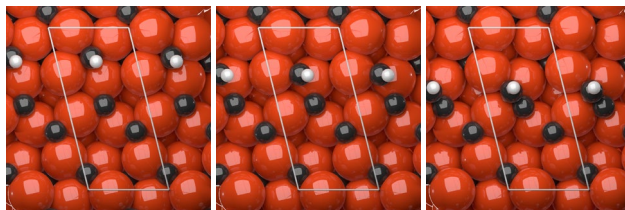
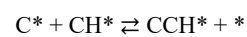
**(011)  $\epsilon$ -Fe<sub>2</sub>C**



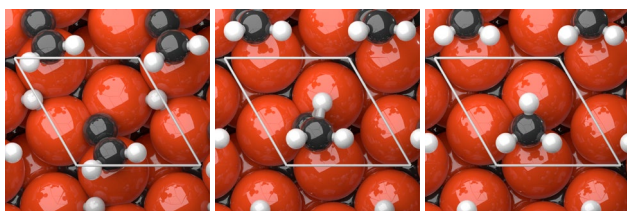
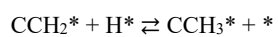
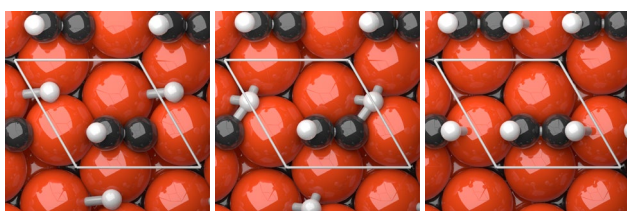
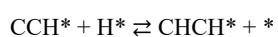
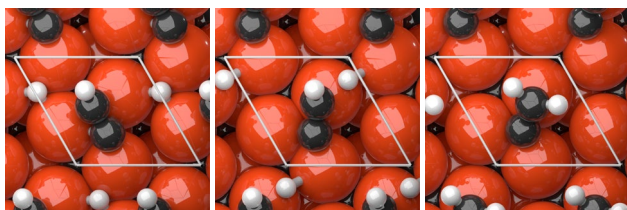
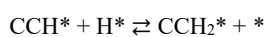
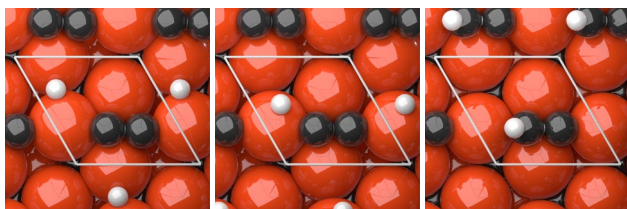
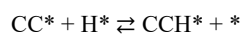
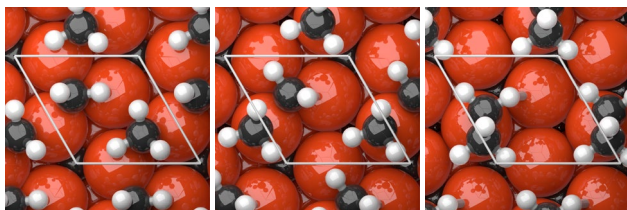
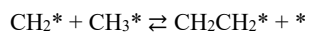
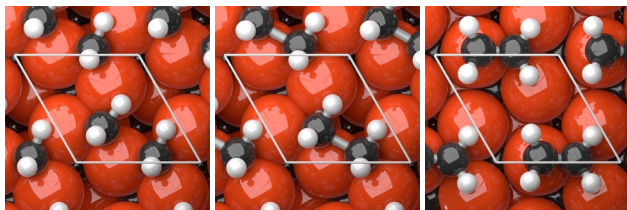
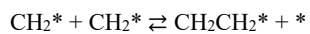
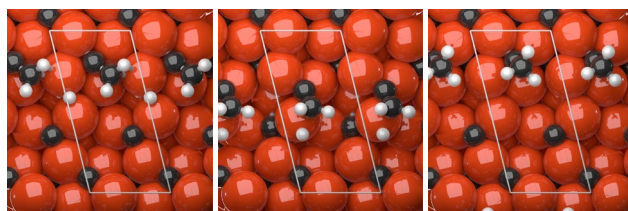
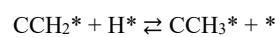
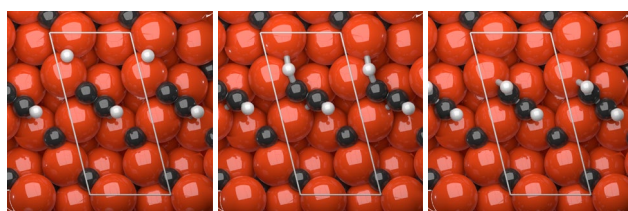
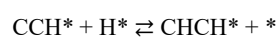
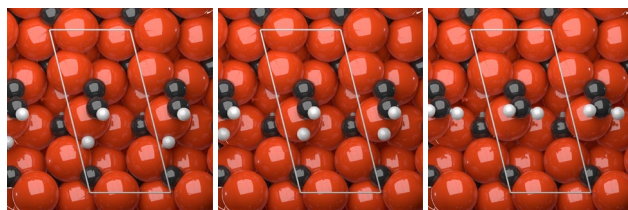
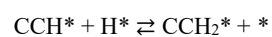
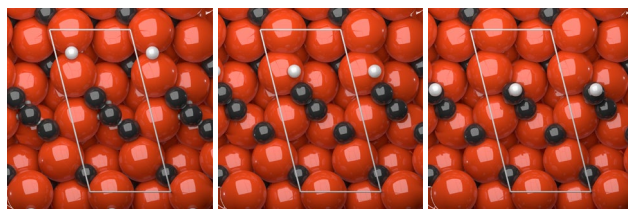
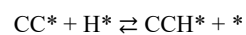
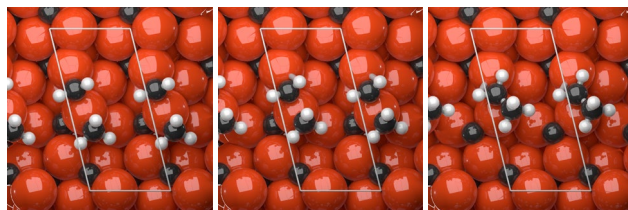
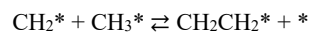
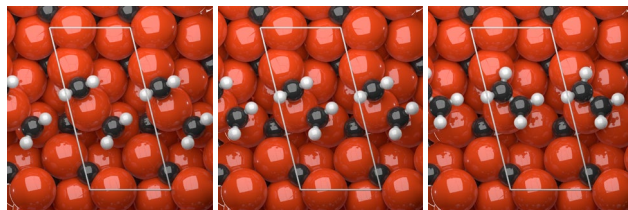
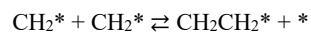


(001)  $\epsilon$ -Fe<sub>2</sub>C(011)  $\epsilon$ -Fe<sub>2</sub>C

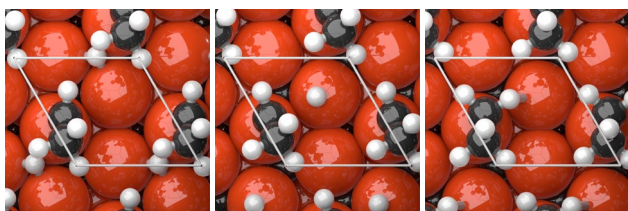
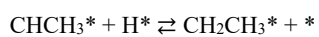
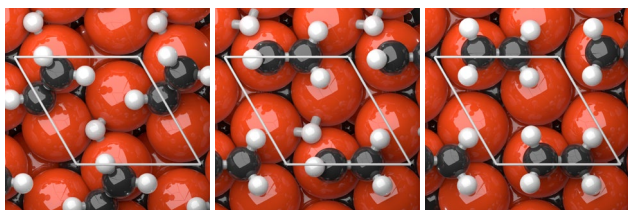
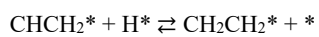
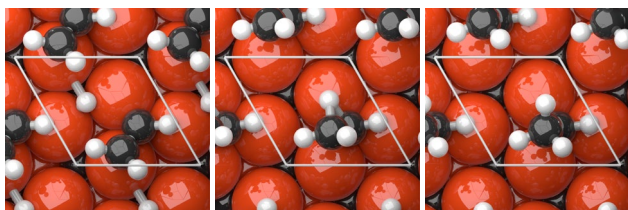
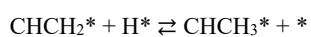
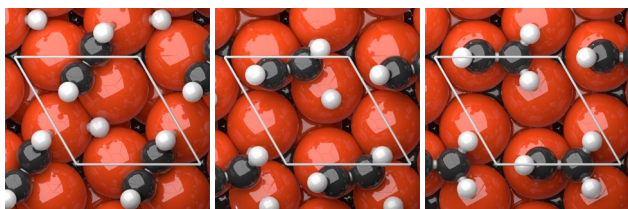
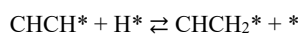
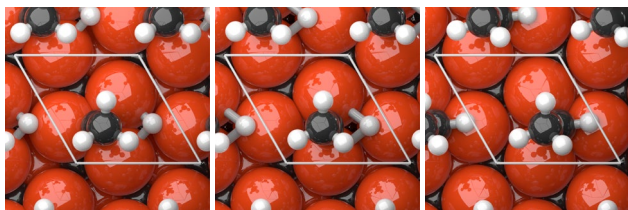
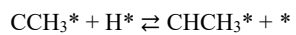
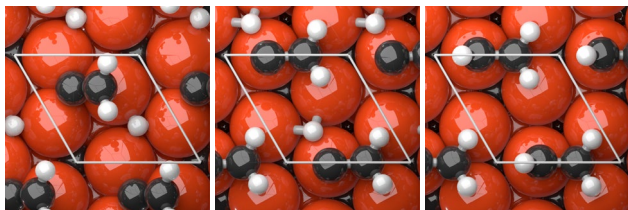
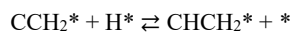
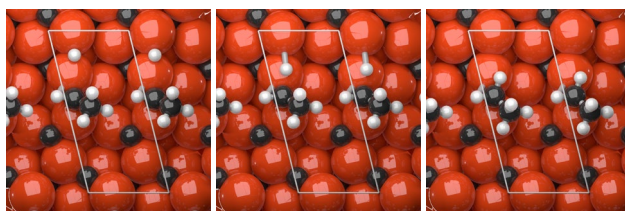
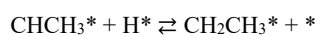
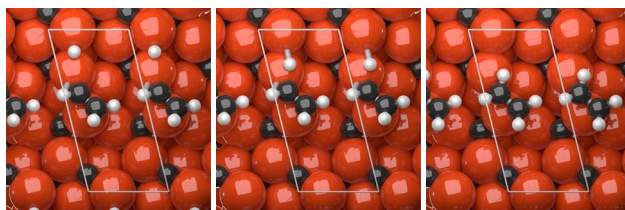
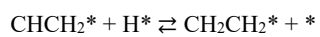
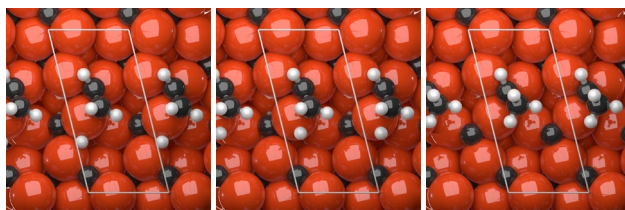
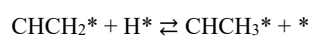
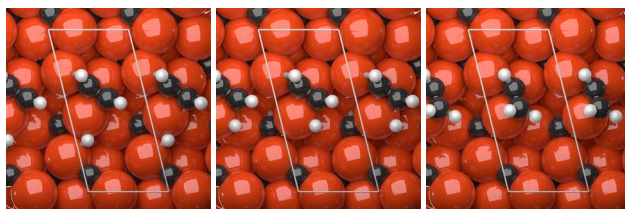
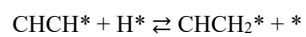
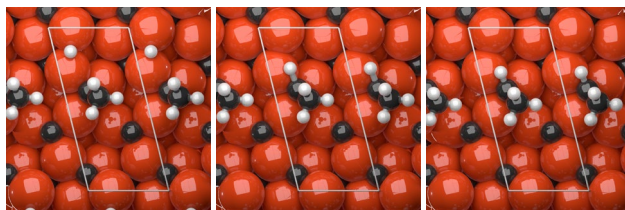
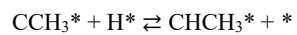
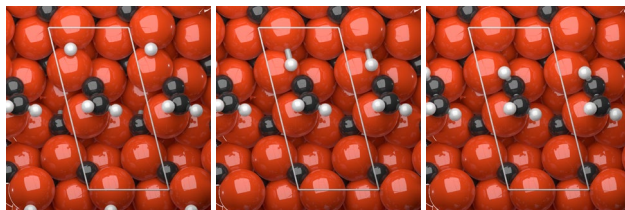
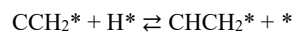


(001)  $\epsilon$ -Fe<sub>2</sub>C(011)  $\epsilon$ -Fe<sub>2</sub>C

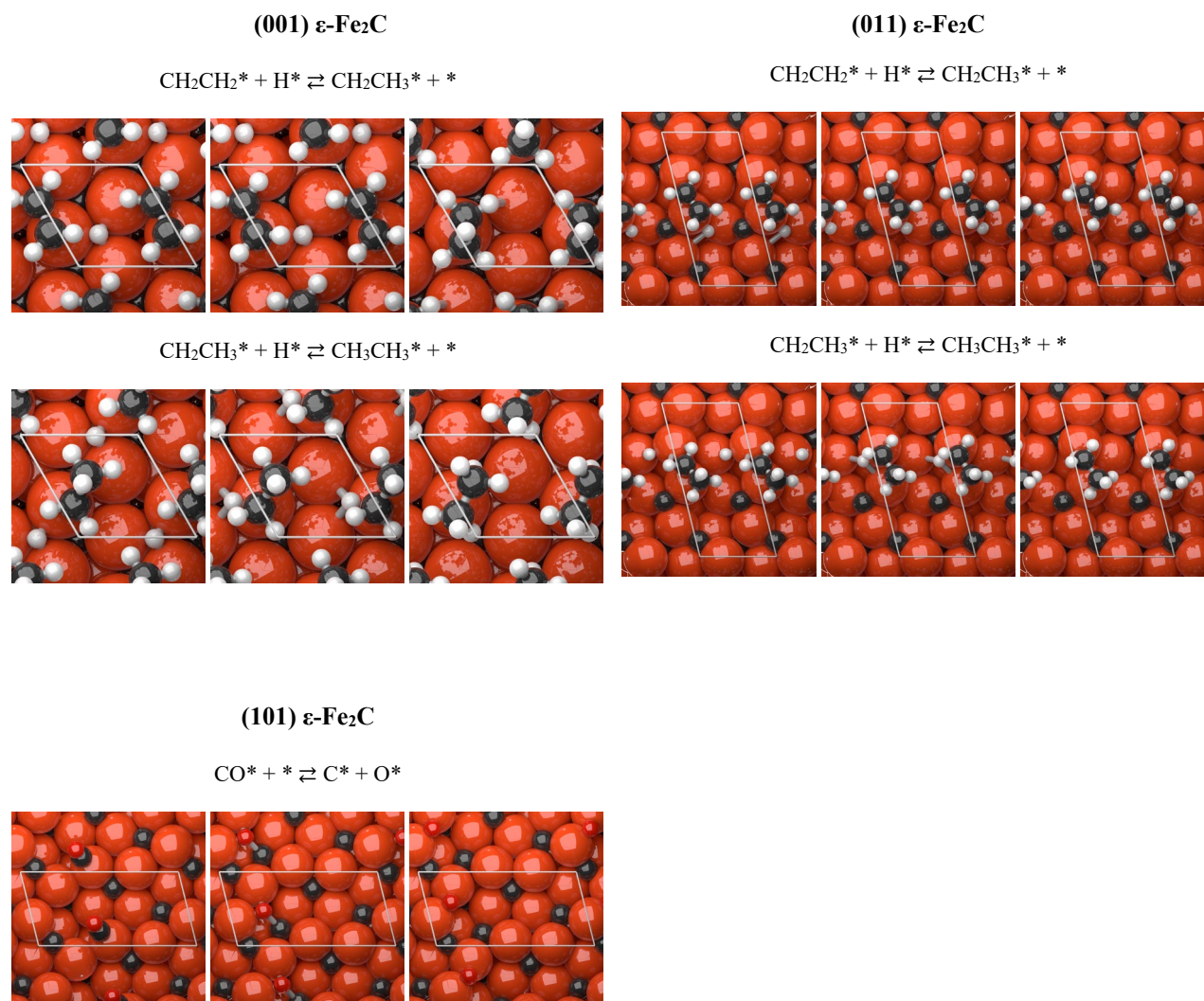


(001)  $\epsilon$ -Fe<sub>2</sub>C(011)  $\epsilon$ -Fe<sub>2</sub>C



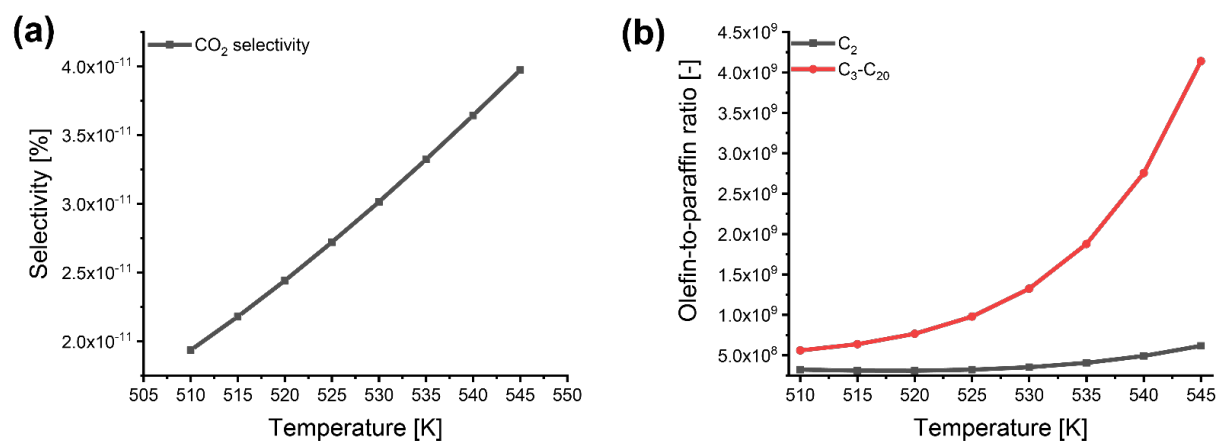
(001)  $\epsilon$ -Fe<sub>2</sub>C(011)  $\epsilon$ -Fe<sub>2</sub>C



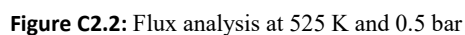


## Appendix C.2 Microkinetics simulations

### Microkinetic modelling



**Figure C2.1:** Microkinetic modelling results for the CSTR model between 510 K and 545 K on the (011) surface at 1 bar. (a)  $\text{CO}_2$  selectivity. (b) Olefin-to-paraffin ratio for  $\text{C}_2$  and  $\text{C}_3$ + species



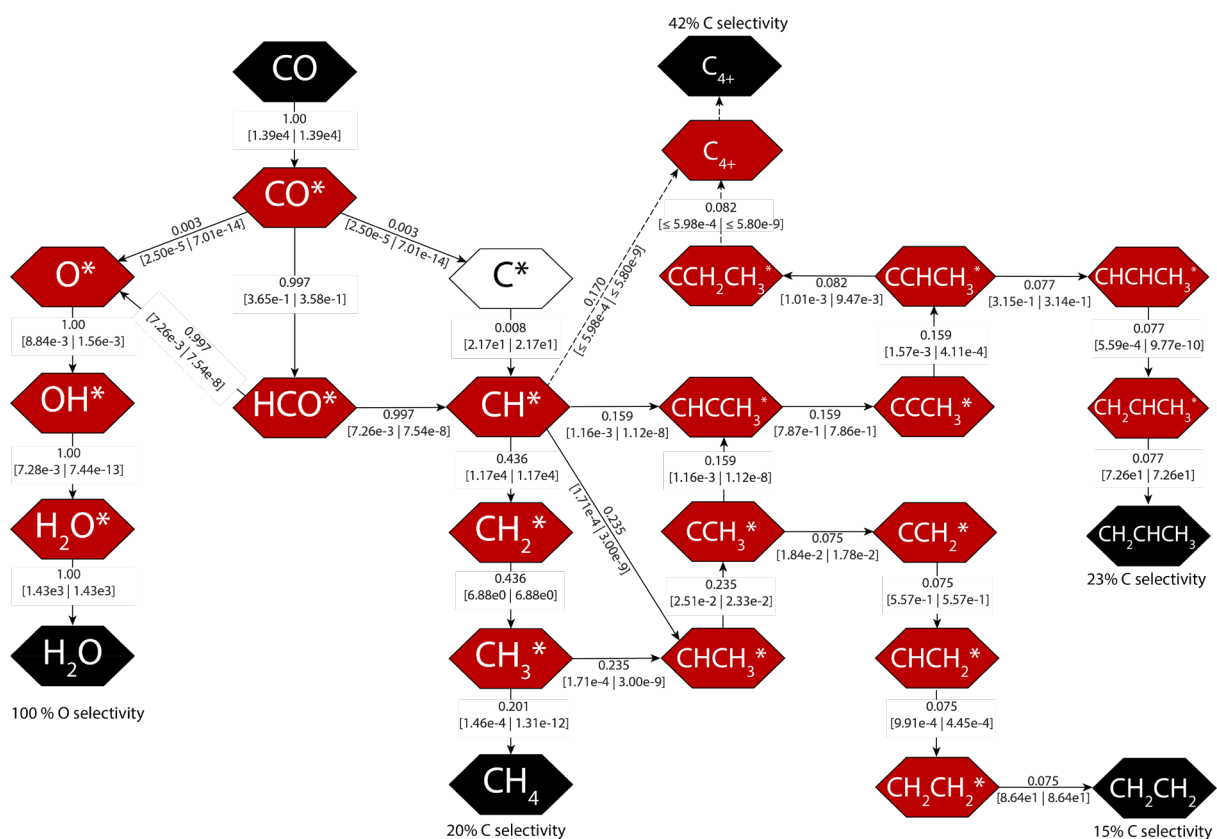


Figure C2.2: Flux analysis at 525 K and 2.5 bar

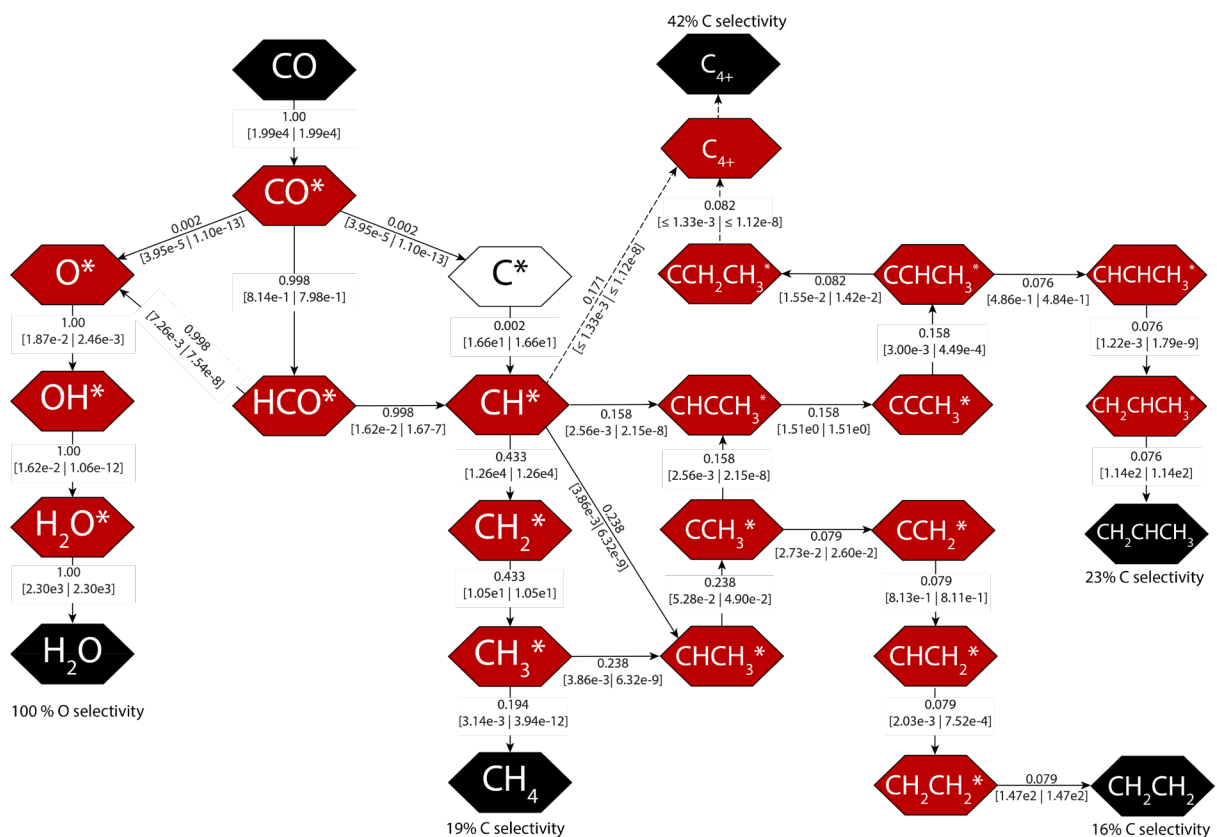


Figure C2.2: Flux analysis at 525 K and 5 bar

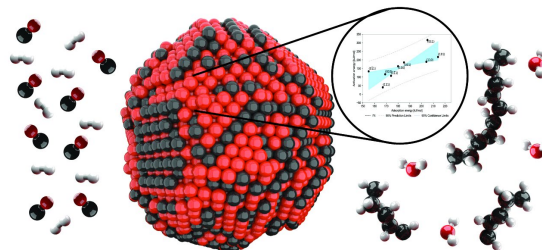
## Vibrational partition functions

**Table C.2.1:** Forward ( $q_f$ ) and backward vibrational partition functions ( $q_b$ ) calculated at 800 K for all reactions up to and including  $C_2$  formation on the terrace (001) and the corrugated (011) surface termination of hexagonal  $\epsilon$ -Fe $_2$ C.

			Terrace (001)		Step (011)	
CO dissociation			$q_f$	$q_b$	$q_f$	$q_b$
CO	$\rightleftharpoons$	C + O	4.42E-02	6.04E-01	2.32E-01	2.67E+00
CO + H	$\rightleftharpoons$	HCO	5.64E-01	1.91E+00	4.99E-01	2.81E+00
HCO	$\rightleftharpoons$	CH + O	5.56E-02	1.60E-01	5.63E-01	7.74E-01
Methanation			$q_f$	$q_b$	$q_f$	$q_b$
C + H	$\rightleftharpoons$	CH	6.37E-01	2.18E-01	1.65E+00	5.65E-01
CH + H	$\rightleftharpoons$	CH <sub>2</sub>	4.13E+00	7.28E-03	2.35E+00	8.37E-02
CH <sub>2</sub> + H	$\rightleftharpoons$	CH <sub>3</sub>	1.54E+00	7.94E-03	5.65E+00	5.88E-01
CH <sub>3</sub> + H	$\rightleftharpoons$	CH <sub>4</sub>	2.37E-01	4.13E-01	5.69E-01	5.13E-01
Oxygen removal via H <sub>2</sub> O/CO <sub>2</sub>			$q_f$	$q_b$	$q_f$	$q_b$
O + H	$\rightleftharpoons$	OH	9.81E-01	6.97E-01	4.44E-01	7.84E-01
OH + H	$\rightleftharpoons$	H <sub>2</sub> O	8.55E-01	5.84E-01	3.10E-01	5.47E-01
OH + OH	$\rightleftharpoons$	H <sub>2</sub> O + O	7.39E-01	4.65E-01	1.39E-01	2.45E-01
CO + O	$\rightleftharpoons$	CO <sub>2</sub>	9.19E-01	4.32E-02	7.00E-01	2.03E-01
C-C coupling			$q_f$	$q_b$	$q_f$	$q_b$
C + C	$\rightleftharpoons$	CC	3.69E-01	5.03E-01	7.12E-01	7.27E-01
C + CH	$\rightleftharpoons$	CCH	2.36E-01	3.31E-01	4.15E-01	4.74E-01
C + CH <sub>2</sub>	$\rightleftharpoons$	CCH <sub>2</sub>	2.41E-01	2.10E-01	1.31E+00	9.96E-01
C + CH <sub>3</sub>	$\rightleftharpoons$	CCH <sub>3</sub>	5.40E-02	9.58E-02	2.52E-01	5.60E-01
CH + CH	$\rightleftharpoons$	CHCH	2.32E-01	3.60E-01	3.15E-01	3.50E-01
CH + CH <sub>2</sub>	$\rightleftharpoons$	CHCH <sub>2</sub>	1.10E+00	7.94E-01	8.67E-01	9.86E-01
CH + CH <sub>3</sub>	$\rightleftharpoons$	CHCH <sub>3</sub>	4.57E-01	1.00E-01	4.77E-01	6.04E+00
CH <sub>2</sub> + CH <sub>2</sub>	$\rightleftharpoons$	CH <sub>2</sub> CH <sub>2</sub>	1.05E-01	2.25E-01	9.44E-01	4.58E-01
CH <sub>2</sub> + CH <sub>3</sub>	$\rightleftharpoons$	CH <sub>2</sub> CH <sub>3</sub>	5.31E-01	2.24E-01	1.69E+00	2.71E+00
C <sub>2</sub> hydrogenation			$q_f$	$q_b$	$q_f$	$q_b$
CC + H	$\rightleftharpoons$	CCH	1.07E+00	7.84E-01	1.51E+00	1.13E+00
CCH + H	$\rightleftharpoons$	CCH <sub>2</sub>	2.85E-02	2.93E-01	1.93E-01	1.69E+00
CCH + H	$\rightleftharpoons$	CHCH	3.56E-02	6.81E-01	1.26E-01	1.68E+00
CCH <sub>2</sub> + H	$\rightleftharpoons$	CCH <sub>3</sub>	9.86E-02	3.08E+00	6.04E-02	2.46E-01
CCH <sub>2</sub> + H	$\rightleftharpoons$	CHCH <sub>2</sub>	6.39E-02	9.19E-01	3.84E-02	7.83E-01
CHCH + H	$\rightleftharpoons$	CHCH <sub>2</sub>	1.50E-01	1.16E+00	1.38E-01	1.86E+00
CCH <sub>3</sub> + H	$\rightleftharpoons$	CHCH <sub>3</sub>	1.14E-01	2.44E-01	7.12E-03	5.54E-01
CHCH <sub>2</sub> + H	$\rightleftharpoons$	CH <sub>2</sub> CH <sub>2</sub>	2.80E-02	1.38E+00	9.64E-02	5.40E-01
CHCH <sub>2</sub> + H	$\rightleftharpoons$	CHCH <sub>3</sub>	1.10E-02	5.11E-02	3.54E-02	5.51E-01
CH <sub>2</sub> CH <sub>2</sub> + H	$\rightleftharpoons$	CH <sub>2</sub> CH <sub>3</sub>	4.02E-02	1.21E-01	1.74E-02	8.02E-02
CHCH <sub>3</sub> + H	$\rightleftharpoons$	CH <sub>2</sub> CH <sub>3</sub>	1.00E-01	3.21E+00	4.03E-01	6.69E-01
CH <sub>2</sub> CH <sub>3</sub> + H	$\rightleftharpoons$	CH <sub>3</sub> CH <sub>3</sub>	4.32E-02	8.11E-01	4.41E-01	1.29E+01

## 6. A quantum-chemical study of CO dissociation mechanism on low-index Miller planes of $\theta$ -Fe<sub>3</sub>C

*This chapter has been published as: R.J.P. Broos, B. Klumpers, B. Zijlstra, I.A.W. Filot, E.J.M. Hensen, Catalysis Today (2019)*



### Abstract

Spin-polarized density functional theory was employed to determine the preferred CO bond dissociation mechanism in the context of Fischer-Tropsch synthesis on low-index Miller surfaces of  $\theta$ -Fe<sub>3</sub>C. Compared to the most reactive (111) surface of bcc-Fe on which CO binds in sevenfold coordination, CO binds in threefold or fourfold sites on the carburized surfaces due to the presence of interstitial C atoms at or below the surface. An important finding is that the lowest activation energies for direct CO bond dissociation are associated with the presence of a B<sub>5</sub> site, similar to metallic surfaces. Three out of nine surfaces, (111), (111) and (010), present such sites, while H-assisted CO dissociation is preferred on (011), (001) and (100) surfaces. The other (011), (110) and (101) surfaces are found to be inert for CO bond scission with CO dissociation barriers close to or exceeding the CO adsorption energy. A kinetic analysis shows that the (111) surface (direct CO dissociation) and the (011) surface (H-assisted CO dissociation via HCO) display comparable CO bond dissociation rates, much higher than the other surfaces. Together, these two surfaces make up approximately 28% of the surface enclosing a Wulff nanoparticle. Using an atomic population analysis, we show that the activation barrier for C-O bond dissociation correlates well with the bond order of adsorbed CO. This implies that pre-activation of CO is important for lowering of the overall activation barrier. The present work demonstrates that the high-temperature  $\theta$ -Fe<sub>3</sub>C phase is highly active towards CO bond dissociation, which is the essential first step in the Fischer-Tropsch reaction. Several of the exposed surfaces present lower overall CO dissociation barriers than  $\alpha$ -Fe (known to be unstable under Fischer-Tropsch conditions) and the  $\chi$ -carbide of Fe (usually assumed to be the most stable phase of Fe-carbide under Fischer-Tropsch conditions).

## 6.1 Introduction

The growing trend to diversify the feedstock mix to cover the energy and transportation fuel demand has led to large-scale chemical processes based on the Fischer-Tropsch (FT) synthesis reaction.[1] In FT synthesis, synthesis gas (a mixture of carbon monoxide and hydrogen) obtained from natural gas and coal is converted to transportation fuels and base chemicals [2]. Approaches to use FT chemistry for the conversion of synthesis gas to light olefins are currently under development.[3]

The CO hydrogenation reactions underlying the FT reaction critically depend on the transition metal catalyst. Fe, Co and Ru provide the highest selectivity towards long-chain hydrocarbons.[1] Fe is attractive because of its cost advantage in comparison to Co and Ru, but also for its high activity in the water-gas-shift (WGS) reaction. The latter aspect is an advantage when synthesis gas compositions with low  $H_2/CO$  ratios (such as synthesis gas derived from coal gasification) are to be converted.

In contrast to Ru and Co for which the metallic phase is considered to be the catalytically active phase, different carbides of iron play an important role in the FT reaction. There is an ongoing debate about which of these phases controls the activity and selectivity of Fe-based catalysts.[1, 4-6] It is therefore crucial to understand the nature of the different iron carbide phases and the mechanism by which they convert carbon monoxide with hydrogen to hydrocarbons.

Investigations on the stability of different iron carbide phases suggests that under typical FT conditions (i.e., high CO partial pressure and temperatures around 550-600 K)  $\chi$ -Fe-carbide and  $\epsilon$ -Fe-carbide are the most stable forms of iron.[4,7] This can explain the widespread experimental research on these two phases in the open literature.[5-13] The structure of  $\theta$ -Fe<sub>3</sub>C has been a topic of great interest in the previous century, as  $\theta$ -Fe<sub>3</sub>C is the most stable phase in steel at high temperatures. Its structure has been determined experimentally through x-ray, electron and neutron diffraction measurements.[14-26]

The  $\theta$ -Fe<sub>3</sub>C phase is a meta-stable iron carbide which is seen as an intermediate in the transition from pure  $\alpha$ -Fe to the more carbon-rich  $\chi$ -phase. In addition, it is identified as the most prevalent phase under high temperatures and low carbon-pressures[7], e.g. at short exposures to FT-conditions, indicating that  $\theta$ -Fe<sub>3</sub>C may play an important role in the high temperature FT-reaction. To this date, the catalytic properties of  $\theta$ -Fe-carbide ( $\theta$ -Fe<sub>3</sub>C) have only been studied in a few works.

CO dissociation is often reported to be one of the rate-limiting steps in FT-synthesis.[2, 5] It is the principle step that has to be facile for a catalyst to be active in the FT mechanism.[27] Herein, we

will study the mechanism and kinetics of CO dissociation over the  $\theta$ -Fe carbide. Although there are existing studies on the CO dissociation mechanism on the  $\theta$ -Fe<sub>3</sub>C(100) surface[9] and on direct CO dissociation on the  $\theta$ -Fe<sub>3</sub>C(001) surface[13], a detailed theoretical evaluation of the catalytic nature of the other low Miller-index surfaces of the  $\theta$ -Fe<sub>3</sub>C has, to the best of our knowledge, not been conducted.

In this study, we will start by exploring which terminations of bulk  $\theta$ -iron are stable and are expected to occur under FT conditions. Next, we will systematically study CO adsorption and direct C-O bond scission on all unique low Miller-index surfaces. Finally, we will compare the direct CO dissociation mechanism with the H-assisted CO dissociation mechanisms, using a simple kinetic model and discuss the feasibility for the  $\theta$ -Fe<sub>3</sub>C surfaces in the FT reaction. Most notably, we will identify a direct CO dissociation pathway over the (111) surface that indicates that this surface termination plays an important role in Fe-based FTS.

## 6.2 Methods

Density functional theory (DFT) computations were performed using the Vienna Ab Initio Simulation Package (VASP)[28-31] with the Perdew-Burke-Ernzerhof GGA exchange correlation functional.[32, 33] For structure optimization, spin-polarized DFT computations were conducted using a plane-wave basis set using the projector-augmented wave method.[34, 35] The cut-off energy for the plane-wave basis set was 400 eV. Orbital occupations were set according to the 1<sup>st</sup> order Methfessel-Paxton method with a smearing coefficient of 0.2 eV.

The  $\Gamma$ -point was used for computations of gaseous CO and H<sub>2</sub>. Gas-phase molecules were centred in a 10x10x10 Å vacuum for the same reason. For the bulk solid computations, a 5x5x5 Monkhorst-Pack  $k$ -mesh was used. It was verified that a larger number of grid-points did not yield significantly more accurate results given the required computational expense. In order to assure that the surface model was not influenced by its own images due to plane-wave periodicity along the surface normal, a vacuum layer of 7.5 Å was added on each side of the surface slab model. To prevent dipole moments over the periodic surfaces, adsorbed species were placed symmetrically on both sides of the surface models. For surface computations, a 5x5x1  $k$ -mesh grid was used. Structural data for bulk  $\theta$ -Fe<sub>3</sub>C was derived from the work of Fruchart et al.[25]  $\theta$ -Fe<sub>3</sub>C has an orthorhombic unit cell with the space group P<sub>nma</sub> (62, P<sub>bnn</sub>) and cell dimensions  $a = 5.082$  Å,  $b = 6.733$  Å,  $c = 4.514$  Å. [14-26] The orthorhombic unit cell is comprised of 8 octahedral iron atoms in Wyckoff  $d$ -positions and 4 tetrahedral iron and carbon atoms in Wyckoff  $c$ -positions as can be seen in Figure 6.1.



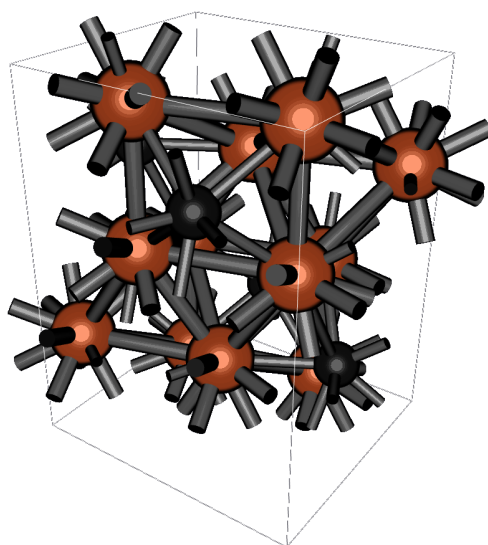


**Figure 6.1:** Orthographic representation of the unit cell for the bulk structure of  $\theta$ -Fe<sub>3</sub>C. The orange and black atoms represent the Fe and C atoms, respectively.

Energy minimization of the structures was performed using the Kosugi algorithm as implemented in VASP. An energy criterion of  $10^{-5}$  eV and  $10^{-4}$  eV was employed for electronic convergence and structural convergence, respectively. All geometry optimizations were conducted using the conjugate-gradient algorithm. Transition states were determined using the climbing-image nudged elastic band (CI-NEB) method.[36] A frequency analysis was performed to confirm that all transition state geometries correspond to a first-order saddle point on the potential energy surface with an imaginary frequency in the direction of the reaction coordinate. Zero-point energy (ZPE) corrections were applied to all calculations. ZPE-corrections were computed through the energies of the vibrational states based on the eigenvalues of the mass-corrected Hessian matrix. This Hessian matrix was constructed using a finite difference approach with a step size of 0.02 Å for the displacement of individual atoms along each Cartesian coordinate. In the frequency analysis, we neglected the contribution of Fe by excluding the corresponding terms in the Hessian matrix as the mass of Fe is significantly higher than that of C, O or H. We corrected the barriers for the migration of fragments after dissociation by considering the energy difference of the geometry directly after dissociation and their most stable adsorption positions at infinite distance. All surfaces were cleaved with respect to the origin of the bulk unit cell, i.e. at a fractional distance of 0.0.

Surface energies were calculated using

$$E_{\text{surface}} = \frac{(E_n - n \cdot E_{\text{bulk}})}{2A}, \quad (6.1)$$

where  $E_n$  refers to the total energy of the slab, containing  $n$  times the bulk cell,  $E_{\text{bulk}}$  to the bulk energy,  $A$  to the area of the surface and  $E_{\text{surface}}$  to the surface energy of the surface. A Wulff particle was obtained from the different surface free energies using VESTA.[37]

To compare the CO dissociation rates on the different surfaces, we employed a simplified kinetic model as previously constructed by Liu et al.[38] For these calculations we used, a temperature of 500 K and a CO pressure of  $3 \cdot 10^{-5}$  Pa, unless otherwise specified. The relatively low pressure was chosen to simulate conditions of low CO coverage, consistent with the low coverage used in the transition-state calculations. For the reaction rate in the hydrogen-assisted mechanisms *via* HCO or COH, we used the overall reaction barrier for C-O bond scission (i.e., the highest barrier encountered in the potential energy diagram with reference to pre-adsorbed CO and H) and a  $\text{H}_2$  pressure of  $6 \cdot 10^{-5}$  Pa. This methodology is the same as assuming a pre-equilibrium between  $\text{CO}^*$  and  $\text{H}^*$  and  $\text{HCO}^*$  or  $\text{COH}^*$ . To compare the relative rates of the direct CO dissociation with the H-assisted CO dissociation mechanisms, a competitive adsorption is taken into account for the direct CO dissociation pathway.

Rate constants  $k$  for the elementary reaction step were calculated using the Eyring equation:

$$k = \nu \exp\left(\frac{-\Delta E_{\text{act}}}{k_{\text{b}}T}\right), \quad (6.2)$$

where  $\Delta E_{\text{act}}$  stands for the activation energy,  $k_{\text{b}}$  for the Boltzmann constant,  $T$  for temperature and  $\nu$  for the pre-exponential factor. This pre-exponential factor can be calculated for the forward and backward reaction and is defined as follows:

$$\nu_{\text{forward}} = \frac{k_{\text{b}}T}{h} \left( \frac{q_{\text{vib}}^{\text{TS}}}{q_{\text{vib}}^{\text{IS}}} \right) \text{ and } \nu_{\text{backward}} = \frac{k_{\text{b}}T}{h} \left( \frac{q_{\text{vib}}^{\text{TS}}}{q_{\text{vib}}^{\text{FS}}} \right), \quad (6.3)$$

where  $\nu_{\text{forward}}$  and  $\nu_{\text{backward}}$  refer to the pre-exponential factors for the forward and the backward reaction, respectively,  $q_{\text{vib}}$  stands for the vibrational partition function of the initial state (IS) and the transition state (TS) and  $h$  for Planck's constant.

In order to understand the underlying chemistry of C-O bond scission on the different surfaces, we have computed the bond orders, using the DDEC6 method as developed by Manz.[39]

### 6.3 Results and Discussion

We carried out DFT calculations in order to investigate the adsorption and reaction energetics of CO dissociation on various  $\theta$ -Fe-carbide surfaces. First, we will present the bulk structure and surface energies of the surface terminations of the  $\theta$ -Fe-carbide. Next, we will discuss CO adsorption and direct CO dissociation. Thereafter, we will discuss H-assisted C-O bond scission pathways for the most feasible surfaces and employ simplified kinetic models. Finally, a bond order analysis is used to rationalize differences in CO dissociation rates in terms of bonding of CO to the various surfaces.

#### 6.3.1 Surface $\theta$ -Fe-carbide models

We focus in this work on low-index Miller surfaces of  $\theta$ -Fe-carbide. Based on the crystal symmetry, nine unique surface planes can be distinguished. An overview of these crystallographically distinct surfaces is given in Table 6.1.

Due to the presence of interstitial carbon in  $\theta$ -Fe-carbide, several surface terminations are possible when the unit cell in a particular direction perpendicular to the Miller plane is cleaved at fractional distances. For this study, we only considered the surfaces cleaved at a fractional distance of 0.0. Table 6.1 lists the free energies of these surfaces, which are in good agreement with available literature data.[40] The only significant difference is the higher stability of the (101) surface over the (111) surface, which may be due to the use of different GGA functionals. The (0 $\bar{1}1$ ) and (1 $\bar{1}1$ ) surfaces included in Table 6.1 are studied here for the first time.

**Table 6.1:** Computed and experimental surface free energies for of the  $\theta$ -Fe<sub>3</sub>C surfaces as well as the relative contribution to the Wulff particle, computed by VESTA.

Surface	Surface energy (J/m <sup>2</sup> )	Surface energy (J/m <sup>2</sup> ) Expt.[40])	Surface area enclosing the Wulff particle (%)	Preferred C-O bond scission mechanism	Overall energy barrier (kJ/mol)
(0 $\bar{1}1$ )	2.00	[-]	17	HCO	74
(001)	2.21	2.05	8	HCO	103
(110)	2.34	2.19	27	HCO	167
(101)	2.39	2.25	14	Direct	217
(111)	2.39	2.22	11	Direct	40
(010)	2.46	2.26	11	Direct	116
(011)	2.51	2.37	6	CCO	198
(100)	2.64	2.47	3	HCO	135
(1 $\bar{1}1$ )	2.65	[-]	3	Direct	107

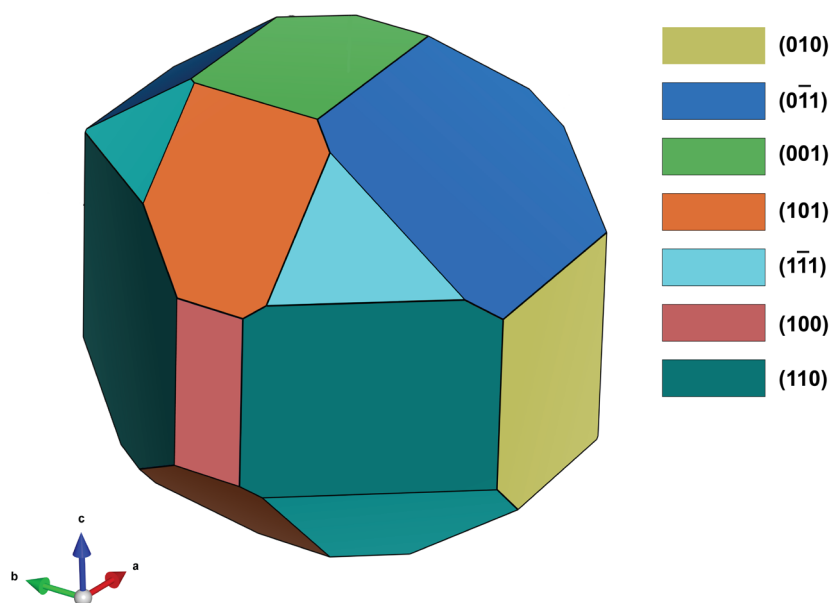


**Figure 6.2:** Wulff-construction for tetrahedral configured  $\theta$ -Fe<sub>3</sub>C based on surface free energies computed through DFT; image created using VESTA.

Figure 6.2 shows a Wulff construction of a sufficiently large  $\theta$ -Fe-carbide nanoparticle. The corresponding predicted surface composition of this Wulff shape is given in Table 6.1. From Table 6.1 and Figure 6.2, it follows that the contribution of different surfaces to the surface area enclosing the Wulff particle decreases in the following order  $(110) > (0\bar{1}1) > (101) > (010) > (111) > (001) > (011) > (100) > (1\bar{1}1)$ . To determine the importance of these surface terminations for the FTS reaction, we investigated C-O bond scission as the important initiation step.

### 6.3.2 CO adsorption energies and dissociation barriers

We first determined the most stable adsorption site for CO for each of the surfaces. These configurations are shown in Figure 6.3. CO adsorption on  $\alpha$ -Fe(111) is included for comparison. Although it is well known that metallic Fe is stable as an active phase in Fe-catalysed FTS, it is highly active for CO dissociation.[41, 42] CO prefers to adsorb in high coordination sites, unless the surface or subsurface contains C atoms. For example, CO adsorbs in a fivefold configuration on the (111) surface of the  $\theta$ -carbide. A sevenfold coordination is possible on  $\alpha$ -Fe (111). The adsorption energies on  $\theta$ -Fe-carbide surfaces vary from 155 kJ/mol for the  $(0\bar{1}1)$  surface to 214 kJ/mol for the (101) surface. A previous investigation of the (100) surface predicted a CO adsorption energy of 177 kJ/mol [9], which is in line with our computed value of 180 kJ/mol.

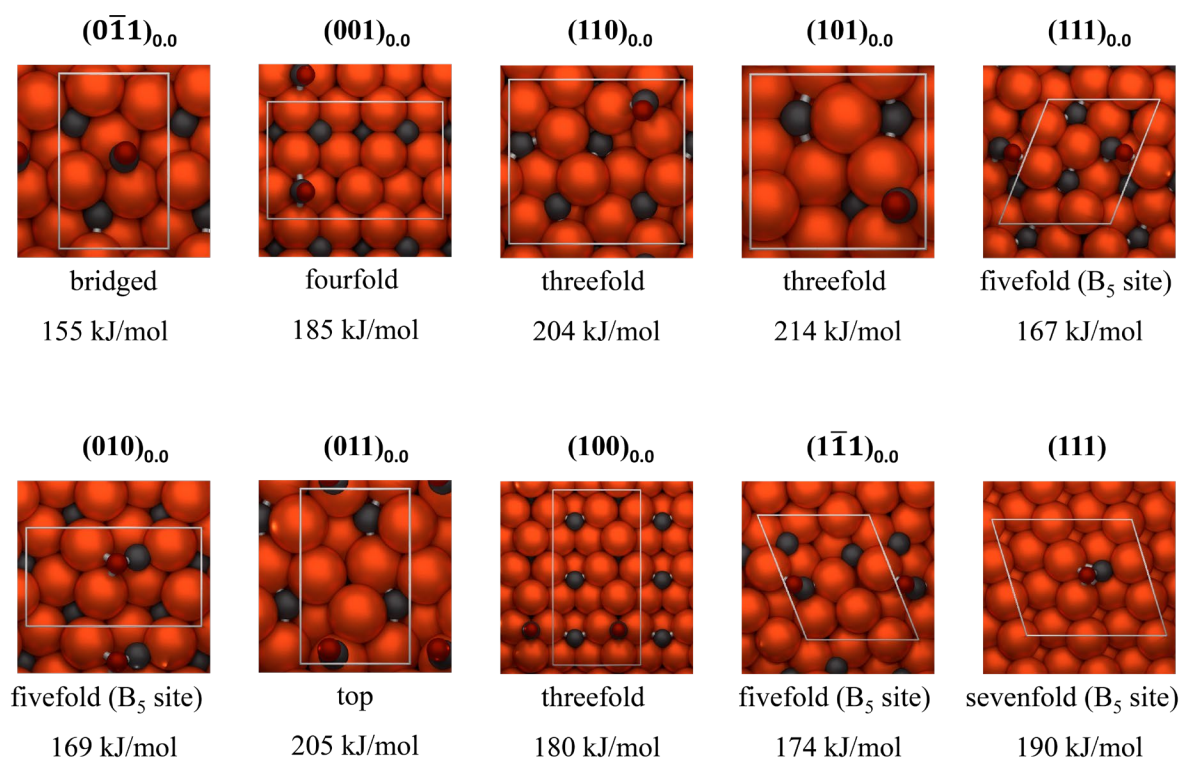


**Figure 6.3:** The most stable adsorption configurations and corresponding adsorption energies of CO on all  $\theta$ -Fe<sub>3</sub>C surfaces and bcc-Fe(111). CO adsorbs in high-coordination sites unless hampered by surface or interstitial C atoms.

We considered direct and H-assisted CO dissociation mechanism. Figure 6.4 shows the overall activation barrier for these CO dissociation pathways on all nine considered surfaces. It follows that direct CO dissociation on the (111) surface has the lowest overall barrier (40 kJ/mol). H-assisted pathways on this surface require to overcome a barrier higher than 100 kJ/mol. Other reactive surfaces are (0 $\bar{1}1$ ) and (001), which can break the CO bond via a HCO intermediate with overall barriers of 72 kJ/mol and 103 kJ/mol. Figure 6.5 shows the relative stabilities of all the reaction intermediates involved in the reaction. The intermediates located closest to the centre are the most stable. Clearly, CO (red) and H (blue) are substantially more stable than HCO (orange) and COH (green) surface intermediates. Comparison of Figures 6.4 and 6.5 shows that CO is less stable compared to H on the surfaces for which the direct CO dissociation mechanism has the lowest overall barrier. Furthermore, the COH intermediate is the least stable of the considered species on all surfaces, except on the (1 $\bar{1}1$ ) surface on which the HCO intermediate is the least stable intermediate. Next, we will discuss the most salient details of the different modes of CO dissociation.

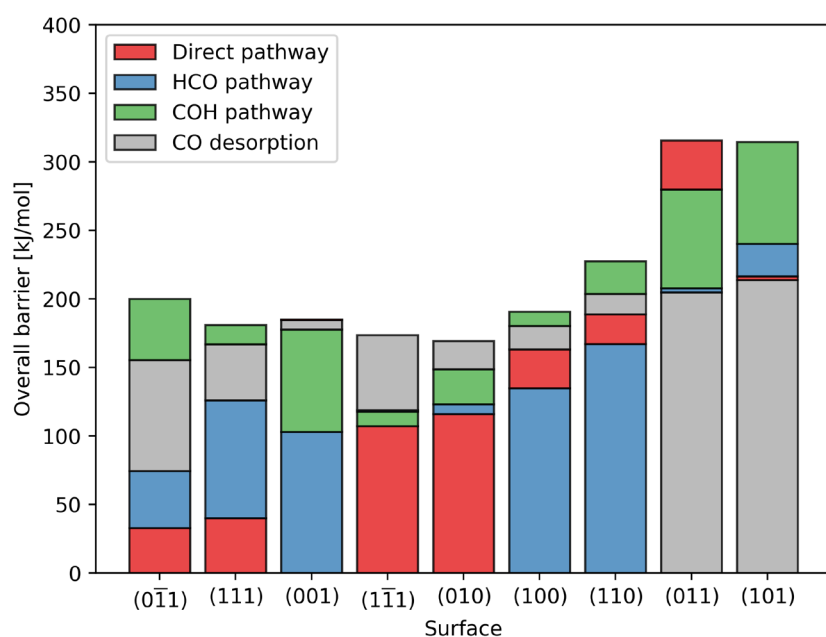


**Figure 6.4:** Overall activation barriers for direct CO dissociation (red) and for CO dissociation involving H-assistance via HCO (blue) and COH (green). CO desorption energies are depicted in grey. For the H-assisted pathways, the overall activation barriers for CO hydrogenation and C-O bond scission are given. The surfaces are ordered left-to-right by increasing overall barrier.

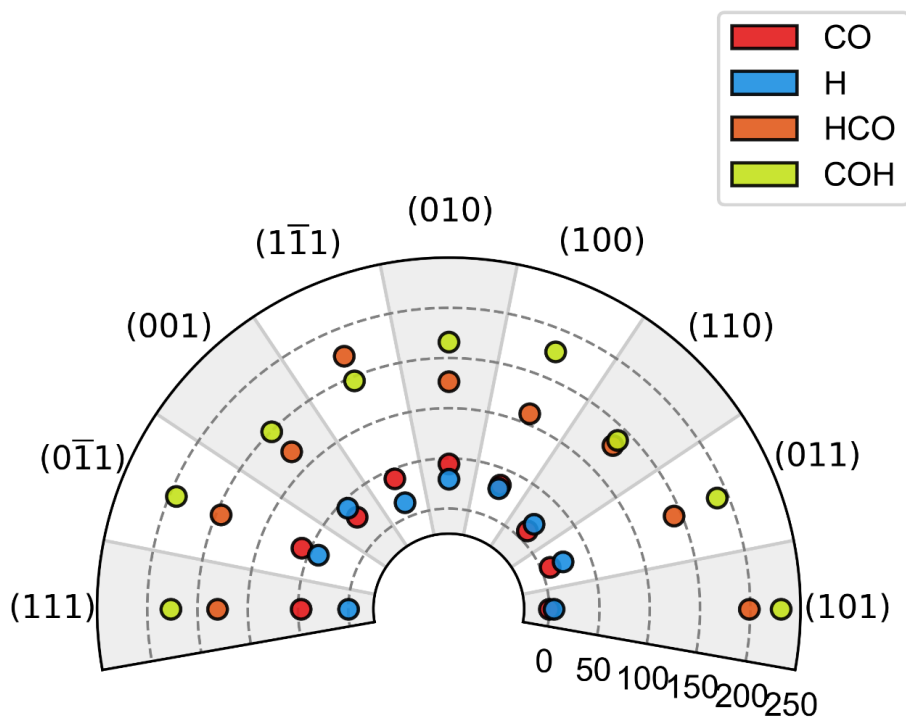


**Figure 6.5:** Stability plot for the surface reaction intermediates. Reaction intermediates located closer to the centre are more stable. The surfaces are ordered left-to-right by increasing overall activation barriers as in Figure 6.4. All energies are given in kJ/mol. The stabilities are referenced to the most stable CO and H adsorption energies.

### 6.3.3 Direct CO dissociation

In the direct CO dissociation mechanism, adsorbed CO dissociates in a single elementary reaction step to C and O. Table 6.2 presents the computed CO adsorption energies, reaction enthalpies and the forward and backwards activation energies for direct CO dissociation on the different surfaces. The corresponding geometries are shown in Appendix D.1. Among the different surfaces, C-O bond scission on the (111) surface resembles closest that on the  $\alpha$ -Fe(111) surface. The barrier on (111) for CO dissociation is only 40 kJ/mol, which is 15 kJ/mol lower than the barrier on  $\alpha$ -Fe(111). Both these surfaces are strongly corrugated. CO dissociation on the (111) surface of  $\theta$ -Fe-carbide is much easier than on Ru(11 $\bar{2}$ 1) (65 kJ/mol) [43] and Co(11 $\bar{2}$ 1) (103 kJ/mol) [38].

**Table 6.2:** Computed CO adsorption energies, reaction enthalpies and forward- and backwards activation energies, for the direct CO dissociation mechanism for crystal forms of  $\theta$ -Fe<sub>3</sub>C and  $\alpha$ -Fe. All energies are given in kJ/mol.

Surface	$E_{\text{ads}}(\text{CO})$ (kJ/mol)	$\Delta H_{\text{rx}}$ (kJ/mol)	$E_{\text{act}}^{\text{f}}$ (kJ/mol)	$E_{\text{act}}^{\text{b}}$ (kJ/mol)
(100)	180	-51	163	214
(010)	169	27	116	89
(110)	204	8	189	181
(011)	205	65	315	250
(001)	185	12	185	173
(101)	214	-49	216	265
(0 $\bar{1}$ 1)	155	27	133	107
(1 $\bar{1}$ 1)	174	-114	107	221
(111)	167	-97	40	137
(111) ( $\alpha$ -Fe)	190	-201	57	258

Similar to the latter two surfaces, the (111) surface of  $\theta$ -Fe-carbide contains a step-edge site with a B<sub>5</sub>-configuration.[44] B<sub>5</sub>-sites exhibit a favourable geometry for CO dissociation because of the favourable overlap of the metal *d*-band with the 2 $\pi^*$  orbital of CO, the low coordinative saturation of the metal atoms and the absence of sharing of metal atoms with C and O in the transition state.[45] The barrier on (1 $\bar{1}$ 1) is substantially higher at 107 kJ/mol.

Compared to these corrugated surfaces, CO dissociation is very difficult on the terrace-like (011) surface (316 kJ/mol) on which CO is adsorbed in a top configuration. In general, barriers on these terrace-like (001), (011) and (101) surfaces are higher than 180 kJ/mol and comparable to the adsorption energy of CO. Considering entropy gain in a CO desorption state, we can state that CO



desorption on these surfaces is preferred to direct C-O bond scission. The barrier computed for the (100) surface of 163 kJ/mol compares well with the result obtained by Jiao et al.[9]

#### 6.3.4 H- and C-assisted CO dissociation

H-assisted CO dissociation was also considered for all surfaces. The computed energy barriers are presented in Table 6.3. HCO and COH pathways and, for the surface with the highest barrier for direct CO dissociation, a CCO pathway was also investigated. Table 6.3 shows that HCO formation is endothermic, while subsequent HCO dissociation is exothermic for all surfaces except for the (010) surface. Thus, the HCO intermediate is unstable on  $\theta$ -Fe-carbide surfaces in general. For the (011), (110) and (101) surfaces, the barriers for HCO formation are of the order of 250 kJ/mol, which is much higher than the barriers determined for direct CO dissociation mechanism. For some of the surfaces, the overall barrier for CO dissociation via HCO is lower than the corresponding barrier for the direct CO dissociation mechanism. Important cases are the (0 $\bar{1}$ 1) and (001) surfaces with a barrier close to or lower than 100 kJ/mol. On the (1 $\bar{1}$ 1), (111) and (001) surfaces, the CO hydrogenation barrier is relatively high with values between 100 kJ/mol and 150 kJ/mol. H-assisted CO dissociation via the HCO intermediate is favoured over direct dissociation on the (001) and (0 $\bar{1}$ 1) surfaces. For the (1 $\bar{1}$ 1) and (111) surfaces, direct CO dissociation is preferred. Relatively facile CO hydrogenation pathways were identified for the (100), (010) and (0 $\bar{1}$ 1) surfaces with barriers of 60 kJ/mol, 59 kJ/mol and 72 kJ/mol, respectively. On the (100) surface, CO dissociation is more favourable via a HCO intermediate compared to direct CO dissociation. For the (010) surface, the barrier of CO dissociation via a HCO intermediate is close to the barrier for direct C-O bond scission. For the (100) surface, Jiao et al. [13] also considered a hydrogen-assisted pathway. They reported a HCO formation energy of 94 kJ/mol and an overall activation barrier of 121 kJ/mol. These values are 34 kJ/mol higher and 14 kJ/mol lower than our results. This difference can be attributed to their use of a co-adsorbed initial state, where we have used a migration-corrected initial state. Huo et al.[13] reported a forward activation barrier of 109 kJ/mol for HCO formation on the (001) surface. This agrees reasonably well with the value we found for H-assisted CO dissociation via the HCO intermediate (100 kJ/mol). Huo et al. did not report barrier for HCO dissociation.

**Table 6.3:** Computed H<sub>2</sub>-adsorption energies, CO adsorption energies for direct adsorption on surface carbon, reaction enthalpies and forward- and backwards activation energies, for the hydrogen-assisted and carbon-assisted mechanism -mechanisms for crystal forms of  $\theta$ -Fe<sub>3</sub>C. All energies are given in kJ/mol.

Surface	$E_{\text{ads}}(\text{H}_2)$ (kJ/mol)	HCO-formation			HCO-dissociation		
		$\Delta H_{\text{rx}}$	$E_{\text{act}}^{\text{f}}$	$E_{\text{act}}^{\text{b}}$	$\Delta H_{\text{rx}}$	$E_{\text{act}}^{\text{f}}$	$E_{\text{act}}^{\text{b}}$
		(kJ/mol)	(kJ/mol)	(kJ/mol)	(kJ/mol)	(kJ/mol)	(kJ/mol)
(100)	110	47	60	13	-96	88	184
(010)	111	53	59	6	1	71	70
(110)	130	100	243	143	-86	66	152
(011)	123	110	256	146	-76	98	174
(001)	85	50	100	50	-75	54	129
(101)	161	194	240	46	-143	46	189
(0 $\bar{1}$ 1)	88	46	72	26	-37	28	65
(1 $\bar{1}$ 1)	140	118	155	37	-162	1	163
(111)	169	83	125	42	-116	43	159

Surface	$E_{\text{ads}}(\text{H}_2)$ (kJ/mol)	COH-formation			COH-dissociation		
		$\Delta H_{\text{rx}}$	$E_{\text{act}}^{\text{f}}$	$E_{\text{act}}^{\text{b}}$	$\Delta H_{\text{rx}}$	$E_{\text{act}}^{\text{f}}$	$E_{\text{act}}^{\text{b}}$
		(kJ/mol)	(kJ/mol)	(kJ/mol)	(kJ/mol)	(kJ/mol)	(kJ/mol)
(100)	109.5	114	166	52	-119	77	196
(010)	110.8	92	115	23	-65	57	112
(110)	130.1	108	218	110	-33	120	153
(011)	123.3	157	193	36	-62	123	185
(001)	85.0	78	203	125	-41	100	141
(101)	161	226	232	6	-190	88	278
(0 $\bar{1}$ 1)	88.4	94	228	134	-92	106	198
(1 $\bar{1}$ 1)	140.3	91	194	103	-146	26	172
(111)	169.4	129	207	78	-131	52	183

Surface	$E_{\text{ads}}(\text{C}_*\text{CO})$	$\Delta H_{\text{rx}}$	$E_{\text{act}}^{\text{f}}$	$E_{\text{act}}^{\text{b}}$
	(kJ/mol)	(kJ/mol)	(kJ/mol)	(kJ/mol)
(011)	84	48	77	125

Hydrogenation of CO to COH on the  $\theta$ -Fe-carbide surfaces involves high barriers ( $>200$  kJ/mol) for all surfaces, except for the (010) surface. While all COH formation reactions are highly endothermic, COH dissociation reactions are exothermic. This shows that the COH intermediates are unstable. The barrier on the (010) surface, however, is relatively low. Henceforth, we may expect that the COH dissociation pathway may compete with direct CO dissociation and HCO dissociation pathways for this particular surface. The reason for the high CO hydrogenation barriers towards COH on the other surfaces is that the coordination of CO in the initial state is unfavourable for hydrogenation of the oxygen atom. On most surfaces, the orientation of the CO molecule is

perpendicular to the surface, resulting in a large distance between the oxygen atom and the surface. Hydrogenation then requires bending of the CO molecule towards the surface which costs energy because it results in less overlap of the metal *d*-band orbitals with the molecular orbitals of CO.

Overall, we can conclude that the activation barriers for COH dissociation to C+OH are comparable to those computed for HCO dissociation to CH+O and lower than values for direct C-O bond dissociation. This can be attributed to weakening of the C-O bond due to protonation of C or O. However, COH formation is much more difficult than HCO formation. Thus, the overall barrier for the COH pathway can be approximated by the COH formation barrier.

We also investigated a carbon-assisted mechanism for the (011) surface because other C-O bond scission pathways were found to be unfavourable on this particular surface. We started from an adsorption state where CO forms a bond with a surface carbon atom. The resulting adsorption energy is lower than typical bonds of CO to Fe sites. The CO adsorption energy that results in the CCO species is 121 kJ/mol higher than the most stable CO adsorption configuration on a Fe site on this surface. Thus, we need to take the formation of the CCO species into account as well. The overall forward activation barrier for CO dissociation from CCO is 198 kJ/mol, which is comparable to the adsorption energy (205 kJ/mol). Thus, CO desorption and dissociation will compete in this way. The moderate reaction barrier can be rationalized by the favourable bridged coordination of the oxygen atom of the CCO-intermediate with the surface Fe atoms. The backward activation energy is somewhat higher due to the relaxation of the surface in the final state, resulting in a lower energy.

### 6.3.5 Kinetic analysis

Based on a simplified kinetic model, we compared the different rates for CO dissociation for direct and H- and C-assisted CO dissociation. All rates were normalized to the rate of direct CO dissociation on the Co(0001), as is shown in Figure 6.6. We also include data for the stepped  $\alpha$ -Fe(111) and the Co(11 $\bar{2}$ 1) surfaces. Relevant kinetic data for Co(11 $\bar{2}$ 1) and Co(0001) were taken from the literature.[38]

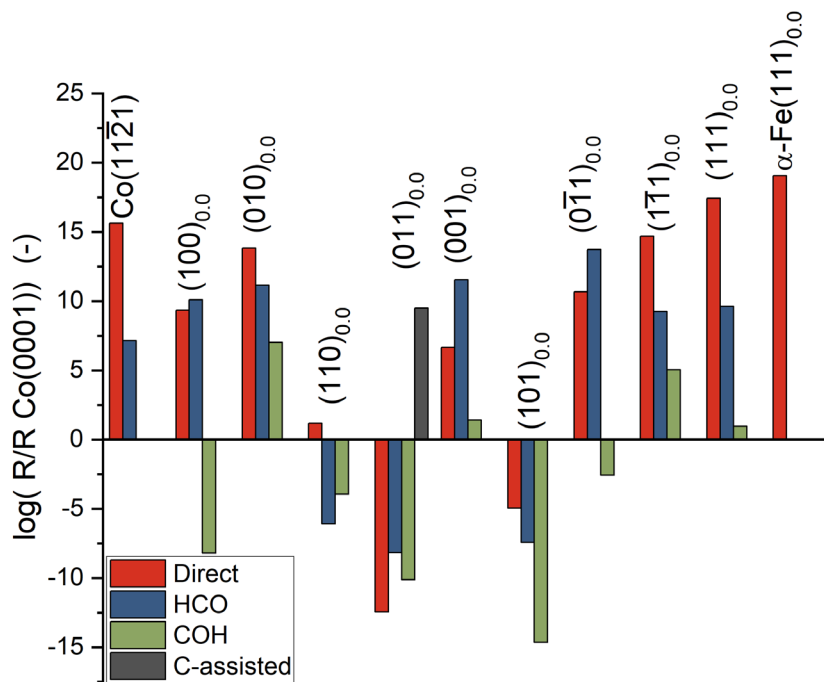


**Figure 6.6:** Reaction rates for direct CO dissociation (red) and assisted CO dissociation via HCO (blue), COH (green) and CCO intermediate (only for (011)). These rates are shown relative to the rate of direct CO dissociation on the Co(0001) surface. Positive values imply a higher reaction rate compared to direct CO dissociation on Co(0001), while negative values represent lower reaction rates. The rate for the Co(11 $\bar{2}$ 1) surface is given for comparison (data for Co surfaces taken from Liu et al. [38]).

The direct CO dissociation mechanism exhibits the largest relative rates for five surfaces, i.e. (111), (1 $\bar{1}$ 1), (010), (011) and (101). The other four surfaces ((100), (0 $\bar{1}$ 1), (011) and (001)) exhibit higher rates for either the H-assisted CO dissociation *via* a HCO intermediate, i.e. (100), (0 $\bar{1}$ 1) and (001), or the C-assisted mechanism for (011). It should be noted that the relative rate for direct CO dissociation on the (100) surface is comparable to the relative rate for H-assisted CO dissociation. All other eight surfaces exhibit a much larger difference in relative rates. The (010) and (1 $\bar{1}$ 1) surfaces show a comparable rate to the stepped Co(11 $\bar{2}$ 1), whereas the (111) surface shows an even higher rate than the stepped cobalt surface.

We have also investigated the role of the partial pressures of CO and H<sub>2</sub> on the relative rates. We find that the rate decreases with increasing rate because the amount of empty sites decreases at higher pressure. Empty sites are needed for CO dissociation. Figure D.2.1 in Appendix D.2 shows the influence of the pressure on the rate of CO dissociation, which was investigated for the cases of direct CO dissociation and H-assisted CO dissociation. The H<sub>2</sub>/CO ratio was kept constant and lateral interactions were neglected. The influence of the H<sub>2</sub>/CO ratio on these results was minor as can be appreciated from Table D.2.1 in Appendix D.2. We also investigated the influence of the surface termination on  $\theta$ -Fe-carbide nanoparticles on the C-O bond scission rate. For this purpose, we used the relative contributions of the different surfaces determined for the Wulff particle (Table

6.1 and Figure 6.2). The complete set of resulting reactivity data is presented in Table D.2.2 in Appendix D.2. An important finding is that the (0 $\bar{1}$ 1) and (111) surfaces present comparable rates which are much higher than the computed rates for the other surfaces. The contribution of these surfaces depends on the overall pressure and we find that with increasing pressure the contribution of the H-assisted CO dissociation mechanism on the (0 $\bar{1}$ 1) surface becomes more important (Figure D.2.2 and D.2.3 in Appendix D.2).

### 6.3.6 The nature of CO activation

In an attempt to identify the underlying electronic factors determining the CO dissociation barrier, we correlated typical reaction descriptors such as reaction energies, adsorption energies and atomic charges to the activation energy of CO dissociation. None of these descriptors however showed a strong correlation with the activation barriers. The absence of a correlation between reaction barrier and adsorption thermodynamics has been found earlier for CO activation on ruthenium surfaces [46], where the stability of the transition state was found to play a role in the absence of a correlation. We did not include a detailed analysis of H-assisted CO activation because the lower C-O bond dissociation barriers are mostly related to protonation of CO, which destabilizes the C-O bond and decreases the C-O bond order. The correlation of the activation energy and the bond order becomes only weak, especially due to stability differences of H atoms on different surfaces (Figure D.3.1 in Appendix D.3).

In our system, the lattice C atoms interact with the dissociating CO in two ways: (i) the C atoms coordinate to the metal atoms by which the interaction between the metal atoms and CO becomes weaker and (ii) there is an electronic repulsion between C and the dissociating CO. These interactions strongly influence the reaction pathway in a non-systematic fashion, explaining the absence of a correlation between reaction energies, adsorption energies or atomic charges and the reaction barriers.

Therefore, we investigated the CO bond order using the DDEC6 atomic population analysis introduced by Manz.[39] This methodology allows for accurate determination of the CO bond order (BO), a direct descriptor of the strength of the C-O bond. The results are provided in Appendix D.3 in Tables D.3.1-D.3.3. Herein, it can be seen that the BO for gaseous CO is 2.5. Upon adsorption of CO, the BO decreases to values in the 1.5-2.3 range (depending on the surface) and the bond order is expectedly zero after CO dissociation.

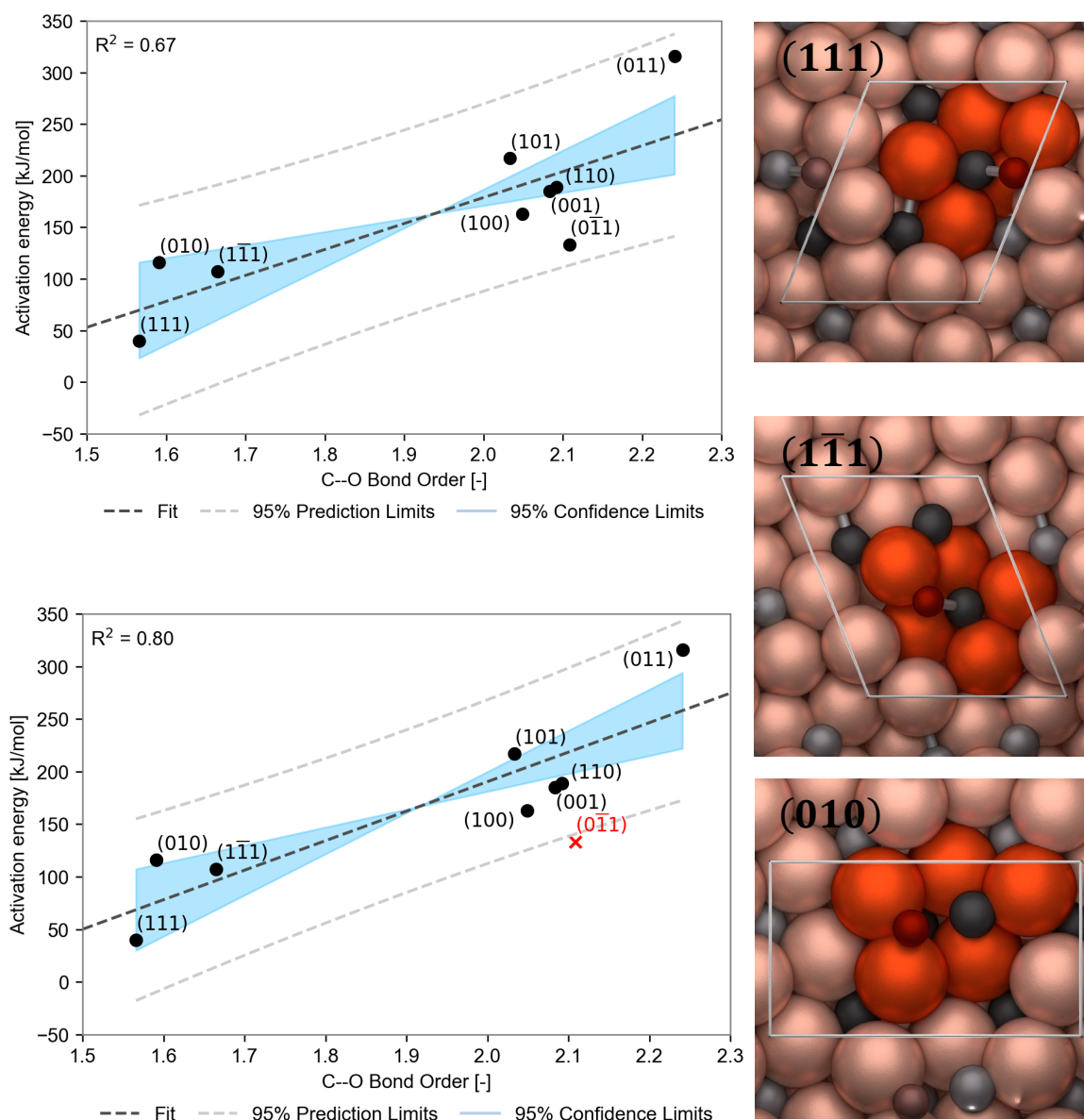


**Figure 6.5:** Linear regression of the activation energy for direct CO dissociation versus the C-O bond order using a dataset consisting of (a) all nine surfaces and (b) without the (011) surface. The central line corresponds to the linear fit. The neighboring grey lines and the blue coloured area indicate the 95% prediction limits and 95% confidence limits, respectively. The position of the outlier has been marked in subfigure (b) by a red cross. The regression coefficients ( $R^2$ ) is shown in the left-top corner of each graph. The transition states of the three surfaces, (111), (111) and (010) (from the top down) with the lowest barrier for direct CO dissociation are shown in subfigure (c). The B<sub>5</sub> sites on these surface have been highlighted.

In Figure 6.5a, the activation energy as a function of the BO of CO in the initial state is shown. Initially, a linear regression of the data only showed a weak correlation as evident from a regression coefficient ( $R^2$ ) of only 0.67. Based on the confidence intervals and the mode of CO adsorption (*i.e.*, bridged), we identified the data point corresponding to the (011) surface as an outlier. Linear

regression on the subset without this data point shows a much higher regression coefficient of 0.80, as shown in Figure 6.5b. Using the concept of BO based on the DDEC6 analysis, it is clear that the activation energy correlates with the BO of CO in the initial state. This correlation can be explained using the Blyholder model.[47] This model, which is strongly inspired by frontier molecular orbital (MO) theory, describes the interaction of CO with a metal surface as the result of electron donation from the  $5\sigma$  MO and simultaneous back-donation into the  $2\pi^*$  MO. The latter causes the C-O bond to weaken, leading to activation of the CO adsorbate and is thus considered favourable for CO dissociation. The low CO dissociation barrier of 40 kJ/mol over the (111) surface is thus caused by its unique topology allowing for a favourable overlap of the molecular orbitals with the metallic  $d$ -band, significantly destabilizing the CO bond in the initial state. This conclusion is further supported when studying the similarity of the active sites of neighbouring data points, i.e. the triplet of data points in the bottom left corner of both graphs in Figure 6.5. From Figure 6.2, it can be seen that the active sites corresponding to these data points, i.e. the (111), (010) and ( $1\bar{1}1$ ) surfaces, are very similar and correspond to a  $B_5$  configuration. The transition states of these surfaces are shown in subfigure (c). The  $B_5$  sites on these surface have been highlighted. From the literature, it is known that such configurations have a favourable barrier for direct CO dissociation. This work now shows that  $B_5$  sites not only effectively catalyse CO dissociation on many metallic surfaces, but also on  $\theta$ - $\text{Fe}_3\text{C}$  and *via* the same mechanism.

## 6.4 Conclusions

All nine  $\theta$ -Fe-carbide surfaces of iron ( $\theta$ - $\text{Fe}_3\text{C}$ ) were investigated for their reactivity towards CO dissociation by density functional theory. Compared to the most reactive (111) surface of bcc-Fe on which CO binds in sevenfold coordination, CO binds in threefold or fourfold sites on the carburized surfaces. This is a direct effect of the presence of interstitial C atoms at or below the surface. Adsorption of O and H is less affected by the presence of C atoms. The surfaces that exhibit a step-edge like geometry ( $B_5$ -site) favour direct CO dissociation. Surfaces with such a  $B_5$  site are the (111), ( $1\bar{1}1$ ) and (010) terminations. For the (111) surface, a very low activation energy of 40 kJ/mol is computed. When we also consider H-assisted mechanisms, the ( $0\bar{1}1$ ), (001) and (100) surfaces are also predicted to be active in CO dissociation. On the other hand, the (011), (110) and (101) surfaces are inert with CO dissociation barriers close to or exceeding the CO adsorption energy. Based on surface free energies, we find that the three most active surfaces, i.e. (111), ( $1\bar{1}1$ ) and ( $0\bar{1}1$ ), make up *ca.* 31% of a Wulff nanoparticle surface, while the moderately active surfaces contribute *ca.* 14%



to the total surface. The remainder of such a Wulff model particle consists of inert surfaces. Using a simplified kinetic model, we show that the (111) surface (direct CO dissociation) and the (0 $\bar{1}$ 1) surface (H-assisted CO dissociation via HCO) display comparable CO bond dissociation rates, much higher than the other surfaces. Using an atomic population analysis, we show that the activation barrier for C-O bond dissociation correlates well with the bond order of adsorbed CO. This implies that pre-activation of CO is important for lowering of the overall activation barrier. The present work shows that the high-temperature  $\theta$ -Fe<sub>3</sub>C phase is highly active towards CO bond dissociation, which is the essential first step in the Fischer-Tropsch reaction. Several of the exposed surfaces present lower overall CO dissociation barriers than  $\alpha$ -Fe (known to be unstable under Fischer-Tropsch conditions) and the  $\chi$ -carbide of Fe (usually assumed to be the most stable phase of Fe-carbide under Fischer-Tropsch conditions). Another salient finding of this work is that direct CO dissociation on  $\theta$ -Fe<sub>3</sub>C preferentially follows a similar mechanism than on metallic surfaces involving a B<sub>5</sub> site.

## References

- [1] H. Jahangiri, J. Bennett, P. Mahjoubi, K. Wilson, S. Gu, A review of advanced catalyst development for Fischer–Tropsch synthesis of hydrocarbons from biomass derived syn-gas, *Catalysis Science & Technology* 4 (2014) 2210-2229.
- [2] I.A.W. Filot, R.J.P. Broos, J.P.M. van Rijn, G.J.H.A. van Heugten, R.A. van Santen, E.J.M. Hensen, First-principles-based microkinetics simulations of synthesis gas conversion on a stepped rhodium surface, *ACS Catalysis* 5 (2015) 5453-5467.
- [3] F. Jiao, J. Li, X. Pan, J. Xiao, H. Li, H. Ma, M. Wei, Y. Pan, Z. Zhou, M. Li, Selective conversion of syngas to light olefins, *Science* 351 (2016) 1065-1068.
- [4] H. Okamoto, The C-Fe (carbon-iron) system, *Journal of Phase Equilibria* 13 (1992) 543-565.
- [5] V. Ordonsky, B. Legras, K. Cheng, S. Paul, A. Khodakov, The role of carbon atoms of supported iron carbides in Fischer–Tropsch synthesis, *Catalysis Science & Technology* 5 (2015) 1433-1437.
- [6] H. Jung, W.J. Thomson, Dynamic X-ray diffraction study of an unsupported iron catalyst in Fischer–Tropsch synthesis, *Journal of Catalysis* 134 (1992) 654-667.
- [7] E. de Smit, F. Cinquini, A.M. Beale, O.V. Safonova, W. van Beek, P. Sautet, B.M. Weckhuysen, Stability and reactivity of  $\epsilon$ - $\chi$ - $\theta$  iron carbide catalyst phases in fischer–tropsch synthesis: controlling  $\mu$ C, *Journal of the American Chemical Society* 132 (2010) 14928-14941.
- [8] M. Pijolat, V. Perrichon, P. Bussiere, Study of the carburization of an iron catalyst during the Fischer–Tropsch synthesis: Influence on its catalytic activity, *Journal of Catalysis* 107 (1987) 82-91.
- [9] L.-J. Deng, C.-F. Huo, X.-W. Liu, X.-H. Zhao, Y.-W. Li, J. Wang, H. Jiao, Density Functional Theory Study on Surface C x H y Formation from CO Activation on Fe<sub>3</sub>C (100), *The Journal of Physical Chemistry C* 114 (2010) 21585-21592.
- [10] S. Booyens, Structure and reactivity of iron single crystal surfaces, Cardiff University (United Kingdom), 2010.
- [11] T. Herranz, S. Rojas, F.J. Pérez-Alonso, M. Ojeda, P. Terreros, J.L.G. Fierro, Genesis of iron carbides and their role in the synthesis of hydrocarbons from synthesis gas, *Journal of catalysis* 243 (2006) 199-211.
- [12] D.B. Bukur, X. Lang, Y. Ding, Pretreatment effect studies with a precipitated iron Fischer–Tropsch catalyst in a slurry reactor, *Applied Catalysis A: General* 186 (1999) 255-275.
- [13] C.-F. Huo, Y.-W. Li, J. Wang, H. Jiao, Insight into CH<sub>4</sub> formation in iron-catalyzed Fischer–Tropsch synthesis, *Journal of the American Chemical Society* 131 (2009) 14713-14721.
- [14] E.C. Bain, X-ray data on cementite, *Chem. And Met. Eng.* 25 (1921).
- [15] A. Westgren, G. Phragmén, Zum Kristallbau des Eisens und Stahls. II, *Zeitschrift für Physikalische Chemie* 102 (1922) 1-25.
- [16] F.W. M. Polanyi, Röntgen-Emissionsspektren der Eisenmodifikationen, *Mitt. Kaiser-Wilhelm-Inst. Eisenforschung* 4 (1922).
- [17] S. SHIMURA, A Study on the Structure of Cementite, *Proceedings of the Imperial Academy* 6 (1930) 269-271.
- [18] S.B. Hendricks, XXXVI. The Crystal Structure of Cementite, *Zeitschrift für Kristallographie-Crystalline Materials* 74 (1930) 534-545.
- [19] H. Lipson, N. Petch, The crystal structure of cementite, Fe<sub>3</sub>C, *Iron and Steel Institute (London)* 142 (1940).
- [20] H.A. Schwartz, Correspondence on the findings of H. Lipson and N.J. Petch regarding the crystal structure of cementite, *J. Iron and Steel Institute* 142 (1940).
- [21] O.K. D. Meinhardt, Strukturuntersuchungen an Karbiden des Eisens, Wolframs und Chroms mit thermischen Neutronen, *Z. das Eisenhüttenwesen* 77 (1962).
- [22] A.I. Gardin, An Electron-Diffraction Study of the Structure of Cementite *Kristallografya* 7 (1963).
- [23] F. Herbst, J. Smuts, Comparison of X-ray and neutron-diffraction refinements of the structure of cementite Fe<sub>3</sub>C, *Acta Crystallographica* 17 (1964) 1331-1332.
- [24] E. Fasiska, G. Jeffrey, On the cementite structure, *Acta Crystallographica* 19 (1965) 463-471.
- [25] P.C. D. Fruchart, R. Fruchart, A. Rouault, J.P. Senateur, Études structurales de composés de type cémentite: Effet de l'hydrogène sur Fe<sub>3</sub>C suivi par diffraction neutronique. Spectrométrie Mössbauer sur FeCo<sub>2</sub>B et Co<sub>3</sub>B dopés au <sup>57</sup>Fe, *J. Solid State Chemistry* 51 (1984) 246-252.

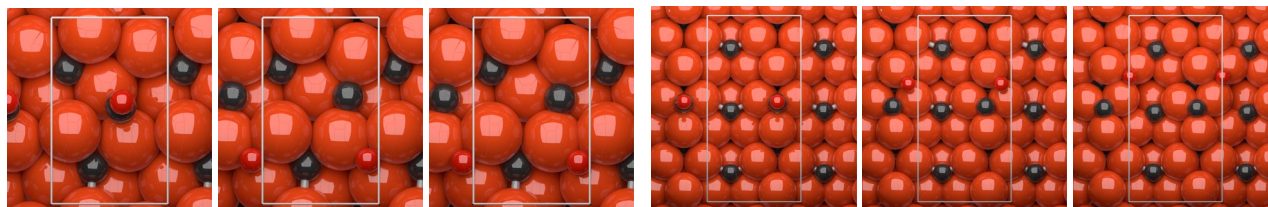
- [26] I. Wood, L. Vočadlo, K. Knight, D.P. Dobson, W. Marshall, G.D. Price, J. Brodholt, Thermal expansion and crystal structure of cementite, Fe<sub>3</sub>C, between 4 and 600 K determined by time-of-flight neutron powder diffraction, *Journal of Applied Crystallography* 37 (2004) 82-90.
- [27] M.E. Dry, The fischer–tropsch process: 1950–2000, *Catalysis today* 71 (2002) 227-241.
- [28] G. Kresse, J. Hafner, Ab initio molecular dynamics for liquid metals, *Physical Review B* 47 (1993) 558.
- [29] G. Kresse, J. Hafner, Ab initio molecular-dynamics simulation of the liquid-metal–amorphous-semiconductor transition in germanium, *Physical Review B* 49 (1994) 14251.
- [30] G. Kresse, J. Furthmüller, Efficiency of ab-initio total energy calculations for metals and semiconductors using a plane-wave basis set, *Computational materials science* 6 (1996) 15-50.
- [31] G. Kresse, J. Furthmüller, Efficient iterative schemes for ab initio total-energy calculations using a plane-wave basis set, *Physical review B* 54 (1996) 11169.
- [32] J.P. Perdew, K. Burke, M. Ernzerhof, Generalized gradient approximation made simple, *Physical review letters* 77 (1996) 3865.
- [33] K. Burke, J. Perdew, M. Ernzerhof, Generalized Gradient Approximation Made Simple [*Phys. Rev. Lett.* 77, 3865 (1996)], *Phys. Rev. Lett.* 78 (1997) 1396.
- [34] P.E. Blöchl, Projector augmented-wave method, *Physical review B* 50 (1994) 17953.
- [35] G. Kresse, D. Joubert, From ultrasoft pseudopotentials to the projector augmented-wave method, *Physical Review B* 59 (1999) 1758.
- [36] G. Henkelman, H. Jónsson, Improved tangent estimate in the nudged elastic band method for finding minimum energy paths and saddle points, *The Journal of chemical physics* 113 (2000) 9978-9985.
- [37] K. Momma, F. Izumi, VESTA 3 for three-dimensional visualization of crystal, volumetric and morphology data, *Journal of applied crystallography* 44 (2011) 1272-1276.
- [38] J.-X. Liu, H.-Y. Su, D.-P. Sun, B.-Y. Zhang, W.-X. Li, Crystallographic dependence of CO activation on cobalt catalysts: HCP versus FCC, *Journal of the American Chemical Society* 135 (2013) 16284-16287.
- [39] T.A. Manz, Introducing DDEC6 atomic population analysis: part 3. Comprehensive method to compute bond orders, *RSC Advances* 7 (2017) 45552-45581.
- [40] W.C. Chiou, E.A. Carter, Structure and stability of Fe<sub>3</sub>C-cementite surfaces from first principles, *Surface Science* 530 (2003) 88-100.
- [41] D.C. Sorescu, D.L. Thompson, M.M. Hurley, C.F. Chabalowski, First-principles calculations of the adsorption, diffusion, and dissociation of a CO molecule on the Fe(100) surface, *Physical Review B* 66 (2002) 035416.
- [42] M.R. Elahifard, M.P. Jigato, J. Niemantsverdriet, Direct versus hydrogen-assisted CO dissociation on the Fe (100) Surface: a DFT study, *ChemPhysChem* 13 (2012) 89-91.
- [43] I.A.W. Filot, R.A. van Santen, E.J.M. Hensen, Quantum chemistry of the Fischer–Tropsch reaction catalysed by a stepped ruthenium surface, *Catalysis Science & Technology* 4 (2014) 3129-3140.
- [44] R. Van Hardeveld, A. Van Montfoort, The influence of crystallite size on the adsorption of molecular nitrogen on nickel, palladium and platinum: An infrared and electron-microscopic study, *Surface Science* 4 (1966) 396-430.
- [45] R.A. van Santen, M. Neurock, S.G. Shetty, Reactivity theory of transition-metal surfaces: a Brønsted–Evans–Polanyi linear activation energy–free-energy analysis, *Chemical reviews* 110 (2009) 2005-2048.
- [46] L. Foppa, C. Copéret, A. Comas-Vives, Increased Back-Bonding Explains Step-Edge Reactivity and Particle Size Effect for CO Activation on Ru Nanoparticles, *Journal of the American Chemical Society* 138 (2016) 16655-16668.
- [47] G. Blyholder, G. Blyholder, *J. Phys. Chem.* 68, 2772 (1964), *J. Phys. Chem.* 68 (1964) 2772.

# Appendix D

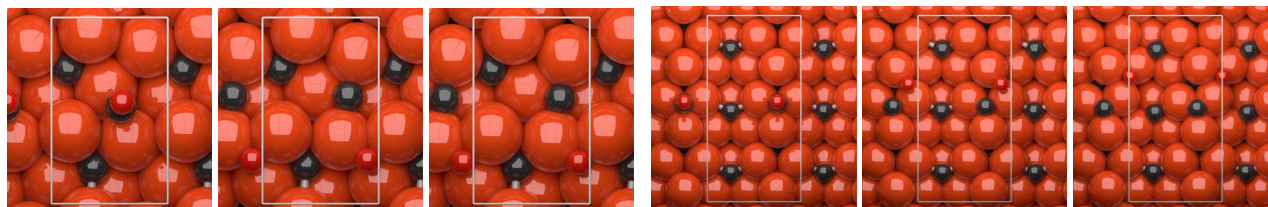
## Appendix D.1 Geometries from DFT

### Direct CO dissociation

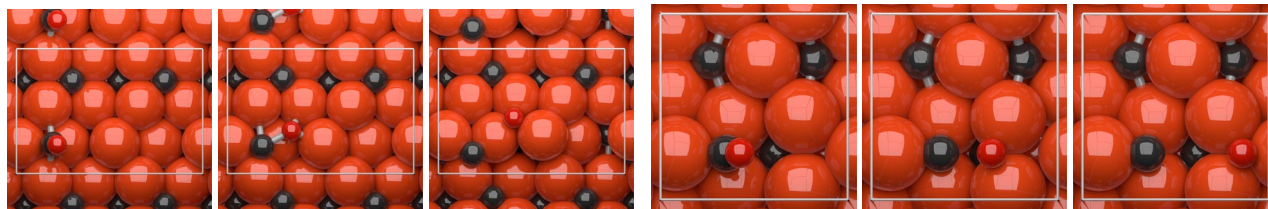
$(0\bar{1}1)$



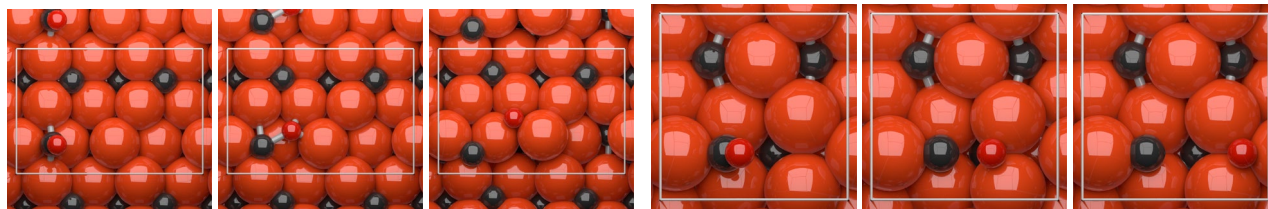
$(100)$



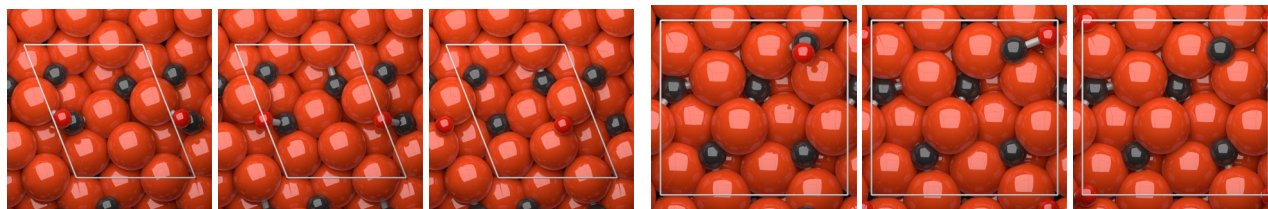
$(001)$



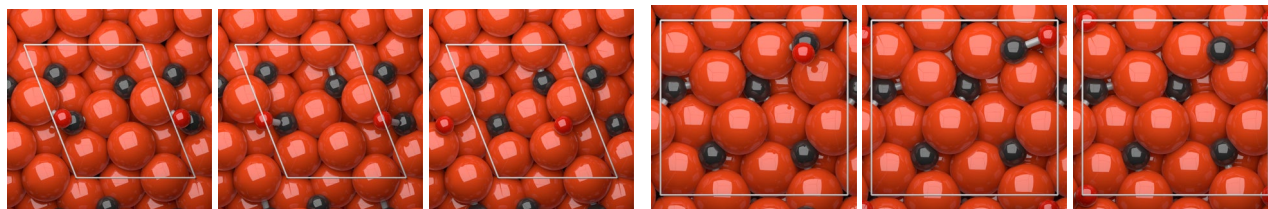
$(101)$



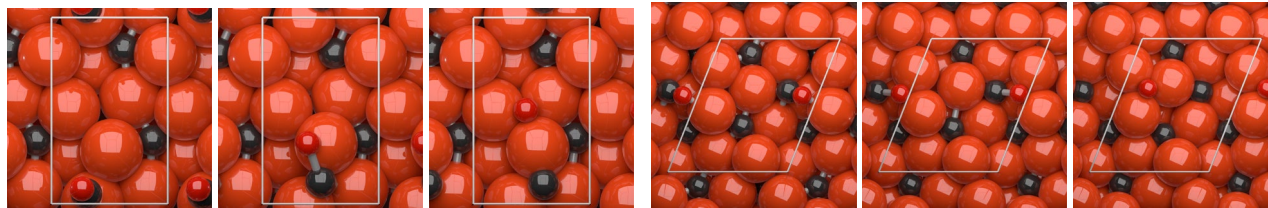
$(1\bar{1}1)$



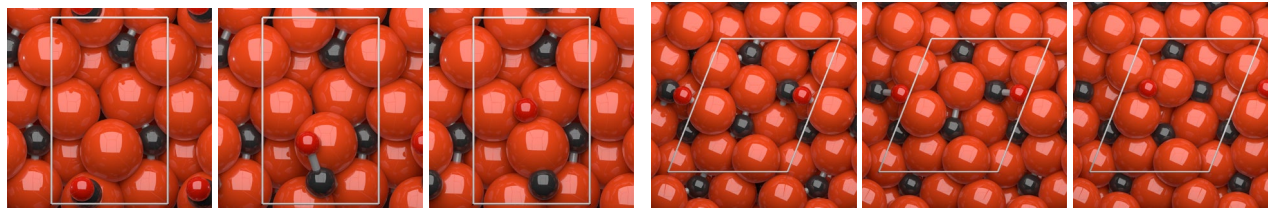
$(110)$



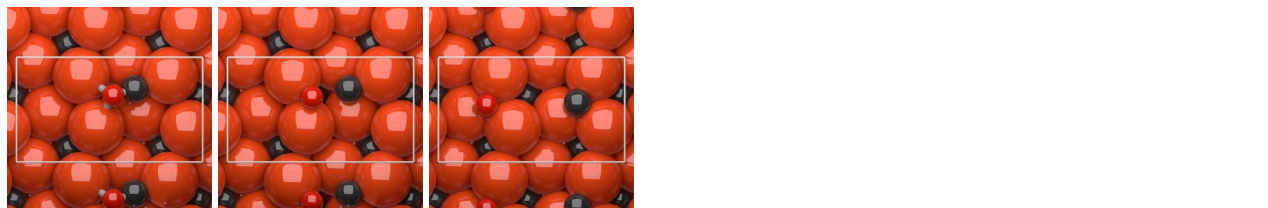
$(011)$



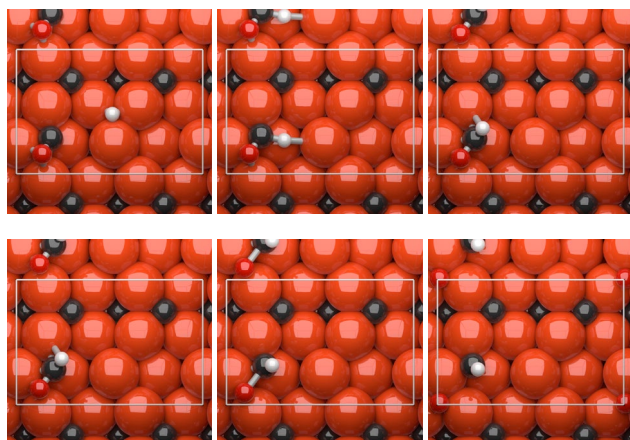
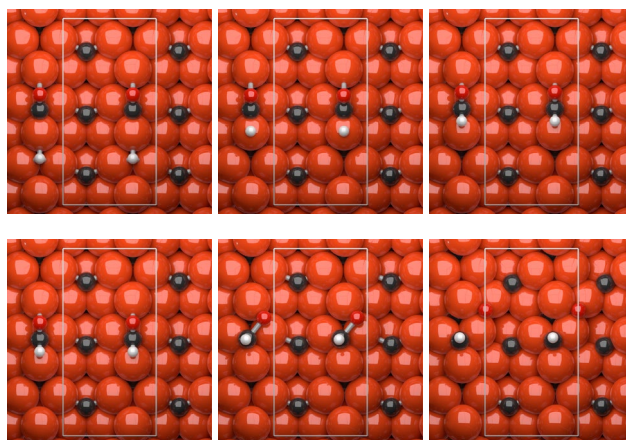
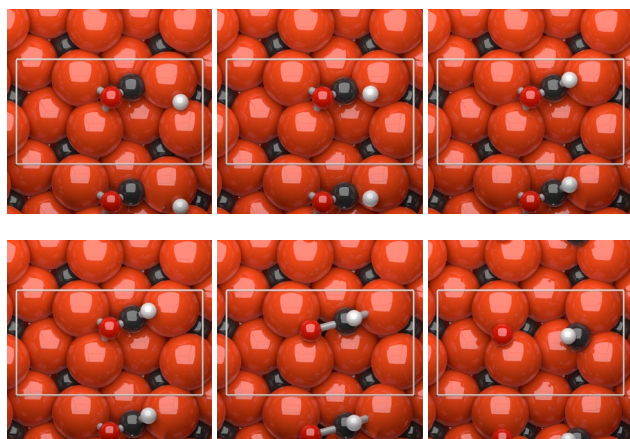
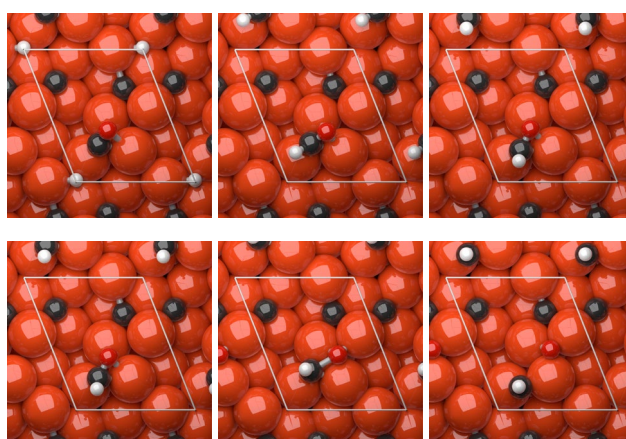
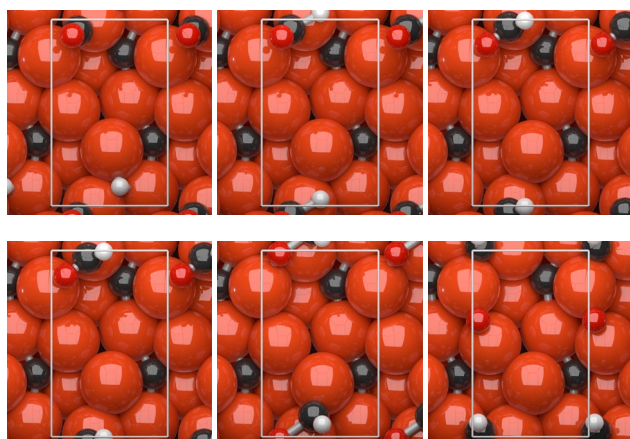
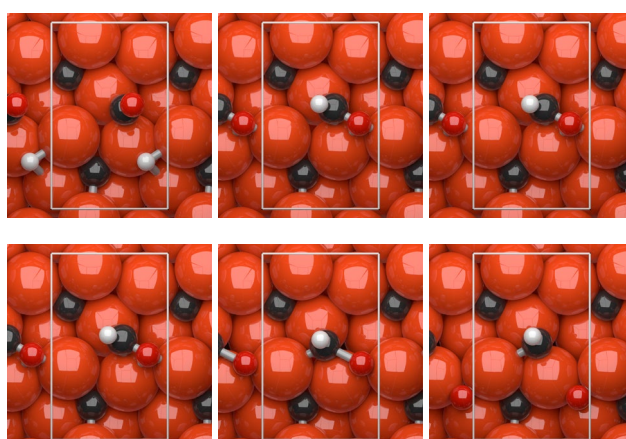
$(111)$



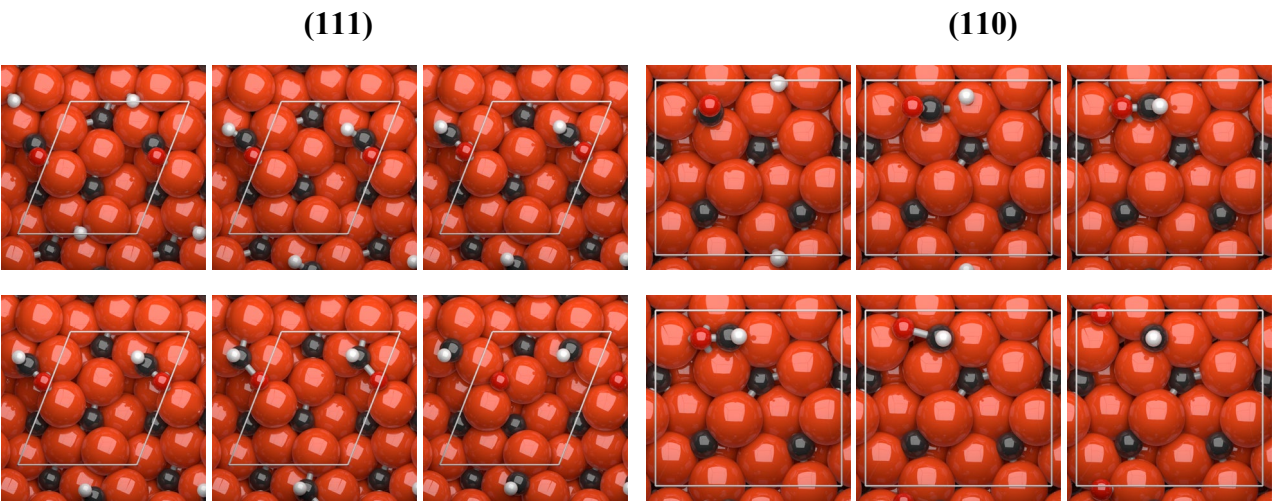
$(010)$



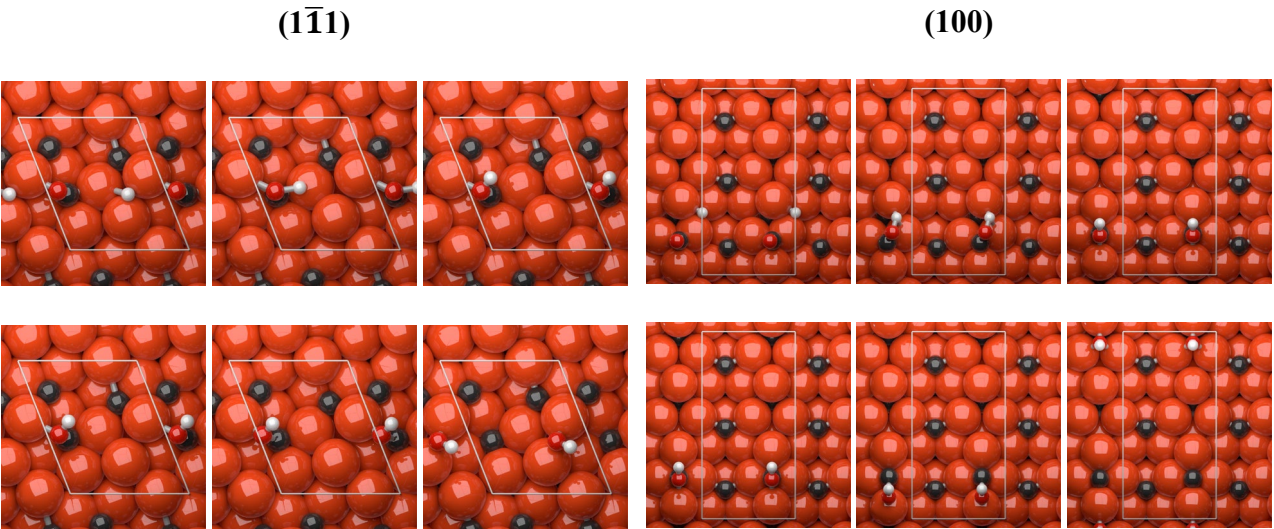
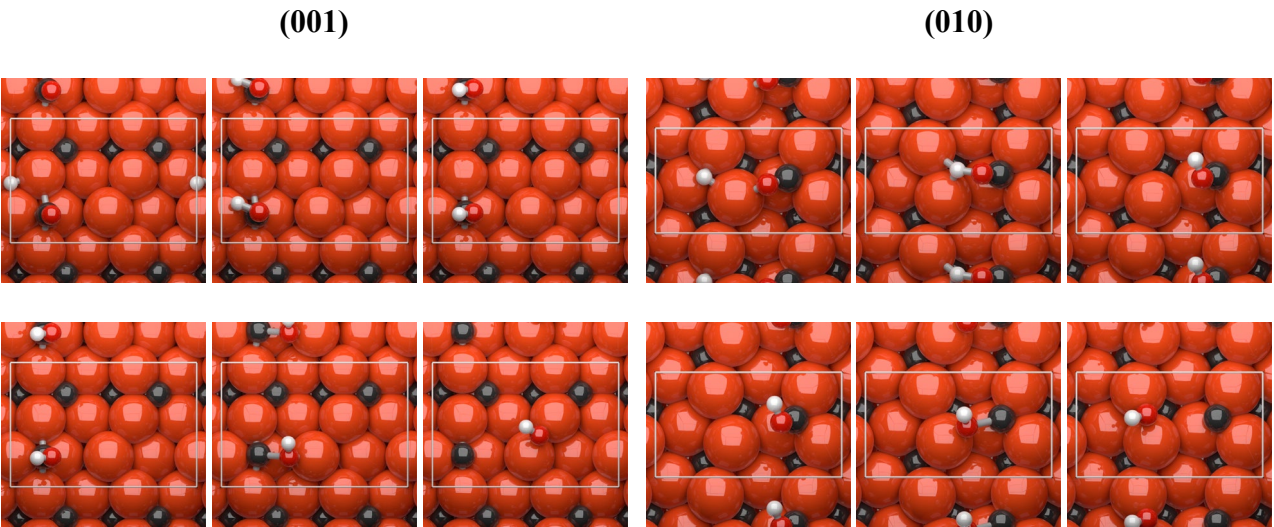


**H-assisted CO dissociation via HCO (001)****(001)****(100)****(010)****(111)****(011)****(011)**

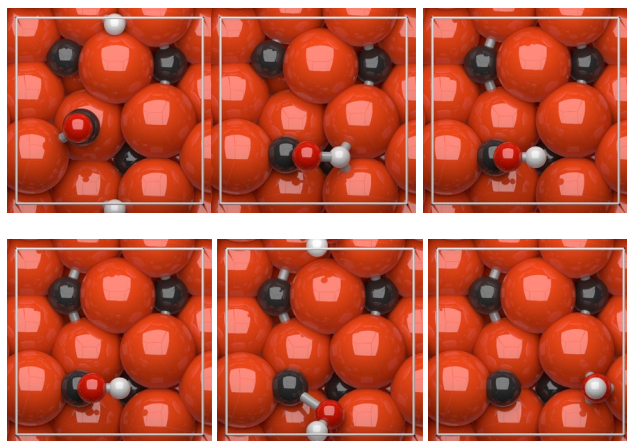
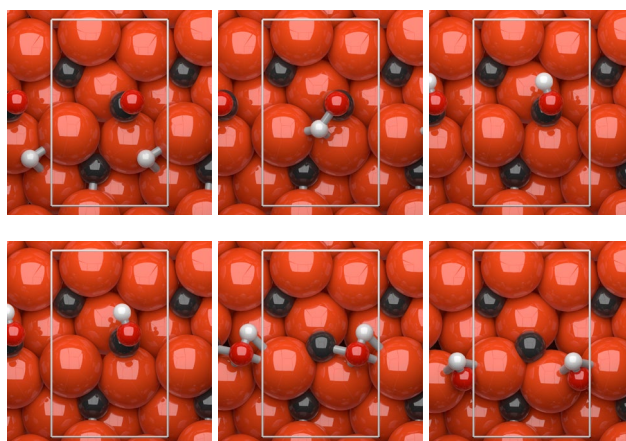
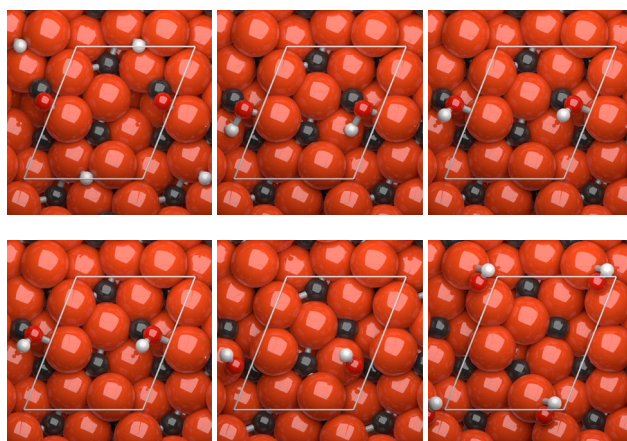
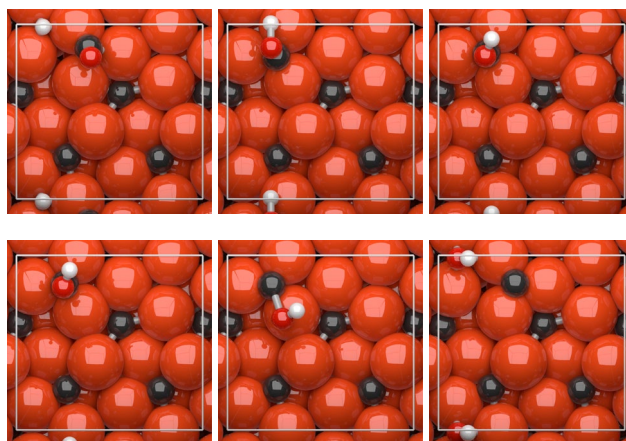
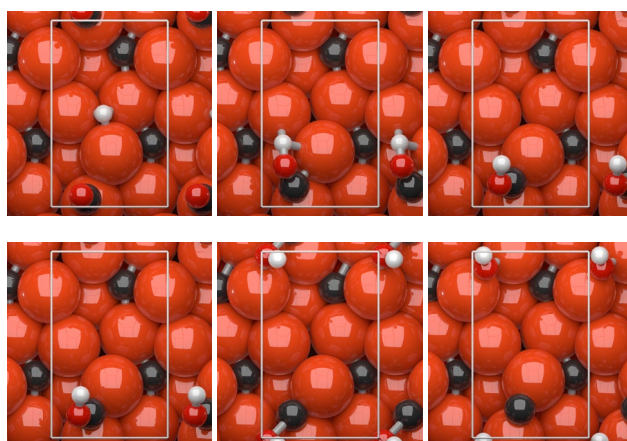




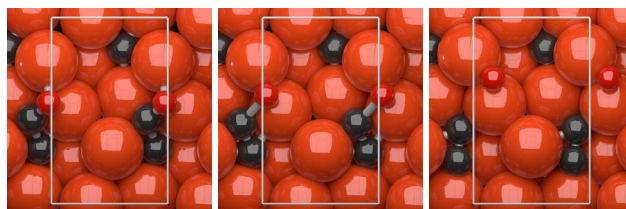
H-assisted CO dissociation via COH(001)





**(101)****(0 $\bar{1}$ 1)****(111)****(110)****(011)**

**Geometries C-assisted CCO dissociation on  
(011)**



## Appendix D.2 Relative reactivity and relative rates

To compare the CO dissociation rates on the different surfaces, we employed a simplified kinetic model, within the scope of transition state theory as introduced by Eyring.[3] For these calculations we used a temperature range between 100 K and 1000 K and a CO pressure range between  $1 \cdot 10^{-5}$  Pa and  $1 \cdot 10^5$  Pa. The plots of the reaction rates have been plotted, unless stated otherwise, at 500 K and at  $1 \cdot 10^5$  Pa with a  $H_2/CO$  of 2:1. We have taken all reactions up to and including the C-O bond scission reaction into account and have not assumed a pre-equilibrium. For the reaction rate in the hydrogen-assisted mechanisms via HCO or COH, we used all reactions up to and including the HC-O and the C-OH scission reactions. To check the influence of the  $H_2/CO$  ratio, the ratio between  $H_2$  and CO was varied between 1 and 2. The kinetics code used for the calculations can be found on GitHub.[4]

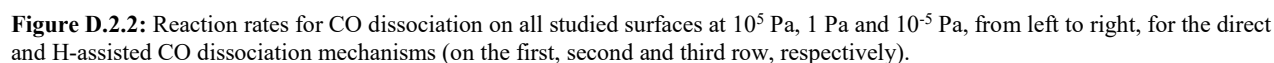
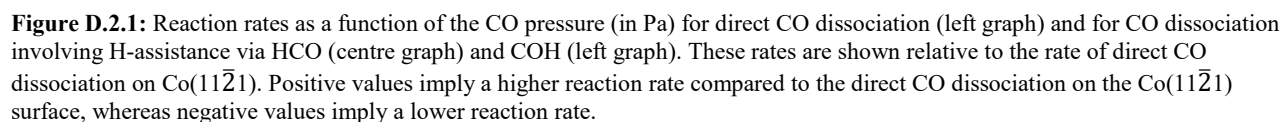
**Table D.2.1:** Relative rates for different  $H_2/CO$  ratios for direct and H-assisted CO dissociation on the low Miller index surfaces.

Direct											
$H_2/CO$	Co(0001)	(100)	(010)	(110)	(011)	(001)	(101)	(0 $\bar{1}$ 1)	( $\bar{1}$ 11)	(111)	$\alpha$ -Fe
2:1	-12.2	-2.2	0.0	-3.6	-16.8	-4.0	-6.4	-1.6	0.0	0.0	0.0
1:1	-12.2	-2.2	0.0	-3.9	-17.1	-4.1	-6.7	-1.6	0.0	0.0	0.0
HCO											
$H_2/CO$	Co(11 $\bar{2}$ 1)	(100)	(010)	(110)	(011)	(001)	(101)	(0 $\bar{1}$ 1)	( $\bar{1}$ 11)	(111)	$\alpha$ -Fe
2:1	-6.0	-2.4	-2.4	-11.4	-13.1	-0.4	-9.8	-0.3	-3.6	-0.5	-
1:1	-6.0	-2.5	-2.4	-11.7	-13.4	-0.4	-10.1	-0.3	-3.6	-0.5	-
COH											
$H_2/CO$	Co(11 $\bar{2}$ 1)	(100)	(010)	(110)	(011)	(001)	(101)	(0 $\bar{1}$ 1)	( $\bar{1}$ 11)	(111)	$\alpha$ -Fe
2:1	-	-8.3	-5.0	-9.9	-15.6	-10.4	-17.2	-15.9	-7.7	-8.5	-
1:1	-	-8.3	-5.0	-10.2	-15.9	-10.4	-17.5	-15.9	-7.7	-8.5	-

**Table D.2.2:** Relative surface reactivity corrected for the surface composition for the low Miller index surfaces

Surface (Mechanism)	Relative reactivity at $10^{-5}$ Pa (%)	Relative reactivity at 1 Pa (%)	Relative reactivity at $10^5$ Pa (%)
(010) (direct)	26	3	0
(001) (H-assisted)	8	0	0
(0 $\bar{1}$ 1) (H-assisted)	21	54	0
( $\bar{1}$ 11) (direct)	7	7	0
(111) (direct/H-assisted)	27 / 10	33 / 2	100/0





### Appendix D.3 Atomic population analysis

**Table D.3.1:** Atomic Bond orders (ABO) and molecular bond orders (BO) and the Atomic Charges and the total charge on the adsorbed CO for all surfaces.  $E_{\text{ads}}$  is the adsorption energy and  $E_{\text{act}}$  the activation barrier for C-O bond scission

Direct CO dissociation mechanism, Initial state									
surface	$E_{\text{ads}}$ (kJ/mol)	$E_{\text{act}}$ (kJ/mol)	ABO C	ABO O	BO C-O	charge on C	Charge on O	Charge CO (avg)	charge CO (total)
(011)	205	316	3.829	2.315	2.2409	0.089	-0.166	-0.0385	-0.077
(101)	214	217	3.92	2.224	2.0334	0.051	-0.204	-0.0765	-0.153
(110)	204	189	3.958	2.228	2.0921	0.021	-0.167	-0.073	-0.146
(001)	185	185	4.066	2.219	2.0833	-0.002	-0.171	-0.0865	-0.173
(100)	180	163	3.996	2.196	2.0494	-0.032	-0.185	-0.1085	-0.217
(010)	169	116	3.819	2.406	1.5909	-0.104	-0.188	-0.146	-0.292
(1 $\bar{1}$ 1)	174	107	4.006	2.295	1.6652	-0.121	-0.21	-0.1655	-0.331
(0 $\bar{1}$ 1)	155	133	3.956	2.242	2.1088	0.033	-0.2	-0.0835	-0.167
(111)	167	40	3.859	2.3	1.566	-0.094	-0.22	-0.157	-0.314

**Table D.3.2:** Atomic Bond orders (ABO) and molecular bond orders (BO) and the Atomic Charges and the total charge on the adsorbed CO for all surfaces.  $E_{\text{ads}}$  is the adsorption energy and  $E_{\text{act}}$  the activation barrier for C-O bond scission

HCO dissociation mechanism, Initial state								
Surface	$E_{\text{act}}$ (kJ/mol)	ABO C	ABO O	BO HC-O	charge on C	Charge on O	Charge CO (avg)	charge CO (total)
(001)	54	3.830605	2.306652	1.2442	-0.18378	-0.170174	-0.17698	-0.35396
(100)	88	3.932343	2.25044	1.5384	-0.07843	-0.182905	-0.13067	-0.26133
(110)	66	3.76989	2.254531	1.3872	-0.11337	-0.205163	-0.15927	-0.31853
(011)	98	3.742268	2.36709	1.6246	0.009066	-0.22298	-0.10696	-0.21391
(101)	46	3.763085	2.245611	1.3775	-0.11474	-0.206008	-0.16037	-0.32075
(010)	71	3.874601	2.372018	1.3299	-0.11963	-0.229244	-0.17444	-0.34888
(1 $\bar{1}$ 1)	37	3.813741	2.304946	1.3765	-0.1261	-0.18808	-0.15709	-0.31418
(0 $\bar{1}$ 1)	133	4.00876	2.340932	2.1793				
(111)	43	3.749453	2.384136	1.3523	-0.12889	-0.216456	-0.17267	-0.34535

**Table D.3.3:** Atomic Bond orders (ABO) and molecular bond orders (BO) and the Atomic Charges and the total charge on the gas phase CO

CO gas phase					
ABO C	ABO O	ABO C-O	charge on C	charge on O	charge CO (total)
2.470947	2.4709	2.4709	0.10762	-0.10762	0

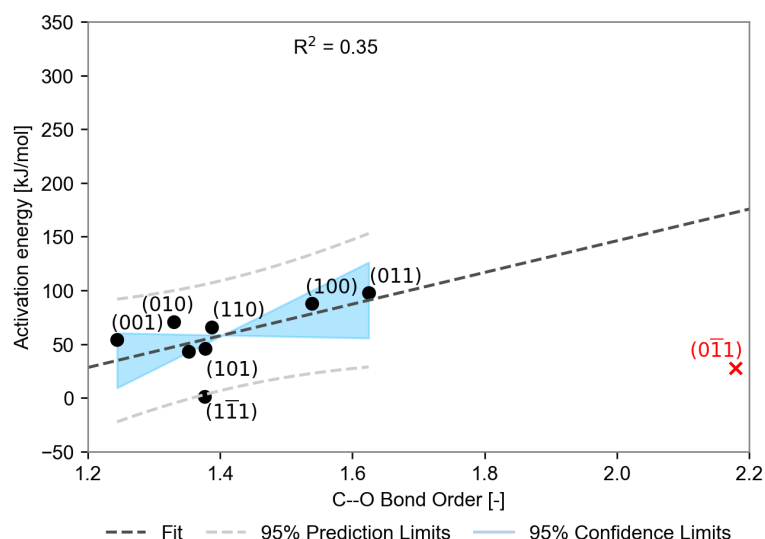


**Figure D.3.1:** Linear regression of the activation energy for the HCO dissociation versus the C-O bond order using a dataset consisting of all nine surfaces without the (01̄1) surface. The central line corresponds to the linear fit. The neighboring grey lines and the blue colored area indicate the 95% prediction limits and 95% confidence limits, respectively. The position of the outlier has been marked in subfigure (b) by a red cross. The regression coefficients ( $R^2$ ) is shown in the left-top corner of each graph.

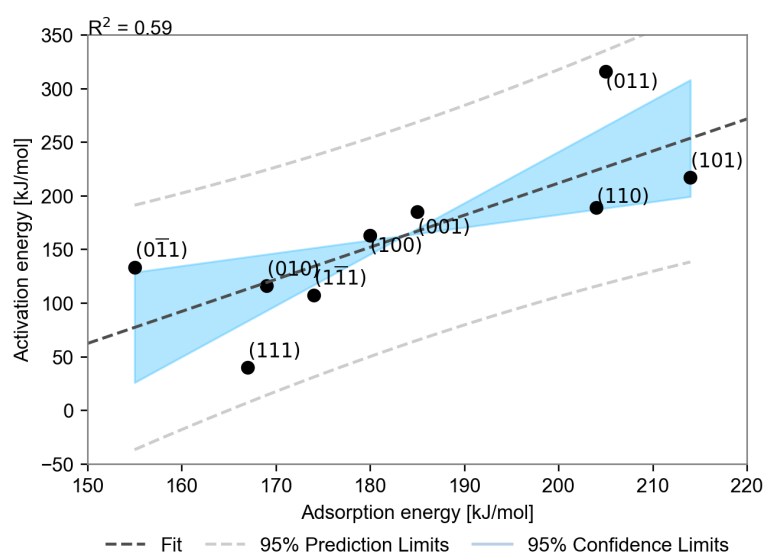


**Figure D.3.2:** Linear regression of the activation energy for the direct CO dissociation versus the Adsorption energy consisting of all nine surfaces. The central line corresponds to the linear fit. The neighbouring grey lines and the blue coloured area indicate the 95% prediction limits and 95% confidence limits, respectively. The regression coefficients ( $R^2$ ) is shown in the left-top corner of the graph.

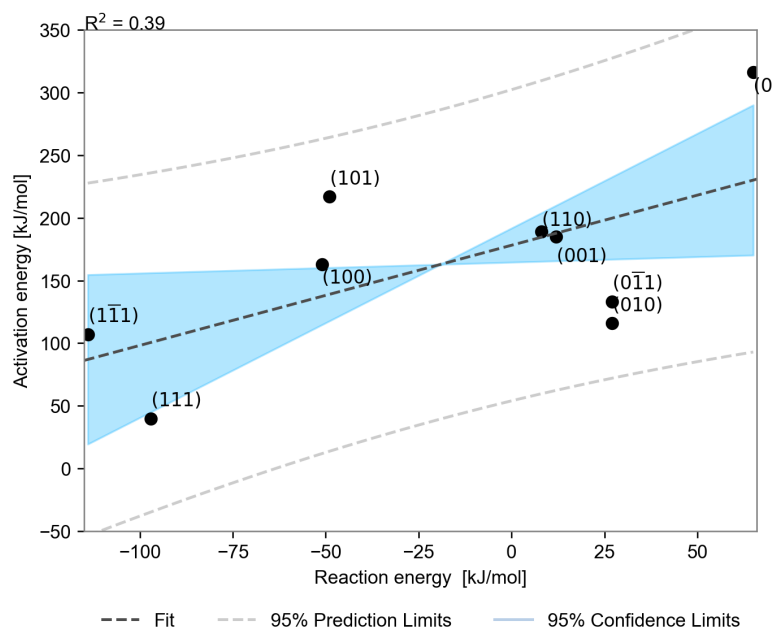


**Figure D.3.3:** Linear regression of the activation energy for the direct CO dissociation versus the reaction enthalpy consisting of all nine surfaces. The central line corresponds to the linear fit. The neighbouring grey lines and the blue coloured area indicate the 95% prediction limits and 95% confidence limits, respectively. The regression coefficients ( $R^2$ ) is shown in the left-top corner of the graph.

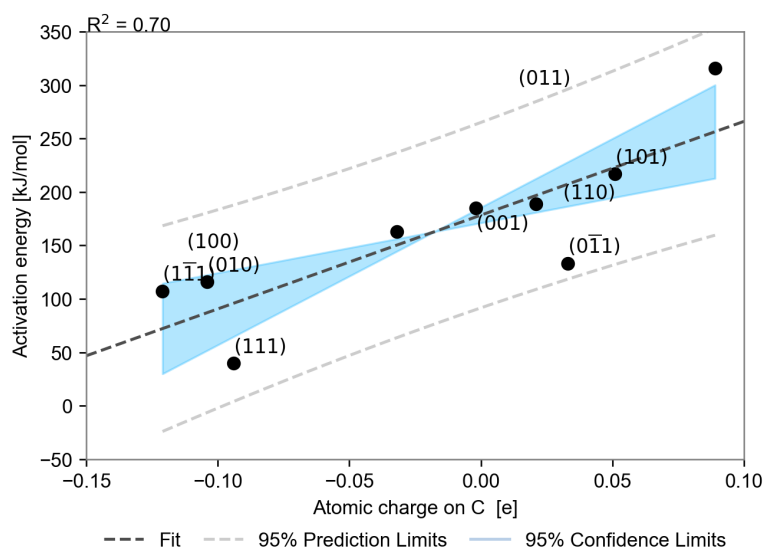


**Figure D.3.4:** Linear regression of the activation energy for the direct CO dissociation versus the atomic charge on the C atom, of all nine surfaces. The central line corresponds to the linear fit. The neighbouring grey lines and the blue coloured area indicate the 95% prediction limits and 95% confidence limits, respectively. The regression coefficients ( $R^2$ ) is shown in the left-top corner of the graph.

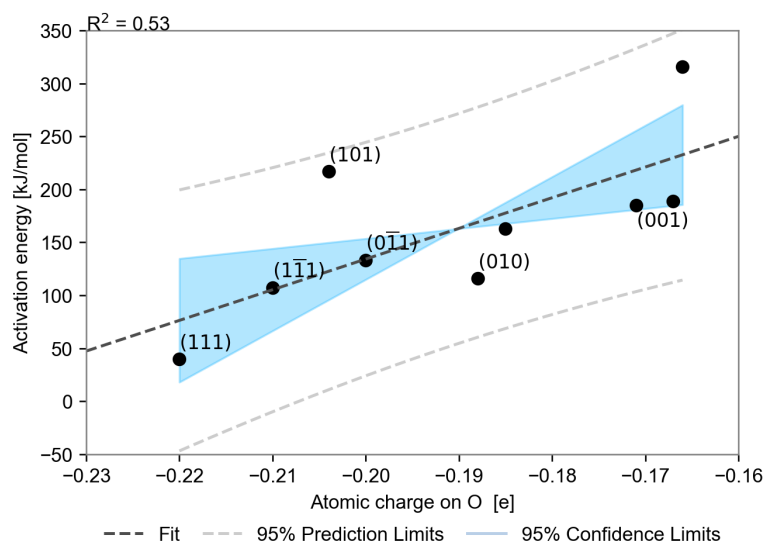


**Figure D.3.5:** Linear regression of the activation energy for the direct CO dissociation versus the atomic charge on the O atom, of all nine surfaces. The central line corresponds to the linear fit. The neighbouring grey lines and the blue coloured area indicate the 95% prediction limits and 95% confidence limits, respectively. The regression coefficients ( $R^2$ ) is shown in the left-top corner of the graph.

# Summary and Outlook

## Computational Modelling of the Fischer-Tropsch Reaction on Iron Carbides

### Summary

Over the last century, humanity witnessed a dramatic increase in its energy demand. Sustainable alternatives such as solar, geothermal and wind power are coming up, but they are relatively sparse at the moment and their growth rate is insufficient to bridge the gap to a society that runs solely on sustainable energy. In the past century, a significant amount of research and investment has been made to reduce the dependency on crude oil by the utilization of other carbon-containing resources. There remains significant interest in using coal in view of its abundance and the low prices in various parts of the world. A prominent heterogeneously catalysed process for the utilization of non-oil-based feedstocks is Fischer-Tropsch synthesis. Herein, synthesis gas derived from carbonaceous feedstock such as natural gas, coal or biomass is selectively converted to liquid fuels and chemicals. Nowadays, natural gas and coal are respectively being used as the feedstock in gas-to-liquid (GTL) and coal-to-liquid (CTL) processes. However, it is expected that biomass and CO<sub>2</sub> can be employed as the feedstock for the Fischer-Tropsch synthesis reaction in either a CO<sub>2</sub>-neutral or even “negative CO<sub>2</sub> emissions” scenario in the near future. The focus of this research has been to understand the Fischer-Tropsch mechanism on different carbidic phases of iron. Specifically, we investigated the FT reaction on the three main carbidic phases of iron, which are Hägg carbide ( $\chi$ -Fe<sub>5</sub>C<sub>2</sub>) (Chapter 3 and 4),  $\epsilon$ -Fe-carbide ( $\epsilon$ -Fe<sub>2</sub>C) (Chapter 5), and  $\theta$ -Fe-carbide ( $\theta$ -Fe<sub>3</sub>C) (Chapter 6).

In **Chapter 2**, an overview is provided for the employed computational methods and the underlying theoretical aspects. We show how stable geometries and transition states can be determined by density functional theory (DFT) and how microkinetic modelling can be used to determine reaction rates and other chemokinetic properties.

In **Chapter 3**, we explored CO adsorption and dissociation on 5 stable surface terminations of the Hägg carbide. The stability of all low-index Miller surfaces of the Hägg carbide was investigated. We then selected stable surfaces that contain stepped B<sub>5</sub>-like sites. Direct and H-assisted CO dissociation (via HCO and COH) were evaluated for these 5 surfaces. It was found that direct and H-assisted pathways for CO dissociation compete on these surfaces. Direct CO dissociation is preferred on B<sub>5</sub>-type surfaces that do not contain C atoms in the subjacent interstices of the Fe lattice and are characterized by strong CO adsorption. For the other surfaces containing subsurface C atoms, H-assisted mechanisms contribute to the overall rate of CO dissociation.

In **Chapter 4**, we explored the FT reaction on  $\chi$ -Fe<sub>5</sub>C<sub>2</sub> by a combination of quantum-chemical calculations and microkinetic modelling. We chose the planar (010)<sub>0.25</sub> and the corrugated (100) surface as model systems to describe the reactions on terrace and step-edge sites, respectively. DFT calculations show that surface oxygen removal by H<sub>2</sub>O formation has the lowest barriers on the corrugated (100) surface, whereas CO<sub>2</sub> formation is preferred on the (010)<sub>0.25</sub> surface. C-C coupling proceeds easiest through C-CH coupling on the (100) surface, while CH-CH coupling has the lowest barrier on the (010)<sub>0.25</sub> surface. Microkinetic modelling was performed for the (100) surface because CO dissociation has a barrier that is too high on the planar surface. Modelling was performed in the zero-conversion limit and in a CSTR model. There are no substantial differences between both models except for the lower olefins-to-paraffins ratio due to the re-adsorption and hydrogenation of olefins. The much lower olefins-to-paraffins ratio observed in experiments indicates that olefins re-adsorption occurs on other surface facets. We predicted a chain-growth probability of 0.5, meaning that C<sub>2</sub>-C<sub>4</sub> olefins are the main reaction products. With increasing temperature, the lower-olefins selectivity increases at the expense of the C<sub>5</sub>+ selectivity. The simulations show that H<sub>2</sub>O is the main O removal product, suggesting that primary CO<sub>2</sub> is not produced on this Fe-carbide phase. The results emphasize the importance of CO dissociation and O removal as rate-controlling steps, CH-CH and CH-CR coupling as the main mechanism for chain-growth and the formation of olefins as the primary hydrocarbon products. CO conversion rates are within one order of magnitude of experimental values, showing that step-edge sites are candidate sites for the FT reaction on Hägg carbide.

In a similar manner, we explored the FT reaction on  $\varepsilon$ -Fe<sub>2</sub>C in **Chapter 5**. DFT showed that CO dissociation proceeds *via* a H-assisted pathway on both the terrace (001) and the step-edge (011) surfaces. Oxygen removal as H<sub>2</sub>O has the lowest overall activation barrier on the (011) surface and involves a direct OH hydrogenation pathway. However, CO<sub>2</sub> formation exhibits the lowest overall barrier for O removal on the (001) surface. C-C coupling preferentially occurs on the (001) surface through C-CH<sub>2</sub> coupling, while CH-CH<sub>3</sub> coupling has the lowest barrier on the (011) surface. For the microkinetic modelling, only the (011) surface was used as the high CO dissociation barrier found for the (001) surface yields unrealistic (i.e. too low) CO consumption rates as compared to the experiment. It was found that C-O bond scission proceeds in a H-assisted manner *via* an HCO intermediate. Consistent with experiments, H<sub>2</sub>O is the main O removal product, suggesting that this carbide phase does not produce primary CO<sub>2</sub>. We showed that CH is the dominant building block in chain-growth, which proceeds mainly by CH-CH<sub>3</sub> and CH-CR coupling. Chain termination occurs by direct hydrogenation of a CHCR species. The overall CO consumption rate was found to be



controlled by the rate of the CH monomer insertion into the growing CHCR hydrocarbon chain. Monomer formation steps prior to monomer insertion were found to be very fast and correspondingly, the positive reaction order in  $H_2$  was contributed to the increased rate of C hydrogenation yielding a higher CH coverage and thus a higher rate of the dominant rate-controlling step. The overall CO consumption rate is mostly limited by coupling reactions with the CH chain-growth monomer. The low CO consumption rate, intermediate chain-growth probability and relatively high  $CH_4$  selectivity are inherent to the operation of  $\epsilon$ - $Fe_2C$  in the chain-growth limit.

In **Chapter 6**, we explored the stability and activity of different CO dissociation pathways on all low-index Miller surfaces of  $\theta$ -Fe-carbide. We found that the rate for direct CO dissociation is only high for surfaces that contain accessible  $B_5$  sites. A simplified kinetic model showed that the (111) surface, containing such a  $B_5$  site, displays the highest CO bond dissociation rate. The (0 $\bar{1}$ 1) surface displays the highest H-assisted CO dissociation, but with a lower activity than the (111) surface. The activation barrier for C-O bond dissociation correlates well with the bond order of adsorbed CO, which implies that pre-activation of CO is important for lowering the overall activation barrier. The present work shows that the high-temperature  $\theta$ - $Fe_3C$  phase is highly active towards CO bond dissociation, which is the essential first step in the Fischer-Tropsch reaction.

## Outlook

Despite the many insights obtained from combining microkinetic modelling with *ab initio* methods, many important phenomena in the Fe-catalysed Fischer-Tropsch reaction remain unclear. Many of these aspects pertain to assumptions fundamental to canonical microkinetic modelling and were thus outside the scope of this thesis, yet far from irrelevant. The two most critical assumptions are the static surface approximation and the mean-field approximation. Recent developments in computational modelling allow to take these aspects into account in the near future. By constructing chemically accurate force fields (e.g., ReaxFF or force fields based on artificial neural networks) that are trained by using DFT data, the modelling of larger systems and/or longer time scales can be pursued at similar accuracy as DFT. A phenomenon such as surface reconstruction under realistic conditions can be studied by, for instance, molecular dynamics simulations. Not only the evolution of a catalytic surface during operation can be studied, it would also be possible to study the activation of the catalyst. With respect to Fe-carbides, the carburization of bulk Fe metal in synthesis gas is an interesting topic. The latter topic is especially interesting as recent experimental studies revealed that the activity and selectivity of the Fe-FTS can be tuned by careful synthesis of pure Fe-carbides

starting from metallic Fe.[1] A prospect that is related to this thesis is that the DFT dataset can be used for the construction of such force fields.

Industrial Fe-based FTS-catalysts are promoted using alkali metals, such as Na and K, to enhance the activity and suppress undesired products. In a joint theoretical-experimental study de Jong and co-workers[2] showed that CH<sub>4</sub> selectivity can be suppressed by the addition of Na and S to an iron-based catalyst with an inert support, like carbon nanofibers or  $\gamma$ -Al<sub>2</sub>O<sub>3</sub>. Herein, the role of Na and S was attributed to the limitation of hydrogenation reactions, leading to an increased chain-growth and the termination step via  $\beta$ -hydride abstraction that cannot give rise to CH<sub>4</sub> production. It is reasonable to expect that promoting agents can fulfil multiple roles in the catalytic process. They can stabilize the nanoparticles, (de-)stabilize intermediates by electron redistribution or directly influence the elementary reaction steps by modification of the minimum energy pathways. Existing studies have mainly focussed on the effect of the stability on the intermediates.[3] A natural extension would be to study the involvement of Na/K atoms in the elementary reaction steps. For this, the dominant adsorption sites and surfaces of these atoms need to be established. The set of possibilities herein is most likely much larger than what is reasonable to study at the DFT level of theory. Hence, force field methods[4] or (non-) linear scaling laws[5, 6] are required to reduce the set of possibilities to a reduced list of candidate structures that are accessible at the DFT level of theory. Furthermore, using density of states, crystal orbital Hamiltonian population (COHP) and DDEC6 analysis techniques, the fundamental role of the promotor on the electronic structure can be studied in more detail from which important design principles can be established.

Mean-field kinetic modelling is usually done using barriers derived from potential energy surfaces determined at low surface coverage. However, typical catalytic surfaces under FT reaction conditions contain many different adsorbates, usually at a relatively high coverage. The effect of coverage on the reaction rate remains a topic of much debate. There are many prominent open research questions pertaining to this field: does a high surface coverage prevent the participation of particular active sites? How do reaction barriers for critical dissociation steps change as a function of surface coverage and how do these effects influence overall activity and product distribution? Another aspect is whether migration of adsorbates on different surface facets that occur on nanoparticles can influence the overall kinetics. Does high coverage prevent such migration by surface diffusion? To answer such challenging questions, the low-coverage mean-field approximation needs to be either loosened or preferably completely abandoned. Interestingly, Zijlstra et al. [7] recently showed that the effect of CO coverage on CO dissociation barriers depends strongly on the surface topology. The flexibility of the adsorbed CO layer at higher coverage on a

step-edge site led to an activation barrier nearly independent of CO coverage, whereas on a planar Co surface, increased CO coverage led to more difficult CO dissociation. Recent method development efforts (that are also used in this thesis) demonstrate that the incorporation of a lateral interaction potential can provide a solution towards describing the strong influence of higher coverage.[8, 9] Abandoning the mean-field approximation on the other hand requires the use of a different approach to solve the kinetics such as kinetic Monte-Carlo modelling. A drawback of the latter approach is that due to the serial nature of these simulations and thus the high computational cost associated, not many successful examples exist, wherein complex chemokinetic systems as large as the Fischer-Tropsch reaction are modelled.

The catalyst is the heart of many industrial chemical processes, yet it can be seen separately from the surroundings it operates in. Often, mass and heat transfer limit the performance of catalysts, implying that the full potential of a catalyst is not used or that unselective reactions may become dominant. This calls for an integrated approach where we could combine first-principles microkinetic theory able to predict kinetics in a wide range of conditions with a hydrodynamic description of chemical reactors. Strong concentration gradients in FT reactors can lead to a higher selectivity to undesired methane. Closely related to this is inefficient removal of the reaction heat, a particular challenge in the highly exothermic FT reaction. This leads to local hot spots in chemical reactors, a lower chain-growth probability and increased methane selectivity and possibly accelerated catalyst deactivation. At the moment, the direct incorporation of microkinetic models in computational fluid dynamics has not been done yet, but smart fitting of kinetic data using computationally cheap evaluation algorithms (e.g., look-up tables, multivariate splines or artificial neural networks) may be a way forward to implement microkinetics indirectly in such macroscale simulations of chemical processes.

## References

- [1] P. Wang, W. Chen, F.-K. Chiang, A.I. Dugulan, Y. Song, R. Pestman, K. Zhang, J. Yao, B. Feng, P. Miao, W. Xu, E.J.M. Hensen, Synthesis of stable and low-CO<sub>2</sub> selective  $\epsilon$ -iron carbide Fischer-Tropsch catalysts, *Science Advances* 4 (2018) eaau2947.
- [2] H.M.T. Galvis, J.H. Bitter, C.B. Khare, M. Ruitenbeek, A.I. Dugulan, K.P. de Jong, Supported iron nanoparticles as catalysts for sustainable production of lower olefins, *Science* 335 (2012) 835-838.
- [3] J. Xie, J. Yang, A.I. Dugulan, A. Holmen, D. Chen, K.P. de Jong, M.J. Louwerse, Size and Promoter Effects in Supported Iron Fischer-Tropsch Catalysts: Insights from Experiment and Theory, *ACS Catalysis* 6 (2016) 3147-3157.
- [4] A.C. Van Duin, S. Dasgupta, F. Lorant, W.A. Goddard, ReaxFF: a reactive force field for hydrocarbons, *The Journal of Physical Chemistry A* 105 (2001) 9396-9409.
- [5] Z.W. Ulissi, A.J. Medford, T. Bligaard, J.K. Nørskov, To address surface reaction network complexity using scaling relations machine learning and DFT calculations, *Nature communications* 8 (2017) 14621.
- [6] F. Calle-Vallejo, D. Loffreda, M.T. Koper, P. Sautet, Introducing structural sensitivity into adsorption-energy scaling relations by means of coordination numbers, *Nature chemistry* 7 (2015) 403.
- [7] B. Zijlstra, R.J.P. Broos, W. Chen, H. Oosterbeek, I.A.W. Filot, E.J.M. Hensen, Coverage Effects in CO Dissociation on Metallic Cobalt Nanoparticles, *ACS Catalysis* 9 (2019) 7365-7372.
- [8] B. Zijlstra, R.J.P. Broos, W. Chen, I.A.W. Filot, E.J.M. Hensen, First-principles based microkinetic modeling of transient kinetics of CO hydrogenation on cobalt catalysts, *Catalysis Today* (2019).
- [9] L.C. Grabow, B. Hvolbæk, J.K. Nørskov, Understanding Trends in Catalytic Activity: The Effect of Adsorbate-Adsorbate Interactions for CO Oxidation Over Transition Metals, *Topics in Catalysis* 53 (2010) 298-310.

## List of Publications

### Publications within the scope of this thesis:

A quantum-chemical study of CO dissociation mechanism on low-index Miller planes of  $\Theta$ -Fe<sub>3</sub>C, Broos, R.J.P., Klumbers, B., Zijlstra, B., Filot, I.A.W. & Hensen, E.J.M., 2019, (Accepted/In press) In : Catalysis Today.

Quantum-Chemical DFT Study of Direct and H- and C-Assisted CO Dissociation on the  $\chi$ -Fe<sub>5</sub>C<sub>2</sub> Hägg Carbide,

Broos, R. J. P., Zijlstra, B., Filot, I. A. W. & Hensen, E. J. M., 10 May 2018, In : Journal of Physical Chemistry C. 122, 18, p. 9929-9938 10 p.

Carbon-efficient conversion of synthesis gas to linear  $\alpha$ -olefins by a highly active  $\chi$ -iron-carbide based catalyst,

Wang, P, Chen, W, Chiang, F.-K., Dong, J., Dugulan, A. I., Broos R.J.P., Feng, B., Chai, J., Song, Y., Lv, Y., Lin, Q., Wang, R., Filot, I.A.W., Men, Z. and & Hensen, E. J. M. (submitted)

### Publications outside the scope of this thesis:

First-principles based microkinetic modeling of Fischer-Tropsch synthesis on cobalt  
Zijlstra, B., Broos, R.J.P., Chen, W., Bezemer, G.L., Filot, I.A.W., Hensen, E.J.M.  
(*in preparation*)

Coverage effects in CO dissociation on Metallic Cobalt Nanoparticles

Zijlstra, B., Broos, R.J.P., Chen, W., Oosterbeek, H., Filot, I. & Hensen, E., 2019, (Accepted/In press) In: ACS Catalysis.

First-principles based microkinetic modeling of transient kinetics of CO hydrogenation on cobalt catalysts, Zijlstra, B., Broos, R.J.P., Chen, W., Filot, I.A.W & Hensen, E.J.M., 2019, (Accepted/In press) In: Catalysis Today.

Kinetic aspects of chain-growth in Fischer-Tropsch synthesis

Filot, I. A. W., Zijlstra, B., Broos, R. J. P., Chen, W., Pestman, R. & Hensen, E. J. M., 1 Apr 2017, In : Faraday Discussions. 197

A quantum-chemical DFT study of CO dissociation on Fe-promoted stepped Rh surfaces, Filot, I. A. W., Fariduddin, F., Broos, R. J. P., Zijlstra, B. & Hensen, E. J. M., 15 Oct 2016, In: Catalysis Today. 275, p. 111-118 8 p.

First-principles-based microkinetics simulations of synthesis gas conversion on a stepped rhodium surface,

Filot, I. A. W., Broos, R. J. P., van Rijn, J. P. M., van Heugten, G. J. H. A., Santen, van, R. A. & Hensen, E. J. M., 2015, In : ACS Catalysis. 5, 9, p. 5453-5467 15 p.

## Acknowledgements

At this point I would like to thank everyone who has made it this far in my thesis (or has started here and is reading my thesis from back to front). Doing research can feel, every now and then, like sitting in a rollercoaster in the dark: Sometimes you progress slowly up, only to go rapidly back down, with a lot of sharp turns and every once in a while a looping and you don't see any of it coming in advance. Yet, when the ride is over, you feel relief and satisfaction at the same time. And, as it is with most research, *"If you're not failing every now and again, it's a sign you're not doing anything very innovative."* (Woody Allen)

The first person I would like to thank is my first promotor, Emiel Hensen. Emiel, thank you for giving me the opportunity to do my PhD project in the IMC group. I had a wonderful time in your group and I have learned a lot from you. Our discussions and your critical feedback have always led to improvements in my work and in this thesis. I am also very grateful for the opportunities you gave me to present my work abroad. You really pushed me and helped me get the very best out of myself. *"The teacher who is indeed wise does not bid you to enter the house of his wisdom but rather leads you to the threshold of your mind."* (Khalil Gibran)

The next person who I would sincerely like to thank is my co-promotor, Ivo Filot. Ivo, I have known you for a very long time and you have inspired me to start in the IMC group. You are a good teacher and it is safe to say that most of my knowledge about theory and computational modelling came from you. Your feedback and help with the complex iron carbide systems and your help with making wonderful pictures was much appreciated. *"Capabelheid is een keuze."* (Ivo Filot)

I would like to thank prof.dr.ir. Krijn de Jong, prof.dr. Gadi Rothenberg, dr.ir. Bernd Ensing, prof.dr.ir. Hans Kuipers and dr.ir. John van der Schaaf for being part of my committee and making time to read my thesis and attend my defence ceremony. *"If I have seen further than others, it is by standing upon the shoulders of giants"* (Isaac Newton)

Bart and Michel, thanks for being my paranymfen during my defence! Bart, you have been my office mate and friend for a long time. You were always prepared to help me out with making beautiful pictures and discussing microkinetic results, even if you were very busy or approaching a deadline yourself. Thanks to you I now know that the answer should never be 106, unless it is, but then it is probably wrong. Michel, I got to know you when you started in our group as a PhD. We had quite some fun during the MCEC activities and I enjoyed travelling to these activities with you. I have



also enjoyed our discussions with both of you guys during lunch time and during drinks. *“True friends are like diamonds; bright, beautiful, valuable, and always in style” (Nicole Richie)*

By the time I have printed my thesis, I have had the pleasure to be paranymf myself in three defences, Farid, Jan and Bart. Thank you for this honour. Farid, you are a very kind soul and have worked very hard to obtain your PhD, but you succeeded. We share a wonderful publication together. Jan, unfortunately you cannot be my paranymf or even attend my defence ceremony. I wish you all the best of luck in Japan, I hope to be able to visit you some day in 札幌市. *“Nothing makes the earth seem so spacious as to have friends at a distance; they make the latitudes and longitudes.” (Henry David Thoreau)*

I want to thank our mini (early-morning) coffee group for their non-scientific discussions about things like the news, Bart, Lingqian, Johan, thank you. We gathered after two hours of working (around 9:00 am) and had short discussions in exactly the same setup every day. Lingqian, I absolutely liked the hot-pot at your house and I enjoyed your hospitality. *“Coffee in, thesis out” (Geniuslabgear.com)*

Tiny, drinking beer with you or solving AIVD kerstpuzzel questions was a real joy for me. There was never a dull moment during lunchtime and I liked your initiative for social activities, like the “men’s night”, going to Slokop Festival in Landhorst or just going to the F.O.R.T. Thank you for the nice times. *“Concordia res parvae crescent” (Gaius Sallustius Crispus)*

Emma, I would like to thank you for your help with all kinds of administrative tasks and of course for the small chats just before entering Emiel’s office. Your bouldering laugh can make a smile on anyone’s face. *“A day without laughter is a day wasted” (Charlie Chaplin)*

I would like to thank the rest of the IMC group members and students, Dimitra, Aleksei, Francesco, Jiachun, Ming-Wen, Lulu, Wei, Marta, Ferdy, Gabriela, Adelheid, Marco, Mónica Yanan, Jan Philipp, Tobias, Nikolay, Panos, Megyan, Shaojie, Liang, Yujie, Zhaochun, Anna, Mengyu, Brahim, Valerii, Freddy, Dannie, Xianhong, Sasha, Aleksei, Robert, Nitin, Floriane, Douglas, Jerome, Tan, Peng, Tim, Xiaofeng, Miao, Hao, Long, Yue, Jiadong, Jasper, Koen, Roos, Michelle, Job, Anouk, Cas, Mariska, Micha, and many others I might have forgotten to name here. *“Great things in science are never done by one person; they’re done by a team of people” (Based on a quote by Steve Jobs)*

Besides the people from the IMC group, I would also like to thank the people from Hybrid Catalysis and other old IMC members for the nice conversations during coffee and during the Friday afternoon

drinks, Arjan, Jos, Gijsbert, Erik, Yoran, William, Marriet, Coen, Remco, Gilbère, Arno, Andreas, thank you. *“It’s 5 o’clock somewhere.” (Jimmy Buffett)*

I want to thank the people I have met during my time at the Scheikundig Technologisch Dispuut Prometheus. Sandra, Peter, Lukas, Tom, Patrick, Joris, Gert-Jan, Juliën, Roderigh, Paul and many more; thank you. *“In Igni Confidimus” (22<sup>nd</sup> senate of Scheikundig Technologisch Dispuut Prometheus)*

There are also some people who helped me relax outside office hours. Thank you to the people from “Tegeltjeswijsheid”, our regular pubquiz team from the Wildeman. Thank you Pepijn, Rim, Jessica, Steven, Eva. I would also like to thank “Nothing cooler than absolute zero” for the times we went pubquizzing in the Carousel. Koen, Jolanda, Robin, Erik. *“None of us is as smart as all of us.” (Ken Blanchard)*

I was fortunate to meet a lot of nice people outside of the university as well. I would like to thank Hemmo and Sanne, my favourite drinking buddies from the good old days at the Bunker and later in Hubble. Thank you for the great times we spent together. *“To alcohol! The cause of... and solution to... all of life's problems” (Matt Groening)*

After a day of hard work, there was no better place for me than the dance floor. The combination of body and brain training was a great exercise for the entire body. As such, it helped me to stay physically and mentally fit and it contributed to the improvement of my social skills. I would like to thank my dance partners and my other friends from Footloose, who have helped me stay fit and relax after a hard day of work. Thank you Eline, Shari, Irene, Olga, Kristina, Wendy, Iris, Yvette, Heleen, Joy, Dio, Maaïke, Stephanie, Sara, Pepijn, Christiaan, Jesper, Kai, Diana, Sam, Lennard, Renée, Kahoo, Jean, Joep, Dennis, Ellen, Cansu, Florian, Mike, and many others I did not mention in this list. I would also like to thank my fellow board members from the 24<sup>th</sup> board of Footloose, Sabrina, Ιάσον, Steven and Dave. *“Dance is the hidden language of the soul.” (Martha Graham)*

Special thanks go to Olga, you have given me a great deal of support during our time together, it was hard leaving you in the morning to go to work. I am very grateful for the time we spend together, and the hours of showcase training for the performances we did at the Parktheater. *“I know you baby” (Skylar Grey)*

Ik wil ook graag mijn familie bedanken voor de steun die ze gegeven hebben en de interesse die ze hebben getoond voor mijn werk over de gehele periode van mijn PhD. Pa, Ma, Wouter, bedankt voor de vele gezellige weekenden en feestdagen in Roosendaal. Wouter, jij hebt mij de nodige keren

kunnen helpen met mijn engels en bent één van de weinigen (en misschien wel de enige buiten mijn vakgebied) die mijn hele thesis gelezen heeft. Ik koester de momenten met jullie en dit heeft mij vaak rust bezorgd, zodat ik daarna weer fris aan de slag kon met mijn onderzoek. Aan alles komt een eind, of meer, het begin van iets nieuws. *“How lucky I am to have something that makes saying goodbye so hard.” (A.A. Milne)*

Now all that is left for me to say is: bedankt, thank you, vielen dank, merci, gracias, obrigada, спасибо, 谢谢, mulțumesc mult, teşekkürler, ευχαριστώ, dè ge bedankt zét dé witte, bedanktj, betanke.

## Curriculum Vitae

Robin Johannes Petrus Broos was born on 10-07-1989 in Roosendaal en Nispen, The Netherlands. After finishing his pre-university education in 2008 at the Gertrudiscollege in Roosendaal, he retained his Bachelor of Science degree in Chemical Engineering at Eindhoven University of Technology in 2012 and continued his Master of Science in Molecular Engineering at the Eindhoven University of Technology, which he finished in 2014 with the distinction *met grote waardering*. He graduated within the Inorganic Materials and Catalysis group of prof. dr. ir. Emiel Hensen. His graduation project was co-supervised by dr. ir. Ivo Filot and was entitled “The Fischer-Tropsch reaction on a stepped (211) rhodium surface”. In 2015 he started a PhD project under the supervision of prof. dr. ir. Emiel Hensen at the Eindhoven University of Technology in the Netherlands, of which the results are presented in this dissertation.



